Higgs to charm at ATLAS from today to tomorrow

by

Xiong Junwen

A dissertation submitted in partial satisfaction of the

requirements for the degree of

Doctor of Philosophy

in

Physics

in the

Graduate Division

of the

University of California, Berkeley

Committee in charge:

Professor Heather Gray, Chair
Professor Kam-Biu Luk
Professor Karl van Bibber

Fall 2024

Higgs to charm at ATLAS from today to tomorrow

Abstract

Higgs to charm at ATLAS from today to tomorrow

by

Xiong Junwen

Doctor of Philosophy in Physics

University of California, Berkeley

Professor Heather Gray, Chair

The Higgs boson, the mass mediator in the Standard Model (SM) of particle physics, was discovered at the Large Hadron Collider (LHC) in 2012. Since then, measuring the decays of the Higgs boson to fermions and validating the SM prediction have been one of the main physics goals of the LHC. The Higgs boson to bottom quark decay ($H \to b\bar{b}$) has been observed by the ATLAS collaboration during the LHC second data run (Run 2). Similarly, upper limits have been set on the probability of the Higgs boson decaying to charm quarks ($H \to c\bar{c}$) using ATLAS Run 2 data.

This thesis presents the latest ATLAS combined measurement of the Higgs boson decays to bottom and charm quarks using Higgs produced in association with vector bosons ($VH \to b\bar{b}, c\bar{c}$). Novel machine learning techniques are used to improve signal purity. The most stringent upper limits are set on $\mu_{VH(c\bar{c})}$ and κ_c to date. The observed (expected) $\mu_{VH(c\bar{c})}$ upper limit is set to 11.3 (10.4) times the SM at the 95% confidence level (CL). The observed (expected) κ_c upper limit at the 95% CL is $|\kappa_c| < 4.2$ (4.1). The expected $\mu_{VH(c\bar{c})}$ upper limit is 3 times smaller compared to the previous analysis. In addition, the measurement sets a stringent constraint on the ratio between the charm and the bottom Yukawa coupling modifiers (κ_c/κ_b) as well. The observed (expected) κ_c/κ_b upper limit at the 95% CL is $|\kappa_c/\kappa_b| < 3.6$ (3.5).

Improving flavor tagging performance can further improve the $VH(\to c\bar{c})$ sensitivity. Including electrons and muons from b-jet and c-jet decays can improve the current flavor tagging performance by around 20%. Furthermore, the current $H \to c\bar{c}$ sensitivity is limited by the available data statistics. To improve the sensitivity in the future, increasing the dataset is the key. At the HL-LHC, the ATLAS detector will collect 3000 fb^{-1} of data over 10 years, almost 20 times more data than the latest Run 2 analysis. However, to cope with the increased data rate and radiation damage, various radiation hardness tests are needed for the innermost layer of the HL-LHC ATLAS detector to inform the detector design and operation. This thesis also presents the first X-ray irradiation campaign at the Berkeley Lab

on testing the prototype inner tracker readout chip, ITkPixV1. The X-ray dose rates are carefully calibrated and the measured ITkPixV1 radiation damage agrees well with the expectation, paving way for future X-ray radiation testing on site for inner tracker production and operation.

Contents

List of Figures

List of Tables

Acknowledgments

I would like to thank everyone who helped me along my PhD. The past six years were challenging and memorable. I would never be able to finish this thesis and enjoy the PhD time without all the support, encouragement, and patience along the way.

First, I would like to thank my advisor, Professor Heather Gray. I'm really grateful for your guidance, wisdom, and presence in the past 4 years, from joining the group, passing the qual exam, finishing the qual task, starting the thesis analysis, moving to CERN, looking for a job, and now writing my thesis. Thanks so much for your firm words whenever things got too stressful and I literally burst into tears. Thanks so much for the detailed comments and unique insights on all my presentations, application materials, and now the thesis! Thanks so much for always pushing me to do better and learn more whenever I feel doubtful or worried.

I am also very grateful for the legacy analysis team, all of the analysis contacts and teammates! Many thanks to Hannah, Elisabeth, and Yanhui for always being so supportive of all the studies and attentive to details and the physics behind. Many thanks to all the fellow teammates, Aoto, Lakmin, Zhuoran, Ricardo, Jingyi, Punit, Romain and many more for all the work we did together, fun meeting discussions and social gatherings! I really appreciate the time at CERN working on the analysis.

I would like to thank Timon, Maurice, Karol, Daniel, Jason, and Hongtao for all the help and efforts in delivering the X-ray irradiation results as well! Many thanks to Timon and Maurice for all the amazing knowledge about RD53B and hardware. Many thanks to Hongtao for all the time working in the pixel annex during COVID with KN95 and Honeywell. Thanks so much for your diligence and all the advice and kindness!

I sincerely enjoy my time at the LBL ATLAS group and would like to thank all my groupmates for this wonderful experience. I would like to thank our group leader, Kevin, for dealing with all the logistic nightmares and looking after everything. Many thanks to our admin, Adam, for heroically handling all the trip logistics. I would like to thank Marjorie for all the candid advice and deep understanding of particle physics. Many thanks to all my groupmates, Ryan, Rebecca, Johannes, Miha, Miao, Zhicai, Jay, Stella, and many more for all the fun time together. Many thanks to Tomohiro for always patiently guiding me through the soft electron study and all the detailed advice on entering the gigantic ATLAS collaboration. And, to LG, Carlo, and Aleksandra, thanks so much for all the R1 lunches! Thanks Fabio for all the Wed coffee! And, special thanks to Aleksandra for diligently celebrating all birthdays and farewells, for all the delicious cakes.

And, I would like to sincerely thank Irina for all the time we worked together on the legacy analysis. Thanks so much for commiserating over bad days for physics and for your watertight merge requests. The analysis work becomes much less stressful with your help. I would also like to thank Maria for all the help with the chip radiation, the legacy analysis, the job search, and the thesis writing. Thanks so much for being my mentor and answering all my stupid questions! Thanks so much for your optimism, high energy, and dexterity with everything! Every maze feels simple when you are leading the way.

I would also like to thank Professor Kam-Biu Luk, Professor Dan Stamper-Kurn, and Professor Saul Perlmutter for giving me the opportunities to explore different research directions. It was a formative and memorable experience. I would also like to thank everyone who helped me during my job search! Many thanks to Heather, Hannah, Kevin, Maurice, Maria, Miao, Aleksandra, Zhicai, and many more. It was very enlightening to see a potential career path from my PhD and thesis work.

Lastly, I would love to thank all my classmates, department, friends, and family for all the support and love in the past 6 years. The PhD experience would be incomplete without you. Many thanks for my cohort, Lizzy, Ben, Yang, Max, Trevor, Tomo, Chi, and many more. For all the COVID zoom reading clubs and time together. Many thanks to Joelle, Donna, and all the administration staff for the smooth PhD teaching and research experience! Many thanks to all of my roommates, Elsie, Jerry, Andre, Florian, and Khoi for all the support and laughter. Thanks Raj for diligently helping me with everything. It is nice to know you all! I would like to especially thank Chiyon for all the therapy sessions and help along the way. And, to my dear parents and family, thanks so much for always being by my side! Many thanks to my dad for listening to all my complaints and worries. Many thanks to my mom for always taking care of my well-being. And, to my grandmas, thanks so much for trying so hard to understand my work and life across the sea! 感谢大家!

I would also like to thank the time at Berkeley, which reinforces my belief in diversity, equity, and inclusion. As a Chinese graduate student, I often found that it is difficult to maintain my identity in the United States. Many thanks to my family and friends and everyone who spent time listening to my fears and furies and sympathizing with my experience. I would love to write my name in its original Chinese characters, Xiong Junwen (熊君雯), in the thesis. However, the Berkeley graduate division does not currently allow non-English characters for author names. I wish this rule can change in the future and people are permitted to keep non-English characters in their names as the thesis authors. 海上生明月，天涯共此时。

Preface

The work presented in the thesis was completed within the ATLAS collaboration. The thesis aims to outline the background and key points of all projects, with my own contributions explained in detail.

Search for Higgs boson decays to charm quarks I was one of the main analyzers and internal note writers for the latest ATLAS Run 2 $VH(\to b\bar{b}, c\bar{c})$ analysis. The analysis results are recently published [1]. The analysis is discussed in Chapter 4. The published plots are labeled "ATLAS Preliminary". Other plots are labeled "ATLAS Work in Progress" as the plots are not approved for public distribution. My main contributions focus on the $VH(\to c\bar{c})$ phase space and are listed below:

- Validated the nominal and alternative Monte Carlo samples of the leading background processes, Z+jets, by checking its yields and shapes.
- Derived the uncertainties over Z+jets acceptance ratios from all nominal variations and alternative samples. Co-developed the uncertainty calculation framework in Python adaptable for other samples such as top and diboson backgrounds.
- Derived the uncertainties of Z+jets shapes using CARL, a machine learning reweighting algorithm. First tested the CARL shape uncertainties in the profile likelihood fit, and established the work flow for other CARL shape derivations.
- Incorporated all Z+jets uncertainties in the profile likelihood fit. Investigated all Z+jets nuisance parameter pulls and constraints to validate the fit performance. And, updated the fit framework, such as nuisance parameter correlation, merging or splitting fit regions, and changing fit variables, to better constrain all the uncertainties.
- Developed the κ interpretation framework and likelihood scan framework for final result interpretations. Validated the unblinded $VH(\to b\bar{b}, c\bar{c})$ results for the $VH(\to c\bar{c})$ 2-lepton phase space in addition to the main published results.

Radiation tolerance testing of ITkPixV1 I was the main person establishing the Berkeley Lab X-ray radiation testing facility and conducted the first month-long radiation campaign of the ITkPixV1 at Berkeley Lab. The results are summarized in Chapter 5. ITkPixV2 has been carefully tested and approved for production. My main contributions to testing ITkPixV1 are listed below:

- Set up the motion stage and the diode fixture for the X-ray calibration. Built the calibration control software for the xy stage, diode readout, and X-ray machine.
- Conducted 12 hour-long calibration measurements for detailing the X-ray dose rates in 2D planes at various z positions and X-ray tube currents. Validated that the X-ray

dose rates decrease with decreasing currents and the beam size increases further from the tube. And, confirmed the ideal dose rate and position for ITkPixV1 irradiation.

- Set up the ITkPixV1 irradiation box with stabilized Peltier cooling, X-ray, chip, and environment monitoring. Conducted the first month-long X-ray irradiation campaign of ITkPixV1 in Berkeley and characterized the chip threshold and ring oscillator performance before and after 415-Mrad irradiation. Confirmed that the ring oscillator radiation damage is as expected.

Soft-electron tagger for the flavor-tagging algorithm I was the main person incorporating the soft-electron information into the current flavor-tagging algorithm `DL1d`. `DL1d` uses deep neural networks (DNN) to differentiate heavy-flavor jets. The results are summarized in Section 3.4. The soft-electron variables are currently being considered for the latest ATLAS flavor tagging algorithm, GN1. My main contributions to developing the soft-electron tagger are listed below:

- Developed and optimized the soft-electron selection criteria and electron variables for the flavor-agging algorithm using the official Monte Carlo samples for `DL1` trainings. Confirmed that the latest DNN electron identification algorithm can effectively select soft electrons.

- Trained `DL1re` and `DL1de` and demonstrated 30% improvements for light-jet rejection compared to baseline `DL1r` and `DL1d`. Tested various settings for hyperparameters using `Optuna` and confirmed that the default setting is optimal.

Chapter 1

Introduction

The history of mankind is about exploration. From the Stone Age, to Confucius, Renaissance, and Industrial Revolution, the intricacy of philosophy, art, and technology is developed and explored to an unprecedented scale. At large scales, we can now explore the history of universe from billions of years ago. At small scales, high-energy colliders enable us to probe a distance less than 10^{-18} m. Ever since Rutherford discovered the proton, a particle smaller than an atom, the quest to explore the elementary building blocks began. Today, after decades of studies, we understand that protons are made of quarks. Similar to the periodic table of elements in chemistry, the 26 known elementary particles are organized in the Standard Model of particle physics.

The Standard Model of particle physics has been developed by both experimental evidence and theoretical postulates. The framework successfully explains the interactions between all elementary particles except gravity. The discovery of the Higgs boson in 2012 at the ATLAS and CMS experiments at the Large Hadron Collider (LHC) was one of the strongest proofs of its validity. Ever since the discovery, there have been a plethora of studies on the newly discovered Higgs boson. All further confirm the Standard Model predictions of the Higgs decays, productions, and other properties. However, we know the story does not end with the current Standard Model of particle physics. Evidence from cosmology points to matter components beyond the known elementary particles. And, Higgs boson, the only scalar particle in the Standard Model and the mass mediator, might be a portal to any new physics currently hidden from sight.

While most Higgs decay channels have been measured, the Higgs boson couplings to lighter quarks are difficult to probe in the LHC due to the busy hadronic environment in proton-proton collisions and the small coupling constants to light masses. This thesis presents the latest ATLAS Higgs to charm search using the Run 2 dataset recorded from 2015 to 2018. The expected $VH(\rightarrow c\bar{c})$ signal strength upper limit is improved by a factor of three compared to the previous analysis, thanks to novel machine learning tools [1, 2]. The analysis also includes the Higgs to bottom phase space, setting a stringent upper limit on the ratio between the charm and the bottom Yukawa couplings.

The excitement of particle physics lies in discovering new physics beyond the current

Standard Model. This may be achieved by accessing higher energies or better precision. While machine learning has been widely used in ATLAS measurements to improve the signal sensitivity, pushing to even higher precision requires more data. The high-luminosity LHC (HL-LHC) aims to deliver 20 times more data than Run 2 from 2029 to 2040. However, the increased luminosity at the HL-LHC means even busier background environment and high radiation damage for the ATLAS detector. The innermost layer of the ATLAS detector thus needs substantial upgrades. This thesis also presents results in characterizing the ATLAS high-luminosity LHC inner-tracker readout chip radiation hardness.

The thesis is structured as follows. Chapter 2 provides a brief overview of the Standard Model of particle physics and the Higgs phenomenology at the LHC. Chapter 3 introduces the Run 2 ATLAS detector and object reconstruction. Chapter 4 discusses the $VH(\rightarrow b\bar{b}, c\bar{c})$ analysis in detail. Chapter 5 gives an overview of the ATLAS high luminosity upgrades, discusses the basic silicon detector properties relevant to the inner tracker upgrade, and describes the first X-ray radiation campaign on the inner tracker readout chip at Berkeley. Chapter 6 gives a brief summary and an outlook for the thesis.

Chapter 2

Theoretical background

The Standard Model of particle physics (SM) was first proposed in the 1970s to explain various phenomena discovered about elementary particles [3]. Since then, the SM has been studied and developed by many particle physics theorists and experimentalists. In this thesis, the SM is the theoretical basis in which results from the Large Hadron Collider (LHC) and the ATLAS experiment can be motivated and interpreted. Section 2.1 discusses the Standard Model theories. Section 2.2 introduces the relevant phenomenology for the LHC and the Higgs boson.

While the SM is hugely successful in explaining various phenomena, in particular the Higgs physics, there are many open questions to be resolved. The energy scale Λ at which new physics occurs may be well above the energy scales that the LHC or future colliders can probe. Looking for hints of beyond the SM (BSM) physics in all possible corners might be the main focus of particle physics for generations to come.

2.1 The Standard Model of particle physics

The Standard Model of particle physics describes the elementary particles and their interactions. The interactions can be summarized in the SM Lagrangian, as discussed in Section 2.1.1. The SM describes three of the four fundamental forces: electromagnetism, strong interactions, and weak interactions [4, 5, 6]. Electromagnetism and weak interactions are *unified* as electroweak (EW) interactions by the Glashow-Salam-Weinberg (GSW) model [7]. However, so far, the SM cannot describe the fourth fundamental force, gravity.

The fundamental interactions in the SM are described by Lorentz invariant quantum field theory (QFT). QFT describes quantum mechanics in the relativistic regime. All elementary particles are treated as fields in QFT. In addition, the SM respects local gauge symmetries. That is, the SM Lagrangian is invariant under local gauge transformations. The symmetry is local, as it is space-time dependent. The SM gauge symmetry is:

$$SU(3)_C \times SU(2)_L \times U(1)_Y \tag{2.1}$$

SU(3), SU(2), and U(1) are all Lie groups with specific Lie algebra and generators of the respective group [8]. In addition to the local symmetries in Equation 2.1, the SM also respects some global symmetries such as charge conservation [4]. Here, charge refers to the electric charge of particles.

Among the three fundamental forces, the strong interaction is governed by *quantum chromodynamics* (QCD) and respects the SU(3) color symmetry. The weak interaction respects the SU(2) left symmetry, as the weak interaction only involves left-handed particles. Electromagnetism is described by quantum electrodynamics (QED) and obeys the U(1) QED symmetry. As mentioned above, electromagnetism and weak interactions are *unified*. The unified electroweak interactions respect the $SU(2)_L \times U(1)_Y$ symmetry. Here, Y stands for hypercharge. More details about QCD, electroweak interactions, and gauge symmetries are discussed in Section 2.1.1. In addition to local gauge symmetries, the masses of elementary particles are generated by electroweak symmetry breaking or the Brout-Englert-Higgs (BEH) mechanism [9]. The BEH mechanism is discussed in Section 2.1.2.

Interaction strengths The three fundamental interactions described in the SM are characterized by different coupling strengths. The fine structure constant α is the coupling strength of QED.

$$\alpha(m_e) = \frac{e^2}{4\pi} \approx 1/137 \tag{2.2}$$

All SM formulas in the thesis use the natural unit: $\hbar = c = 1$. Here, c is the speed of light, $\hbar$ is the reduced Planck constant, $e = 0.303$ is the electric charge, and m_e is the electron mass. The coupling strengths are evaluated at specific energies. The strong interaction coupling strengths are α_s and g_s. The coupling strength α_s follows the convention in the fine structure constant and has a factor of 4π compared to g_s.

$$\alpha_s(m_Z^2) = \frac{g_s^2}{4\pi} \approx 0.118 \tag{2.3}$$

where m_Z is the Z-boson mass. The weak interaction coupling strengths are α_W and g.

$$\alpha_W = \frac{g^2}{4\pi} \approx 1/30 \tag{2.4}$$

The QED and the strong interaction coupling strengths α and α_s are evaluated at $q = m_e$ and $q^2 = m_Z^2$, where q is the force carrier momentum. This is due to the *running* of coupling constants. That is, the interaction strength depends on the scale at which it is evaluated. More details are discussed in Section 2.1.1. At the energy scales discussed above, the strong-interaction strength is the largest among the three interactions. The weak interaction coupling strength is larger than the electromagnetic interaction. However, electroweak interactions are suppressed by $1/v^2$, where v is the vacuum expectation value around 246 GeV. At a low-energy scale around 100 GeV, the weak interactions are negligible.

Elementary particles All SM elementary particles are listed in Figure 2.1. There are three types of particles: *matter particles*, *vector bosons*, and *scalar boson*.

- **Matter particles:** The matter particles are fermions with spin 1/2. In the SM Lagrangian, they are represented as Dirac spinors, which are 4-component wave functions and satisfy the Dirac equation. There are three generations of matter particles, with the first generation being the lightest particles and the third generation the heaviest. Within the matter particles, there are two types:
  - *Quarks:* Quarks have color charge and interact through strong interactions in addition to electroweak interactions. The color charge for strong interactions are equivalent to the electric charge in electromagnetism. The *up*, *charm*, and *top* quarks can be grouped as the *up-type* quarks. The electric charge of the up-type quarks is 2/3 and that of the down-type quarks is -1/3.
  - *Leptons:* The leptons are colorless and interact only through electroweak interactions. Neutrinos are chargeless, while electrons, muons, and tau-leptons have a -1 electric charge. From neutrino oscillation experiments, neutrinos are known to have small mass. The current electron anti-neutrino mass limit is set at 0.8 eV, orders of magnitude smaller than the known electron mass [10]. There are three neutrino flavors: electron, muon, and tau flavor neutrinos.
- **Vector bosons:** The force carriers for the three forces described in the SM are vector bosons with spin 1. As the forces respect the SM gauge symmetry, the vector bosons are also called gauge bosons. Gluons are the force mediator of QCD. Photons are the force mediator of QED. W bosons are the force mediator of weak interactions, which is chiral and violates the parity. Together, photons, W and Z bosons are the force mediators of electroweak interactions. Gluons and photons are massless. W and Z bosons are massive. Gluons, photons, and Z bosons have zero charge. W bosons have ± 1 electric charge, W^+ and W^-. More details about vector boson interactions are discussed in Section 2.1.1.
- **Scalar boson:** There is only one scalar, i.e. spin-0, boson in the SM, the Higgs boson. The Higgs boson is generated from the BEH mechanism. The Higgs boson breaks the electroweak symmetry $SU(2)_L \times U(1)_Y$ to $U(1)_{QED}$. This generates mass for the $W^{\pm}$ and Z bosons and keeps the photons massless. More details of the interactions between the Higgs boson, vector bosons, and matter particles are discussed in Section 2.1.2.

In addition to particles, there are *antiparticles*. Particles and antiparticles have the same properties such as mass and spin. However, when particles have charge, the antiparticles have the opposite charge as the particles. In the SM Lagrangian, particles undergo *charge conjugation* to become their antiparticles. The photon, the Z boson, and the Higgs boson are their own antiparticles. Whether neutrinos are their own antiparticles is currently investigated by many neutrinoless double beta decay ($0\nu\beta\beta$) experiments [11]. The anti-gluons have the anti-color charge of gluons. More details are discussed in Section 2.1.1.1.

In the SM, the weak interaction has *chirality*. The chiral states are the eigenstates of the γ^5 matrix. The γ^5 matrix is defined by four 4×4 Dirac matrices, where $\gamma^5 = i\gamma^0\gamma^1\gamma^2\gamma^3$. A particle can be decomposed into its left-handed and right-handed chiral components. The chiral states of a fermion field ψ can be written in terms of the left-handed and right-handed projection operators: $P_R = 1/2(1 + \gamma^5)$ and $P_L = 1/2(1 - \gamma^5)$.

$$\psi = P_L\psi + P_R\psi = \psi_L + \psi_R \tag{2.5}$$

Here, ψ_L and ψ_R are the left- and right-handed components of ψ. At high energies, the chiral eigenstates are approximately the same as the helicity eigenstates. The spin is parallel to the momentum for right-handed particles and anti-parallel for left-handed particles. In weak interactions, W bosons interact only with *left-handed* particles and *right-handed* antiparticles.

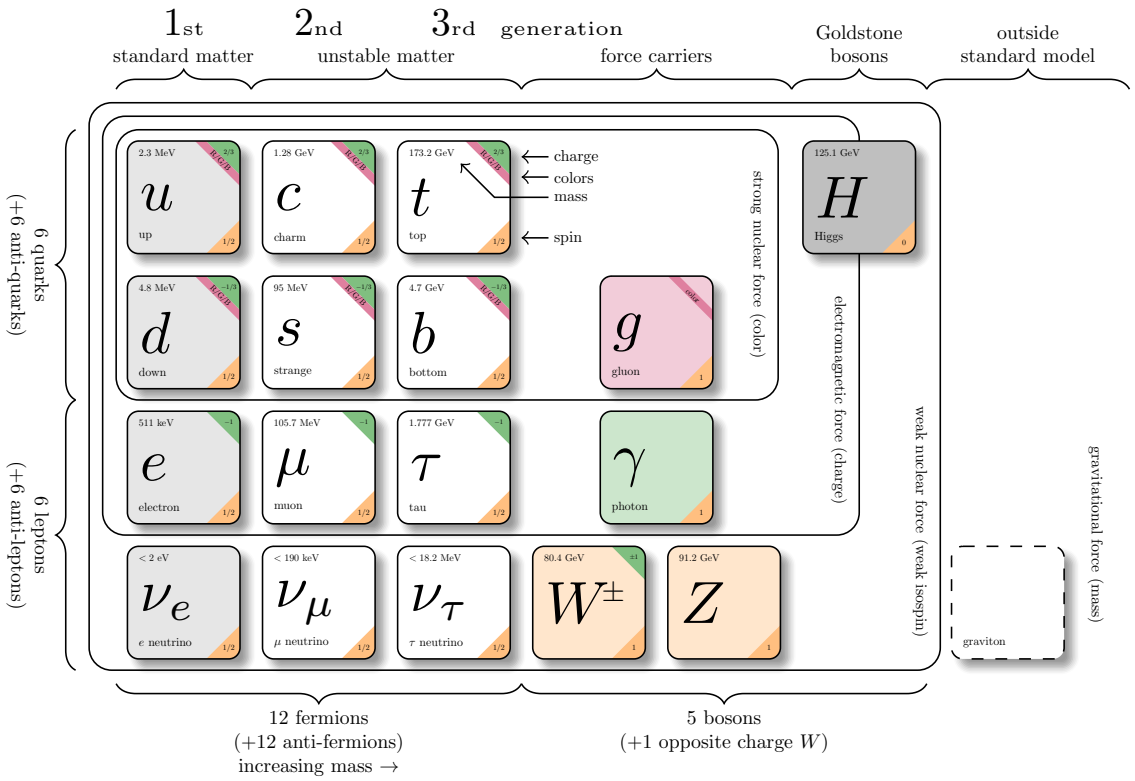

Figure 2.1: All SM particles [12]. All matter particles are listed in squares in the left three columns. The electric charges of the particles are shown in green bars at the top right corners of the squares. The color charges of the particles are shown in pink bars. The spin of the particles are shown in orange bars at the bottom right corners of the squares. The mass of the particles are written at the top left corners of the squares. Quarks are shown in the first two rows and leptons in the last two rows. The four known force carriers and the Higgs boson are listed in squares next to the matter particles with different color backgrounds. The hypothetical graviton, the force carrier of gravity, is also listed next to all known SM particles.

2.1.1 The Standard Model Lagrangian

The SM Lagrangian in Equation 2.6 captures the SM elementary particle interactions under the $SU(3)_C \times SU(2)_L \times U(1)_Y$ symmetry, QCD and electroweak interactions. When calculating the interaction cross sections, the interaction rates from initial-state particles i to final-state particles f are captured in the matrix element, $-i\mathcal{M}_{fi}$. The matrix element can be read directly from the Lagrangian using Feynman rules. Table 2.1 shows the representations

of all fermions in the SM local gauge symmetries and their quantum numbers.

$$\begin{aligned}\mathcal{L}_{\mathcal{SM}} = &-\frac{1}{4}\sum_{a=1}^{8} G^a_{\mu\nu}G^{\mu\nu}_a - \frac{1}{4}B_{\mu\nu}B^{\mu\nu} - \frac{1}{4}\sum_{a=1}^{8} W^a_{\mu\nu}W^{\mu\nu}_a \\ &- \sum_{i=1,2,3}\ \sum_{f=q_L,u_R,d_R,l_L,e_R} \overline{f}_i i\gamma^\mu \mathcal{D}_\mu f_i \\ &+ (\mathcal{D}_\mu\phi)^\dagger(\mathcal{D}^\mu\phi) - V(\phi) \\ &- \sum_{i,j}\Big((y_u)_{ij}\overline{q}_{Li}\tilde{\phi}u_{Rj} + (y_d)_{ij}\overline{q}_{Li}\phi d_{Rj} + (y_e)_{ij}\bar{l}_{Li}\phi e_{Rj} + h.c.\Big)\end{aligned} \tag{2.6}$$

In the equation above, the particles are represented by fields and Dirac spinors:

$$q_{Li}, \quad \overline{q}_{Li}, \quad u_{Ri}, \quad \overline{u}_{Ri}, \quad d_{Ri}, \quad \overline{d}_{Ri}, \quad l_{Li}, \quad \bar{l}_{Li}, \quad e_{Ri}, \quad \overline{e}_{Ri} \tag{2.7}$$

When particles interact, the incoming particle to an interaction vertex is represented by a spinor f. And, i runs through the three generations of fermions. The outgoing particle from the vertex is represented by an adjoint spinor $\overline{f} = f^\dagger\gamma^0$. γ^0 is one of the four 4×4 Dirac matrices. All particle fields are divided into left-handed and right-handed particles. The left-handed particles are grouped in isospin doublets as shown in Table 2.1. So far, right-handed neutrinos have not been observed and are thus not included in the SM Lagrangian [13]. In the quark sector, *up*-type and *down*-type quarks have different Yukawa matrices, y_u and y_d, as discussed in Section 2.1.2.

The force carriers are represented by the fields:

$$G^a_\nu, \quad W^a_\mu, \quad B_\mu, \quad \phi, \quad \tilde{\phi} \tag{2.8}$$

Here, ∂_μ is the four-derivative and G^a_ν is the gluon field. And, W^a_μ and B_μ are the $SU(2)_L \times U(1)_Y$ gauge bosons. The subscript μ of G^a_μ, W^a_μ, and B_μ refers to the components of the four-potential. How W^a_μ and B_μ are mapped to the physical W bosons, Z bosons, and photons is discussed in Section 2.1.1.2. Moreover, ϕ and $\tilde{\phi}$ are the scalar Higgs fields. And, $\tilde{\phi}$ is the conjugate Higgs field: $\tilde{\phi} = i\sigma^2\phi^*$, where σ^2 is one of the three 2×2 Pauli matrices.

Particle	$SU(3)$ representation	$SU(2)_L$ representation	$SU(2)_L$ I_3	$U(1)$ Y	Q
$q_{Li} = \begin{pmatrix} u_{Li} \\ d_{Li} \end{pmatrix}$	**3**	**2**	1/2 -1/2	1/6	2/3 $-1/3$
u_{Ri}		**1**	0	2/3	2/3
d_{Ri}		**1**	0	$-1/3$	1/3
$l_{Li} = \begin{pmatrix} \nu_{eLi} \\ e_{Li} \end{pmatrix}$	**1**	**2**	1/2 $-1/2$	$-1/2$ $-1/2$	0 -1
e_{Ri}		**1**	0	-1	-1

Table 2.1: Quark and lepton SU(3) and SU(2) representations and quantum numbers. **3**, **2**, and **1** represent SU(3) triplet, SU(2) doublet, and SU(3) or SU(2) singlet. I_3 is the third component of SU(3) isospin. U(1) Y is the U(1) hypercharge. Q is the electric charge. i refers to the three generations of fermions.

2.1.1.1 Quantum chromodynamics (QCD)

The strong interaction is described by quantum chromodynamics (QCD). As discussed above, gluons are the force carriers of the strong interaction. The underlying local gauge symmetry of QCD is the SU(3) color symmetry. The eight generators of the SU(3) symmetry, T^a, are defined by the eight 3×3 Gell-Mann matrices, λ_a. $T^a = 1/2\lambda_a$. The eight generators correspond to eight gluon fields.

The QCD Lagrangian is defined as:

$$\mathcal{L}_{QCD} = -\frac{1}{4}\sum_{a=1}^{8} G^a_{\mu\nu} G^{\mu\nu}_a - \sum_{f=t,b,c,s,u,d} (\overline{q} i\gamma^\mu \mathcal{D}_\mu q - m_q \overline{q} q) \tag{2.9}$$

Here, the field strength and covariant derivative are defined by:

$$G^a_{\mu\nu} = \partial_\mu G^a_\nu - \partial_\nu G^a_\mu + g_s f^{abc} G^b_\mu G^c_\nu \tag{2.10}$$

$$D_\mu = \partial_\mu - i g_s G^a_\mu T^a \tag{2.11}$$

As discussed before, g_s is the strong coupling constant and G^a_μ is the gluon field. Moreover, f^{abc} is the gauge group structure constant, defined as $[T^a, T^b] = i f^{abc} T^c$.

The gauge-invariant kinetic interaction between the gluons and the fermion matter is described by the covariant derivative in Equation 2.11. The SU(3) color symmetry is also non-Abelian, meaning that the group generators do not commute with each other. The non-Abelian gauge theory is also called the Yang-Mills theory. The gluon self-interaction is described by the field strength tensor term, $G^a_{\mu\nu} G^{\mu\nu}_a$, in Equation 2.9.

The SU(3) color states have three degrees of freedom, labeled red, green, and blue, represented by three orthogonal 3×1 vectors. The quarks carry one of the three colors. The gluons are an octet of the color states. Except quarks and gluons, other SM particles do not have colors or experience strong interactions.

As shown in Table 2.1, leptons are colorless SU(3) singlets, whereas quarks are color triplets under the SU(3) fundamental representation. The QCD exhibits color confinement, meaning that the individual quarks or gluons cannot be observed directly and only hadronic colorless singlet states can be observed.

Renormalization The interaction cross sections determined in experiments are calculated from the SM Lagrangian using Feynman diagrams. Feynman diagrams expand the matrix elements into a perturbation series. For each tree-level leading-order (LO) Feynman diagram, there is an infinite set of higher-order loop corrections. Renormalization absorbs the infinite set of corrections into the coupling constants at an arbitrary renormalization scale μ_r. The renormalization scale is the physical scale where the quantities are renormalized and needs to be considered when assessing the theoretical uncertainties as discussed in Section 4.4.

After renormalization, the coupling constants are momentum-dependent as shown in Equations 2.2-2.3. This is called the *running* of the coupling constants.

In the case of QCD, α_s decreases significantly with increasing momentum. At 1 GeV, α_s is of $\mathcal{O}(1)$. The quarks are bound into hadrons and perturbation theory cannot be used. Above 100 GeV, α_s is sufficiently small; quarks can be treated as free particles and perturbation theory can be used. This phenomenon is called *asymptotic freedom*.

2.1.1.2 Electroweak interactions

$W^a_{\mu\nu}$ and $B_{\mu\nu}$ are the field strength tensors of electroweak interactions. Similar to QCD, the $SU(2) \times U(1)$ electroweak interactions are non-Abelian and include self-interactions between the gauge bosons described by the field strength tensors:

$$W^a_{\mu\nu} = \partial_\mu W^a_\nu - \partial_\nu W^a_\mu + g\epsilon^{abc} W^b_\mu W^c_\nu \tag{2.12}$$

$$B_{\mu\nu} = \partial_\mu B_\nu - \partial_\nu B_\mu \tag{2.13}$$

The SU(2) generators T^a are defined in terms of the three 2×2 Pauli matrices, $T^a = 1/2\sigma^a$. The Levi-Civita symbol, ϵ^{abc}, is the gauge group structure constant, $[\sigma^a, \sigma^b] = 2i\epsilon^{abc}\sigma^c$. The three generators correspond to three W^a_ν fields.

The interactions between the W bosons and the fermions are chiral. The interactions between the left-handed and right-handed leptons and quarks are defined as:

$$-\sum_i \left(\bar{l}_{Li} i\gamma^\mu \mathcal{D}_\mu l_{Li} + \bar{e}_{Ri} i\gamma^\mu \mathcal{D}_\mu e_{Ri} + \bar{q}_{Li} i\gamma^\mu \mathcal{D}_\mu q_{Li} + \bar{u}_{Ri} i\gamma^\mu \mathcal{D}_\mu u_{Ri} + \bar{d}_{Ri} i\gamma^\mu \mathcal{D}_\mu d_{Ri}\right) \tag{2.14}$$

$$\mathcal{D}_\mu f_{Li} = \left(\partial_\mu - igW^a_\mu T^a - ig'YB_\mu\right) f_{Li} \tag{2.15}$$

$$\mathcal{D}_\mu f_{Ri} = (\partial_\mu - ig'Y B_\mu)\, f_{Ri} \tag{2.16}$$

where g is the $SU(2)_L$ coupling constant and g' is the $U(1)_Y$ coupling constant. The electroweak coupling g, g', and e are related as follows:

$$g = \frac{e}{\sin\theta_w} = 0.64 \qquad g' = \frac{e}{\cos\theta_w} = 0.34 \qquad \tan\theta_w = g'/g \tag{2.17}$$

where θ_W is the weak mixing angle and Y is the hypercharge. The electric charge is related to the hypercharge as following:

$$Q = I^3 + Y \tag{2.18}$$

where I^3 is the third component of the SU(2) weak isospin. All quark and lepton charge and weak isospin are summarized in Table 2.1. All right-handed quarks and leptons are $SU(2)_L$ weak isospin singlets. On the other hand, left-handed quarks and leptons are defined as weak isospin doublets. The left-handed top and bottom particles differ by one electric charge but have the same hypercharge. Right-handed neutrinos have not been observed and are not included in the SM [13].

Physical bosons The physical $W^\pm$ bosons can be obtained from the gauge eigenstates as:

$$W^\pm_\mu = \frac{1}{\sqrt{2}}(W^1_\mu \mp iW^2_\mu) \tag{2.19}$$

The third component of the W^a_μ field, W^3_μ, is neutral and mixes with the B_μ field. The physical neutral Z bosons and photons can be obtained from the gauge eigenstates as:

$$\begin{pmatrix} A_\mu \\ Z_\mu \end{pmatrix} = \begin{pmatrix} \cos\theta_W & \sin\theta_W \\ -\sin\theta_W & \cos\theta_W \end{pmatrix} \begin{pmatrix} B_\mu \\ W^3_\mu \end{pmatrix} \tag{2.20}$$

where the weak mixing angle θ_W is the rotation angle in switching the basis. The mass eigenstates arise from the BEH mechanism discussed in Section 2.1.2.

CKM matrix While the strength of weak interactions is the same for all leptons (*lepton universality*), W bosons preferentially decay to $u\overline{d}$ and $c\overline{s}$ [14]. And, the quark flavor changes through interactions with the W bosons. CKM (Cabibbo–Kobayashi–Maskawa) matrix contains the weak interaction flavor changing strengths. The CKM matrix is embedded in Equation 2.15, the electroweak interactions between gauge bosons and left-handed quarks. In the equation, u_L and d_L quarks are in the flavor basis. The quarks can be rotated to the mass basis by: $u_L \to (U_{u_L})_{ij} u_{Li}$ and $d_L \to (U_{d_L})_{ij} d_{Li}$. The CKM matrix is defined as: $V_{CKM} = U^\dagger_{u_L} U_{d_L}$. The diagonal entries of the CKM matrix tend to be around 1. Unlike W bosons, the Z boson and photon interactions are not affected by the CKM matrix and do not change quark flavors. Similarly, quark flavors are conserved in QCD and QED as well.

Weak interactions are chiral and do not conserve *parity*. Parity operators invert the spatial coordinates of particles. Parity is conserved in QED and QCD. Overall, the quark

sector of weak interactions does not conserve *CP-symmetry*, which means that the interaction rates are different under charge conjugation and parity operators. CP violation from the CKM matrix is one of the few known CP-violating effects in the SM that could accommodate the matter-antimatter asymmetry. However, it is not enough to explain the observed matter-antimatter asymmetry [15].

2.1.2 The BEH mechanism

The BEH mechanism introduces a scalar Higgs boson into the SM, breaks the EW symmetry, and thus generates masses for particles. The Higgs Lagrangian is defined by [4, 6]:

$$\mathcal{L}_{Higgs} = (\mathcal{D}_\mu \phi)^\dagger (\mathcal{D}^\mu \phi) - V(\phi) \tag{2.21}$$

$$V(\phi) = -\mu^2 \phi^\dagger \phi + \lambda (\phi^\dagger \phi)^2 \tag{2.22}$$

where the covariant derivative $\mathcal{D}_\mu$ is the same as in Equations 2.15. And, μ and λ are free parameters controlling the Higgs potential. In addition, the Yukawa coupling between the Higgs field and the quark sector follows:

$$\mathcal{L}_{Yukawa,quark} = \sum_{i,j} \Big((y_u)_{ij} \overline{q}_{Li} \tilde{\phi} u_{Rj} + (y_d)_{ij} \overline{q}_{Li} \phi d_{Rj} \Big) + h.c. \tag{2.23}$$

where *h.c.* stands for the Hermitian conjugate. The Higgs conjugate field: $\tilde{\phi} = i\sigma^2 \phi^*$. The Yukawa coupling between the Higgs field and the lepton section is described as:

$$\mathcal{L}_{Yukawa,lepton} = \sum_{i,j} (y_e)_{ij} \bar{l}_{Li} \phi e_{Rj} + h.c. \tag{2.24}$$

While the interactions between the Higgs boson and the massive vector bosons are embedded in the covariant derivative, the Yukawa couplings between the Higgs boson and the fermions are appended to the SM Lagrangian in an ad hoc fashion.

Electroweak symmetry breaking The BEH mechanism breaks the electroweak symmetry $SU(2)_L \times U(1)_Y$ to $U(1)_{QED}$ by introducing a Higgs doublet ϕ:

$$\phi = \begin{pmatrix} \phi^+ \\ \phi^0 \end{pmatrix} = \frac{1}{\sqrt{2}} \begin{pmatrix} \phi_1 + i\phi_2 \\ \phi_3 + i\phi_4 \end{pmatrix} \tag{2.25}$$

Like other weak isospin doublets, the electric charges of the upper and lower components differ by one. For $\mu^2 > 0$ and $\lambda > 0$, the Higgs potential $V(\phi)$, illustrated in Figure 2.2, has an infinite set of minima at:

$$\phi^\dagger \phi = \frac{1}{2} \left(\phi_1^2 + \phi_2^2 + \phi_3^2 + \phi_4^2 \right) = \frac{v^2}{2} = \frac{\mu^2}{2\lambda} \tag{2.26}$$

where v is the vacuum expectation value of the Higgs field. The Higgs field can be expanded around one specific minima in the unitary gauge and thus break the electroweak symmetry as:

$$\phi = \frac{1}{\sqrt{2}} \begin{pmatrix} 0 \\ v + h(x) \end{pmatrix} \tag{2.27}$$

where $h(x)$ is the massive scalar Higgs boson and x is the spacetime coordinate. With the expression in Equation 2.27, the covariant derivative term in Equation 2.21 describes the interaction between the three gauge bosons and the Higgs boson. The masses of the gauge bosons are determined as:

$$m_W = \frac{1}{2} g v, \quad m_Z = \frac{1}{2} v \sqrt{g^2 + g'^2} = \frac{m_W}{\cos \theta_W}, \quad m_A = 0 \tag{2.28}$$

The mass of photon, m_A, is zero. The masses of the Higgs boson is:

$$m_h = \sqrt{2\lambda} v \tag{2.29}$$

The couplings between the Higgs boson and the massive gauge bosons are shown in Figure 2.3. The Higgs boson does not directly couple to any massless particles. It can interact with massless particles through loops of massive particles such as the top quark or the W boson. The Higgs potential term also allows the Higgs trilinear and quartic self-interactions.

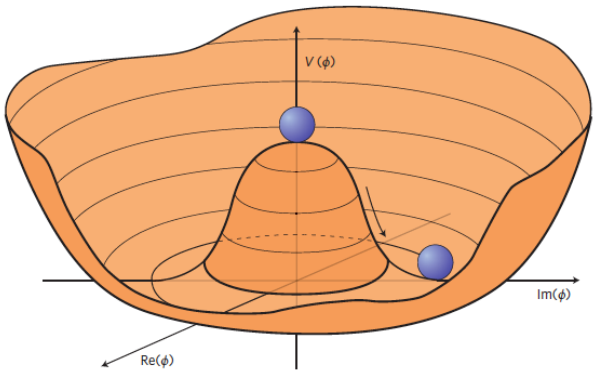

Figure 2.2: Illustration of the Mexican-hat shaped Higgs potential with an infinite set of minima [16].

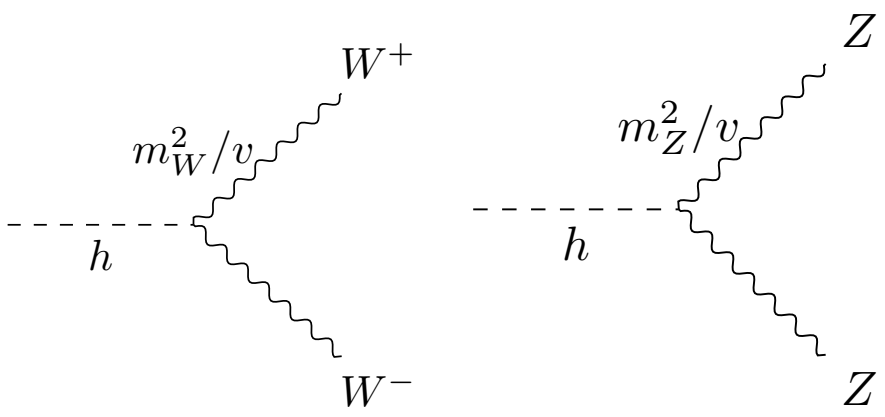

Figure 2.3: The couplings between the Higgs boson and the massive gauge bosons.

Higgs-to-fermion Yukawa couplings The couplings Higgs-to-fermions are illustrated in Equations 2.23-2.24. For leptons, the Yukawa coupling matrix, $(y_e)_{ij}$, can be diagonalized without affecting any other parts of the Lagrangian, such as kinematic interactions. The diagonalized Yukawa matrix is expressed in terms of lepton masses: $(y_e)_i = \sqrt{2}(m_e)_i/v$.

For quarks, two Yukawa matrices, $(y_u)_{ij}$ and $(y_d)_{ij}$, can be diagonalized. The diagonalized mass matrices have: $(y_u)_i = \sqrt{2}(m_u)_i/v$ and $(y_d)_i = \sqrt{2}(m_d)_i/v$. The quark mass basis interacts with the W bosons differently through the CKM matrix, as discussed in Section 2.1.1. In summary, the Higgs couplings to fermions are shown in Figure 2.4. As the right-handed neutrinos are not found or included in the SM, the neutrino mass may or may not be generated by the BEH mechanism. One postulate of generating the neutrino mass from Higgs is the seesaw mechanism [4].

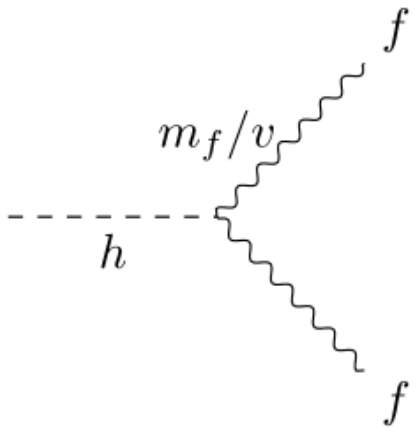

Figure 2.4: Couplings between the Higgs boson and fermions.

2.1.3 Free parameters in the SM

In summary, the SM Lagrangian in Equation 2.6 has 23 free parameters. Many measurable quantities are interrelated, giving strong experimental tests to the validity of the SM. All latest experimental measurements of the free parameters are summarized by the Particle Data Group [17].

- **Yukawa couplings:** 9 Yukawa couplings, $(y_e)_i$, $(y_u)_i$, and $(y_d)_i$, between the Higgs boson and the fermions. In the SM, the Yukawa coupling strengths are determined by the fermion mass and the Higgs vacuum expectation value. Yukawa couplings can be measured through Higgs productions and decays. In this thesis, both the Higgs-charm and Higgs-bottom couplings, y_c and y_b, are measured.

- **Higgs potential:** 2 parameters of the Higgs potential, μ and λ. Or equivalently, the Higgs mass m_h and the vacuum expectation value v, with $m_h = 125.11 \pm 0.11$ GeV [18] and $v \approx 246$ GeV [17].

- **Coupling constants:** 3 coupling constants, g_s, g, and g' for strong and electroweak interactions. Or equivalently, α, α_s, and α_W in Equations 2.2-2.4. The masses of the W and Z bosons are related to the vacuum expecation value v and the coupling strengths g and g'.

- **CKM matrix and PMNS matrix:** 8 mixing angles between the CKM matrix and the PMNS matrix. The 3×3 CKM matrix can be parameterized by 4 parameters. Given the focus of this thesis, the PMNS matrix is not discussed. Similar to the CKM matrix, the PMNS matrix is the rotation matrix between the mass eigenbasis and the flavor eigenbasis of the three neutrino flavors [4].

- **Strong CP phase:** θ_{QCD}. The strong CP phase θ_{QCD} is related to the strong CP problem and governs the negligible CP violation in QCD.

2.2 LHC phenomenology and Higgs physics

The previous section provides an overview of the SM and describes the fundamental forces. High-energy colliders can generate heavy particles such as the Higgs boson and are an optimal platform to test the theoretical predictions. In this section, Section 2.2.1 discusses the phenomenology behind proton-proton collisions at the LHC. Section 2.2.2 introduces Higgs physics at the LHC. And, Section 2.2.3 quickly discusses the event generation steps in ATLAS.

2.2.1 LHC phenomenology

As discussed above, due to asymptotic freedom, at high energies, quarks can be viewed as free particles. The LHC collides protons at high energies. The valence quarks (u, u, d) and sea quarks inside protons collide with each other as point-like partons. Thus, the cross sections of high energy proton-proton collisions can be summarized as [19]:

$$\sigma_{pp\to f}(s,\mu_r^2,\mu_f^2) = \sum_{i,j}\int_0^1 dx_1 \int_0^1 dx_2\, f_i(x_1,\mu_f^2)\, f_j(x_2,\mu_f^2)\, \hat{\sigma}_{ij\to f}(\hat{s},\mu_r^2,\mu_f^2) \tag{2.30}$$

where s is the is the total center-of-mass energy of the colliding protons. The renormalization scale μ_r is discussed in Section 2.1 and μ_f is the factorization scale. The functions $f_i(x_1,\mu_f^2)$ and $f_j(x_2,\mu_f^2)$ are parton distribution functions (PDFs) of the colliding partons including gluons, up and down quarks, etc. The PDFs are integrated over the momentum fractions x_1 and x_2. For the valence up and down quarks inside protons:

$$\int_0^1 u_V(x)\,dx = 2, \qquad \int_0^1 d_V(x)\,dx = 1 \tag{2.31}$$

The second part of Equation 2.30, $\hat{\sigma}_{ij\to f}$, is the cross section of the hard-scattering event from initial partons i and j to the final state f. And, $\hat{s}$ is the center-of-mass energy of the colliding partons.

Equation 2.30 is enabled by *factorization*. Factorization means that calculations follow: $\sigma = f \otimes H$, where f is the universal non-perturbative PDFs and H is the short-distance perturbative hard scattering. The physical scale at which factorization holds is the factorization scale μ_f. Both the PDFs and the hard scatter cross section depend on the μ_f choice. Similar to the renormalization scale, the factorization scale affects the final observables and should be considered as a theoretical uncertainty.

PDFs can be extracted from various high-energy experiments [17, 20]. Different experiments, such as LHC, Tevatron, and HERA, offer PDF measurements at different phase space. An example of the PDFs is shown in Figure 2.5. The PDFs are also dependent on the choice of α_s.

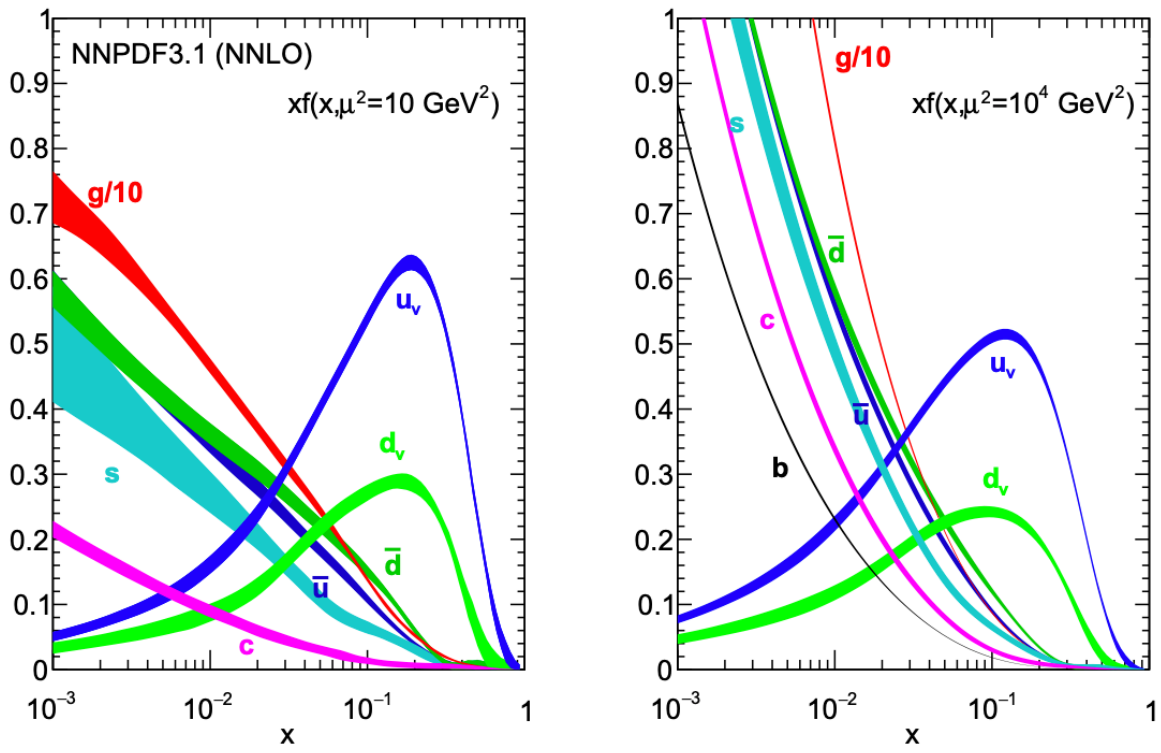

Figure 2.5: PDFs evaluated at $\mu_r = \mu_f = \mu = 10\,\mathrm{GeV}^2$ (left) and $100\,\mathrm{GeV}^2$ (right) [21]. The gluon PDFs dominate at low momentum. And, $u_V(x) \approx 2d_V(x)$. The PDFs can be evaluated at a large range of energy levels. At higher energies, protons tend to have higher fraction of low momentum quarks [4].

2.2.2 Higgs productions and decays

The Higgs boson is the mass mediator of the SM theory, as discussed in Section 2.1. It is the only scalar gauge boson, meaning spin = 0. It arises not from local gauge symmetries but from electroweak symmetry breaking.

The Higgs boson is related to various important questions in particle physics [22]. To name a few: the vacuum stability of the universe [23], the baryogenesis phase transition [24], and the dark sector [25].

The LHC offers exciting opportunities to understand the role of the Higg bosons in our universe. In this section, the production and decay channels of the Higgs boson at the LHC are discussed. Knowing the Higgs production cross section $\sigma(pp \to H)$ and the Higgs decay branching ratio $BR(H \to X)$, the cross section for any given process $\sigma(pp \to H \to X)$ can

be calculated as:

$$\sigma(pp \to H \to X) = \sigma(pp \to H) \times \mathrm{BR}(H \to X) = \sigma(pp \to H) \times \frac{\Gamma_H^X}{\Gamma_H^{\mathrm{total}}} \tag{2.32}$$

where $\Gamma_H^{\mathrm{total}}$ is the total decay width of the Higgs boson and Γ_H^X is the partial decay width to the final state X. The branching ratio $\mathrm{BR}(H \to X)$ is thus the probability of Higgs decaying to the final state X.

Production channels at the LHC Main production channels with the largest cross sections are shown in Figure 2.6: gluon-gluon fusion (*ggF*), vector-boson fusion (*VBF*), associated production with a vector boson (*VH* or *Higgstrahlung*), associated production with a pair of top or bottom quarks (*ttH*, *bbH*), and lastly associated production with a single top quark (*tH*). Their Feynman diagrams are shown in Figure 2.7.

The most common production channel is *ggF* as the gluon PDF contribution is large at low momentum in the LHC, as shown in Figure 2.5. The Higgs boson does not interact directly with massless gauge bosons, so the ggF contribution is at the loop level. The main contribution to the loop is the top quark, as the top Yukawa coupling is the largest due to the large top mass $y_{top} = m_{top}/v \sim 1$. The second largest production channel is *VBF*. Two vector bosons radiated by two quarks fuse to create a Higgs boson. The VBF events can be identified by two high-energy forward jets [26].

The Higgstrahlung channel is a relatively small production channel compared to ggF and VBF. However, leptons from vector-boson decays help trigger Higgstrahlung events and thus suppress large QCD backgrounds in the $VH(\to b\bar{b}, c\bar{c})$ analysis. The VH channel is currently the most sensitive channel for probing the Higgs-charm coupling. The ttH channel allows the Higgs-top Yukawa coupling to be directly probed [27].

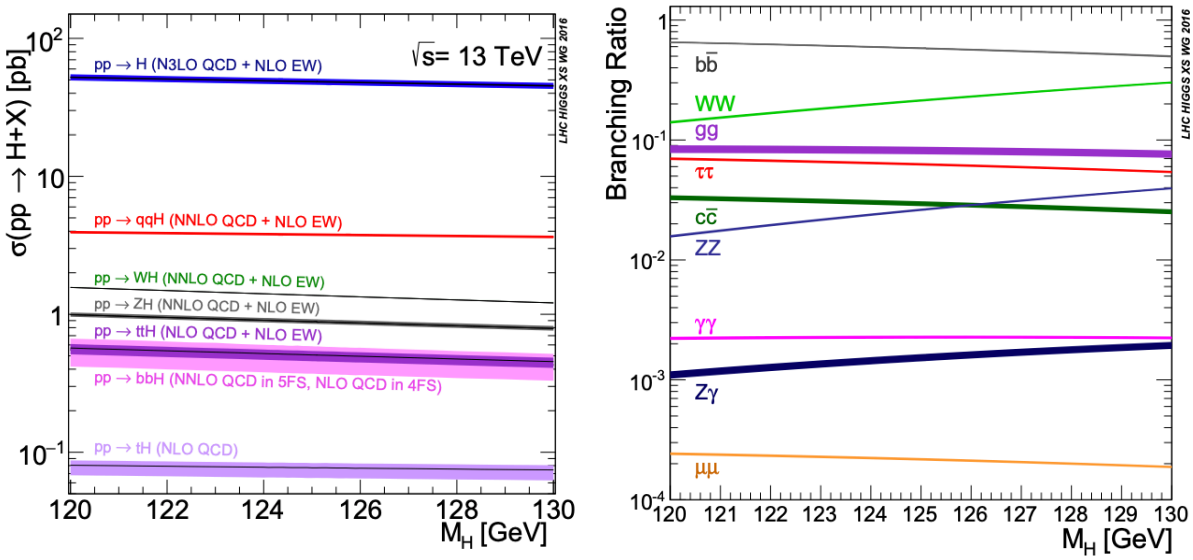

Figure 2.6: Main Higgs production cross sections (left) and decay branching ratios (right) with respect to m_H [28]. The production cross sections are calculated at the center of mass energy = 13 TeV. The production cross sections increase with collision energies. The branching ratios are independent of the collision energies. On the left plot, $pp \to H$ refers to ggF and $pp \to qqH$ refers to VBF.

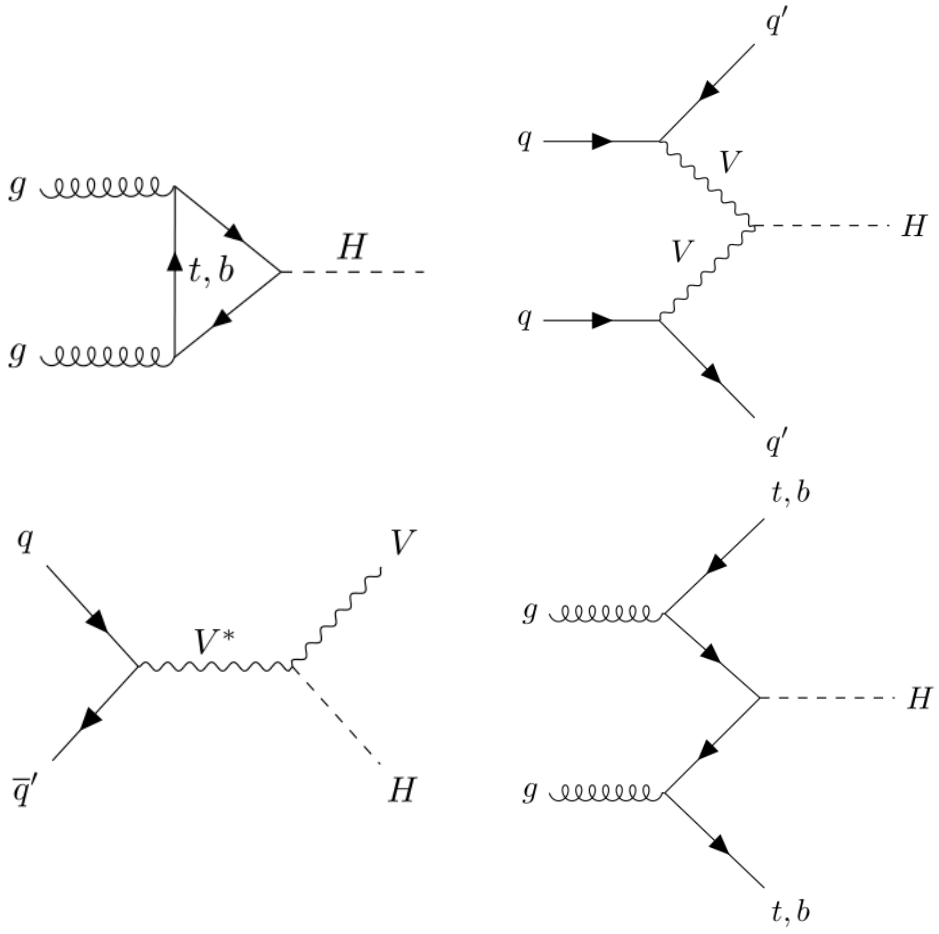

Figure 2.7: Example Feynman diagrams for *ggF* (top left), *VBF* (top right), *VH* (bottom left), *ttH*, and *bbH* (bottom right).

Higgs decay channels The most common decay channels are shown in Figure 2.6. The Higgs coupling strength to massive fermions is proportional to the fermion mass, while the Higgs coupling strength to massive bosons is proportional to the boson mass squared. The decay widths are proportional to the matrix element squared $|\mathcal{M}_{fi}|^2$. Therefore, the Higgs branching ratio BR is proportional to the fermion mass squared.

Given the Higgs mass around 125 GeV, the Higgs decay to $t\bar{t}$ is not allowed kinematically. The Higgs-top coupling can be directly probed in the ttH production channel. The bottom quark (b-quark) is the heaviest quark to which the Higgs boson can decay. Therefore, the $H \to b\bar{b}$ decay channel is the most common decay channel ($BR \sim 58\%$). In comparison, the BR of Higgs to charm is approximately 3%.

The Higgs decay to a pair of massive gauge bosons is not allowed kinematically as well. One of the gauge bosons must be off-shell (not on the resonant mass shell). The branching ratios for the Higgs decays to massive vector bosons are suppressed because of the off-shell mass. In addition, similar to the ggF production channel, the Higgs boson can also decay to massless bosons indirectly through loops of massive particles. Beyond the SM, the Higgs boson can decay to any lighter BSM particles such as various dark-matter candidates as well.

Experimental status of the Higgs physics The Higgs boson was discovered at the LHC during Run 1 in 2012 by the ATLAS and CMS experiments [29, 30]. Since then, many important Higgs properties have been measured and show good agreement with the SM predictions [31, 32]. Noticeably,

- **Higgs spin, CP, mass, and width:** The Higgs boson has no spin, in agreement with the SM. The charge conjugation and parity properties are consistent with it being CP-even. As discussed in Section 2.1, the Higgs mass is a free parameter in the SM. The current most precise Higgs mass measurement is from ATLAS [18]:

$$m_h = 125.11 \pm 0.11\,\text{GeV} \tag{2.33}$$

  The latest CMS Higgs mass measurement agrees with the ATLAS result and shows: $m_h = 125.38 \pm 0.14\,\text{GeV}$ [33]. Both CMS and ATLAS use the $H \to \gamma\gamma$ and $H \to ZZ^* \to 4l$ decay channels to measure the Higgs mass because the final decay products can be precisely reconstructed and thus give good mass resolutions.

  The total decay width of the Higgs boson, Γ_H^{total}, can be calculated from all the SM Higgs decays. The theoretical prediction is about 4.09 MeV [28]. The Higgs total width cannot be directly measured through the Higgs mass resonant line shape at the LHC due to its small value [34, 35]. The current most sensitive measurement is performed by comparing the on-shell Higgs production with the off-shell Higgs production in the ZZ decay channel. The on-shell Higgs production is dependent on the Higgs width Γ_H^{total} while the off-shell is not. The Higgs width can be extracted through the ratio. Currently, the most precise measurement constrains the total width to be less than 5.3 MeV at 95% confidence level [36, 37].

- **Coupling to bosons and fermions:** To understand the Higgs couplings to bosons and fermions, measurements are performed for individual production and decay channels, as shown in Figure 2.8. The leading Higgs production and decay channels are precisely measured.

  Furthermore, the couplings between the Higgs boson and particles are assessed using the κ modifiers [38]. The κ modifiers modify the Higgs couplings to a particle p without affecting the kinematic distribution and assess the agreement between the measurements and the SM predictions. For example: $\sigma_{WH}/\sigma_{WH}^{SM} = \kappa_W^2$ and $\Gamma_{WW^*}/\Gamma_{WW^*}^{SM} = \kappa_W^2$. When the measurement agrees with the SM, κ should be around unity. The $VH(\rightarrow b\bar{b}, c\bar{c})$ results in Chapter 4 are also interpreted in the κ framework. The Higgs-charm and Higgs-bottom SM Yukawa coupling strengths (y_c and y_b) are modified as $\kappa_c y_c$ and $\kappa_b y_b$. More details about the signal strength parameterizations in terms of κ_c and κ_b are discussed in Section 4.6.3.

  The measurements of the κ modifiers are shown in Figure 2.9. All κ modifiers are presented with positive signs as only the sign difference between κ_F and κ_V is physical and the fermion κ modifiers (κ_F) and the vector boson κ modifiers (κ_V) have been shown to have the same sign [31]. The latest constraint from ATLAS on κ_c is not listed in the plot. The previous ATLAS observed 95% confidence level (CL) upper limit is: $|\kappa_c| < 8.5$ [2]. The CMS κ_c constraint is more precise at $1.1 < |\kappa_c| < 5.5$ [39]. Chapter 4 discusses the final ATLAS Run 2 $VH(\rightarrow b\bar{b}, c\bar{c})$ analysis, which sets the most stringent limit on κ_c to date. The observed (expected) κ_c upper limit at the 95% CL is $|\kappa_c| < 4.2$ (4.1).

  In addition, the differential cross sections of the Higgs production and decay channels are measured in the simplified-template-cross-section (STXS) framework [28]. Differential cross sections mean that cross sections are extracted in different bins of kinematic distributions instead of inclusively. There are also direct invisible Higgs decay searches [40]. Lastly, the projected HL-LHC precisions for the κ modifiers are around a few % compared to around 10% as shown in Figure 2.9 [41].

- **Self-coupling:** Measuring the Higgs self-coupling is important, as it can directly determine the Higgs potential shape λ as discussed in Equation 2.21. The Higgs self-coupling is directly probed by measuring the cross section of producing two Higgs (di-Higgs). The di-Higgs measurements can be performed in various decay channels such as $HH \rightarrow b\bar{b}\tau\tau$, $HH \rightarrow b\bar{b}b\bar{b}$, and $HH \rightarrow b\bar{b}\gamma\gamma$. The latest μ_{HH} upper limit is 2.9 times the SM prediction at 95% confidence level [42]. At the end of HL-LHC, the combined ATLAS and CMS projected significance of di-Higgs is 4σ [41].

- **Effective field theory (EFT):** Lastly, EFT is an effective tool to look for new physics, at the energy scale Λ, above the current energy scale reachable at the LHC. Operators at higher-dimension d, $\mathcal{O}_i^{(d)}$, can be appended to the dimension-4 SM Lagrangian with $1/\Lambda^{d-4}$ suppression [43]. Constraints can be set for the Wilson coefficients of the higher-dimension operators. All SM operators are of dimension 4 as the

known dimension of space-time is four. This approach is called the SM effective field theory (SMEFT). Most SMEFT operators are dimension-6 operators [44]. The Higgs cross section measurements can be interpreted with BSM cross section terms from SMEFT operators and constrain the SMEFT Wilson coefficients and thus the scale of new physics [43]. However, SMEFT interpretation might introduce additional shape effects to the fit compared to the default SM results.

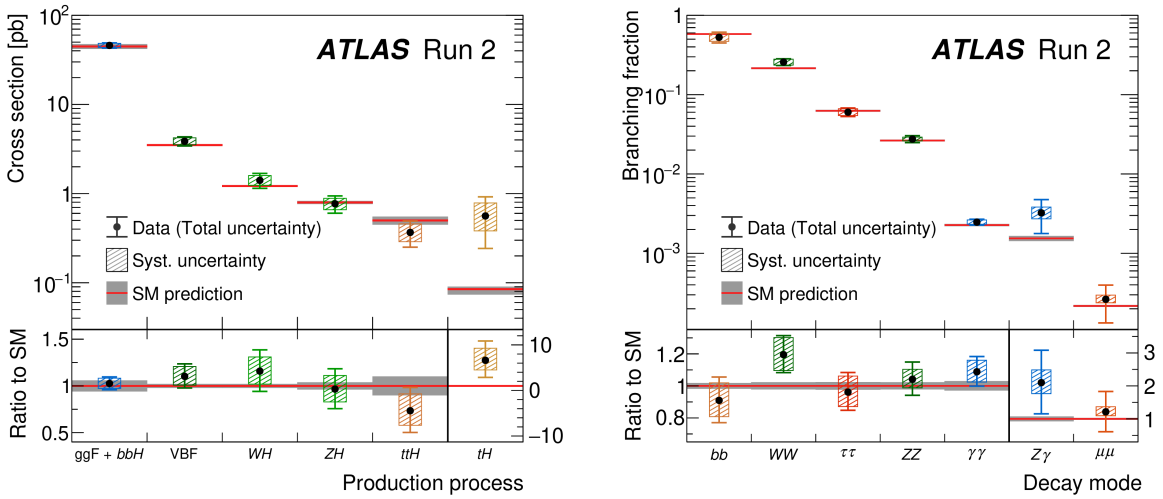

Figure 2.8: Higgs production rate (left) and decay rate (right) measurements in different channels [31]. The bottom panels show the ratio between the measurements and the SM predictions, σ_i/σ_i^{SM} and BR_i/BR_i^{SM}. The bottom panels are split to two parts in both plots. The right axes are for the right sides of the panels. The tH production channel 95% confidence level upper limit is 15 times the SM prediction. The tH and ttH measurements are negatively correlated due to overlapping signal regions. The total uncertainties and the systematic uncertainties are shown in error bars and blocks with diagonal lines. Most channels are limited by systematic uncertainties. Most measurements are roughly aligned with the SM predictions.

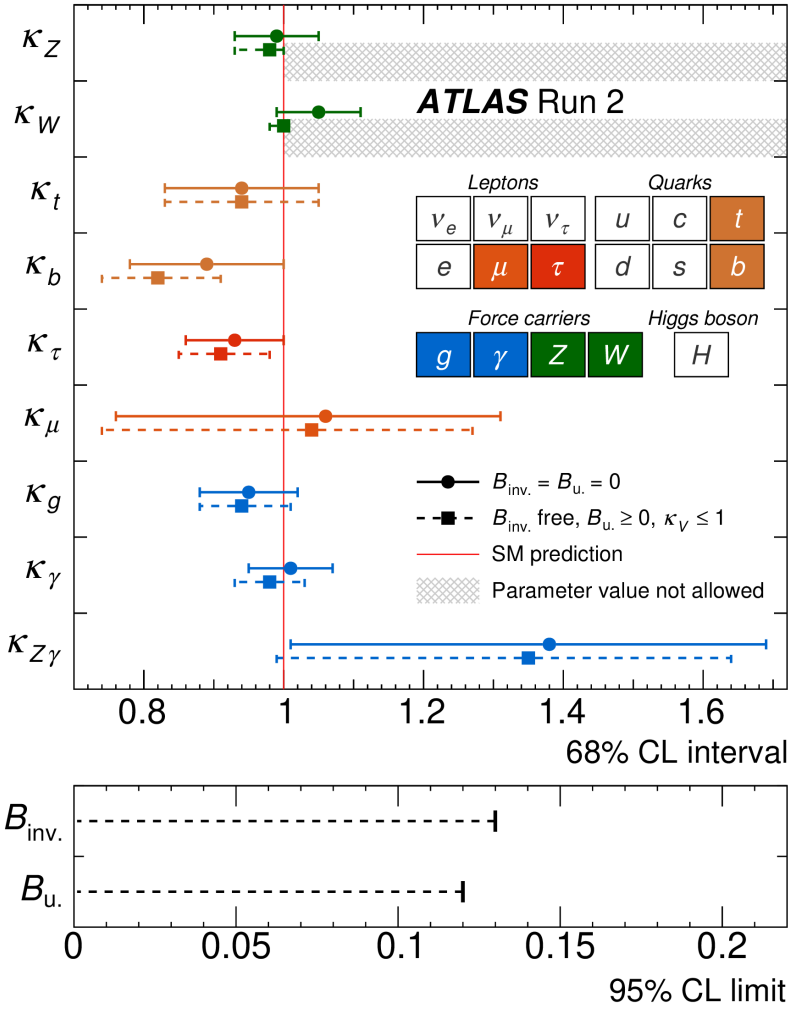

Figure 2.9: Higgs κ modifiers [31]. The bottom panel is the upper limits on undetected non-SM Higgs decays $\mathcal{BR}_u$ or invisible Higgs decays $\mathcal{BR}_{inv}$. All κ modifiers center around 1, showing the robustness of the SM. The Higgs couplings to lighter particles such as the s-quark are difficult to measure at the LHC due to the small branching ratios. The Higgs-charm coupling is not listed on this plot but is discussed in detail in Chapter 4. Lastly, the Higgs couplings to gluons and photons are at the loop level as discussed above. The $\kappa_{Z\gamma}$, κ_γ, and κ_g modifiers are functions of the other modifiers [38].

BSM: enhanced Higgs couplings While the Higgs couplings to bosons and fermions have been carefully studied, the Higgs couplings to first generation and second generation down-type quarks, u, d, and c, have not been discovered. Many BSM theories predict enhanced couplings to these quarks [45, 46, 47, 48, 49]. The couplings might also be reduced in other BSM theories [50]. The potential BSM enhancements strongly motivate setting more stringent upper limits on Higgs-to-charm, which is the main focus of this thesis. Potential BSM enhancements could occur in two different scenarios: new physics at the TeV scale and a second Higgs doublet ϕ'.

The new physics impact on the light quark Yukawa couplings, y_q, can be interpreted in the EFT scenario, $y_q \sim \mathcal{O}(f\frac{v^2}{\Lambda^2})$ [45, 46]. The parameter v is the vacuum expectation value, Λ is the new physics scale, and f is the Wilson coefficient of the new physics. Here, light quarks refer to all quarks lighter than the b-quark, including the u, d, s, and c-quarks. Setting $\Lambda \sim 1.5$ TeV and $f \sim \mathcal{O}(1)$, the light quark couplings would be comparable to the SM b-quark coupling, $y_q \sim \mathcal{O}(y_b^{SM})$. This EFT scenario is general and has not been excluded. However, measurements of the charm Yukawa coupling, such as the $VH(\rightarrow b\bar{b}, c\bar{c})$ analysis, can exclude this postulate by showing that y_c is smaller than y_b^{SM}.

Adding a second Higgs doublet ϕ' could also enhance the light quark couplings [47, 48, 49]. For example, the quark mass matrices can have the form $M = M^{(0)} + M^{(1)}$, where $M^{(0)}$ is generated by the SM Higgs ϕ defined in Equation 2.27 and $M^{(1)}$ is generated by the second Higgs field ϕ'. The matrix $M^{(1)}$ can be written in forms where only first two generation masses are affected, matching experimental constraints. The Higgs-charm couplings can be enhanced up to a factor of three [48].

2.2.3 Simulation of events

Simulating events is an important step in comparing the SM predictions to the experimental measurements. Event simulations apply relevant theories discussed above and the idea of factorization. Simulation events serve many purposes, such as evaluating theoretical predictions, calibrating detectors, and optimizing analysis frameworks. Given the complexity of the theory predictions, simulations are generated using Monte Carlo (MC) techniques. A large number of random events are generated from the probability density functions [51]. The methodology of event simulation is discussed below, while the specific event simulation settings used in the analysis are discussed in Section 4.4.

A schematic of event generation is shown in Figure 2.10. MC events roughly follow the five steps before being used in analyses [52]:

- **Hard scattering:** The cross section computations following Equation 2.30 using the parton density functions. The matrix elements are calculated from the SM Lagrangians using Feynman rules.
- **Parton shower:** The gluons and quarks from the high-energy hard scattering then radiate to produce additional gluons and quarks. This process is known as the parton shower and can be calculated using perturbative QCD.

- **Hadronization:** Lower energy gluons and quarks then hadronize into bound states at around 1 GeV. As discussed in Section 2.1, perturbation theories are no longer valid in this region. Predictions are made using phenomenological models. In addition, non-perturbative simulations also include the *underlying* events. The underlying events are a collection of soft interactions from the remaining partons in proton collisions. Furthermore, the *initial state radiation* (ISR) and the *final state radiation* (FSR) are also simulated in the hadronization process, as shown in Figure 2.10 [19]. ISR and FSR are emissions from incoming and outgoing partons.

- **Pileup:** The *pileup* is additional pp collisions other than the collision of interest. Pileup events are simulated using a data-driven method [53].

- **Detector simulation and reconstruction:** Lastly, before data simulation comparison, the generated events are passed through detector simulation packages such as `GEANT4` and `AtlFast` [54, 55]. The packages simulate ATLAS detector geometry, material, and response. The interactions between the truth-level particles from the Monte Carlo generators and the detector materials are simulated. Afterwards, the detector energy deposits from the truth particles are digitized and read out. The simulations are then reconstructed using the same reconstruction methods as the data.

There are many Monte Carlo generators available for simulating the hard scattering and the hadronization. The typical generators include: SHERPA [56], POWHEG [57], PYTHIA [58], HERWIG [59], and MADGRAPH [60]. Event generators such as SHERPA and PYTHIA are general-purpose and can cover from hard scattering, parton shower, to hadronization. Unlike SHERPA, PYTHIA can also be used with other generators such as POWHEG and generate only parts of the process such as parton shower. MADGRAPH can only generate hard scattering processes and is often used as an alternative generator to assess modeling uncertainties. All generators simulate processes at different orders of the perturbation theory. The leading order (LO) expansion considers only tree-level Feynman diagrams. Higher-order calculations include loop corrections and are more accurate. More details of the event generators and simulated events used in the $VH(\to b\bar{b}, c\bar{c})$ analysis are discussed in Section 4.4.

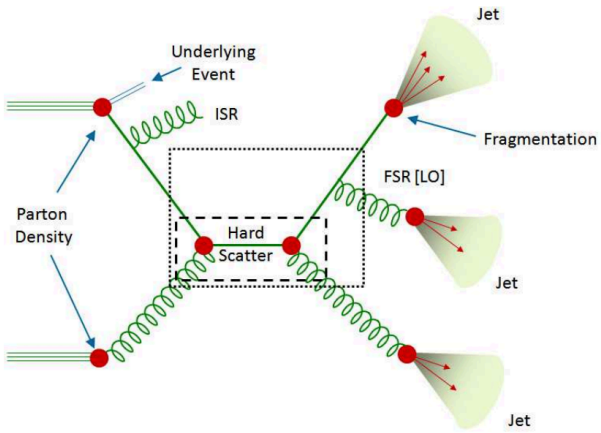

Figure 2.10: The event generation schematic [19].

Chapter 3

Experimental setup

This chapter aims to give an overview of the experimental setup for the $VH(\rightarrow b\bar{b}, c\bar{c})$ analysis. First, Section 3.1 introduces the Large Hadron Collider (LHC). Then, Section 3.2 discusses the ATLAS detectors used for data collection. Lastly, Section 3.3 introduces how particles detected by the ATLAS detector are reconstructed for data analysis. Given the importance of identifying heavy-flavor jets for the analysis, Section 3.4 discusses in more detail how machine learning is used to tag jet flavors. The $VH(\rightarrow b\bar{b}, c\bar{c})$ analysis uses LHC Run 2 data collected with the ATLAS detector. Therefore, the following discussion focuses on the detector performance in Run 2.

3.1 Large Hadron Collider

The Large Hadron Collider (LHC) is the world's largest particle accelerator [61]. The circumference of the LHC is 27 km. The LHC is located at CERN, the European Organization for Nuclear Research, at the border of France and Switzerland, near Geneva [62]. The LHC collides protons or ions. The LHC had three data collection runs, as summarized in Table 3.1. Additional data runs are planned for the HL-LHC from the 2030s. In this section, more details of the LHC operation, performance, and experiments are discussed.

Runs	**Year**	$\sqrt{s}$ **(TeV)**	**Total integrated luminosity recorded (fb^{-1})**
Run 1	2010 – 2012	7, 8	28
Run 2	2015 – 2018	13	156
Run 3	2022 – 2025	13.6	101

Table 3.1: Proton collision runs of the LHC. In the third column, the parameter $\sqrt{s}$ is the collision energy. The last column lists the total integrated luminosities recorded by ATLAS [63, 64, 65]. During LHC Run 1, the Higgs boson was discovered [29, 30]. LHC Run 3 is currently ongoing and more data is expected.

LHC operation The LHC accelerator complex is shown in Figure 3.1. The acceleration proceeds in stages. The injection chain starts at Linac4, Proton Synchrotron Booster (PSB), Proton Synchrotron (PS), and finally goes to Super Proton Synchrotron (SPS) before entering the main LHC tunnel [61].

The accelerating facilities uses radio-frequency (RF) cavities to accelerate the beam to 450 GeV after SPS before the main LHC tunnel. In the LHC tunnel, 16 RF cavities accelerate each colliding beam from 450 GeV to 6.5 TeV.

In addition to acceleration, the LHC uses 1232 dipole magnets to bend the beams to circulate inside the ring. The peak beam energy and the LHC circumference are limited by the peak dipole field of 8.3 T [66]. Quadrupole magnets are used to focus the beam to μm transverse emittance. Higher-order corrector magnets are placed along the tunnel to fine-tune the beams.

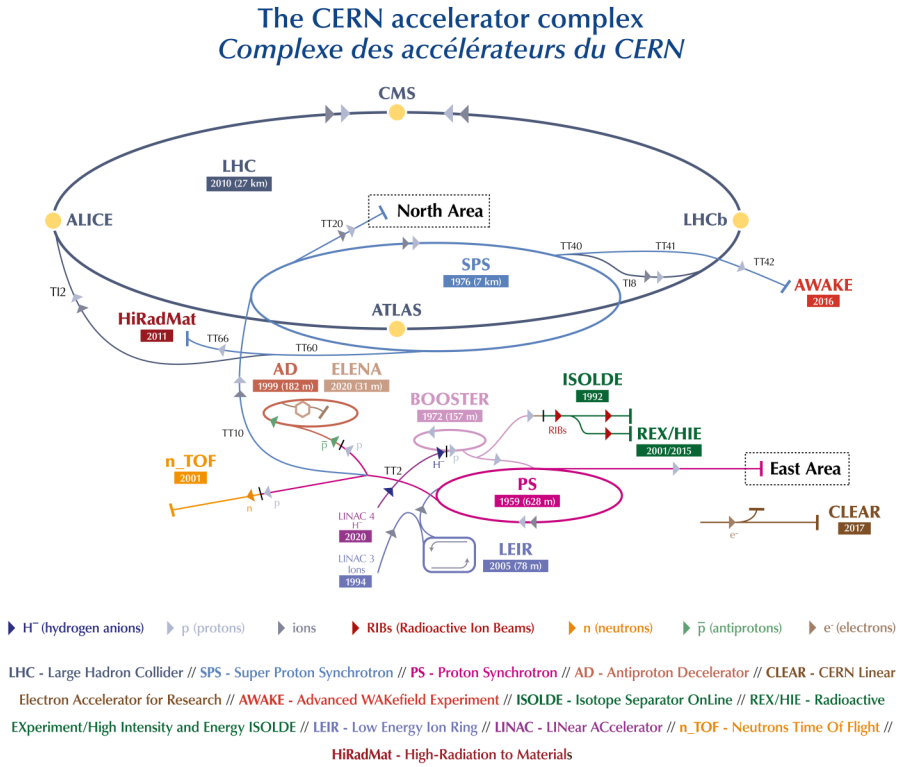

Figure 3.1: The LHC accelerator complex [67].

LHC performance The LHC collides proton bunches with up to 10^{11} protons head on every 25 ns ($f_{col} = 40$ MHz). There are several important LHC performance parameters for the LHC experiments. First, the collision energy is usually denoted by $\sqrt{s}$, the center-of-mass energy. The parameter s is a Lorentz invariant quantity defined as:

$$s = (p_1 + p_2)^2 \tag{3.1}$$

where p_1 and p_2 are the 4-momenta of the colliding protons.

Second, the instantaneous and integrated luminosities. The number of observed events for a specific process is calculated as:

$$N = \sigma \int L(t)dt \tag{3.2}$$

where σ is the cross section of the process at the LHC energy and $L(t)$ is the *instantaneous* luminosity. The *integrated* luminosity is the instantaneous luminosity integrated over time.

The instantaneous luminosity L can be estimated based on some beam parameters:

$$L = \frac{N_b^2 n_b f_{rev}}{4\epsilon_n \beta^*} \tag{3.3}$$

Here, N_b is the number of particles per bunch, n_b is the number of bunches per beam, and f_{rev} is the revolution frequency. The parameter ϵ_n is the normalized transverse beam emittance, which measures the beam spread in the transverse direction, perpendicular to the beam direction. The parameter β^* is the β function value at the collision point. Similar to the emittance, the β function describes the beam envelop variation along the beam axis [68]. Some LHC beam parameters are listed in Table 3.2. The instantaneous and integrated luminosities are measured in ATLAS by dedicated detectors [68]. At LHC Run 2, ATLAS recorded 139 fb^{-1} of data at a peak luminosity of 21×10^{33} cm^{-2}s^{-1} and $\sqrt{s} = 13$ TeV as shown in Figure 3.2 [64]. The unit conversion is: 1 fb = 10^{-43} cm^2. The Run 2 luminosity uncertainties are sub-percent [68].

Parameter	**Value**
Number of bunches per proton beam (n_b)	2808
Number of protons per bunch (N_b)	1.2×10^{11}
Bunch Spacing (ns)	25

Table 3.2: Key beam parameters of the LHC [62].

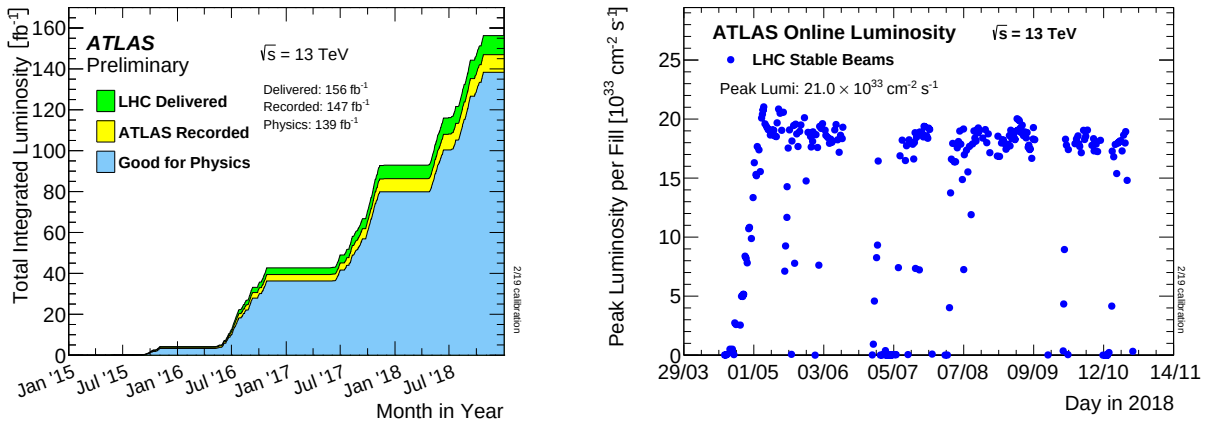

Figure 3.2: Integrated luminosity (left) and peak luminosity (right) recorded by the ATLAS detector during Run 2 [64].

In addition to $\sqrt{s}$ and $L(t)$, another important LHC performance parameter is the pileup, μ. The pileup μ is the mean number of additional inelastic interactions per bunch crossing.

Equation 3.4 defines μ in terms of the luminosity. High pileup increases background noise for signals and stresses the detector system. High pileup is a side effect of high luminosity. It is thus important to mitigate high pileup in the high luminosity environment.

$$\mu = \frac{L\sigma_{inel}}{f_{rev}n_b} \tag{3.4}$$

Here, σ_{inel} is the cross section of inelastic pp collision. There is in-time and out-of-time pileup. In-time pileup is additional pp collisions in the same bunch-crossing as the collision of interest. Out-of-time pileup results from additional pp collisions in neighboring bunch crossings of the collision of interest [53]. Figure 3.3 shows the luminosity as a function of μ. The average of μ, $\langle\mu\rangle$, is approximately 33 during Run 2.

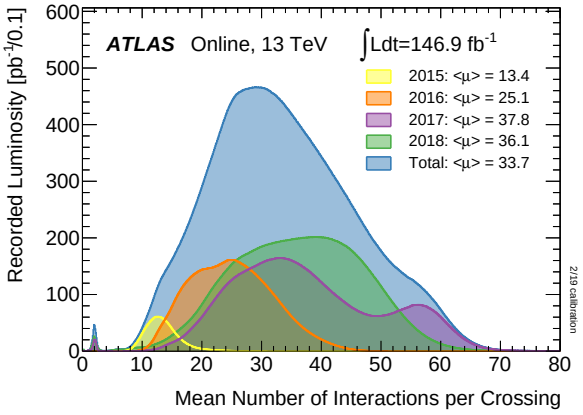

Figure 3.3: Recorded luminosity as a function of the mean number of interactions per crossing, μ, during Run 2 [64].

LHC experiments There are 4 main experiments along the LHC tunnel as shown in Figure 3.1. Both CMS [69] and ATLAS [70] are high-luminosity experiments focusing on proton-proton collision physics. Details of the ATLAS detector are discussed in Section 3.2.

LHCb uses a forward detector to study B hadrons and look for CP violation that hints at new physics in rare heavy-flavor decays [71]. In Run 1 and 2, LHCb collects data with a luminosity around 10^{32} cm^{-1}s^{-1} [72].

Lastly, in addition to proton-proton collisions, the LHC can also collide heavy ions. Both ATLAS and CMS record heavy-ion data in addition to proton-proton collisions. Meanwhile, ALICE is a dedicated heavy-ion experiment [73]. ALICE studies quark-gluon plasma and strongly interacting QCD matter. In addition to the four large experiments, there are also smaller experiments located at the LHC such as FASER [74].

3.2 ATLAS detector

To achieve various physics goals and study Higgs physics at the LHC, the ATLAS detector [70] is designed to have:

- fast and radiation-hard electronics and sensor elements
- high detector granularity to resolve overlapping objects
- large coverage in pseudorapidity and full azimuthal angle

In addition, as shown in Figure 3.4, the ATLAS detector is designed to include several sub-detectors to achieve good particle identification. Specifically:

- Magnet system: deflect charged particle tracks in the detectors and allow good momentum resolution.
- Inner detector (ID): charged-particle momentum resolution and high reconstruction efficiency; close to the interaction region to resolve secondary vertices;
- Calorimetry: electron and photon identification in the electromagnetic calorimeter (ECAL); full-coverage hadronic calorimeter (HCAL) for jet and missing transverse energy (MET) measurements;
- Muon spectrometer (MS): muon identification and momentum resolution; determine charge of high p_T muons;
- Trigger and DAQ: efficient triggering on low p_T objects with sufficient background rejections;

The tracking momentum resolution and calorimeter energy resolution of the ATLAS sub-detectors are important measures of the detector performance. The ATLAS sub-detector resolution goals are listed in Table 3.3. The performance goals are carefully studied in simulations and set by considering both the physics motivation and the detector constraints.

The discussion in this section focuses on the Run 2 ATLAS detector. After Run 2, the ATLAS detector has gone through several phase I upgrades to prepare for Run 3 [75]. After Run 3, ATLAS phase II upgrades for the high luminosity LHC (HL-LHC) are planned to be installed. More details about phase II upgrades are discussed in Chapter 5.

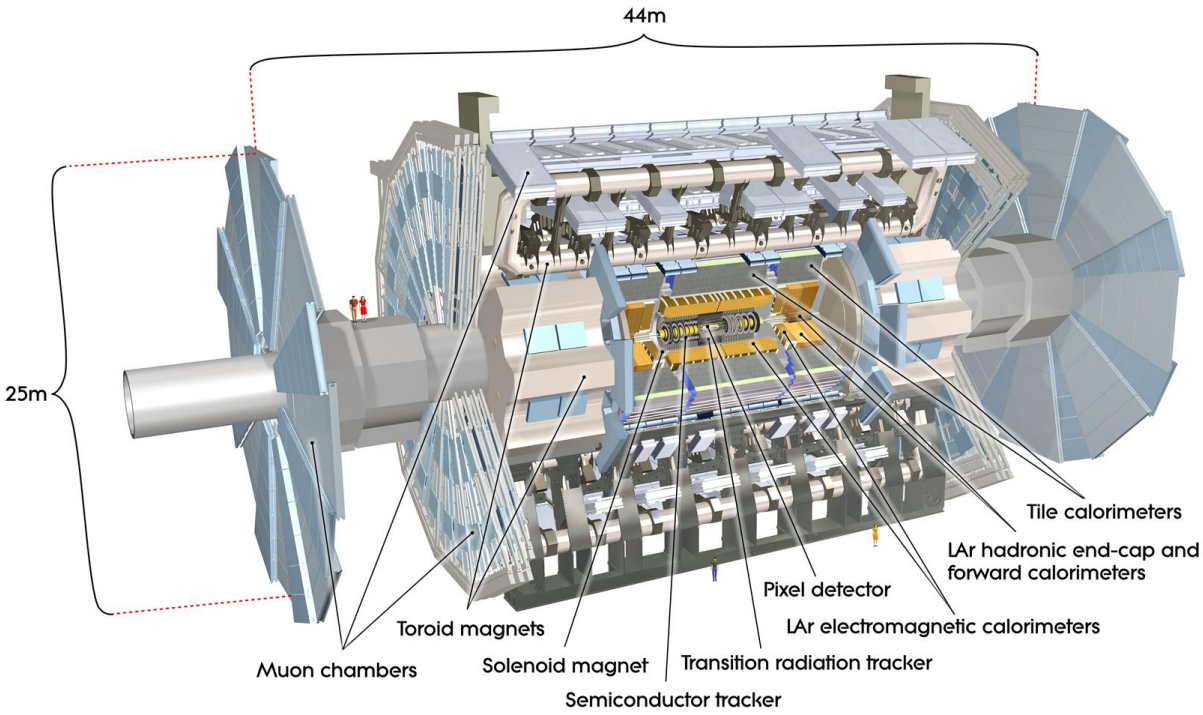

Figure 3.4: The full ATLAS detector [70].

Detector component	**Required resolution**	**η coverage**	
		Measurement	Trigger
ID	$\sigma_{p_T}/p_T = 0.05\% \oplus 1\%$	$\pm$ 2.5	
ECAL	$\sigma_E/E = 10\%/\sqrt{E} \oplus 0.7\%$	$\pm$ 3.2	$\pm$ 2.5
HCAL			
barrel and end-cap	$\sigma_E/E = 50\%/\sqrt{E} \oplus 3\%$	$\pm$ 3.2	$\pm$ 3.2
forward	$\sigma_E/E = 100\%/\sqrt{E} \oplus 10\%$	$3.2 < \eta < 4.9$	$3.2 < \eta < 4.9$
MS	$\sigma_{p_T}/p_T = 10\%$ at $p_T = 1$ TeV	$\pm$ 2.7	$\pm$ 2.4

Table 3.3: ATLAS sub-detector momentum and energy resolution goals [70]. The symbol $\oplus$ represents addition in quadrature. The units of E and p_T are in GeV.

3.2.1 Detector coordinate and particle kinematics

The ATLAS detector is forward-backward symmetric with respect to the interaction point. The magnet system has an eight-fold azimuthal symmetry around the calorimeters. The detector coordinate system is shown in Figure 3.5.

The coordinate system is right-handed, with the x-axis pointing to the center of the LHC tunnel, y-axis pointing upwards, and z-axis pointing along the beam line. Following the spherical coordinate convention, θ measures from the z-axis and ϕ measures from the x-axis in the transverse plane.

The coordinate system is important to physics measurements as the event kinematics are described in terms of the coordinates. The incoming beam travels along the z-axis. Therefore, the transverse momenta p_T should sum up to zero due to conservation of momentum, i.e.:

$$\sum p_T = \sum |\mathbf{p}| \sin(\theta) = 0 \tag{3.5}$$

Similar to the transverse momentum, the transverse energy E_T is defined as [76]:

$$E_T = \frac{E}{\cosh(\eta)} \tag{3.6}$$

Here, η is defined in Equation 3.8 and E is the energy. While the transverse momenta sum to zero, particles are often boosted in the longitudinal direction along the beam. Rapidity y is used to describe angles in the θ direction, as the difference in y, Δy, is invariant under boosts along the z-axis. The rapidity y is defined as:

$$y = \frac{1}{2} \ln \left(\frac{E + p_z}{E - p_z} \right). \tag{3.7}$$

When particles have high energies, the particle mass is negligible compared to the particle energy. And, the rapidity can be approximated by the pseudo-rapidity η:

$$\eta = -\ln \left(\tan \frac{\theta}{2} \right). \tag{3.8}$$

And, the angular separation between two objects are defined as:

$$\Delta R_{12} = \sqrt{\Delta\phi_{12}^2 + \Delta\eta_{12}^2}, \tag{3.9}$$

where $\Delta\phi_{12}$ and $\Delta\eta_{12}$ are the ϕ and η differences between two objects. The invariant mass of a system of particles (i) is defined using the four-momentum p^μ [4]:

$$p^\mu p_\mu = \left(\sum_{i=1}^{N} E_i \right)^2 - \left(\sum_{i=1}^{N} \mathbf{p}_i \right)^2 \tag{3.10}$$

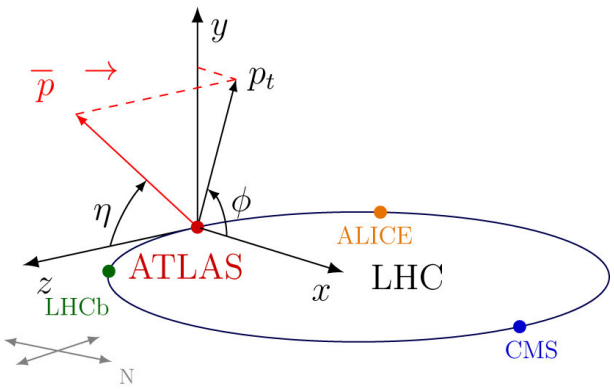

Figure 3.5: The ATLAS coordinate system [77].

3.2.2 Magnet system

The ATLAS magnet system consists of one solenoid and three toroids (one barrel and two end-caps), as shown in Figure 3.6. Given the Lorentz force, the charged particle deflection is different for positively and negatively charged particles, allowing for positive and negative charge reconstruction. The magnetic fields are also required to measure the momentum. Specifically,

- The solenoid provides a 2 T axial magnetic field for the ID, deflecting charged particle tracks in the ϕ direction.
- The barrel and end-cap toroids produce 0.5 T and 1 T fields for the MS, deflecting muon tracks in the η direction.

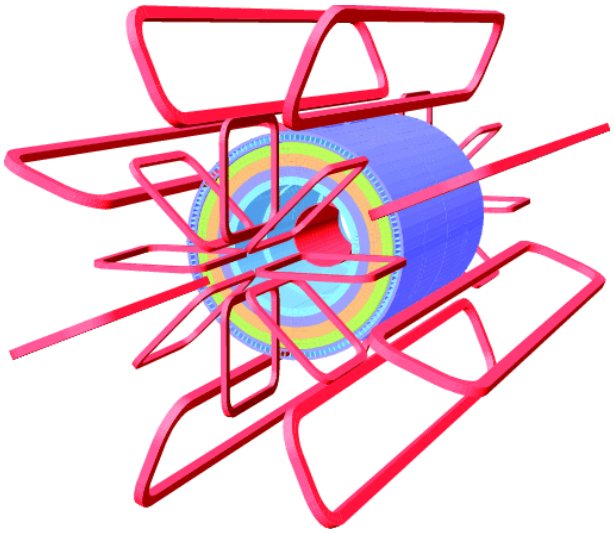

Figure 3.6: The ATLAS magnet system. The toroid coils and solenoid windings are shown in pink. The magnetized tile calorimeters are also displayed [70].

3.2.3 Inner detector

The ATLAS inner detector (ID) is the innermost layer of the ATLAS sub-detectors. The ID schematic is shown in Figure 3.7. The inner detector consists of three sub-systems, the pixel detector (including the Insertable B-Layer, IBL), the silicon strip tracker (SCT), and the transition radiation tracker (TRT). The ID covers the pseudorapidity range of $|\eta| < 2.5$ and the radius from 3 cm to 1 m [78]. Both the pixel detector and the SCT use silicon sensors. Charged particles transverse the sensors, ionize the silicon sensors, and create current pulses in the sensor readout. The silicon detector is an important focus of Chapter 5. More details about the silicon detector mechanism are discussed in Section 5.2. The ID is planned to be upgraded for the HL-LHC and the HL-LHC ID upgrades are discussed in Section 5.1.

At the inner detector, charged particle tracks are deflected due to the solenoidal field. The inner detector records hits when charged particles transverse. *Hits* are ionization signals above certain thresholds. The hits can be reconstructed as tracks and the particle charge and momentum can be inferred. More details of track reconstruction are discussed in Section 3.3.1.

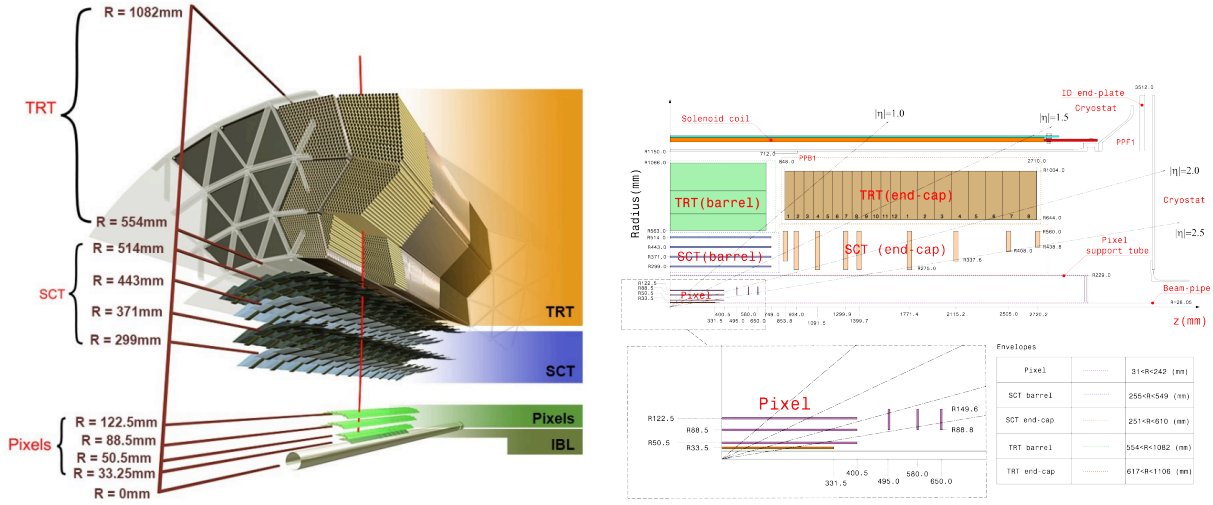

Figure 3.7: The ATLAS inner detector from the z-axis (left) and along the z-axis (right) [78] [79].

Pixel detector The pixel detector consists of three barrel layers and three endcap layers perpendicular to the beam axis on each end of the detector. As shown in Figure 3.7, the three barrel layers spans the radii from 51 mm to 123 mm. The Insertable B-Layer (IBL) was installed at r = 33 mm after Run 1.

The pixel detector has high granularity (92 million readout channels). The pixel layers are segmented in ϕ and z (R) in the barrel (endcap). The sensor has a thickness of 250 μm. The IBL pixel pitch is 50 $\times$ 250 μm. The spatial resolution of the IBL is about 10 μm in $R\phi$ and 67 μm in z (R) for the barrel (endcap) [80]. The outer layers have a pixel pitch of 50 $\times$ 400 μm. The pixel detector high granularity and hit resolution are essential for tracking efficiency, measuring primary and secondary vertices, determining impact parameters, and flavor tagging.

Silicon strip tracker (SCT) The SCT detector covers the radial range from 299 mm to 514 mm. It uses the same silicon sensor mechanism as the pixel detector [81]. The main difference is that the SCT has less granularity in the z direction. The SCT detector has 4 barrel layers and 9 endcap disks on each side. In each barrel layer, two strip sensors are glued back-to-back but at 40 mrad stereo angle. This forms a 2-dimension space point and gives more hit information in the z-direction. Similarly, in the endcap region, the 40 mrad stereo angle gives more granular information in the radial direction. The strip pitch is 80 μm. The hit resolution of the SCT is 17 μm in $R\phi$ and 580 μm in z (R) in the barrel (endcap).

Transition radiation tracker (TRT) The outermost layer of the inner detector is the TRT. The TRT detector is a gaseous straw-tube tracker. It consists of 300 thousand drift tubes with a diameter of 4 mm. The tubes are filled with a gas mixture of 70% Xe. Due to a gas leak in Run 1, some parts are refilled with an argon based gas mixture [82]. Inside each tube, there is a tungsten wire. When charged particles transverse the TRT, it ionizes the gas and creates a current.

In addition to recording charged particle tracks, the TRT can also contribute to particle identification. The space between the straws is filled with polymers. When charged particles transverse a material boundary, transition radiation is generated. This effect depends on the relativistic factor $\gamma = E/m$ and is the strongest for electrons [83].

The TRT covers the radius from 554 mm to 1082 mm and $\eta < 2$. The maximum straw length is 150 cm. The $R\phi$ ($Z\phi$) resolution of the barrel (endcap) is 130 μm. There is no z (R) resolution in the barrel (endcap). In the barrel region, the TRT tubes are split in halves at $z = 0$. Particles typically generate more than 30 hits across the TRT.

Tracking momentum resolution The particle momentum resolution is related to the track position resolution. In the limit of a large number of track hits (N), the tracking momentum resolution can be approximated as [84]:

$$\frac{\sigma_{p_T}}{p_T} \approx \sqrt{\frac{720}{N+4}} \left(\frac{\sigma_x p_T}{0.3BL^2} \right) \tag{3.11}$$

where σ_x is the intrinsic resolution of the measurements, B is the magnetic field, and L is the distance between the first measurement and the N^{th} measurement in the bend plane. The momentum resolution scales linearly with p_T as the high-momentum tracks bend less in B fields. Similarly, the higher the B field is and the larger the tracker, the better the momentum resolution. Setting B = 2 T, N = 13, $\sigma_x = 30$ μm, and L = 1 m, the momentum resolution for a 100 GeV particle is approximately 3%, close to the performance goal listed in Table 3.3.

3.2.4 Calorimetry

The ATLAS electromagnetic (EM) and hadronic calorimeters are layers immediately after the inner detector. The calorimeters measure the energy of neutral and charged particles and contain most electromagnetic and hadronic showers. The calorimeter signals are fast and can be used for triggering. More details of triggering are discussed in Section 3.2.6.

The calorimeter schematic is shown in Figure 3.8. The electromagnetic calorimeters consist of barrel (EMB) and endcap (EMEC) components. The hadronic calorimeters are composed of the tile calorimeter and the liquid argon (LAr) hadronic endcap calorimeter (HEC). The LAr forward calorimeter (FCal) consists of three layers. The first layer is designed for electromagnetic calorimetry and the second and third layers for hadronic calorimetry [85]. The material, η coverage, granularity, and thickness of the detectors are listed in Table 3.4.

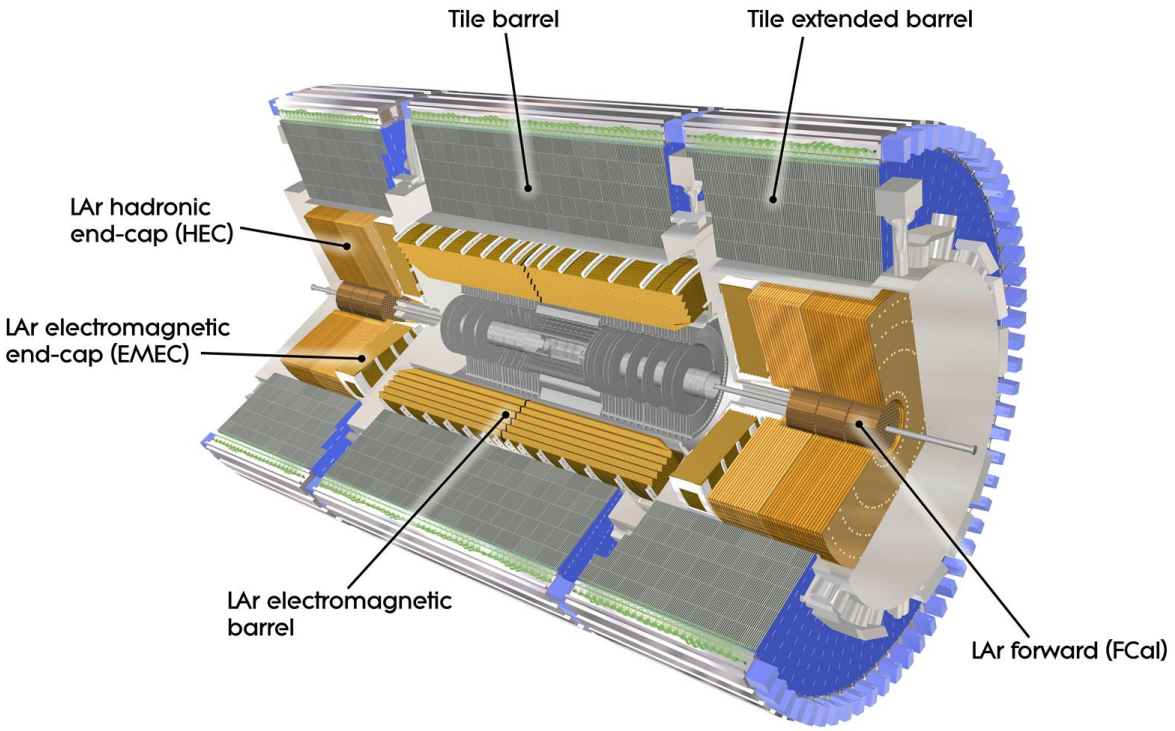

Figure 3.8: The ATLAS calorimeter system [70].

Detector	**Absorber-active material**	η **coverage**	**thickness**
LAr EMB	lead-LAr	$\|\eta\| < 1.475$	$> 22X_0$
LAr EMEC	lead-LAr	$1.375 < \|\eta\| < 3.2$	$> 24X_0$
Tile barrel	steel-scintillator	$\|\eta\| < 1.0$	$\sim 10\lambda$
Tile extended barrel	steel-scintillator	$0.8 < \|\eta\| < 1.7$	$\sim 10\lambda$
LAr HEC	copper-LAr	$1.5 < \|\eta\| < 3.2$	$\sim 12\lambda$
LAr FCal	copper/tungsten-LAr	$3.1 < \|\eta\| < 4.9$	$\sim 10\lambda$

Table 3.4: Main parameters of the ATLAS calorimeter [70, 86, 85].

EM and hadronic calorimeters All ATLAS calorimeters are sampling calorimeters rather than homogeneous calorimeters where the entire detector volume can produce signals [17]. The sampling calorimeters interleave absorber layers with active layers. The electromagnetic or hadronic shower develops in dense absorber layers. Charged particles from the shower generate ionization signals in the liquid argon. In the case of scintillators, ionizing particles from the shower induce scintillation light.

The electromagnetic calorimeters (ECALs) are designed to measure the electron and photon energy deposits through electromagnetic interactions. The hadronic calorimeters (HCALs) measure the energies of fragmenting quarks and gluons (jets) through hadronic interactions. More details about the electron, photon, and jet reconstruction are discussed in Section 3.3. While electrons, photons, and jets generate calorimeter signals, particles such as neutrinos do not. They are reconstructed as the missing transverse energy (MET). More details are discussed in Section 3.3.3.

In ECALs, high energy electrons (photons) lose energy by bremsstrahlung (pair production). Bremsstrahlung refers to that electrons emit photons when interacting with the absorber atomic nuclei. The shower development is governed by the radiation length of the material, X_0. The radiation length is defined as the mean distance over which the electron loses all but 1/e (37%) of its energy by bremsstrahlung,

$$E = E_0 e^{-x/X_0}. \tag{3.12}$$

Therefore, lead, used by the ATLAS LAr EMB and EMEC components, is a good absorber material for electromagnetic calorimetry due to its high atomic number and short radiation length. Most electromagnetic showers can be contained within $22X_0$. Higher energy particles tend to travel further in the calorimeters.

For HCALs, most hadronic showers interact with the calorimeter material by strong interactions. Instead of X_0, the length scale of hadronic shower is described by the *nuclear interaction length*, λ_0, the mean distance travelled by a hadronic particle before undergoing an inelastic nuclear interaction. λ_0 is usually an order of magnitude larger than X_0, setting a larger HCAL volume than ECAL [87]. In ATLAS, the ECAL covers the radius from 1.15 m to 2.25 m and the HCAL covers from 2.28 m to 4.25 m [70, 88]. The ATLAS tile barrel detector is 5.6 m long in the z direction and the extended barrels are 2.6 m long each.

In addition, HCAL tends to have worse energy resolution as shown in Table 3.3. A substantial fraction of nuclear interactions may release energies that cannot be detected, such as the binding energy of nucleons. Thus, the detected energy may fluctuate from event-to-event.

The FCal consists of both electromagnetic and hadronic calorimetry, covering $3.1 < |\eta| < 4.9$. FCal is important for measuring forward jets and improving MET reconstruction. All ATLAS calorimeters have fine granularity in the ϕ and η directions, which gives good position resolutions of shower clusters. The LAr EMB component has $\Delta\eta \approx 0.003$ to 0.05 and $\Delta\phi \approx 0.025$. By comparison, segmentation in the radial direction is coarse. For example, the LAr EMB component is only segmented into three layers in the radial direction.

Calorimeter energy resolution The calorimeter energy resolution can be parametrized as [17]:

$$\frac{\sigma_E}{E} = \frac{a}{\sqrt{E}} \oplus \frac{b}{E} \oplus c. \tag{3.13}$$

The *stochastic* term a represents intrinsic shower fluctuations and dead materials in front of the calorimeters. For sampling calorimeters, a is proportional to $\sqrt{t/f}$, with t being the sampling plate thickness and f the sampling fraction. The energy resolution of the sampling EM calorimeter is typically around 10%, higher than the homogeneous EM calorimeter of a few %. Therefore, the thinner the sampling plate and the larger the sampling fraction, the better the energy resolution.

The term b is due to electronic *noise* in readout. This source can be reduced by calibration and is negligible in ATLAS calorimeters. The *constant* term c represents detector non-uniformity, calibration uncertainties, and radiation damage. The measured calorimeter resolution is close to the performance goal in Table 3.3.

3.2.5 Muon spectrometer

The outermost layer of the ATLAS detector is the muon spectrometer (MS). Unlike electrons, photons, and jets, muons lose energy in the detector mainly by ionization interactions. Therefore, muons transverse the calorimeters with few interactions and are measured through ID and MS tracks. The MS measures the muon tracks deflected by the toroidal field. The ATLAS muon spectrometer serves two main purposes: precision measurement of muon tracks and triggering on muon tracks.

The schematic of the muon spectrometer is shown in Figure 3.9. The main parameters of the MS are shown in Table 3.5. The tracking chambers consist of the Monitored Drift Tube (MDT) chambers and the Cathode-Strip Chambers (CSC). The trigger chambers consist of the Resistive Plate Chambers (RPC) and the Thin Gap Chambers (TGC). As shown in Figure 3.9, the muon barrel system is located on and between toroid coils, while the endcap system is located in front and behind the endcap toroid coils. The ATLAS muon systems have about 1 million readout channels.

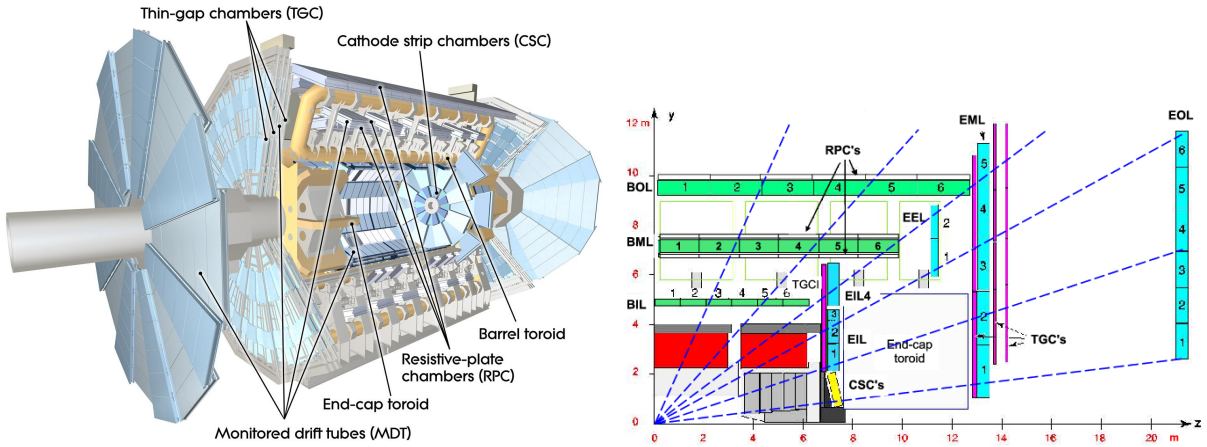

Figure 3.9: The ATLAS muon spectrometer with magnets (left) and from the side (right) [70]. The MDT barrel chambers are shown in green and the endcap chambers in cyan. The RPC, TGC, and CSC systems are marked by their names as well.

Detector	**Purpose**	**Location**	η **coverage**	$\sigma(z/R)$	$\sigma(R\phi)$	**timing**
MDT	Tracking	barrel, endcap	$\|\eta\| < 2.7$	35 μm(z)	-	-
CSC	Tracking	endcap	$2 < \|\eta\| < 2.7$	40 μm(R)	5 mm	7 ns
RPC	Trigger	barrel	$\|\eta\| < 1.05$	10 mm (z)	10 mm	1.5 ns
TGC	Trigger	endcap	$1.05 \mid < \eta\| < 2.4$	2-6 mm	3-7 mm	4 ns

Table 3.5: ATLAS muon spectrometer main parameters [70].

Precision tracking chambers Monitored Drift Tube chambers (MDT) are used in both the endcap and barrel regions for precision tracking. Similar to the inner detector TRT, MDTs use aluminum drift tubes with a 30 mm diameter and a central wire. The tubes are filled with a gas mixture of argon and CO_2. Muons ionize the gas and generate currents when passing through. In the MDT barrel and endcap, drift tubes are oriented along ϕ. Tube lengths range from 1 m to 6 m [89].

As shown in Figure 3.9, the MDT barrel and endcap chambers are placed at various radial and z positions, around $4 \lesssim R \lesssim 10$ m and $7 \lesssim |z| \lesssim 21$ m. Each chamber has 3-8 drift tube layers. In the innermost layer of the endcap region, the CSC system is used instead of the MDTs. At large η and close to the interaction point, high event rates are expected. Unlike MDT, CSC places the anode wires in a plane orthogonal to the strip cathodes. This system with multiple anode wires is also called a multiwire proportional chamber. Similar to MDT, the CSC chambers are filled with a gas mixture with 80% argon. Muons transverse the detector and generate ionization signals.

The wires are oriented radially at the endcap, while the strip cathodes are either parallel or perpendicular to the wires. MDTs do not have good resolution in the ϕ direction due to the long tube lengths. Compared to MDTs, CSCs can achieve spatial resolution in both R and ϕ directions and better timing resolution. At high η, CSCs can handle higher background rates.

Trigger chambers In addition to precision tracking, Resistive Plate Chambers (RPC) and Thin Gap Chambers (TGC) are installed parallel to MDT in the barrel and endcap regions as shown in Figure 3.9. In addition to triggering on muons, the trigger chamber can offer auxiliary information about the muon momentum and coordinates and identify bunch-crossing at the LHC.

RPCs uses a gas gap (2 mm) between two parallel resistive plates. The ionization tracks generate avalanches between the plates. The avalanches of ionization signals are then recorded by the readout strip on the back of the resistive plates [90]. As shown in Figure 3.9, there are three RPC stations. Each station has two perpendicular detector layers, each measuring η and ϕ coordinates.

In the endcap regions, Thin Gap Chambers (TGC) are used. Similar to the CSC, multiwire proportional chambers are used. The wires are placed parallel to the azimuthal directions as the MDT wires, measuring the radial, bending coordinates. The strips are oriented perpendicular in the radial directions, giving azimuthal coordinates. Compared to CSC, TGCs have a shorter wire-to-cathode distance, allowing shorter drift time and better timing resolution for triggering.

3.2.6 Trigger and DAQ

The ATLAS trigger and data acquisition system (TDAQ) is shown in Figure 3.10. The triggering system decides whether or not to keep an event from a given bunch-crossing for

future studies. The DAQ system stores the data temporarily while the trigger decision is being made and transfers accepted events to storage. Given the high instantaneous luminosity, collision rate, and pileup as discussed in Section 3.1, a high selectivity in triggering and signal purity is as important as the triggering efficiency. The ATLAS Run 2 trigger system is composed of two levels:

- Level-1 trigger (L1): hardware-based with custom-made electronics; reduces event rates from the LHC collision rate of 40 MHz to about 100 kHz
- High level trigger (HLT): software-based with commercially available hardware; reduces event rates from L1 100 kHz to 1.5 kHz with a data rate of roughly 2 GB/s [70].

In DAQ, once an event is accepted by L1, the sub-detector front-end electronics (FE) transfer the data to the Readout Drivers (ROD). The data collection network eventually passes events to HLT and sends HLT-accepted events to the permanent storage at CERN.

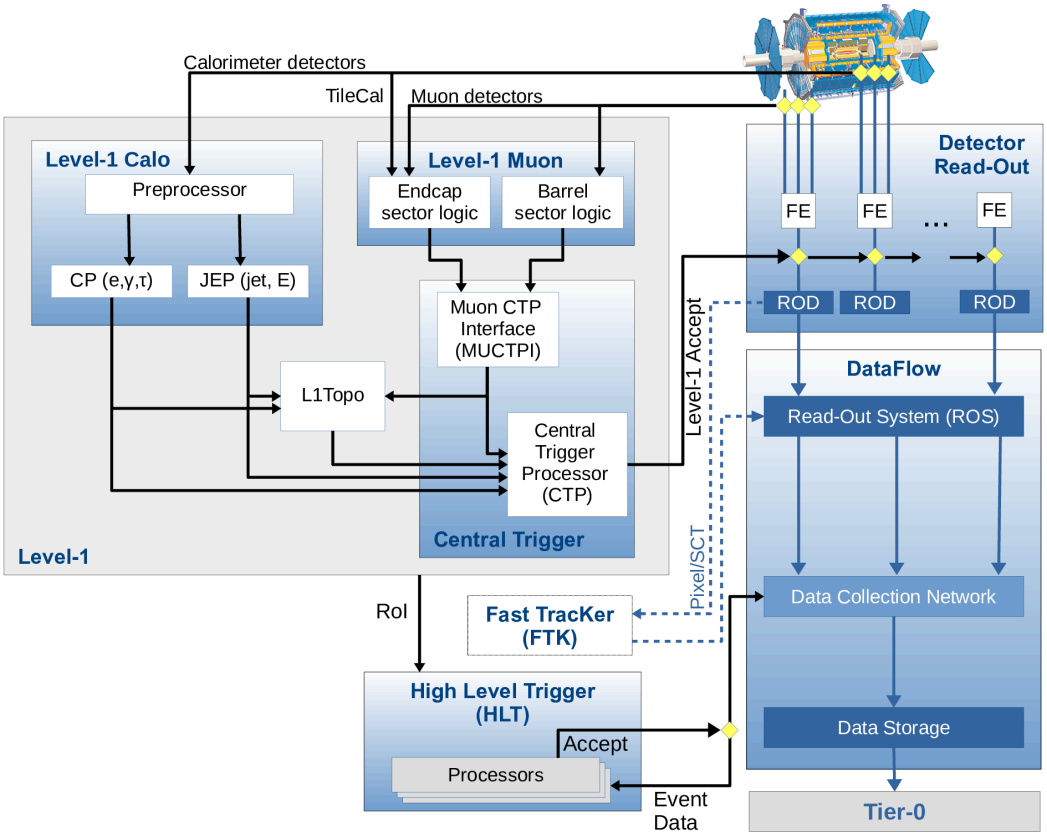

Figure 3.10: The ATLAS TDAQ diagram in Run 2 [91]. Note that while Fast TracKer (FTK) is included in the schematic, it was not used by the HLT during Run 2 [92].

Level-1 trigger The L1 trigger consists of four components: the calorimeter trigger (L1Calo), the muon trigger (L1Muon), the topological trigger (L1Topo), and the Central Trigger Processor (CTP), as shown in Figure 3.10.

The L1Calo trigger takes trigger towers from the calorimeters discussed in Section 3.2.4 and identifies high E_T (defined in Equation 3.8) electron, photon, hadronically-decayed tau leptons, and jet candidates [93]. The trigger tower is of the size: $\Delta\eta \times \Delta\phi = 0.1 \times 0.1$, summed over finer calorimeter cells. It can also identify large missing transverse energies (the proxy for neutrinos). More detailed offline object reconstruction used for physics analysis is discussed in Section 3.3.

The L1Muon trigger receives hits with bunch-crossing information from RPC and TGC as discussed in Section 3.2.5. L1Muon selects muon candidates by requiring coincidence of hits and tracks that can extrapolate to the interaction point. The dimensions of muon RoIs (Regions-of-Interests) have similar granularity as the L1Calo trigger towers.

Lastly, L1Calo and L1Muon trigger information about muons, electrons, photons, MET, tau, and jets is passed to both the CTP and L1Topo. L1Topo combines calorimeter and muon L1 triggers and allows selection over complex physics quantities 3.10. CTP eventually combines all L1Calo, L1Muon and L1Topo trigger information, makes the L1 trigger decision, and sends the decision to detector front-ends for readout [94]. The L1 latency time is about 2 μs. In addition, CTP also uses information from the ATLAS forward detectors such as LUCID [94].

High level trigger In addition to making L1 trigger decisions, the L1 triggers identify and send RoIs to the High level trigger (HLT). The HLT then uses full detector granularity at the RoIs to make the final trigger decision. The HLT processing time can take up to 2 s [95].

3.3 Object reconstruction

As seen in the previous section, the ATLAS detector aims to detect various physics objects such as electrons, photons, muons, hadronic taus, missing transverse energy (MET), and jets, illustrated in Figure 3.11. Sophisticated algorithms are used to reconstruct and calibrate those physics objects from the detector signals. Signals from different detectors are often combined in the reconstruction. For example, charged particles such as muons might leave signals in both the ID and the muon spectrometer. In this section, all reconstructed physics objects are discussed with an emphasis on the objects that are used by the $VH(\rightarrow b\bar{b}, c\bar{c})$ analysis in Chapter 4.

The section is structured as follows: Section 3.3.1 discusses the inner detector track reconstruction and primary vertex reconstruction and Sections 3.3.2 to 3.3.3 on electron and photon, muon, jet, MET, and tau reconstruction.

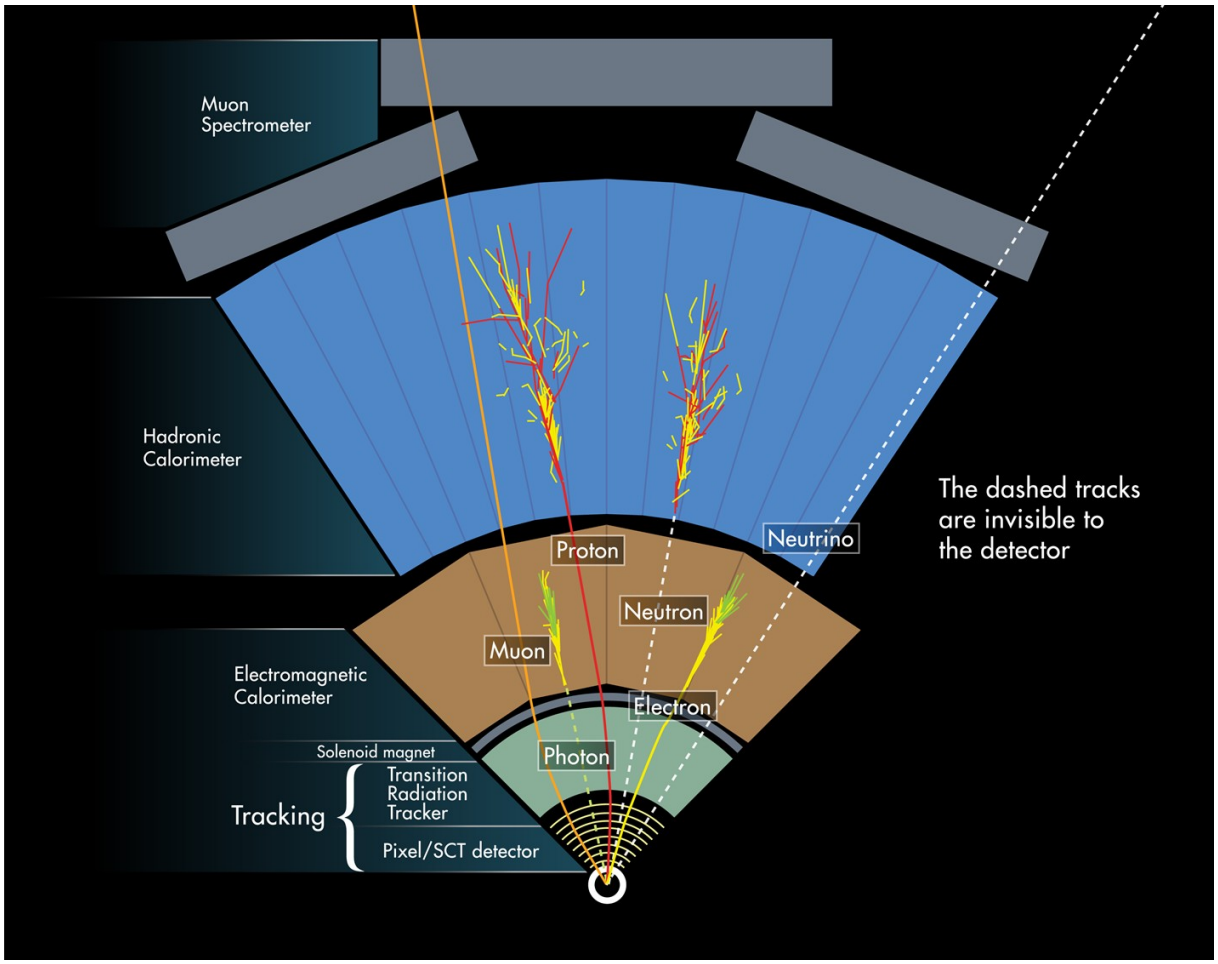

Figure 3.11: ATLAS detectors and physics objects [96].

3.3.1 Tracks and primary vertex

When charged particles transverse the inner detector (ID), the ionization signal is reconstructed as clusters. The clusters are connected to form tracks for charged particles. The tracking information is an extremely important input for all physics object reconstruction including the vertex, electrons, photons, muons, jets, flavor tagging, etc.

Tracks The track reconstruction in ATLAS Run 2 follows roughly 4 steps [97]:

- **Form space points from clusters:** first, clusters are formed by finding signals on neighboring cells in the pixel and strip detector (SCT). From the clusters, three-dimensional space points are created. Each cluster equates one space point in the pixel

detector. For the SCT, clusters on both sides of a strip layer are combined to form three dimensional space points.

- **Find space-point-seeded tracks:** track finding starts with space-point triplets (seeds). A number of criteria such as impact parameter and momentum requirements are placed on the seeds. These criteria maximize the fractions of seeds that result in good-quality tracks. Seeds passing the selection are then sent to a Kalman filter to complete the track candidate within the silicon detector.
- **Resolve ambiguities:** completed track candidates are then sent to the ambiguity solver. The ambiguity solver uses a scoring system favoring candidates that are likely the trajectory of a charged particle. For example, it penalizes tracks with holes (missing clusters along the track). It also limits the number of shared clusters between tracks. Shared clusters are different from merged clusters, where multiple charged particles deposit charge signals. Shared clusters tend to be from incorrect assignments. More criteria are set on the track candidates such as track p_T and and impact parameters.
- **TRT extension**: finally, successful track candidates within the coverage of TRT ($|\eta| < 2$) are extended into the TRT. The TRT extension can improve momentum resolution due to its large radius measurements.

The reconstructed tracks are parameterized by 5 parameters as shown in Figure 3.12 and Table 3.6.

Parameter	**Definition**
q/p	the ratio of the charge of the reconstructed track divided by the magnitude of its momentum;
ϕ	the azimuthal angle of the track's momentum in the transverse plane, measured from $[\pi, -\pi]$
θ	the polar angle of the track's momentum with respect to the z-axis, measured from $[0, 2\pi]$
d_0	the transverse impact parameter, defined as the distance measured from the point of the closest approach on the track to the beam line in the transverse plane
z_0	the longitudinal impact parameter, analogous to d_0, defined as the distance measured from the point of the closest approach on the track to the beam spot in the longitudinal plane

Table 3.6: ATLAS track parameters [98, 97, 99].

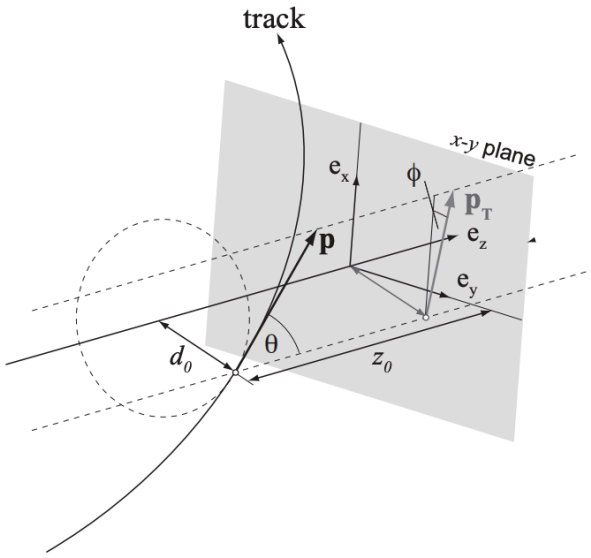

Figure 3.12: ATLAS reconstructed track parameters with a perigee representation [100].

Primary vertices The primary vertex (PV) tries to identify the location of the hard scatter in an event. The PV reconstruction is closely related to the track reconstruction.

The PV reconstruction starts from a subset of reconstructed tracks discussed above with tighter requirements such as the number of hits, impact parameter, and transverse momentum [101]. From those tracks, the PV is reconstructed in two steps:

- **Select the seed position of the first vertex:** the seed position in the transverse plane is determined from the center of the luminous region. The luminous region can be determined online during data taking through inner detector tracks at the high level trigger (HLT). The z-coordinate is determined from the z-coordinates of the tracks at their points of closest approach to the beam-spot center.

- **Iterative PV fit:** the fitting algorithm proceeds iteratively, each time down-weighting less compatible tracks and recomputing the vertex position. Tracks incompatible with the vertex by the 7σ are disassociated from the vertex.

Remaining tracks are used to find the next primary vertex candidate until no tracks are left in the event. All vertices with at least two associated tracks are retained as valid primary vertex candidates. In addition, during the fitting process, tracks outside the beam spot are removed due to their low compatibility with PV candidates. The reconstructed primary vertex with the largest $\sum p_T^2$ of tracks is defined as the hard-scatter PV.

The PV reconstruction process described does not require prior beam spot knowledge. Such PV candidates can be used to reconstruct the beam spot offline during the Tier-0

calibration and data preparation after events are accepted by the HLT and before events are distributed to higher tier computing facilities [102]. The measured beam spot sizes from Run 2 are shown in Figure 3.13.

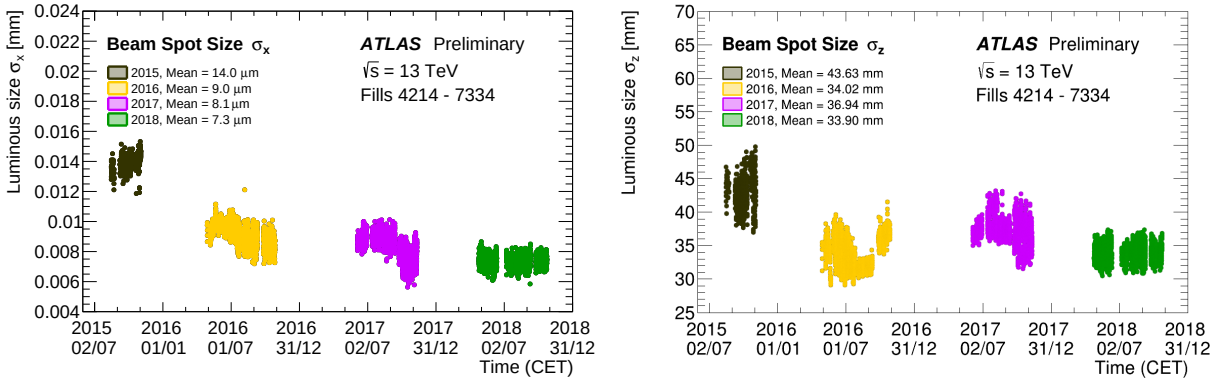

Figure 3.13: The size of the LHC beam spot measured in the x-axis (left) and the z-axis (right) in ATLAS during Run 2 [103].

3.3.2 Electrons, photons, muons, and hadronic tau-leptons

As discussed previously, the ATLAS electromagnetic calorimeter (ECAL), including the EMB, EMEC and the first layer of FCal, and muon spectrometer aim to detect electrons, photons and muons. For electrons and muons, the inner detector tracks described in the previous section are also important reconstruction ingredients. In this thesis, electrons and muons are of particular importance for the $VH(\to b\bar{b}, c\bar{c})$ analysis in Chapter 4. This section focuses on discussing the electron and muon reconstruction and briefly discusses the photon reconstruction.

In addition to electrons and muons, τ-leptons can also be reconstructed from the ATLAS detectors. Leptonically decayed τ-leptons are hard to distinguish from prompt electrons or muons. This section only discusses hadronic τ reconstruction. Hadronic τ-leptons are used in the $VH(\to b\bar{b}, c\bar{c})$ analysis for event categorizations.

Electrons and photons For many physics analyses, the electrons from prompt particle decays are the signals of interest. In the $VH(\to b\bar{b}, c\bar{c})$ analysis, for example, electrons from prompt W and Z boson decays are used to reconstruct the vector bosons. This section focuses on the reconstruction of prompt electrons. In the next section, non-prompt electrons (soft) from the decays of heavy flavor jets are also discussed as they are useful for identifying the flavor of the jets.

For reconstructing the prompt electron, there are four main components [104]:

- **Reconstruction:** The electron reconstruction matches the inner detector track with the ECAL energy cluster. The ECAL clusters are reconstructed using a sliding-window algorithm [105]. Localized energy clusters are found by sliding a window of fixed $\Delta\eta \times \Delta\phi$ across the ECAL towers. The tracks used in the electron reconstruction are reconstructed as described in the previous section but with a subsequent Gaussian sum filter (GSF) fitting procedure to recover ID electron bremsstrahlung [104, 106]. Finally, the cluster is matched to the electron track candidate by requiring small angular separation between the track and the cluster. For example, $|\eta_{\text{cluster}} - \eta_{\text{track}}| < 0.05$.

- **Identification:** The electron identification uses a likelihood-based (LH) method. The probability density functions (pdfs) of discriminating parameters for the signal (prompt) and background electrons are used to compose likelihoods. The signal and background likelihoods form a discriminant. Loose, medium, and tight working points are chosen by cutting on the discriminant while maintaining 93%, 88%, 80% of signal efficiency respectively.

- **Isolation:** After reconstructing and identifying electron candidates, further isolation selection criteria can be set. The isolation criteria utilize the fact that prompt electrons tend to have little activity in the vicinity. That is, there are few particles near prompt electrons. The isolation criteria are usually defined in terms of upper cuts on $E_{T,cone}^{isol}$ (cluster energy near the signal within a cone of ΔR) and p_T^{iso} (track energy near the signal). Electron candidates with higher $E_{T,cone}^{isol}$ or p_T^{iso} above certain thresholds tend to be less isolated.

- **Calibration:** Finally, before the electron candidates can be used in physics analysis, energy corrections are applied to both the energy scale (E) and the energy resolution (σ_E) by comparing the simulation with the data using $Z \to ee$ decays [107]. The electron identification efficiencies are also compared between the data and the Monte Carlo (MC) simulation for $J/\psi \to ee$ and $Z \to ee$. The overall data-MC scale factor uncertainties are up to 5%.

The photon reconstruction, identification, isolation, and calibration are similar to the electron case. In reconstruction, unconverted photons do not have tracks in the inner detector (ID). The photon identification is cut-based instead of likelihood-based. The photon calibration uses $Z \to \mu\mu\gamma$.

Muons Similar to the electron reconstruction, muon reconstruction follows four steps: reconstruction, identification, isolation, and calibration [108].

- **Reconstruction:** Tracks from the muon spectrometer (MS) are first reconstructed by fitting together hits from different layers in a combinatorial search. Then, the MS tracks are combined with the ID tracks (Section 3.3.1). The muon reconstruction is primarily based on ID and MS tracks. Information from calorimeter energy deposits is used, for example, when muons have large energy losses in the calorimeters.

- **Identification:** Similar to prompt electron identification, the goal is to select prompt muons, for example, from W and Z boson decays. The identification sets various requirements on discriminating variables such as the χ^2 of the combined track fit. Different working points at different signal efficiencies are set.

- **Isolation:** The muon isolation is also based on two isolation variables: $p_T^{varcone30}$ (track momentum sum near the muon) and $E_T^{topocone20}$ (transverse energy around the muon). For $p_T^{varcone30}$, the track momentum is summed over a cone of variable sizes depending on p_T^{μ}, $\Delta R < \min(10\text{ GeV}/p_T^{\mu}, 0.3)$. For $E_T^{topocone20}$, the transverse energy is summed over topological cell clusters in a cone around the muon. The *topo-clusters* are different from the fixed-size sliding-window algorithm [109]. The topological clustering algorithm clusters neighboring cells as long as the signal is significant compared to the noise.

- **Calibration:** The final calibration on the muon p_T and momentum resolution $\sigma(p_T)$ compares data and simulation of $J/\Psi \to \mu\mu$ and $Z \to \mu\mu$ decays. The muon identification efficiencies are also measured by comparing the $J/\psi \to \mu\mu$ and $Z \to \mu\mu$ data and the Monte Carlo (MC) simulation. The data-MC scale factor uncertainties are sub-%.

Hadronic tau-leptons τ-leptons are the heaviest leptons with a mass of 1.78 GeV [110, 111]. With a lifetime of 2.9×10^{-13} s, a 40 GeV τ-lepton can travel about 2 mm in the detector before decaying. The τ-leptons decay both leptonically and hadronically (65% of the time). τ-leptons are called leptonic or hadronic based on their decay modes. The leptonic τ-leptons decay to $e\nu\overline{\nu}$ or $\mu\nu\overline{\nu}$, where the electrons and muons tend to be efficiently reconstructed [14]. It is hard to distinguish prompt electrons and muons from leptonic τ. Leptonic τ-leptons are usually used in analyses as electrons or muons.

On the other hand, the hadronic τ decays contain either one or three charged pions (72% or 22%). In addition, neutral pions might also be produced. The hadronic τ candidates are reconstructed explicitly using jets and tracks. The jet reconstruction is discussed in detail in Section 3.3.3.

The identification of hadronic τ uses a Recurrent Neural Network (RNN) trained on $\gamma^* \to \tau\tau$. The inputs to the RNN are differentiating kinematic variables such as the shower depth. Based on the RNN outputs, *loose, medium* and *tight* working points are defined. The RNN algorithm achieves good performance in identifying hadronic τ-leptons and rejecting QCD jets.

3.3.3 Jets and MET

In addition to the electron, photon, and muon reconstruction described in the previous section, ATLAS also reconstructs jets and missing transverse energy (MET). MET is used as a proxy for neutrinos as neutrinos cannot be directly detected in the ATLAS detectors.

Jet reconstruction Jets are collimated sprays of charged and neutral hadrons. Quarks and gluons from the high-energy interactions fragment and hadronize to jets [112]. In the case of $VH(\rightarrow b\bar{b}, c\bar{c})$, b and c quarks are observed in the detector as jets. Jets are important physics objects for the analysis.

For jet reconstruction, two algorithms are used in sequence: first, the particle flow (PFlow) algorithm; then, the anti-k_t algorithm. The PFlow algorithm manages track-cluster energy subtraction and produces inputs for the anti-k_t algorithm, which performs the final jet clustering.

The PFlow algorithm uses the ID tracks and calorimeter topo-clusters. The ID tracks are discussed in Section 3.3.1. The *topo-clusters* are introduced in Section 3.3.2. Compared to the fixed-size sliding-window algorithm, the topo-clusters are more suitable for hadronic final state reconstruction such as jets. The PFlow algorithm first matches tracks to clusters and modifies the cluster energy based on track momentum and expected cluster energy [113].

The ensemble of tracks and topo-clusters from the PFlow algorithm is then used in the anti-k_t algorithm to reconstruct jets. The anti-k_t algorithm defines two distances [114]:

$$d_{ij} = \min(p_{Ti}^{-2}, p_{Tj}^{-2}) \frac{\Delta_{ij}^2}{R^2} \tag{3.14}$$

$$d_{iB} = p_{Ti}^{-2} \tag{3.15}$$

where p_{Ti} and p_{Tj} are the transverse momenta of the objects i and j. The objects can be any input objects to the anti-k_t algorithm or combined objects from the anti-k_t algorithm. And, $\Delta_{ij}^2 = (y_i - y_j)^2 + (\phi_i - \phi_j)^2$. Here, y is the rapidity defined in Equation 3.7 and ϕ is the azimuthal angle. R is the radius parameter that roughly defines the maximum size of the jet. And, d_{iB} stands for the distance between object i and the beam. The algorithm groups objects as follows: for two objects, if $d_{ij} < d_{iB}$, combine object i and j; otherwise, define i as a jet and remove it from the object collection. The procedure is repeated until no objects are left.

The reconstructed jets from the anti-k_T algorithm are illustrated in Figure 3.14. The anti-k_T algorithm is infrared and collinear (IRC) safe, i.e., the set of hard jets remains unchanged by collinear splitting or soft emission [112]. In addition, the hard jet cone boundaries are not perturbed by soft jets, as shown in the figure. In the $VH(\rightarrow b\bar{b}, c\bar{c})$ analysis, the radius parameter R is chosen as 0.4 and 1.0, corresponding to the small-R jets and the large-R jets. In the case of $VH(\rightarrow b\bar{b}, c\bar{c})$, large-R jets are used to approximate Higgs bosons with large transverse momenta in the boosted Higgs-to-bottom decays. This is because small-R jets tend to merge as one large-R jet in the boosted phase space [115].

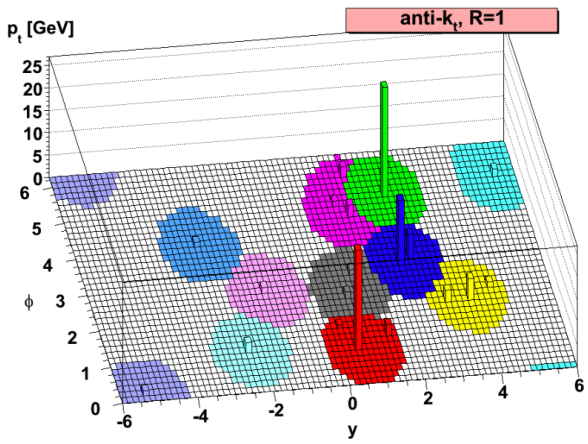

Figure 3.14: Jets reconstructed from the anti-k_T algorithm [114].

Jet calibration Jet calibration contains two main parts, the jet energy scale (JES) calibration and the jet energy resolution (JER) calibration. The JES calibration aims to restore the electromagnetic (EM) scale jet energy to the truth jet particle-level energy scale. As discussed in Section 3.2.4, fractions of the non-EM energy might be undetected in the calorimeter. The JES calibration follows several steps that are applied to the four-momentum of the jets [116]. The first three steps are only applied to simulation using truth information, while the last step is applied to data to match data with simulation. The JES calibration steps are summarized as follows:

- **Pileup correction:** The pileup corrections remove excess jet energy due to additional proton-proton interactions with the same (in-time) or nearby (out-of-time) bunch crossings. The correction uses the jet area and transverse momentum of the event, the number of primary vertices (N_{pv}) and the mean number of interactions per bunch crossing (μ) defined in Equation 3.4.

- **Absolute simulation based calibration:** The jet energy response R is defined as the mean of a Gaussian fit to the E^{reco}/E^{true} distribution. R is calculated in energy and η bins. At this step, the jet calibration factor is taken as the inverse of R. This factor corrects the jet energy to the truth particle level.

- **Global sequential (GS) calibration:** After the previous step, the JES is still dependent on the flavor and energy of the jet constituent particles. GS calibration uses six observables, such as the energy fraction measured in each layer, to reduce dependence of the jet response on each observable while conserving the overall energy scale.

- **Residual calibration:** Lastly, a final correction is applied to data to account for imperfect descriptions of the detector response. The correction is performed by balancing

the jet momentum with reference objects in events such as Z+jets. The response to the forward jets are also corrected using central jets in η.

In addition to calibrating the JES, measuring the JER is also important. The jet energy resolution (σ_{p_T}) parameterization is the same as in Equation 3.13. The readout noise term in σ_{p_T} scales as N/p_T. The JER measurement is simple compared to the JES calibration that involves multiple steps applied to both the simulation and the data. The JER measurement is extracted from the Gaussian fit of the dijet momentum balance.

The final correction on data for the residual JES calibration is shown in Figure 3.15. The final correction is approximately 3% at low p_T and decreases at higher p_T. Figure 3.15 also presents the final JER measurements.

Both JES and JER have a large number of systematics. The main contribution is from the in situ residual calibration in the case of JES and the in situ dijet calibration for JER as shown in Figure 3.16. The total uncertainty on JES is about 5% at low p_T. The JES uncertainties also include the flavor dependence including the flavor response and composition uncertainties for quark- versus gluon-initiated jets. For heavy-flavor jets, the flavor uncertainty focuses on light-flavor versus heavy-flavor jets. More details about the light-flavor and heavy-flavor jets are discussed in Section 3.4. The JES and JER calibration described above are mainly used for the small-R jets. For large-R jets, the jet energy and mass calibration follow similar simulation-based procedures [117]. More details about the jet uncertainties included in the $VH(\to b\bar{b}, c\bar{c})$ analysis are discussed in Section 4.2.

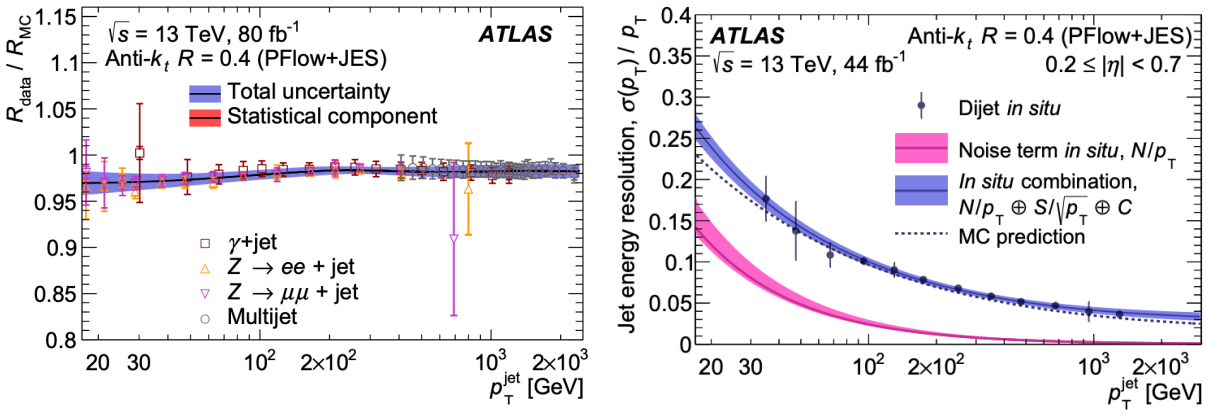

Figure 3.15: The final JES correction (left) and JER measurements (right) [116]. On the left, the y-axis is the ratio of jet response in data to MC. The data points are from calibrations performed in $\gamma + jet$, Z+jet where Z bosons decay to ee or $\mu\mu$, and multi-jet. The purple error bands are the total uncertainties from the final residual calibration on data. The statistical component in pink band is too small to be visible in most regions. The data point total uncertainties and statistical uncertainties are shown in outer and inner horizontal ticks. On the right, the measurements for JER are from dijet events. The y-axis is the relative jet energy resolution. The dijet data points and their total uncertainties are shown in black dots. The total relative jet energy resolution and its uncertainties, matched to the data points, are shown in the purple band. The pink band illustrates the noise component contribution.

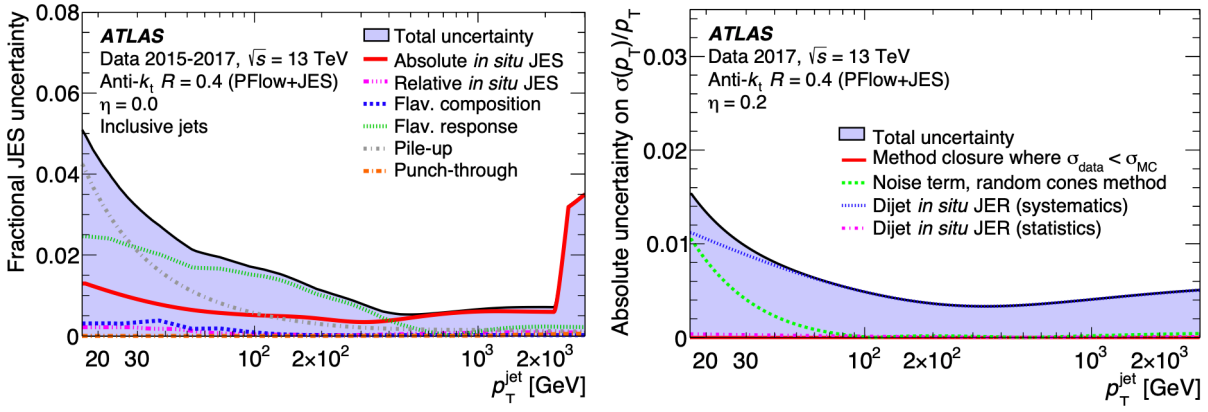

Figure 3.16: The JES uncertainty (left) and the JER uncertainty (right) [116].

Suppression of background jets In addition to the energy calibration procedures described above, two approaches are used to suppress background jets, Jet Vertex Tagger (JVT) and jet cleaning selection criteria. Compared to the signal jets from the hard scatter of interest, background jets are from pileup or other processes.

In the case of JVT, the goal is to reject pileup jets using two discriminating variables, corrJVF and R_{pT}. corrJVF is the based on the jet-vertex-fraction and corrected for the total number of pileup tracks. R_{pT} is the ratio between track transverse momentum from the hard-scatter vertex (defined in Section 3.3.1) to all associated tracks in the jet. A k-nearest neighbor (kNN) algorithm is used to estimate the likelihood, named JVT, for a jet to be from hard scatter in the 2-dimensional plane of corrJVF and R_{pT}. The probability is calculated as the ratio of the number of hard-scatter jets divided by the number of hard-scatter plus pileup jets found in a local neighborhood around the point. Working points with different hard-scatter jet efficiencies can be set by cutting on JVT [118].

JVT is based on tracking information and thus can only be used at $|\eta| < 2.5$ in the coverage of the inner detector. To reject pileup jets in the forward region ($2.5 < |\eta| < 4.5$), the forward JVT (fJVT) uses the normalized projection of the missing transverse momentum on the forward jet transverse momentum direction. Pileup forward jets tend to have larger fJVT [119].

Lastly, the jet cleaning selection criteria aim to remove three additional sources of background jets [120]:

- **Beam induced backgrounds (BIB):** due to proton losses upstream of the interaction point. The losses induce secondary cascades that lead to high energy muons identified as fake jets.
- **Cosmic-ray showers:** high energy muons from the cosmic rays reaching the ATLAS detector.
- **Calorimeter noise:** most permanent or sporadic noises are rejected by data quality inspection. For example, the large-scale coherent noise from the LAr calorimeter high voltage system can be flagged and vetoed by a quality factor that reflects if the pulse shapes look like argon ionization pulse shapes [121]. However, a small fraction of noise remains and needs additional rejection criteria.

To reject these background jets, tight and loose jet cleaning cuts are set on various parameters based on the LAr calorimeter pulse shape in each cell, energy deposit fractions in each layer, track momentum fraction, etc. The complete cut settings are discussed in detail in [120]. The selection criteria ensure high jet efficiencies while removing fake jets.

Missing transverse energy All reconstructed objects discussed above, the electrons, photons, muons, jets, and τ-leptons, are particles that can leave signals, as shown in Figure 3.11. However, particles, such as neutrinos and some dark matter candidates beyond the Standard Model (BSM), do not leave any signals. These particles are quantified using the

missing transverse energy, E_T^{miss} or MET. As discussed in Equation 3.5, the transverse momenta of all particles should sum to zero [122]. This allows quantifying E_T^{miss} in the transverse direction perpendicular to the beam axis. However, any momentum in the forward direction, close to the beam line, is difficult to quantify due to the lack of detector coverage and momentum balance. Therefore,

$$\mathbf{E}_T^{miss} = -\sum \mathbf{p}_T^{\mu} - \sum \mathbf{p}_T^{e} - \sum \mathbf{p}_T^{\gamma} - \sum \mathbf{p}_T^{\tau_{had}} - \sum \mathbf{p}_T^{jet} - \sum \mathbf{p}_T^{soft} \tag{3.16}$$

where $\mathbf{E}_T^{miss} = (E_x^{miss}, E_y^{miss})$ is the vectorial sum of all transverse momenta. The first five terms are the *hard* terms associated with reconstructed prompt particles with large momentum. The last term is the *soft* term, which refers to reconstructed tracks associated with the hard-scatter vertex but not hard objects. The MET response, resolution and systematic uncertainties are evaluated using $Z \to \mu\mu$ and $W \to e\nu$ events. The MC and data agree within uncertainties and no additional scale factors are derived for E_T^{miss}.

3.4 Flavor tagging

This section focuses on the flavor tagging performance. Identifying the jet flavor is important for many physics analyses, such as the $VH(\to b\bar{b}, c\bar{c})$ analysis. There are four jet flavors defined in this section: b-jets, c-jets, τ-jets, and l-jets. b-jets, c-jets, and τ-jets are jets containing b-hadrons, c-hadrons, and hadronic τ-leptons. b- and c-hadrons are from b- and c-quark hadronization. b-hadrons tend to decay to c-hadrons first in the decay chain before further decaying [14].

b-jets and c-jets are often referred to as heavy-flavor jets. While hadronic τ-leptons can be identified using the RNN algorithm discussed in Section 3.3.2, some hadronic τ-leptons might be misidentified as heavy flavor jets and are thus included in some flavor tagging algorithm evaluation, as shown in Table 4.7. l-jets are light-flavor jets that do not contain those heavy particles but come from *u, d, s*-quark or gluon hadronization. Light-flavor and heavy-flavor jets are considered separately, as heavy-flavor hadrons tend to have longer lifetimes.

Different jet flavors have different characteristics, enabling flavor tagging algorithms. For l-jets,there are also differences between gluon-initiated and quark-initiated jets [123]. However, the current ATLAS flavor tagging algorithm does not explicitly differentiate these two types.

In this section, Section 3.4.1-3.4.2 introduce the ATLAS flavor tagging algorithm and its calibration. Section 3.4.3 presents the improved baseline flavor tagging algorithm with soft electrons.

3.4.1 DL1r

DL1r is the Run 2 flavor tagging algorithm used in the $VH(\to b\bar{b}, c\bar{c})$ analysis [124]. Machine learning (ML) tools have been used in ATLAS flavor tagging since early Run 2. The first

Run 2 algorithm, MV2, is based on boosted decision trees [125]. DL1r is a multi-layer neural network that takes in variables from various low level algorithms. The DL1r outputs are flavor tagging discriminants. The low level algorithms directly use inner detector tracks, primary vertices (PVs), and jets to form discriminating variables for `DL1r`.

Inputs	Variables	Definitions
Kinematics	p_T	Jet p_T
	$\|\eta\|$	Jet $\|\eta\|$
IP2D, IP3D	$\log(P_b/P_{light})$	Likelihood ratio of b-jets to l-jets
	$\log(P_b/P_c)$	Likelihood ratio of b-jets to c-jets
	$\log(P_c/P_{light})$	Likelihood ratio of c-jets to l-jets
RNNIP	P_b	b-jet probability
	P_c	c-jet probability
	P_{light}	l-jet probability
SV1	m(SV)	Invariant mass of tracks at the secondary vertex assuming pion mass
	f_E(SV)	Jet energy fraction of the tracks associated with the secondary vertex
	$N_{TrkAtVtx}$(SV)	Number of tracks used in the secondary vertex
	$N_{2TrkVtx}$(SV)	Number of two-track vertex candidates
	L_{xy}(SV)	Transverse distance between the primary and secondary vertices
	L_{xyz}(SV)	Distance between the primary and secondary vertices
	S_{xyz}(SV)	Distance between the primary and secondary vertices divided by its uncertainty
	$\Delta R(\mathbf{p}_{jet}, \mathbf{p}_{vtx})$(SV)	ΔR between the jet axis and the direction of the secondary vertex relative to the primary vertex
JetFitter	m(JF)	Invariant mass of tracks from displaced vertices
	f_E(JF)	Jet energy fraction of the tracks associated with the displaced vertices
	$\Delta R(\mathbf{p}_{jet}, \mathbf{p}_{vtx})$(JF)	ΔR between the jet axis and the vectorial sum of momenta of all tracks attached to displaced vertices
	S_{xyz}(JF)	Significance of the average distance between PV and displaced vertices
	$N_{TrkAtVtx}$(JF)	Number of tracks from multi-prong displaced vertices
	$N_{2TrkVtx}$(JF)	Number of two-track vertex candidates (prior to decay chain fit)
	$N_{1-trk\text{ vertices}}$(JF)	Number of single-prong displaced vertices
	$N_{\geq 2-trk\text{ vertices}}$(JF)	Number of multi-prong displaced vertices
	$L_{xyz}(2^{nd})$(JF)	Distance of 2^{nd} vertex from PV
	$L_{xy}(2^{nd})$(JF)	Transverse displacement of the 2^{nd} vertex
	$m_{Trk}(2^{nd})$(JF)	Invariant mass of tracks associated with the 2^{nd} vertex
	$E(2^{nd})$(JF)	Energy of the tracks associated with the 2^{nd} vertex
	$f_E(2^{nd})$(JF)	Jet energy fraction of the tracks associated with the 2^{nd} vertex
	$N_{TrkAtVtx}(2^{nd})$(JF)	Number of tracks associated with the 2^{nd} vertex
	$\eta_{trk}^{min,max,avg}(2^{nd})$(JF)	Min., max. and avg. pseudorapidity of tracks at the 2^{nd} vertex

Table 3.7: DL1r input variables [124].

Inputs The 36 DL1r inputs are listed in Table 3.7. Except for the first two jet variables, all the other 34 input variables are derived from *low-level* algorithms: impact-parameter based (IP-based) algorithms, *IP2D, IP3D and RNNIP*, secondary-vertex-tagging algorithm, *SV1*, and topological multi-vertex finding algorithm, *JetFitter* [124]. The algorithms aim to explore three basic differences between different flavors of jets:

- **Lifetime:** The lifetime of b-hadrons (c-mesons, τ-leptons) is about 1.5 ps (1 ps, 0.3 ps) [17]. Therefore, the energetic heavy particles tend to fly a few millimeters before decaying, creating a secondary vertex (SV) displaced from the primary vertex in jets. The displaced vertices also lead to larger impact parameters for the heavy particles.

- **Mass:** The b-quark, c-quark, and τ-leptons have masses around 1 to 4 GeV, orders of magnitudes larger than the light-flavor quarks. Therefore, the reconstructed invariant mass at the SV tends to be larger for the b-jets, c-jets, and τ-jets.

- **Decay products:** The b-jets and c-jets tend to have more decay products from vertices than the l-jets. In the case of b-jets, b-hadrons decay to c-hadrons first, creating a tertiary vertex in jets.

All inputs are derived from jets, tracks, and PVs. The hard-scatter vertex is the reference point for secondary vertices and track impact parameters d_0 and z_0. The tracks are matched to jets by setting ΔR(track, jet). The ΔR settings vary with the jet p_T, being wider for low p_T jets. The track impact parameters are signed with respect to the jet axis and the PV. The impact parameter sign is defined as positive (negative) if the track intersects the jet axis in the transverse plane in front of (behind) the PV [126]. The b-jet and c-jet impact parameters (IPs) tend to be more positive while the l-jet IPs are symmetric about zero, as shown in Figure 3.17. The track IP significance is defined as the ratio of the IP to its uncertainty.

The main features of the low-level algorithms are as follows:

- **IP2D, IP3D, RNNIP:** IP2D, IP3D, and RNNIP are three different algorithms using track impact parameters to differentiate b-jets, c-jets, and l-jets. The impact parameter distributions are shown in Figure 3.17. Both IP2D and IP3D are likelihood-based algorithms. Log-likelihood ratio discriminants are composed from probability density functions (pdfs) of b-jets, c-jets, and l-jets impact parameter significance. IP2D uses only the signed transverse IP significance, S_{d_0}. IP3D uses both S_{d_0} and S_{z_0}. RNNIP uses a recurrent neural network (RNN) to explore more track input variables and the correlation between tracks and output b-jet, c-jet, and l-jet probabilities.

- **SV1:** SV1 aims to reconstruct a single displaced secondary vertex (SV) in a jet. The reconstruction starts by finding two-track vertices with all tracks associated with the jet. Two-track vertices from K^0_s, Λ decays, photon conversions, or hadronic interactions with the detector material are rejected using the invariant mass (Equation 3.10) of vertices or track impact parameters. SV1 iteratively fit all tracks contributing to the cleaned set of vertices to one vertex. In each iteration, the track with the largest χ^2 is

removed. The fit is repeated until a reasonable χ^2 is achieved and $m(SV) < 6$ GeV. Eight SV variables are computed as inputs to DL1. Three examples are shown in Figure 3.18.

- **JetFitter:** Unlike SV1, `JetFitter` finds more than one secondary vertex inside the jet, aiming to reconstruct the decay chain of PV $\rightarrow$ b-hadron $\rightarrow$ c-hadron. It then uses a Kalman filter to update all vertex position and find the optimal b-hadron flight axis with fitted vertices along it. There are 17 `JetFitter` variables used in DL1, such as the invariant mass, energy fraction, etc.

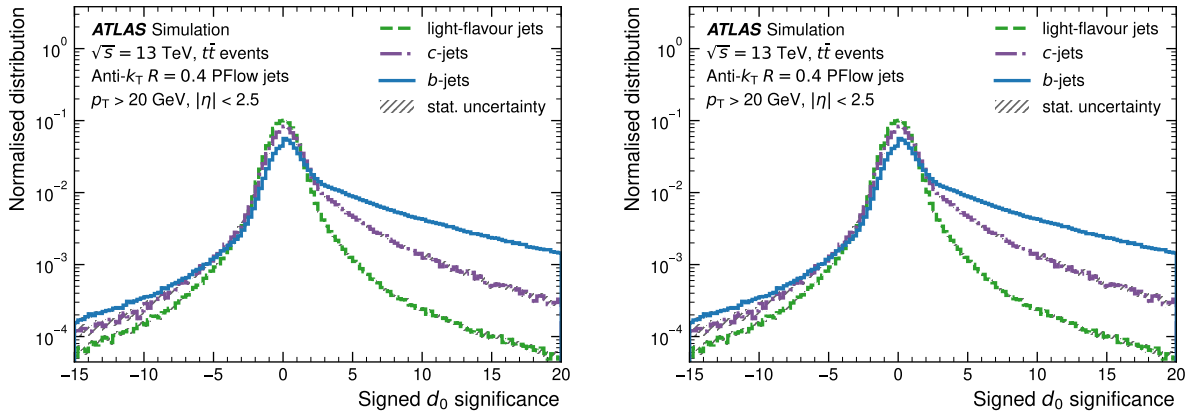

Figure 3.17: The transverse (left) and longitudinal (right) signed impact parameter significance [124]. The impact parameter of b-jets and c-jets tend to be larger and more positive then l-jets.

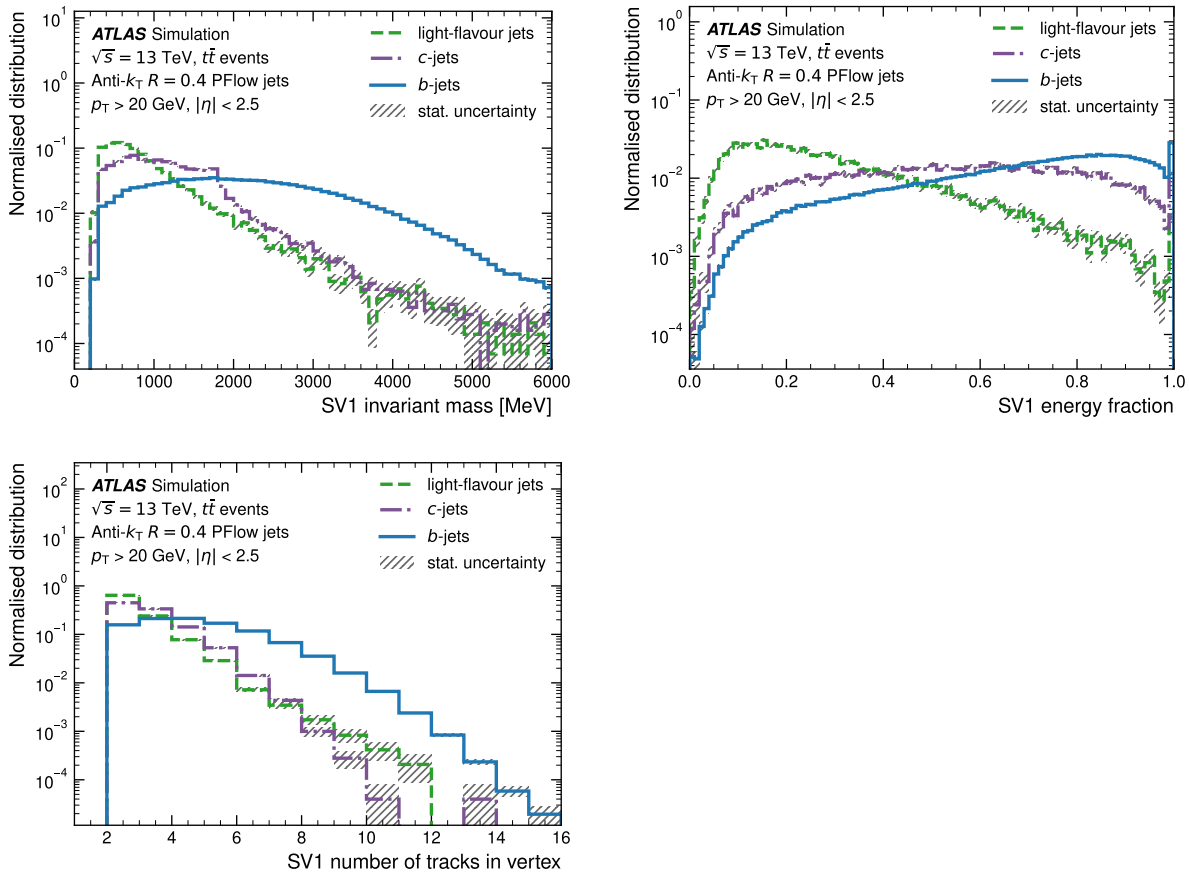

Figure 3.18: SV1 m(SV) (top left), f_E(SV) (top right), and $N_{TrkAtVtx}$(SV) (bottom left) [124]. b-jets tend to have high SV invariant mass, energy fraction (see dead-cone effects [127]), and decay multiplicities (large number of tracks associated with the SV).

Hyperparameter	**Value**
Number of input variables	36
Number of hidden layers	8
Number of nodes per layer	[256, 128, 60, 48, 36, 24, 12, 6]
Learning rate	0.01
Training batch size	15000
Activation function	ReLu
Number of training epochs	200
Free (trainable) parameters	59275
Training sample size	22 M jets

Table 3.8: DL1r training parameters [124].

Training and performance After defining all 36 input variables listed in Table 3.7, `DL1r` inputs a sample of 22 million (22M) jets to a fully connected multilayer neural network. The neural network parameters are listed in Table 3.8. The training uses `TensorFlow` with the `Keras` front-end and the `Adam` optimizer [128, 129].

The jet training sample are a mix of $t\bar{t}$ (70%) and $Z' \to q\bar{q}$ (30%) events, where Z' jets tend to have higher p_T. Before training, the jets are resampled to have a uniform distribution in p_T and $|\eta|$ for each flavor. All jet variables are also shifted to be zero-centered and normalized to one.

The outputs of `DL1r` are the b-jet, c-jet, and l-jet probabilities. The probabilities are used to form two discriminants: D^b_{DL1r} and D^c_{DL1r}.

$$D^b_{DL1r} = \ln\left(\frac{p_b}{f_c \cdot p_c + (1 - f_c) \cdot p_{light}}\right) \tag{3.17}$$

$$D^c_{DL1r} = \ln\left(\frac{p_c}{f_b \cdot p_b + (1 - f_b) \cdot p_{light}}\right) \tag{3.18}$$

Here, f_c (=0.018) and f_b (=0.2) are the effective background fractions. The values are optimized for rejecting background jets while maintaining b-jet or c-jet efficiencies.

The final DL1r performance is evaluated using D^b_{DL1r} and D^c_{DL1r}, as shown in Figure 3.19. Different cuts can be applied to D^b_{DL1r} (D^c_{DL1r}) to select b-jet (c-jet) candidates. The efficiency of b-jet and c-jet selection ($\epsilon_{b,c}$) is defined as:

$$\epsilon_{b,c} = \frac{N^{b,c}_{selected}}{N^{b,c}_{total}} \tag{3.19}$$

Here, $N^{b,c}_{selected}$ refers to the number of b-jets or c-jets selected above specific D^b_{DL1r} or D^c_{DL1r} cuts. And, $N^{b,c}_{total}$ refers to the total number of b-jets or c-jets that have been reconstructed in the sample evaluated. The rejection factors of background b-jet, c-jet or l-jet are defined as: $1/\epsilon_b$, $1/\epsilon_c$ or $1/\epsilon_l$. The final `DL1r` efficiency and rejection of b-jet and c-jet are shown in Figure 3.20. At 60% b-jet efficiency, the rejection factors for c-jets and l-jets are approximately 40 and 3000. At 20% c-jet efficiency, the rejection factors for b-jets and l-jets are approximately 20 and 200. The rejection power of `DL1r` is much better than individual low level algorithms.

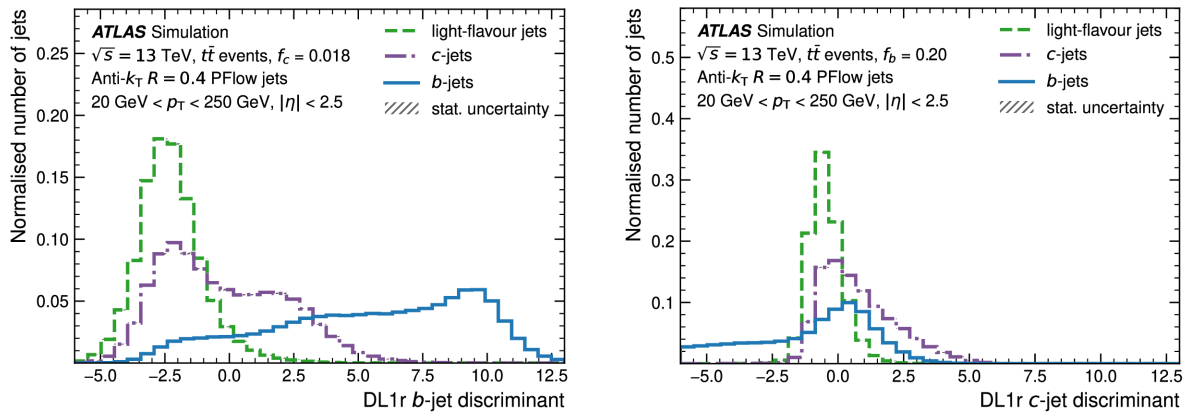

Figure 3.19: D^b_{DL1r} (left) and D^c_{DL1r} (right) [124].

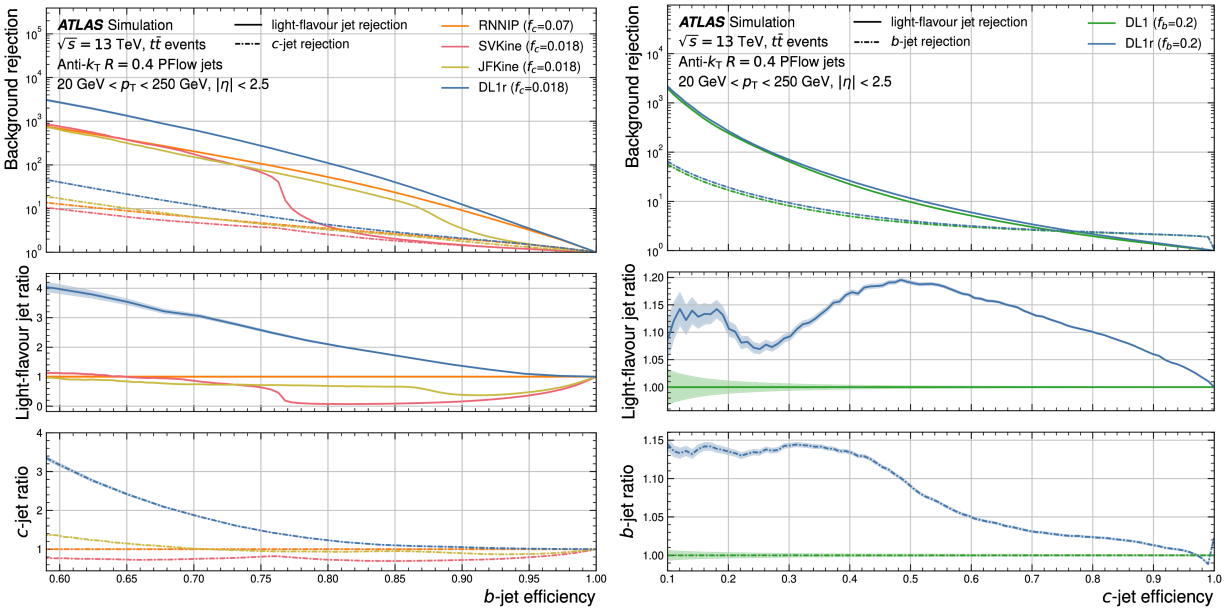

Figure 3.20: D^b_{DL1r} (left) and D^c_{DL1r} (right) [124]. For the left plot, `RNNIP`, `SVKine`, and `JFKine` refer to the stand-alone performance from `RNNIP`, `SV1`, and `JetFitter`. For the right plot, `DL1` refers to a previous flavor tagging algorithm without the `RNNIP` low level algorithm. The `DL1r` algorithm improves the b-jet (l-jet) rejection by around 15% (10%) at 20% c-jet efficiency.

3.4.2 Calibration

The flavor tagging efficiencies need to be calibrated to account for differences between data and simulation before being used in the analysis. The flavor tagging efficiency calibrations derive scale factors (SF) to correct the simulation efficiencies ($\epsilon_{simulation}$) to the measured efficiencies in the data (ϵ_{data}). The scale factors are derived as a function of the jet p_T.

$$SF = \frac{\epsilon_{data}}{\epsilon_{simulation}} \tag{3.20}$$

The scale factors are derived separately for b-jets, c-jets, and l-jets. The respective calibrations require selecting samples of enriched b-jets, c-jets, and l-jets.

b-jet calibration The b-jet calibration uses di-leptonic $t\bar{t}$ decays [130]. Events are categorized using the leading and sub-leading jet p_T. Signal regions with high-purity two b-jet events are selected using the invariant mass of the leading jet-lepton pairs. In each signal and control region, events are further categorized according to the b-tagging discriminants of the two leading jets. The b-jet tagging efficiencies are then measured using a log-likelihood fit. The final signal region b-jet tagging efficiency and scale factors are shown in Figure 3.21. The b-tagging efficiency scale factors are approximately one for most jet p_T bins. The total uncertainty is approximately a few percent in most jet p_T ranges. The uncertainty is larger than 5% for jet p_T below 30 GeV.

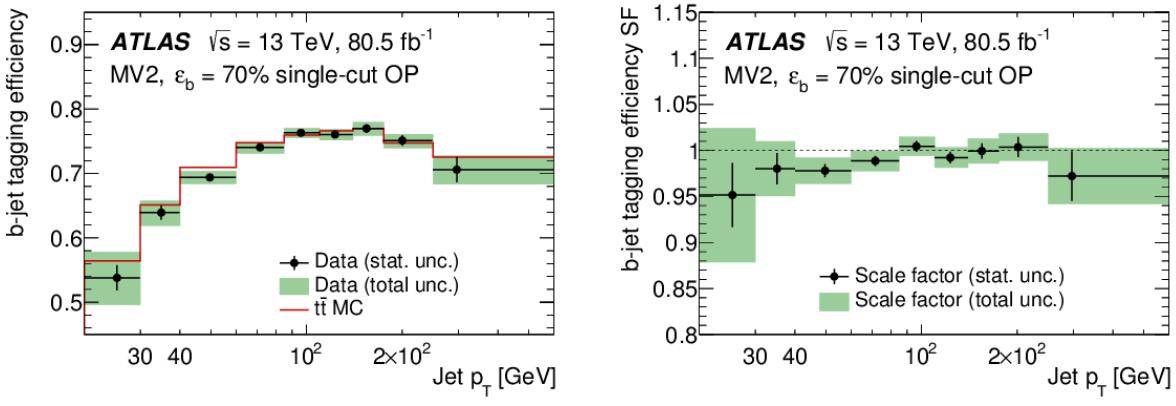

Figure 3.21: The signal region b-tagging efficiency (left) and scale factors (right) [130]. The statistical and systematic uncertainties are shown in the green bar for the scale factors.

l-jet calibration The l-jet calibration uses Z+jets samples. It is particularly challenging due to the small mis-tag efficiency from `DL1r`. A negative tag method is used to enrich the l-jet fractions in `DL1r` (`DL1rFlip`) [131]. As shown in Figure 3.17, the impact parameters of

b-jets tend to be more positive. `DL1rFlip` inverts the signs of all track impact parameters. When the `DL1rFlip` samples are evaluated using the nominal `DL1r` algorithm and working points, the b-jet fraction decreases significantly as indicated in Figure 3.22. However, the l-jet efficiency (ϵ_l) remains the same between the two algorithms.

At each jet p_T and `DL1rFlip` discriminant interval, the l-jet efficiency scale factors are measured by performing a likelihood fit on the invariant mass of the secondary vertex. The l-jet scale factor uncertainties range from around 10% to 20% at different b-tagging working points.

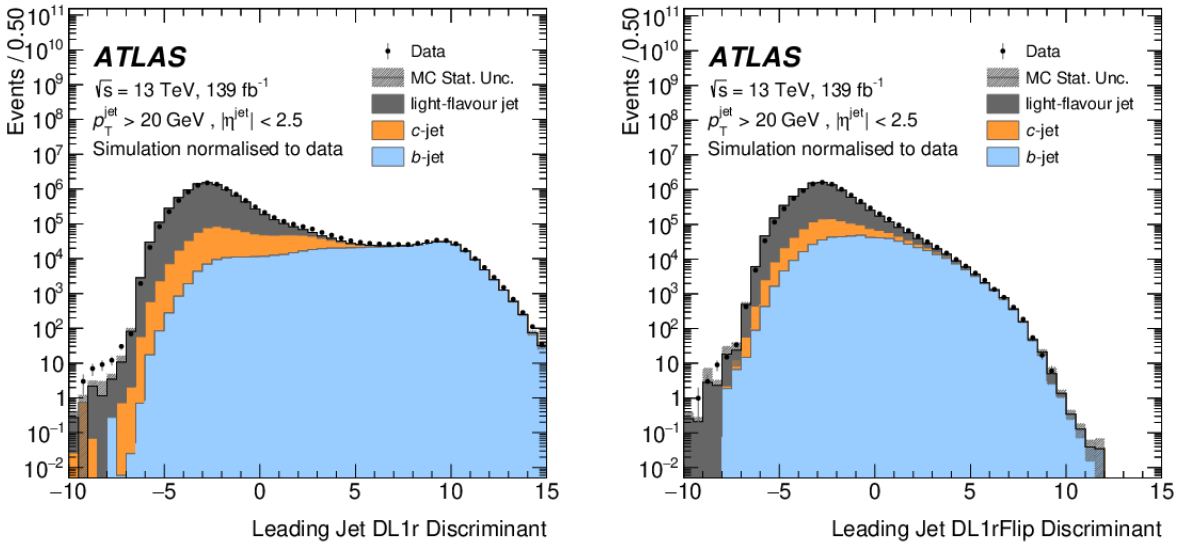

Figure 3.22: The `DL1r` (left) and `DL1rFlip` (right) discriminants [131]. b-jet fractions are lower at high `DL1rFlip` values.

c-jet calibration Lastly, the c-jet calibration uses semi-leptonic $t\bar{t}$ decays [132]. The branching ratio of a W boson to final states containing a charm-quark is about 33% [17]. b-jet and l-jet scale factors are applied prior to extracting the c-jet scale factors. The c-jet tagging efficiency scale factors are then derived by performing a χ^2 fit in all jet p_T and tagging intervals. The uncertainties of the c-jet scale factors are approximately 10% dominated by the $t\bar{t}$ modeling uncertainties.

3.4.3 Soft electrons

To improve the flavor tagging algorithm performance, there are two main approaches: 1) adding additional information and 2) developing more advanced algorithms. The first approach might be possible by exploiting soft lepton variables. The second approach is explored

in the GN1 upgrade of the DL1 algorithms [133]. As discussed in Section 3.4.1, the current DL1r algorithm exploits the differences between b-jets, c-jets, and l-jets through secondary vertices and decay products. In addition, 39%(17%) of b-hadron and c-hadron decays include leptons [17]. As these leptons tend to have smaller p_T compared to the prompt leptons, they are called soft leptons. The soft lepton information recorded by the calorimeters and the muon spectrometer is not currently considered in DL1r. Adding soft muons to DL1r increases c(l) jet rejection by 10%(25%) at 70% b-tagging efficiency. Similar performance improvements are expected for soft electrons, which is discussed in this section.

Machine learning Machine learning has been an important tool for event reconstruction and identification in particle physics since the 2010s [134, 135]. Machine learning is a subset of artificial intelligence [136]. Figure 3.23 illustrates the difference between classical programming and machine learning. Classical programming derives answers given data and rules, while machine learning aims to find a set of rules given the data and answers. Event reconstruction and identification in particle physics and in particular collider physics tend to use large datasets and Monte Carlo simulations in high dimensions. This makes them a suitable playground for machine learning applications. For example, in flavor tagging, without machine learning, it is difficult to define rules based on a large number of variables and efficiently classify millions of b-jets, c-jets, and l-jets.

DL1r uses *deep neural networks* (DNN) for jet flavor identifications. The training is *supervised*, mapping data to known targets [136]. In general, machine learning algorithms can be either supervised or unsupervised. Unsupervised learning does not have target values and are useful for purposes such as anomaly detection. Deep neural networks are currently one of the most popular machine learning algorithms [136]. Another type of supervised ML algorithm is boosted decision trees, which is used in Chapter 4 to enhance signal sensitivities [137]. Deep neural networks can be configured in different ways, such as the graph neural networks and transformers [138, 139]. In DNN, all 36 jet variables are input to layers of neurons or nodes. Neurons here are loosely inspired by biological neurons [140]. Deep refers to a large number of neuron layers. At each neuron, the input variables are weighted and sent through an activation function as shown in Figure 3.24. The activation function used for the internal layers in DL1r is ReLu (rectified linear unit) as listed in Table 3.8. The ReLu function is defined as: $f(z_j) = max(0, z_j)$ [141]. Activation functions introduce non-linearity into the neural networks. After the 8 hidden layers in DL1r, the final output layer uses softmax activation function [142]:

$$f(\mathbf{z})_j = \frac{e^{z_j}}{\sum_k e^{z_k}}. \tag{3.21}$$

In the case of DL1r, the softmax activation function takes in a vector of three components from the output layer: $\mathbf{z} = (p_b, p_c, p_l)$. After the softmax activation function, each component is within [0, 1] and all three components add up to 1. Those components are thus equivalent to the probabilities of a jet being a b-jet, c-jet or l-jet.

The performance of neural networks is assessed through a loss function and the truth label of the jets, $\mathbf{q} = (q_b, q_c, q_l)$. In `DL1r`, a categorical cross-entropy or log loss function is used:

$$L(\mathbf{q}, \mathbf{z}) = -\frac{1}{N} \sum_{i=1}^{N} \sum_{j=1}^{C} q_{i,j} \log(z_{i,j}). \tag{3.22}$$

Here, N is the total number of jets used in the training. And, the index C is three in the case of `DL1r` as there are three jet categories [143].

During trainings, the loss function is minimized through gradient descent and backpropagation [136, 144]. Each individual neuron weight and bias is updated as:

$$\theta_i' = \theta_i - \alpha \frac{1}{m} \sum_{m} \frac{\partial L}{\partial \theta_i}. \tag{3.23}$$

Here, α is the step size of each descent and called *learning rate*. Instead of summing over the full training sample size N as in Equation 3.22, the gradient is taken over a random batch size m, as shown in Equation 3.23. The batch size m thus refers to a subset of the full training size N, over which the neuron weights and biases can be updated. The parameter θ_i can be the weight or bias of any neuron in the neural network. Training is performed over multiple epochs until the loss function stabilizes. In one epoch, all neurons are updated over the full training sample in multiple batches. The number of epochs refer to the number of times over which the full sample should be trained. Batch size, learning rates, the number of epochs, the number of nodes per layer, and the total number of hidden layers as shown in Table 3.8 are all important hyperparameters to tune for the training performance. Different activation functions might affect the training performance as well.

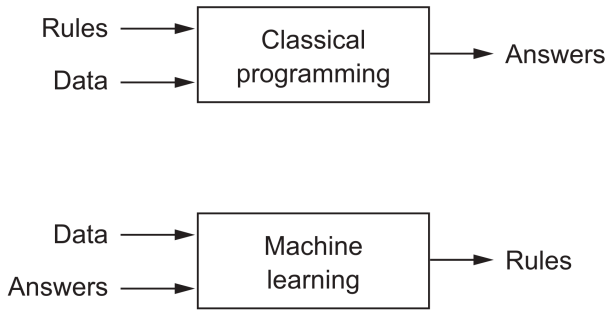

Figure 3.23: Classical programming versus machine learning [136].

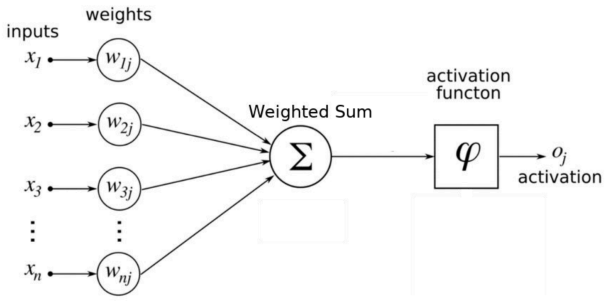

Figure 3.24: Input weights and the activation function at each neuron [145]. For any neuron j, n inputs form the weighted sum: $z_j = \sum x_i w_{ij} + b_j$. Here, b_j is the bias of the neuron. The final output from the neuron is: $o_j = f(z_j)$, where f is the activation function.

Soft electron selection and variables The first step of adding soft electron candidates to the `DL1r` algorithm is to select soft electron candidates. The latest ATLAS electron identification (ID) algorithm uses neural networks and outputs the probability of an electron from heavy flavor decays, p_{hf} [146]. This identification algorithm was developed after the likelihood-based ID algorithm discussed in Section 3.3 and is not used in the $VH(\to b\bar{b}, c\bar{c})$ analysis. The electron ID algorithm uses various electron candidate track and calorimeter information. Some of the training variables are listed in Table 3.10. The highest p_{hf} electron within the jet ($\Delta R(e, \text{jet}) < 0.4$) is selected as the soft electron candidate for the jet.

Once the electron candidates inside jets are selected, a total of 28 soft electron variables are added to the `DL1r` algorithm to enhance the flavor tagging performance. The 28 variables are listed in Table 3.9-3.10. The 28 electron variables are selected based on the experience from low level `DL1r` algorithms and electron identification trainings. In addition to selecting soft electron candidates, p_{hf} is also used in the `DL1re` training. The electron variables for p_{hf} training are also added in `DL1re` to further improve the performance as shown in Table 3.10. The distributions of four soft electron variables are shown in Figure 3.25. Those variables are from different variable types and tend to be highly ranked, meaning that they have large impact over the final training results.

More b-jets and c-jets tend to have higher soft electron p_{hf}. Slightly more b-jets tend to have more positive soft electron signed d_0. However, for $\Delta\eta_1$ and R_{had1}, the distributions are similar across all three jets, dominated by the fake soft electrons added to the jets. Some electron variables have large outliers due to the transition region between the barrel and endcap ($1.37 < |\eta| < 1.52$) [147]. Outlier cuts are set for these electron variables. The outlier cuts do not affect the final `DL1re` training performance.

type	name	description
Kinematics	p_T	Transverse momentum of the electron
	$p_{T,e}/p_{T,jet}$	Transverse momentum of the electron divided by jet transverse momentum
	p_T^{rel}	The transverse momentum of muon relative to the jet axis: $\sqrt{p_e^2 - ((\overrightarrow{p_{jet}} \cdot \overrightarrow{p_e})/p_{jet})^2}$
	$\|\eta\|$	Absolute value of the electron pseudorapidity
	$\Delta R(jet, e)$	The angular separation between electrons and jets
Tracking	signed d_0 and its significance	Signed transverse momentum [126]
	signed z_0 and its significance	Signed longitudinal momentum
Miscellaneous	p_{hf}	The probabilities of an electron coming from b or c hadron decays [146]
	p_T^{iso}/p_T	The sum of track p_T in a cone of $\Delta R = 0.3$ around the electron divided by electron p_T
	IsDefault	If an electron candidate exists inside a jet, IsDefault = 0; otherwise, = 1

Table 3.9: 12 of the soft electron variables added to the `DL1re` training. Kinematic variables such as $p_{T,e}/p_{T,jet}$ show the relationship between the electron candidate and the jet. Tracking impact parameters are signed according to the flavor tagging convention discussed in Section 3.4.1.

type	name	description
Tracking	n_{pix}	Number of hits in the pixel detector
	n_{sct}	Number of hits in the SCT detector
	$\Delta p/p$	Momentum lost by the track between the perigee and the last measurement point divided by the momentum at perigee
	eProbabilityHT	Likelihood probability based on transition radiation in the TRT
Track-cluster matching	$\Delta\eta_1$	$\Delta\eta$ between the cluster position in the first layer and the extrapolated track
	$\Delta\phi_{\text{res}}$	$\Delta\phi$ between the cluster position in the second layer of the ECAL and the momentum-rescaled track, extrapolated from the perigee, times the charge
	E/p	Ratio of the cluster energy to the track momentum
First layer of ECAL	w_{stot}	Shower width, $\sqrt{\sum E_i(i-i_{\max})^2/(\sum E_i)}$, where i runs over all strips in a window of $\Delta\eta\times\Delta\phi \approx 0.0625\times 0.2$, corresponding typically to 20 strips in η, and $i_{\max}$ is the index of the highest-energy strip
	E_{ratio}	Ratio of the energy difference between the maximum energy deposit and the energy deposit in a secondary maximum in the cluster to the sum of these energies
	f_1	Ratio of the energy in the first layer of ECAL to the total energy in the ECAL
Second layer of ECAL	$w_{\eta 2}$	Lateral shower width, $\sqrt{(\sum E_i\eta_i^2)/(\sum E_i) - ((\sum E_i\eta_i)/(\sum E_i))^2}$, where E_i is the energy and η_i is the pseudorapidity of cell i and the sum is calculated within a window of 3×5 cells
	R_ϕ	Ratio of the energy in 3×3 cells over the energy in 3×7 cells centered at the electron cluster position
	R_η	Ratio of the energy in 3×7 cells over the energy in 7×7 cells centered at the electron cluster position
Third layer of ECAL	f_3	Ratio of the energy in the third layer to the total energy in the ECAL
Hadronic leakage	R_{had1}	Ratio of E_T in the first layer of the hadronic calorimeter leakage to E_T of the ECAL cluster
	R_{had}	Ratio of E_T in the hadronic calorimeter to E_T of the ECAL cluster

Table 3.10: The additional 16 soft electron variables added the `DL1re` training. These 16 variables are used in the p_{hf} training. The definition of all variables is found in [147].

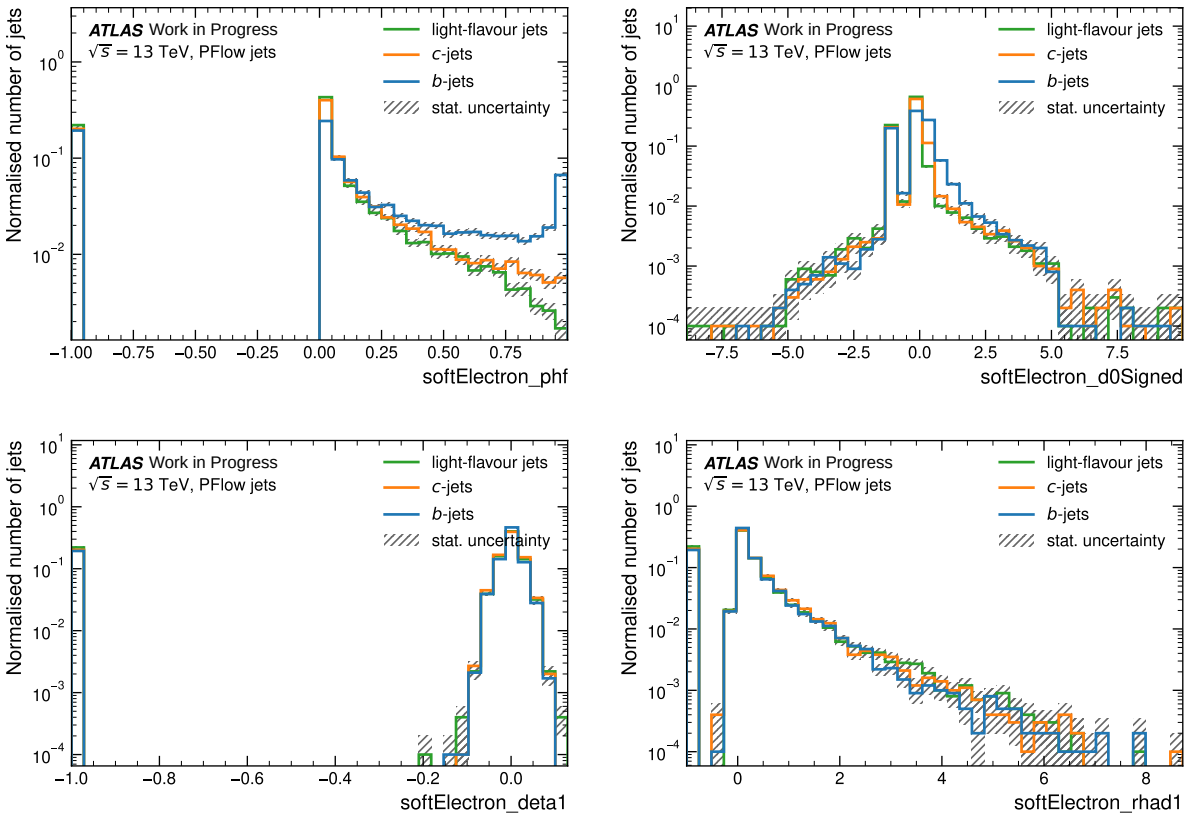

Figure 3.25: Selected `DL1re` variable distribution for b-jets, c-jets, l-jets. Top left: p_{hf}; top right: signed d_0; bottom left: $\Delta\eta_1$; bottom right: R_{had1}. For jets without soft electron candidates, the variables are set to default values -1.

DL1re performance The training size is increased to 24 million jets from the default 22 million in Table 3.8. With the increasing number of soft electron variables, a large training size above 24 million is needed to achieve good performance. `Optuna` was used to optimize the `DL1re` hyperparameters [148]. 50 different trials are performed at various batch sizes, learning rates, numbers of nodes per layer, and numbers of hidden layers. The default `DL1r` hyperparameters are shown to be optimized for `DL1re` as well.

The final `DL1re` performance with soft electron candidates and variables added to the default `DL1r` training is shown in Figure 3.26. The efficiencies and rejections for `DL1re` are defined in the same way as `DL1r` in Equation 3.19. At 70% b-jet efficiency (marked by the vertical dash red lines), the c-jet and l-jet rejections are improved by $10 - 20\%$. Similarly, at 20% c-jet efficiency, the b-jet and l-jet rejections improve by $10 - 20\%$.

Soft electrons are currently being tested in the latest `GN1` flavor tagging algorithms. The improvements are independent of the baseline flavor tagging algorithms. Once the algorithm is finalized, calibrating the flavor tagging algorithm with soft leptons is the next exciting milestone before the algorithm can be deployed in the analysis. The calibration with soft leptons might require new techniques as flavor tagging performance keeps improving and fewer background jets are accepted at the various working points.

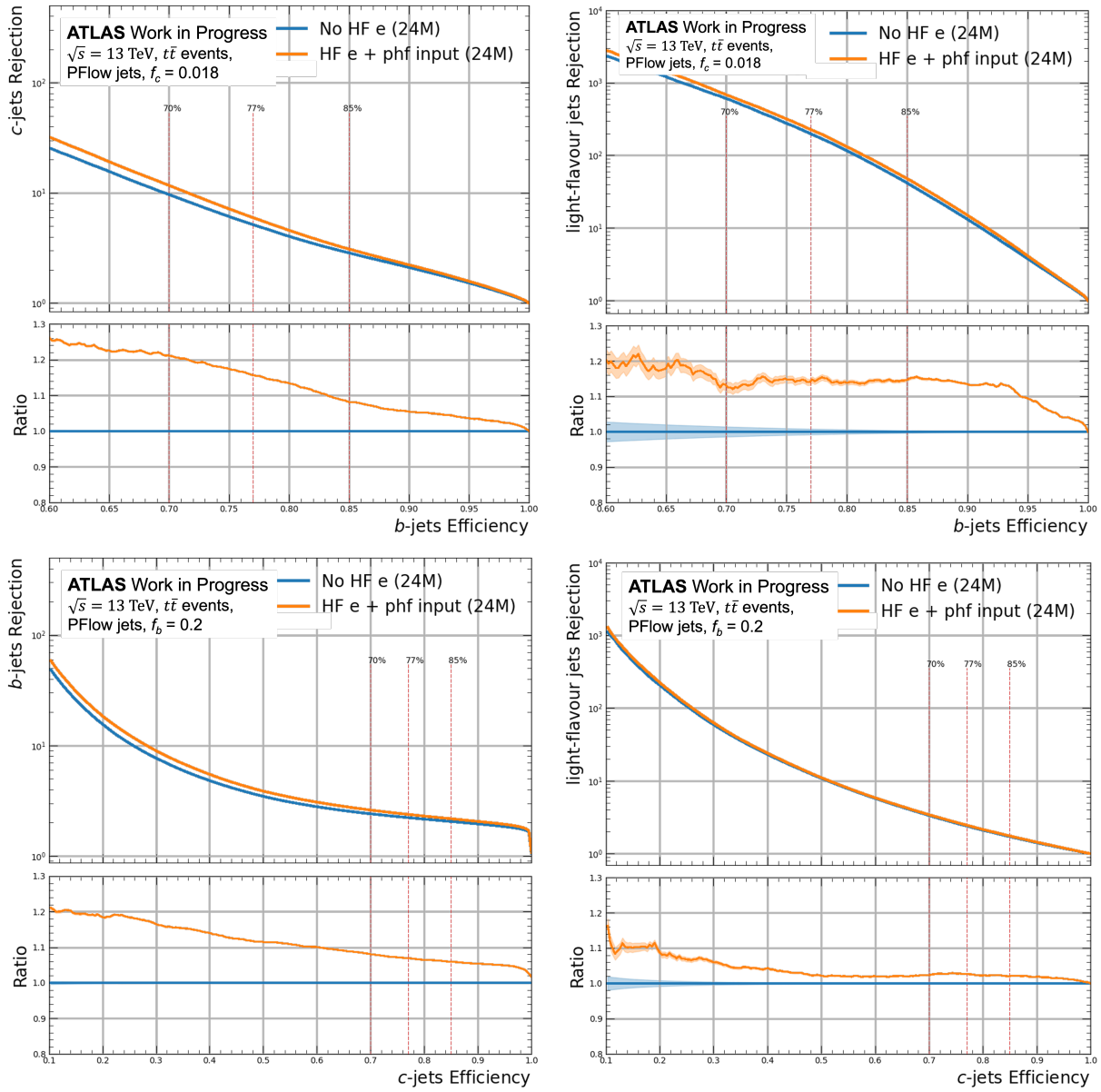

Figure 3.26: `DL1re` performance. Top: b-jet efficiencies at various c-jet (left) and l-jet (right) rejections. Bottom: c-jet efficiencies at various b-jet (left) and l-jet (right) rejections. The `DL1r` performance is shown in blue and `DL1re` in orange. Vertical red dash lines mark the 70%, 77%, and 85% tagging efficiencies.

Chapter 4

The VH(bb/cc) analysis

4.1 Introduction

The Higgs boson is an important part of the Standard Model of particle physics (SM), closely tied to how particles acquire mass in the SM. This chapter discusses the latest $VH(\to b\bar{b}, c\bar{c})$ measurement from ATLAS [1]. The measurement uses the VH production mode. The decay channels where the Higgs boson decays to a pair of charm quarks $H \to c\bar{c}$ and a pair of bottom quarks $H \to b\bar{b}$ are measured simultaneously.

The Higgs-fermion coupling was first observed in the ttH production mode by ATLAS and CMS [149, 150]. The $H \to b\bar{b}$ decay mode was observed shortly after by ATLAS and CMS in Run 2 using the VH production mode [151, 152]. The VH production mode allows efficient triggering on the leptons from vector boson decays and suppresses large QCD multi-jet backgrounds. The $H \to b\bar{b}$ decay mode can be assessed in other production channels as well, such as the vector-boson fusion channel [153, 154]. The $VH(\to b\bar{b}, c\bar{c})$ analysis discussed in this thesis uses the VH production mode.

Since the $H \to b\bar{b}$ discovery, three additional ATLAS analyses explored $H \to b\bar{b}$ in precision differential measurements using the STXS (simplified template cross section) framework and the full Run 2 dataset (139 fb^{-1}). The three analyses focus on:

- *Resolved* $VH(\to b\bar{b})$: measure Higgs decays with low Lorentz boosts [155]; the two b-jets are reconstructed as small-R (small-radius) jets.
- *Boosted* $VH(\to b\bar{b})$: measure highly boosted Higgs decays [156]; the Higgs candidate are reconstructed with one large-R jet.
- *Combined* $VH(\to b\bar{b})$: combine resolved and boosted $VH(\to b\bar{b})$ [157]; $p_T^V < 400$ GeV uses the resolved $VH(\to b\bar{b})$ strategy and $p_T^V \geq 400$ GeV uses the boosted strategy.

In addition to measuring the Higgs coupling to the third-generation fermions, there have been efforts measuring the Higgs coupling to the second- and first-generation fermions. The Higgs decays to muons were measured by CMS and ATLAS [158, 159]. The CMS $H \to \mu\mu$

measurement reached 3 σ significance [158]. Upper limits are also set for the Higgs-electron couplings by ATLAS and CMS [160, 161]. The ATLAS $H \to ee$ upper limit is $\mathcal{O}(10^5)$ times the SM prediction. In addition, measuring the Higgs decays to mesons can constrain the Higgs coupling to the c-quarks and s-quarks [162, 163, 164, 165].

$H \to c\bar{c}$ is one of the most common Higgs decay modes that has not been observed ($BR = 2.89\%$). It is susceptible to modifications in various new physics scenarios, as discussed in Section 2.2.2. Similar to $H \to b\bar{b}$, the most sensitive searches use the VH production mode. There are also searches in other production channels, such as the gluon-gluon fusion and vector-boson fusion channels [166, 167]. Using the full Run 2 dataset, ATLAS and CMS measured:

- **ATLAS** $VH(\to c\bar{c})$: an upper limit of 26 times the signal strength predicted by the SM for $VH(\to c\bar{c})$ (26 $\times$ SM) with an expected limit of 31 $\times$ SM; $|\kappa_c| < 8.5$ [2]; specifically, the observed (expected) upper limit from the 2-lepton channel is 49 $\times$ SM (51 $\times$ SM) at the 95% confidence level.
- **CMS** $VH(\to c\bar{c})$: 14.4 $\times$ SM with an expected limit of 7.6 $\times$ SM; $1.1 < \kappa_c < 5.5$ [39];

Due to the similarity of $VH(\to b\bar{b})$ and $VH(\to c\bar{c})$ decays, it is possible to measure these decay modes simultaneously. Combined measurements allow measuring simultaneously κ_c, κ_b, and the ratio κ_c/κ_b. In addition, the main backgrounds in the $VH(\to b\bar{b})$ and $VH(\to c\bar{c})$ phase spaces are similar. Combining the two phase spaces can better constrain the background processes.

Therefore, the $VH(\to b\bar{b}, c\bar{c})$ analysis discussed in this chapter defines a common analysis strategy between $VH(\to b\bar{b})$ and $VH(\to c\bar{c})$, correlates modeling and experimental uncertainties, and performs a combined coherent measurement of $VH(\to b\bar{b})$ and $VH(\to c\bar{c})$. The $VH(\to b\bar{b})$ analysis combines the resolved and boosted phase space similar to the combination [157]. Furthermore, the use of multivariate analysis greatly improved the $VH(\to c\bar{c})$ upper limit in the $VH(\to b\bar{b}, c\bar{c})$ analysis.

Analysis overview The $VH(\to b\bar{b}, c\bar{c})$ analysis combines $VH(\to b\bar{b})$ and $VH(\to c\bar{c})$ as shown in Figure 4.1. The transition between the *resolved* $VH(\to b\bar{b})$ phase space and the *boosted* phase space occurs at $p_T^V = 400$ GeV. The resolved $VH(\to b\bar{b})$ and $VH(\to c\bar{c})$ phase spaces are defined using the `DL1r` pseudo-continuous flavor tagging working points (PCFT). The $VH(\to b\bar{b})$ phase space is characterized by two b-tagged jets, while the $VH(\to c\bar{c})$ c-tagged jets. All c-tagged jets have b-tag scores below the 70% efficiency working point, making the $VH(\to b\bar{b})$ and $VH(\to c\bar{c})$ phase space orthogonal to each other. The finer PCFT bins also improve the signal sensitivities.

In the $VH(\to c\bar{c})$ phase space, unlike the $VH(\to b\bar{b})$ case, a stand-alone boosted $VH(\to c\bar{c})$ region is not included. Therefore, the 400 GeV cap is not used in $VH(\to c\bar{c})$. The overlap between the resolved $VH(\to c\bar{c})$ and boosted $VH(\to b\bar{b})$ phase space is negligible.

In all three phase spaces, three different analysis channels are defined based on the vector-boson decay modes:

- *0-lepton*: $Z \to \nu\nu$;
- *1-lepton*: $W \to l\nu$;
- *2-lepton*: $Z \to ll$ (main focus of the thesis).

Here, l refers to electrons or muons. τ-leptons are not used in defining the lepton channels as τ-leptons are not used in triggering and are more challenging to reconstruct. Some events in 0-lepton have one reconstructed hadronic τ-lepton and are considered as 1-lepton events. The thesis work focuses on the 2-lepton channel and the corresponding main background, Z+jets.

The analysis phase space is further split into *signal regions* (to maximize signal sensitivities) and *control regions* (to estimate background processes). The main backgrounds in the analysis are V+jets and top processes. Here, V stands for the vector bosons, either the W bosons or the Z boson. Other minor backgrounds include diboson and multijet. The control regions tend to constrain the main backgrounds, while the minor backgrounds have little impact on the final signal strengths.

The signal and control regions are further split in terms of the jet multiplicity, p_T^V, and the number of tagged c-jets due to differences in kinematics and normalization. In total, there are approximately 150 regions used in the fit. More details about trigger, objects, flavor tagging working points, experimental uncertainties, and regions used in the analysis are discussed in Section 4.2.

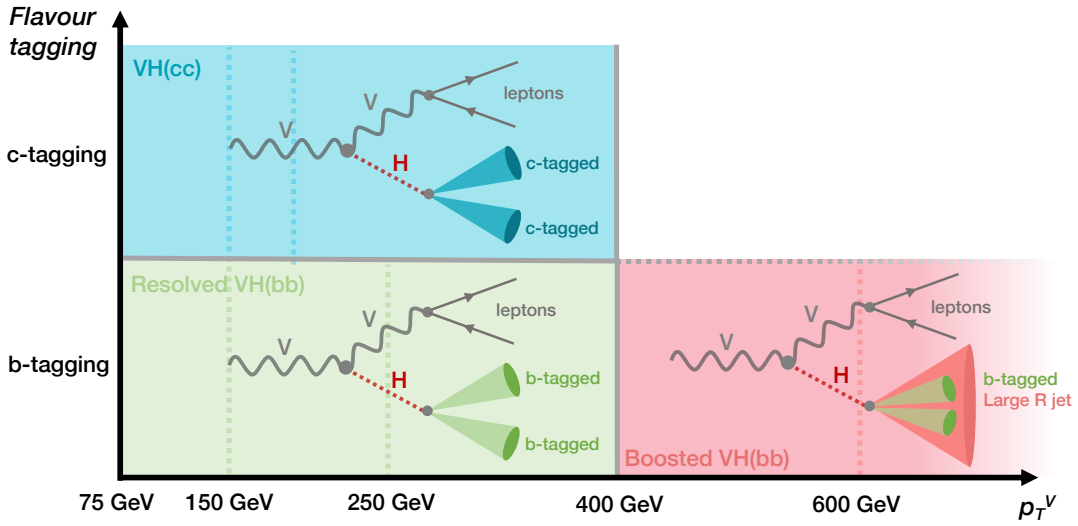

Figure 4.1: The combined $VH(\to b\bar{b}, c\bar{c})$ analysis phase space [168].

Multivariate analysis (MVA) Section 4.3 discusses the multivariate analysis methods used in $VH(\to b\bar{b}, c\bar{c})$. Boosted decision trees (BDT) are trained on discriminating event-level variables to differentiate between signal and background events. The BDT discriminants are then used as the fitted distribution in the final statistical analysis. MVA techniques are used in the previous resolved $VH(\to b\bar{b})$ analysis but not in resolved $VH(\to c\bar{c})$ or boosted $VH(\to b\bar{b})$. Introducing MVA in this analysis greatly improves the $VH(\to c\bar{c})$ signal sensitivity. More details about the MVA input variables and training are discussed in Section 4.3.

Background modeling The data and the signal and background samples used in the analysis are introduced in Section 4.4. *modeling uncertainties* are derived in the analysis using nominal samples, their variations (e.g., QCD scale variations), and alternative samples. Different types of uncertainties are derived including the normalization uncertainties, acceptance ratio uncertainties and shape uncertainties. In particular, CARL (calibrated likelihood ratio estimator), a machine learning reweighting package, is used to assess MVA shape uncertainties [169]. The application of CARL is particularly important for the MVA analysis, as it allows MVA output shape uncertainties to have physical meanings at the input variable level. More details about the signal, V+jets, top and diboson modeling uncertainties are discussed in Section 4.5.

Statistical analysis Lastly, a *binned profile likelihood* fit model is used to extract the signal strengths of $VH(\to b\bar{b})$ and $VH(\to c\bar{c})$. Different interpretations are calculated including the $VH(\to b\bar{b})$ signal significance, expected and observed upper limits at the 95% confidence level (CL) for $VH(\to c\bar{c})$, and the Higgs-bottom and Higgs-charm coupling modifier ratio (κ_c/κ_b). More details of the statistical analysis are discussed in Section 4.6.

4.2 Objects and events

This section discusses object reconstruction, event selection, and event categorization. Building on the physics object discussion in Section 3.3, Section 4.2.1 discusses the working points used in $VH(\to b\bar{b}, c\bar{c})$. Section 4.2.2 discusses the trigger used for the analysis and the event selection criteria based on the physics objects. Section 4.2.3 introduces the signal and control region definitions and the final jet energy correction.

4.2.1 Object reconstruction

This section discusses the electron, muon, hadronic τ-lepton, jet, and E_T^{miss} selections. Section 4.2.1.1 discusses the PCFT scheme. Section 4.2.1.2 discusses the experimental uncertainties from all physics objects and flavor tagging.

Electrons, muons and hadronic τ-leptons The electron selection criteria are shown in Table 4.1. The VH-loose, ZH-Signal, and WH-Signal electrons are used later in event selections. Here, ZH (WH) means that the Higgs boson is produced in association with a Z (W) boson. The tighter p_T requirements for the signal electrons are limited by the trigger thresholds discussed in Section 4.2.2. Tighter WH-Signal electron requirements suppress the multi-jet background in the 1-lepton channel.

The muon selection criteria are shown in Table 4.2. The hadronic τ-lepton selection criteria are shown in Table 4.3.

For both electrons and muons, the impact parameter requirements for d_0^{sig} and $|\Delta z_0 \sin\theta|$ reject tracks with large impact parameters. Those tracks tend to come from pileup, away from the hard-scattering collision of interest. The η coverage is 2.5 and 2.7 for the inner detector and the muon spectrometer respectively. Therefore, the electron $|\eta|$ range is set as less than 2.47 and the muon $|\eta|$ range is set as less than 2.7 or 2.5 [170].

Electron Selection	p_T	η	ID	d_0^{sig} w.r.t. BL	$\lvert\Delta z_0 \sin\theta\rvert$	Isolation
VH-Loose	> 7 GeV	$\lvert\eta\rvert < 2.47$	LH Loose	< 5	< 0.5 mm	Loose_VarRad
ZH-Signal	> 27 GeV	— Same as VH-Loose —				
WH-Signal	> 27 GeV	$\lvert\eta\rvert < 2.47$	LH Tight	< 5	< 0.5 mm	HighPtCaloOnly

Table 4.1: Electron selection criteria. In the fourth column, ID stands for *identification* and lists the electron identification working points used in the analysis. LH stands for *likelihood* and refers to the likelihood-based electron ID algorithm. *LH Loose* and *Tight* refer to the 93% and 80% electron ID efficiency working points. Looser working points have higher electron ID efficiency but worse background rejections. The fifth column, d_0^{sig} w.r.t. BL, lists the transverse impact parameter significance with respect to the beam-line. The sixth column, Δz_0, lists the longitudinal impact parameters relative to the primary vertex. The last column lists the electron isolation criteria used. The ZH-Signal electrons have the same selection criteria as the VH-Loose electrons except the tighter p_T cut.

Muon Selection	p_T	η	ID	d_0^{sig} w.r.t. BL	$\lvert\Delta z_0 \sin\theta\rvert$	Isolation
VH-Loose	> 7 GeV	$\lvert\eta\rvert < 2.7$	Loose quality	< 3	< 0.5 mm	Loose_VarRad
ZH-Signal	> 27 GeV	$\lvert\eta\rvert < 2.5$		— Same as VH-Loose —		
WH-Signal	> 25 GeV when $p_T^V > 150$ GeV > 27 GeV when $p_T^V < 150$ GeV	$\lvert\eta\rvert < 2.5$	Medium quality	< 3	< 0.5 mm	HighPtTrackOnly

Table 4.2: Muon selection criteria. The muon selection table has the same columns as the electron selection table above. The *loose quality* (*medium quality*) muon identification working point has a muon identification efficiency of 98% (97%) for muon p_T above 5 GeV [108].

Lepton	p_T	η	n_{trk}	ID
τ	> 20 GeV	$\lvert\eta\rvert < 2.5$	1 or 3 tracks	Loose

Table 4.3: Hadronic τ-lepton selection criteria. The fourth column n_{trk} refers to the number of tracks associated with the hadronic τ-leptons. The number of tracks is either one or three as the hadronic τ decays contain either one or three charged pions. The *loose* working points correspond to the 85% (75%) identification efficiency for the 1-track (3-track) hadronic τ-leptons [111].

Jets Jets are of particular importance for the $VH(\to b\bar{b}, c\bar{c})$ analysis, as the final Higgs candidates are reconstructed from two heavy-flavor jets. There are three kinds of jets used in the analysis:

- *Small-R jets (R = 0.4):* Higgs-candidate reconstruction and event categorization in the resolved regime;
- *Large-R jets (R = 1.0):* Higgs-candidate reconstruction in the boosted regime;
- *Variable-R (VR) track jets:* b-tagging inside the large-R jets and event categorization in the boosted regime;

The selection criteria for the small-R jets are listed in Table 4.4. In addition to the signal jet, high η forward jets are used in event categorization. Forward jets have $2.5 < |\eta| < 4.5$ outside the inner detector coverage. The forward jets are mainly measured by FCal, the LAr forward calorimeter. Similar to the central small-R jets, the forward small-R jets have the radius parameter $R = 0.4$.

The large-R jet and variable-R (VR) track jets selection requirements are listed in Table 4.5. Variable-R track jets have a jet-p_T dependent radius parameter: $\mathrm{R}(p_T) = \rho/\ p_T$. Here, $\rho = 30$ GeV and track jets have $R_{max} = 0.4$ and $R_{min} = 0.02$. The parameters are optimized for b-tagging performance in the boosted $VH(\to b\bar{b})$ regime. VR track jets are built entirely from the inner detector tracks without calorimeter information [171]. In the analysis, they are used for b-tagging inside large-R jets.

Jet Category	Tight Jet Cleaning	p_T	η	JVT/fJVT
Signal Jet	true	> 20 GeV	< 2.5	JVT > 0.5 for $\lvert\eta\rvert < 2.4$, $p_T < 60$ GeV jets
Forward Jet	true	> 30 GeV	$2.5 < \lvert\eta\rvert < 4.5$	fJVT < 0.5 for $p_T < 120$ GeV jets

Table 4.4: Small-R jet selection criteria. The second column lists whether tight jet cleaning is used for jet collections. The last column lists the cuts on JVT and fJVT.

Jet Category	Selection Requirements
Large-R jets	$p_{\mathrm{T}} > 250\,\mathrm{GeV}$
	$\lvert\eta\rvert < 2.0$
VR Track jets	$p_{\mathrm{T}} > 10\,\mathrm{GeV}$
	$\lvert\eta\rvert < 2.5$

Table 4.5: `Large-R` jet and `variable-R` track jet selection criteria.

Missing transverse energy (E_T^{miss}) E_T^{miss} is used as a proxy for neutrinos in the 0-lepton and 1-lepton channels. The ratio $E_T^{miss}/\sqrt{S_{\mathrm{T}}}$ is the quasi-significance of E_T^{miss} and a variable used in the MVA training. The variable is defined as follows:

$$E_T^{miss}/\sqrt{S_{\mathrm{T}}} = \frac{E_T^{miss}}{\sqrt{\sum p_{\mathrm{T}}^{e} + \sum p_{\mathrm{T}}^{\mu} + \sum p_{\mathrm{T}}^{\mathrm{jet}}}} \ , \tag{4.1}$$

Here, S_{T} is the scalar sum of the charged lepton and jet p_T in the event.

Overlap removal When two objects have a small angular separation (ΔR), the two objects are called overlapped. When overlaps occur, it is likely that one of the objects is counted twice. Therefore, one of the two objects is removed to avoid double-counting. For example, when a hadronic τ-lepton overlaps with an electron or a muon (i.e., $\Delta R < 0.2$), the hadronic τ-lepton candidate is removed. Similarly, when leptons overlap with the jets, jets are removed in the events [172].

4.2.1.1 Flavor tagging

In this section, the pseudo-continuous flavor tagging (PCFT) scheme used in the resolved $VH(\to b\bar{b}, c\bar{c})$ is discussed. In addition, the boosted $VH(\to b\bar{b})$ flavor tagging working points and the flavor tagging calibration in the resolved and boosted phase space are also discussed. The finer flavor tagging bins from PCFT improve the signal sensitivities in the $VH(\to b\bar{b}, c\bar{c})$ analysis.

The traditional flavor tagging scheme is cut-based. Events failing the tagging requirements are discarded. An alternative approach is to reweight events according to their probabilities of passing the tagging requirements without discarding the events [168, 173]. This approach is called truth tagging. Truth tagging keeps the MC statistics and allows smoother templates. Truth tagging is used for MVA training samples. It is also used in low statistic regions in the statistical analysis such as the boosted phase space. The current truth tagging algorithm accurately reproduces the cut-based distributions. Thus, unlike the previous analysis, no additional systematic uncertainties are needed to address the differences [2].

Pseudo-continuous flavor tagging (PCFT) The pseudo-continuous flavor tagging scheme consists of orthogonal b-tagging and c-tagging regions as shown in Figure 4.2. The corresponding bin edges are listed in Table 4.6. The scheme is called pseudo-continuous. In the previous $VH(\to c\bar{c})$ analysis, only one c-tagging working point is defined. The PCFT scheme now uses two c-tagging working points or three c-tagging bins. The increased number of bins improves the signal sensitivities, as more loosely tagged c-jets are included in the analysis and the c-tagging bins help defining control regions for constraining the main backgrounds. In addition, the b-tagging bins are used in the MVA training. Ideally, more bins can be defined. However, further increasing the number of bins makes flavor tagging calibrations more challenging. Therefore, the PCFT scheme is used.

In the PCFT scheme, each jet has b-tagging (D^b_{DL1r}) and c-tagging (D^c_{DL1r}) scores. All jets are categorized into the five PCFT bins by making two-dimensional cuts on the b-tagging and c-tagging scores. The five bins are labeled as: untagged, c-loose, c-tight, b-60%, and b-70% bins. The flavor tagging efficiencies for the 5 bins are listed in Table 4.7. The *loose* (*tight*) c-tagging bins, labeled as c-loose (c-tight), have roughly 20% (24%) of c-tagging efficiencies. At the c-tagging bins, the τ-jet mis-tag efficiencies are approximately 20% as well due to the similar decay signatures of c-jets and τ-jets. In addition, the l-jet mis-tag efficiency is higher in the c-tagging bins than the b-tagging bins due to the shorter lifetime of charm hadrons. The b-60%, and b-70% b-tagging bins have roughly 60% and 10% of b-tagging efficiencies respectively.

Boosted flavor tagging The PCFT scheme is only used in the resolved $VH(\to b\bar{b}, c\bar{c})$ phase space due to limited statistics in the boosted phase space. The boosted $VH(\to c\bar{c})$ phase space is not considered in the analysis. For the boosted $VH(\to b\bar{b})$ regime, only b-tagging is applied to the variable-R track jets. There are four track jet tagging bins: 85%, 77%, 70%, 60%. To maximize the signal yield, all jets that pass the 85% b-tagging working point ($\epsilon_b = 85\%$) are used.

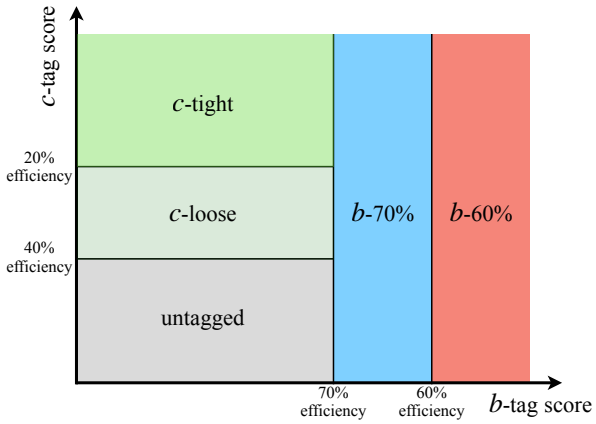

Figure 4.2: PCFT working points [168].

PCFT bin	bin name	$DL1r_c\ lim_{low}$	$DL1r_c\ lim_{up}$	$DL1r_b\ lim_{low}$	$DL1r_b\ lim_{up}$
0	untagged	none	0.6735	none	3.245
1	c-loose	0.6735	1.76	none	3.245
2	c-tight	1.76	none	none	3.245
3	b-70	none	none	3.245	4.565
4	b-60	none	none	4.565	none

Table 4.6: The PCFT bin edges. The symbols lim_{low} and lim_{up} denote the lower and upper limits respectively of the `DL1r` scores.

PCFT bin	PCFT bin name	b-jet ϵ_{jet}	c-jet ϵ_{jet}	light jet ϵ_{jet}	tau-jet ϵ_{jet}
1	c-loose	11.5%	20.5%	6.5%	18.5%
2	c-tight	4.8%	24.2%	0.9%	19.5%
3	b-70	11.2%	5.2%	0.13%	1.7%
4	b-60	58%	2.65%	0.051%	0.49%

Table 4.7: The flavor tagging efficiencies (ϵ) for tagging b-jets, c-jets, l-jets and τ-jets in the PCFT bins measured from a $t\bar{t}$ sample.

Flavor tagging efficiency calibration After setting the working points, the flavor tagging efficiencies are calibrated for the five PCFT bins for b-jets, c-jets, and l-jets. The calibration scale factors between data and MC simulations are defined in Equation 3.20. The c-jet scale factors are also used for the τ-jets.

The nominal calibrations use different simulation samples from the analysis samples. Therefore, additional MC-to-MC scale factors are derived for the samples used in the analysis (POWHEG+PYTHIA 8 for signal, $t\bar{t}$, and single top processes and SHERPA 2.2.11 for V+jets and diboson processes) [174]. The final efficiency scale factor equation with the MC-to-MC components is shown in Equation 4.2. The final b-jet, c-jet, and l-jet efficiency scale factors for the POWHEG+PYTHIA 8 samples are shown in Figure 4.3.

The scale factors are mostly around unity. The b-jet scale factor in the loose c-tagging bin and the c-jet scale factor in the 60% b-tagging bin are above unity. The b-jet scale factor uncertainties tend to be small (less than 10%) in all bins except the no c-tag bin. The c-jet scale factor uncertainties are slightly larger (around 10%) in most bins. The l-jet scale factor uncertainties can be up to 20% in the b-tagging bins, but the uncertainty is small in the no c-tag bin.

$$SF_{alternative} = \frac{\epsilon_{data}}{\epsilon_{nominal}} \times \frac{\epsilon_{nominal}}{\epsilon_{alternative}} \tag{4.2}$$

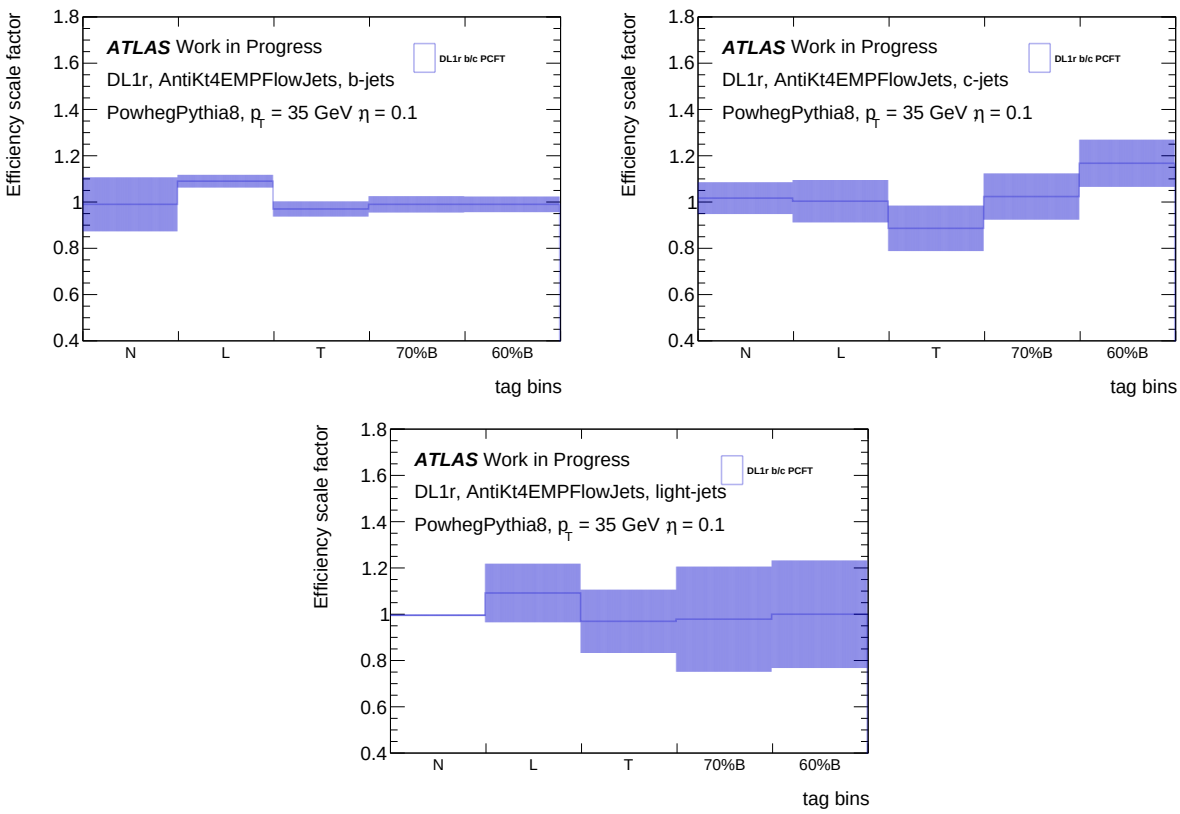

Figure 4.3: The scale factors applied to the POWHEG+PYTHIA 8 samples for the p_T = 35 GeV and $\eta = 0.1$ bin [168]. (top left) b-jet, (top right) c-jet, and (bottom) l-jet. The l-jet scale factor is set to 1 for the 60% b-tagging bin with the same uncertainty as the 70% b-tagging bin. The scale factors are derived following Equation 4.2.

Boosted flavor tagging calibration The boosted flavor tagging calibration is similar to the calibration in the resolved phase space. At high p_T (above 300 GeV), the calibration uncertainties need to be extrapolated from the low p_T regions due to the limited statistics of the data. For the POWHEG+PYTHIA 8 samples, the b-jet and c-jet scale factor uncertainties are approximately 10% for jet p_T above 150 GeV. The l-jet scale factor uncertainty is approximately 20% for jet p_T above 150 GeV.

4.2.1.2 Experimental uncertainties

The experimental uncertainties are uncertainties on the reconstructed physics objects, flavor tagging, triggers, luminosity, and the pileup distribution. They are considered as both shape and normalization uncertainties in the statistical analysis and fully correlated in all regions. The luminosity uncertainty is estimated from the low luminosity van der Meer scan and

then extrapolated to the high luminosity physics data region [68]. The uncertainty on the combined Run 2 luminosity is sub % [175].

The pileup uncertainty accounts for the differences in the pileup distribution between simulation and data. The pileup uncertainty is assessed by varying the nominal pileup scale factor from 1.0/1.03 to 1.0/0.99 or 1.0/1.07 [172, 176]. The pileup uncertainty has a small contribution to the final signal strength uncertainty.

The trigger uncertainties account for the uncertainties of the trigger efficiencies [172]. Triggers are used to select events in the analysis. The electron, muon, and E_T^{miss} triggers are used in the analysis and discussed in Section 4.2.2. The E_T^{miss} trigger uncertainties are measured in [172] and the lepton trigger uncertainties are assessed in [177, 178]. The E_T^{miss} trigger efficiency uncertainties are less than 10%. The impact of the trigger efficiency uncertainties on the signal strengths is assessed along with the reconstructed leptons or E_T^{miss} and is small in the fit.

The experimental uncertainties of the reconstructed physics object are assessed through calibrations discussed in Section 3.3. The electron efficiency and energy scale and resolution uncertainties are included [172]. The electron efficiency uncertainties are included as three separate uncertainties for electron reconstruction efficiency, electron identification efficiency, and electron isolation efficiency. The muon reconstruction and isolation efficiency and momentum scale and resolution uncertainties are also included. The hadronic-τ efficiency and energy scale uncertainties are included as well. Overall, the lepton uncertainties have small contribution in the total signal strength uncertainties compared to jet and flavor tagging uncertainties.

The jet uncertainties are from the JES and JER calibrations. The uncertainties from the major sources, such as the flavor response, flavor composition, and heavy-flavor, are included individually. The large number of remaining uncertainties are reduced by applying the uncertainty reduction scheme [172, 116]. The uncertainty components are decomposed into orthogonal terms. The largest orthogonal terms are included as effective uncertainties. This method is called the principle component analysis. There are around 40 effective jet uncertainties for small-R jets. The large-R jet JES, JER, JMS (jet mass scale), and JMR (jet mass resolution) are included in a similar fashion. The JVT and fJVT efficiency uncertainties are also included [172, 118]. No jet uncertainties are included for the VR track jets, as they are not used in Higgs reconstruction. The flavor tagging uncertainties are expected to cover uncertainties from VR track jets. The E_T^{miss} uncertainties are also included.

The flavor tagging efficiency uncertainties are included separately for small-R jets and VR track jets [172]. Flavor tagging was not performed for the large-R jets, and thus no flavor tagging uncertainties are considered for large-R jets. The flavor tagging uncertainties are also considered separately for b-jets, c-jets, l-jets, and τ-jets following the calibration in Section 4.2.1.1. The number of uncertainties is reduced through the principle component analysis. There are around 20 to 40 effective uncertainties for each jet flavor. The VR track jets are used in the boosted region, and thus high p_T extrapolation uncertainties are included for the VR track jets. No high p_T extrapolation uncertainty is needed for the small-R jets in the resolved phase space.

4.2.2 Trigger and event selection

After reconstructing the objects and tagging the jet flavors, signal events can be selected to maximize the signal sensitivity. The full event selection is shown in Table 4.8-4.9.

Trigger Different combinations of L1 and HLT trigger requirements form different trigger items used to select the $VH(\to b\bar{b}, c\bar{c})$ events. The trigger thresholds limit the electron and muon p_T thresholds. In the individual lepton channels:

- 0**-lepton**: triggered by the E_T^{miss} trigger. The reconstructed E_T^{miss} is required to be above 150 GeV, where the E_T^{miss} trigger efficiency plateaus.
- 1**-lepton**: the electron channel (e channel) is triggered by the single electron trigger. The electron channel selects W bosons that decay to one electron and one neutrino. The muon channel (μ channel) is triggered by the single muon trigger for p_T^V below 150 GeV and the E_T^{miss} trigger for p_T^V above 150 GeV, since the E_T^{miss} trigger has higher efficiencies above 150 GeV. Here, p_T^V is the transverse momentum of the vector boson. The μ channel selects W bosons that decay to one muon and one neutrino.
- 2**-lepton**: similar to the 1-lepton triggers, the electron channel is triggered by the single electron trigger. The muon channel is triggered by the single muon trigger for p_T^V below 250 GeV and the E_T^{miss} trigger for p_T^V above 250 GeV, as the E_T^{miss} trigger efficiency is better than the muon trigger above 250 GeV in 2-lepton.

The triggers discussed above for each lepton channel are also summarized in Table 4.8 for the resolved $VH(\to b\bar{b}, c\bar{c})$ and Table 4.9 for the boosted $VH(\to b\bar{b})$. In addition, as shown in Table 4.8, there are cuts on S_T, the scalar sum of the jet p_T, in 0-lepton and 1-lepton. In 1-lepton, the cut is only needed when the E_T^{miss} trigger is used. Those S_T cuts aim to mitigate the mismodeling of jet momentum at low E_T^{miss} trigger efficiencies.

Analysis regime	resolved $VH(\to b\bar{b})$	$VH(\to c\bar{c})$
	Common Selections	
Jets	≥ 2 signal jets	
Candidate jet tagging	2 B-tags	≥ 1 T-tag
Leading Higgs candidate jet p_T	> 45 GeV	
Sub-leading Higgs candidate jet p_T	> 20 GeV	
m_{bb} or m_{cc}	> 50 GeV	
ΔR(jet1, jet2)	Upper cut $\Delta R < \pi$	
	0-lepton channel	
Trigger	E_T^{miss} triggers	
S_T	> 120 GeV (2 jets), >150 GeV (3p jets)	
Leptons	0 VH-loose lepton	
E_T^{miss}	> 150 GeV	
m_T^W	> 10 GeV (for events with at least one hadronic τ)	
Additional jet tagging	no T-tag	no B-tag
Jets	≤ 4 jets	≤ 3 jets
$\lvert\min\Delta\phi(E_T^{\text{miss}}, \text{jet})\rvert$	$> 20°$ (2 jets), $> 30°$(3 jets)	
$\lvert\Delta\phi(E_T^{\text{miss}}, H)\rvert$	$> 120°$	
$\lvert\Delta\phi$(jet1, jet2)$\rvert$	$< 140°$	
	1-lepton channel	
Trigger	e channel: single electron trigger μ channel: single muon trigger ($p_T^V < 150$ GeV) and E_T^{miss} triggers (above)	
Leptons	1 WH-signal lepton no second VH-loose lepton	
S_T	> 120 (2 jets), >150 GeV (3 jets) (μ channel with E_T^{miss} trigger)	
m_T^W	> 20 GeV ($75 < p_T^V < 150$ GeV only)	
Additional jet tagging	no T-tag	no B-tag
Jets	≤ 3 jets	
E_T^{miss}	> 30 GeV (e channel)	
hadronic τ-veto	no hadronic τ	
	2-lepton channel	
Trigger	e channel: single electron trigger μ channel: single muon trigger ($p_T^V < 250$ GeV) and E_T^{miss} triggers (above)	
Leptons	2 VH-loose leptons (≥ 1 ZH-signal lepton) Same flavor, opposite charges for muons	
m_{ll}	$81 < m_{ll} < 101$ GeV	
Additional jet tagging	-	no B-tag

Table 4.8: Summary of the event selection in the resolved $VH(\to b\bar{b}, c\bar{c})$ phase space. The control region selections differ in some requirements. More details are discussed in Section 4.2.3. B-tag means that the jets are in the b-60% or b-70% bin. T-tag stands for the tight c-tag, as defined in Figure 4.2. 3p jets refer to 3plus jets, meaning that the number of jets is larger than or equal to three. The m_{bb} or m_{cc} cut is applied before the Higgs candidate energy correction in Section 4.2.3.1.

Selection	0-lepton channel	1-lepton channel		2-lepton channel	
		e sub-channel	μ sub-channel	e sub-channel	μ sub-channel
Trigger	E_T^{miss}	Single electron	E_T^{miss}	Single electron	E_T^{miss}
Leptons	0 VH-loose lepton	1 WH-signal lepton no second VH-loose lepton no hadronic τ		$\geq$ 1 ZH-signal lepton 2 VH-loose leptons	
E_T^{miss}	> 250 GeV	> 50 GeV	-	-	
p_T^V	$p_T^V > 400$ GeV				
Large-R jet	at least one large-R jet, $p_T > 250$ GeV, $\lvert\eta\rvert < 2$				
Track-Jets	at least two track-jets, $p_T > 10$ GeV, $\lvert\eta\rvert < 2.5$, matched to the leading large-R jet				
Higgs candidate b-jet tagging	exactly two B-tags of the leading three track-jets matched to the leading large-R				
Track jet tagging outside of the leading large-R jet	No B-tags				
m_J	> 50 GeV				
$\min \Delta\phi(E_T^{miss}, \text{jets})$	$> 30°$	-			
$\Delta\phi(E_T^{miss}, H_{\text{cand}})$	$> 120°$	-			
m_{ll}	-			66 GeV $< m_{ll} <$ 116 GeV	
lepton flavor	-			two leptons with the same flavor	
lepton charge	-			opposite charge for muons	

Table 4.9: Event selection for the three lepton channels in the boosted $VH(\rightarrow b\bar{b})$ phase space. Here, B-tags mean that the VR track jets are selected by the 85% b-tagging working point.

Vector boson selection As discussed in Section 4.1, the analysis is split into three lepton channels:

- **0-lepton:** There are two kinds of events in the 0-lepton channel: events with zero or at least one hadronic-τ. The transverse momentum of the vector boson p_T^V is defined by Equations 4.3-4.4 in the two cases:

$$p_T^V = E_T^{miss} \tag{4.3}$$

$$\mathbf{p_T^V} = \mathbf{E_T^{miss}} + \mathbf{p_T^\tau} \tag{4.4}$$

  Here, p_T^τ is the transverse momentum of the highest p_T hadronic-τ. The transverse mass of the reconstructed W boson (m_T^W) from the hadronic-τ and the E_T^{miss} is defined as:

$$m_T^W = \sqrt{2p_T^l E_T^{miss}(1 - cos(\Delta\phi(l, E_T^{miss})))} \tag{4.5}$$

  An additional cut is applied to m_T^W for events with at least one hadronic τ to remove fake τ-leptons. Later for the modeling studies and profile likelihood fit, 0-lepton events

with ≥ 1 hadronic-τ are moved to the 1-lepton channel, as they are typically 1-lepton events.

- 1**-lepton:** The events have exactly one WH-signal lepton (defined in Table 4.1-4.2) and no additional VH-loose leptons. The p_T^V is defined as:

$$\mathbf{p_T^V} = \mathbf{E_T^{miss}} + \mathbf{p_T^l} \tag{4.6}$$

  Here, p_T^l is the transverse momentum of the lepton.

- 2**-lepton:** The 2-lepton events have exactly two VH-loose leptons with ≥ 1 ZH-signal lepton. The two leptons are required to have the same flavor (either e or μ). The two muons are required to have opposite charges. Due to the impact of charge mis-identification, this is not required for the electrons. The vector boson invariant mass can be fully reconstructed from the two leptons (Equation 3.10). Therefore, the dilepton invariant mass m_{ll} is required to be within the Z boson mass range.

Higgs candidate selection

- **Resolved phase space:** The b-tagged and c-tagged jets are used to reconstruct the Higgs candidates. The $VH(\rightarrow b\bar{b})$ phase space selects events with exactly two b-tagged jets (defined in Figure 4.2). Jets above the 60% working point and in both b-60% and b-70% bins are considered b-tagged. The b-60% and b-70% bin labels are only used in the MVA training. The b-60% and b-70% PCFT bins are defined in Figure 4.2. The two b-tagged jets reconstruct the Higgs candidate (H_{cand}). The leading and sub-leading jets are ordered by p_T. The $VH(\rightarrow b\bar{b})$ events are also required to have no tight c-tags (T-tag) for the additional jets in the 0-lepton and 1-lepton channels. Here, additional jets refer to jets other than the leading and sub-leading jets for Higgs reconstruction. This requirement is not needed in 2-lepton as the $t\bar{t}$ contamination in 2-lepton is small.

  The $VH(\rightarrow c\bar{c})$ phase space selects events with at least 1 tight c-tag (T-tag). The leading and sub-leading jets are determined by ordering: tight c-tag > loose c-tag > no c-tag. Within the same tagging category, jets are ordered by p_T. For example, if there are two tight c-tag jets, the higher p_T jet is considered the leading jet. The leading and sub-leading jets reconstruct the Higgs candidate. All $VH(\rightarrow c\bar{c})$ phase space is required to have no B-tags and thus has no overlap with the resolved $VH(\rightarrow b\bar{b})$ phase space.

- **Boosted phase space:** The boosted $VH(\rightarrow b\bar{b})$ Higgs candidates are reconstructed from the leading p_T large-R jet. The VR track jets are ghost-associated with the large-R jets as sub-jets. Ghost association means that the 'ghost' version of the track jet is contained within the large-R jet after reclustering, where the 'ghost' version has the same direction as the original track jet but infinitesimally small p_T [179, 180].

The large-R jet should have exactly two sub-jets among the three leading sub-jets to be b-tagged. The boosted b-tagging working point is 85%, as discussed in Section 4.2.1.1. No b-tagged track jets are allowed outside of the Higgs candidate large-R jet to remove top backgrounds.

Lastly, for all reconstructed Higgs candidates in the $VH(\to b\bar{b}, c\bar{c})$ phase space, due to mis-modeling at the low Higgs invariant mass, a 50 GeV lower cut is applied. In Table 4.8, the cut is applied for m_{bb} or m_{cc} in the resolved $VH(\to b\bar{b})$ or $VH(\to c\bar{c})$ phase space respectively. In Table 4.9, the cut is applied for the invariant mass of the Higgs candidate large-R jet (m_J) in the boosted $VH(\to b\bar{b})$ phase space.

Background suppression In addition to selecting the vector boson and the Higgs candidate, more cuts are applied to remove backgrounds in the 0-lepton and 1-lepton channels.

- 0**-lepton:** The *anti-QCD* cuts are applied in the 0-lepton channel to remove the multi-jet background. The variables used are: $|\min\Delta\phi(E_T^{\text{miss}}, \text{jet})|$, $|\Delta\phi(E_T^{\text{miss}}, H)|$, and $|\Delta\phi(\text{jet1, jet2})|$. The multi-jet background tends to have low values of $|\min\Delta\phi(E_T^{\text{miss}}, \text{jet})|$. For the $|\min\Delta\phi(E_T^{\text{miss}}, \text{jet})|$ calculation, only the three leading signal jets are considered in the resolved phase space. Similarly, in the boosted $VH(\to b\bar{b})$, only small-R jets with $p_T > 70$ GeV outside the Higgs candidate large-R jet are considered for $|\min\Delta\phi(E_T^{\text{miss}}, \text{jet})|$.

  The variable $|\Delta\phi(\text{jet1, jet2})|$ is only used in the resolved phase space. In the boosted phase space, both track jets are matched to the large-R jet with small $\Delta\phi$ in between. With the anti-QCD cuts, the multi-jet background in the 0-lepton channel is negligible (around 1%).

- 1**-lepton:** To suppress the multi-jet background, in the e channel in 1-lepton, the E_T^{miss} is required to be larger than 30 GeV. The remaining multi-jet background in 1-lepton is approximately a few %.

  In addition, a τ-veto is applied to reject a specific kind of $t\bar{t}$ decays. When the $t\bar{t}$ events decay to b-quarks and W-bosons, one of the W-bosons decays to τ-leptons and neutrinos, and the τ-leptons decay hadronically, the signature is similar to $VH(\to b\bar{b}, c\bar{c})$. Overall, the remaining $t\bar{t}$ background after applying the τ-veto is large (up to 40% in some signal regions) in the 1-lepton channel.

4.2.3 Signal and control regions

After identifying events with the *VH* signatures, further requirements can be set to divide the signal regions and control regions. All signal and control regions used in the analysis are shown in Figure 4.4. There are approximately 60 signal regions and 90 control regions. The signal regions are used to extract the signal strength in the statistical analysis. They are categorized by the number of jets (n-jet) and p_T^V ranges. The $VH(\to c\bar{c})$ signal regions are further categorized by the number of c-tags.

Signal region categorization The signal and control regions are divided by the number of jets and p_T^V.

- **n-jet:** The number of selected jets (n-jets) in the events counts as signal+forward jets. Different lepton channels have different n-jet regions. Note that for the n-jet categorization, the p_T of the non-Higgs candidate jets is required to be above 30 GeV.
  - $VH(\to b\bar{b})$ **0-lepton:** 2-, 3-, 4-jet
  - $VH(\to b\bar{b})$ **1-lepton:** 2-, 3-jet
  - $VH(\to b\bar{b})$ **2-lepton:** 2-, 3-, 4p-jet (≥ 4 jets)
  - $VH(\to c\bar{c})$ **0-lepton and 1-lepton:** 2-, 3-jet
  - $VH(\to c\bar{c})$ **2-lepton:** 2-, 3p-jet (≥ 3 jets)

  In $VH(\to c\bar{c})$ 0-lepton and 1-lepton, only 2- and 3-jet categories are used due to high $t\bar{t}$ contamination with four or more jets. The 4- and 4p-jet categories are used in $VH(\to b\bar{b})$ 0-lepton and 2-lepton to enhance the STXS sensitivities. However, the $VH(\to b\bar{b})$ 1-lepton 4-jet category suffers from high $t\bar{t}$ contamination.

- p_T^V**:** The regions are further split into p_T^V bins. Different p_T^V bins have different signal and background distributions. The p_T spectrum of the reconstructed Higgs boson is harder than the backgrounds. The resolved $VH(\to b\bar{b})$ p_T^V bins are listed below:
  - **Resolved** $VH(\to b\bar{b})$ **0-lepton:** 150-250, 250-400 GeV
  - **Resolved** $VH(\to b\bar{b})$ **1-lepton and 2-lepton:** 75-150, 150-250, 250-400 GeV

  The resolved $VH(\to b\bar{b})$ bins are capped at 400 GeV to avoid overlap with the boosted $VH(\to b\bar{b})$ phase space. In the $VH(\to c\bar{c})$ phase space, the 400 GeV cap is not used, as a boosted $VH(\to c\bar{c})$ region is still to be investigated.

In addition, as shown in Figure 4.4, the $VH(\to c\bar{c})$ signal regions are further divided according to the number of c-tags: two tight c-tags (2tt), one tight and one loose c-tag (2lt), and one tight and one no c-tag (1nt). The 2tt and 2lt signal regions are merged together as the 2xt-tag signal regions. All $VH(\to b\bar{b})$ signal regions have two b-tags (2b).

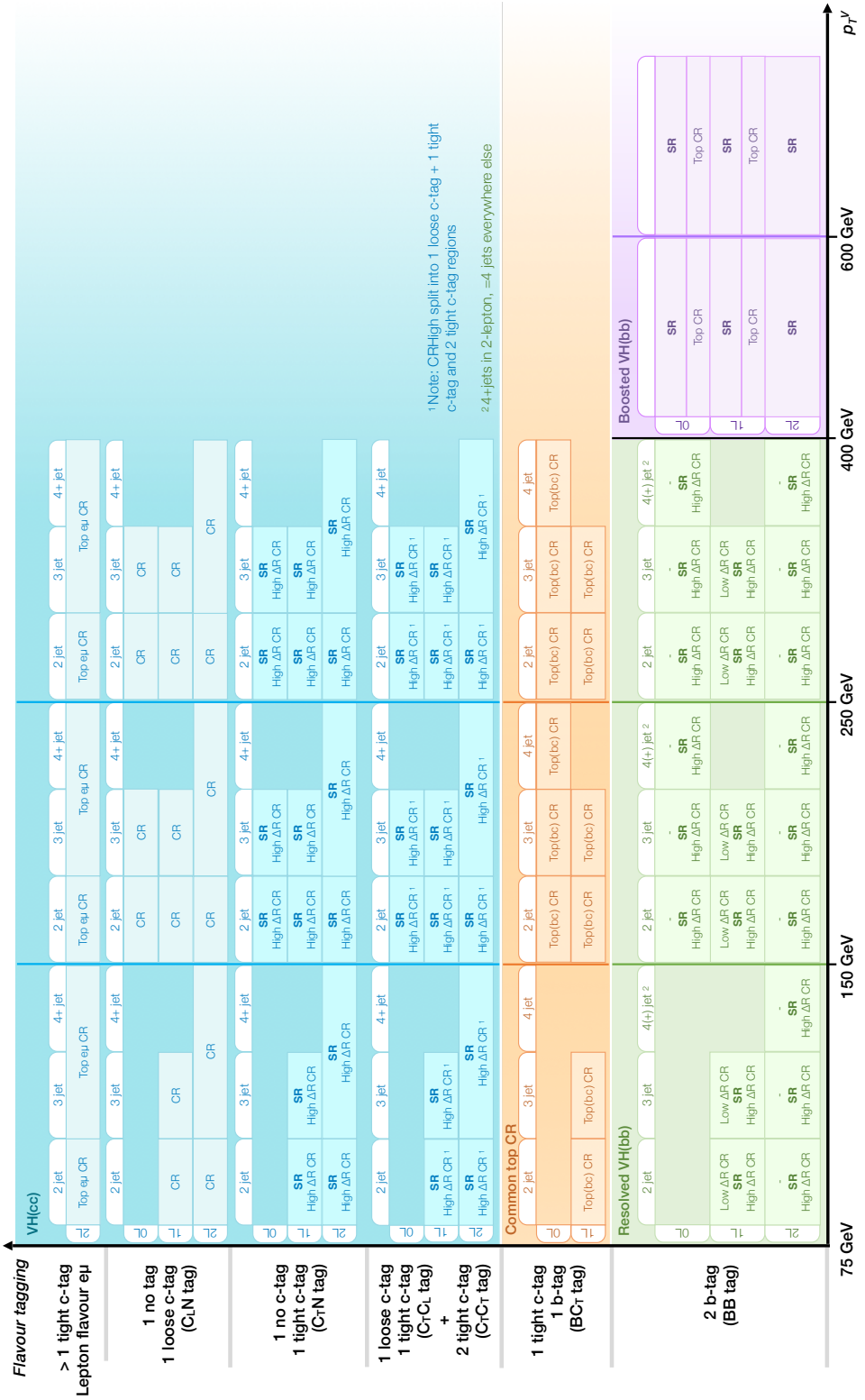

Figure 4.4: $VH(\rightarrow b\bar{b}, c\bar{c})$ analysis regions [1].

The control regions are designed to constrain the main backgrounds: V+jets and the top processes. The detailed selection for all control regions in the resolved phase space, in addition to the event selection discussed in Table 4.8, is listed in Table 4.10. The control regions have different ΔR cuts and b- or c-tags from the signal regions. In addition, while most control regions fit the kinematic distributions, certain control regions such as the top-$e\mu$ control regions in 2-lepton, fit only the normalization instead of kinematic distributions.

Analysis regime	resolved $VH(\to b\bar{b})$	$VH(\to c\bar{c})$
High ΔR(jet1, jet2) CR	ΔR(jet1, jet2) cut separating the SR and the High ΔR CR	
Low ΔR(jet1, jet2) CR	ΔR(jet1, jet2) cut separating the SR and the Low ΔR CR	-
$V + light$ CR	no B- and T-Tag, exactly 1 L-tag	
Top(BC) CR	≥ 1 B-Tag, ≥ 1 T-Tag	
Top-$e\mu$ CR	Different flavor leptons ($e\mu$ or μe)	

Table 4.10: Summary of the control region selections in the resolved $VH(\to b\bar{b}, c\bar{c})$. In addition to the signal event selections listed in Table 4.8, additional cuts are used in the control regions. Here, the ΔR(jet1, jet2) cuts refer to the continuous cuts in the 2D plane of ΔR and p_T^V. Both the high and low ΔR control region cuts are displayed in Figure 4.5. The high ΔR control region cut equations are listed in Table 4.11. The low ΔR control region cut equations are discussed in [168]. L-tag stands for the loose c-tag.

Control region categorization

- **High ΔR control region:** The high ΔR control region is designed to constrain the normalization and shapes for the V+jets and $t\bar{t}$ backgrounds. Continuous cuts in ΔR(jet1, jet2) are applied as a function of p_T^V. Figure 4.5 shows the signal yields in the 2D plane of ΔR and p_T^V. The ΔR cuts allow most signal events stay in the signal regions. Table 4.11 lists the high ΔR control region cut equations. The cuts are determined by fitting exponential functions in the 2D plane of ΔR and p_T^V to allow certain percentages of signal events in the signal regions. For example, about 95% of 2-jet signal events are kept in the signal regions.

  As shown in Table 4.8, ΔR has an upper cut at π to remove mis-modeling at high ΔR. The upper cut is used in both the signal regions and the high ΔR control regions. In addition, as shown in Figure 4.4, while the signal regions are merged as the 2xt-tag regions, the high ΔR control regions are split as the 2lt-tag and 2tt-tag regions to better

constrain the mixed-flavor V+jets background ($V + mf$) and the heavy-flavor $V + hf$ background. More details about the V+jets background categorization is discussed in Section 4.5.1.

- **Low ΔR control region:** The low ΔR regions are also used to constrain the background in the $VH(\rightarrow b\bar{b})$ 1-lepton channel, as the low ΔR control regions are enriched in the $W + hf$ events.

- **V+light control region:** The V+light control regions are defined by changing the tagging selections from the $VH(\rightarrow c\bar{c})$ signal regions to enrich the light-flavor V+jets background ($V + lf$). The leading jet is a loose c-tagged jet and the sub-leading jet has no c-tags (1ln-tag). The V+light control regions have high purity of $V + lf$ events.

- **Top control region in 0-lepton and 1-lepton:** The top control regions aim to constrain the top(bc) and top(bl) components. Therefore, the 0-lepton and 1-lepton top control regions require ≥ 1 tight c-tag and ≥ 1 b-tag. The Higgs candidates in the top control regions are reconstructed from the leading p_T b-tagged jet and the tight c-tagged jet.

- **Top-$e\mu$ control region in 2-lepton:** In the 2-lepton channel, the top backgrounds are mainly di-leptonic $t\bar{t}$ events. A pure $t\bar{t}$ control region with $\sim 90\%$ top events can be built by requiring opposite-flavor leptons ($e\mu$). In addition, the events need to have at least one tight c-tag. In $VH(\rightarrow c\bar{c})$ 2-lepton, top related systematics are not highly ranked and have little impact on the signal strength. In $VH(\rightarrow b\bar{b})$, the top-$e\mu$ events are used as a template for the signal region.

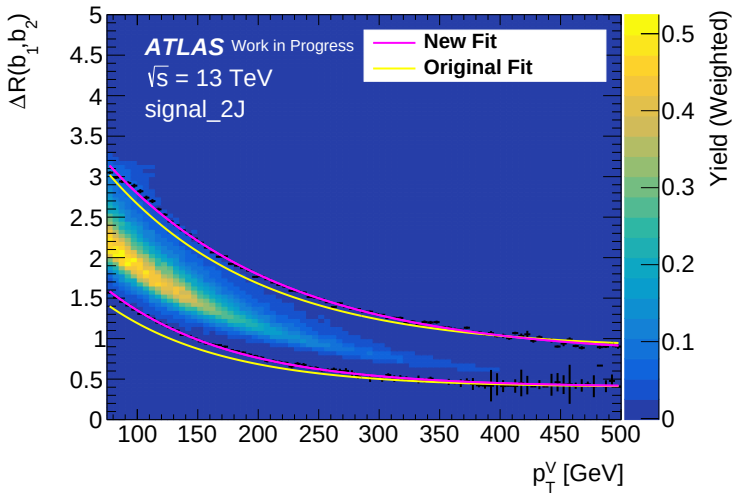

Figure 4.5: High and low ΔR control region cuts in the 2-lepton 2-jet region [168]. The high and low ΔR cuts are shown in the purple curves. The signal region is between the high ΔR and low ΔR cuts. The high ΔR region is above the high ΔR cut and the low ΔR region is below the low ΔR cut.

Category	Cut
$2-jet$	$\Delta R > 0.787 + e^{1.387-0.007\times p_T^V}$
$3-jet$	$\Delta R > 0.684 + e^{1.204-0.006\times p_T^V}$
$4-jet$	$\Delta R > 0.8627 + e^{0.9837-0.004077\times p_T^V}$
$5p-jet$	$\Delta R > 1.667 + e^{0.5189-0.005038\times p_T^V}$

Table 4.11: The high ΔR control region cuts in all lepton channels in $VH(\to b\bar{b}, c\bar{c})$ [168].

Different regions fit different variables in the final statistical analysis. All signal regions use the MVA discriminants in the final fit. Most control regions use the reconstructed Higgs mass, m_H (equivalently labeled m_{bb}, m_{cc}, or m_J). Some regions fit p_T^V instead of m_H to constrain the SHERPA 2.2.1 p_T^V uncertainties of the different V+jets samples such as $V+lf$ and $V+hf$. More details about SHERPA 2.2.1 p_T^V constraints are discussed in Section 4.5.3. In summary, the resolved phase space fit variables are as follows:

- High ΔR control regions: fit a single bin in 0-lepton; in 1-lepton and 2-lepton, fit m_H in 2tt-tag and 2lt-tag regions and fit p_T^V in 2b-tag and 1tn-tag regions.
- V+light control regions: fit a single bin in 0-lepton; in 1-lepton and 2-lepton, fit p_T^V.
- Top control regions in 0-lepton and 1-lepton: fit m_H.

- Top-$e\mu$ control regions in 2-lepton: fit a single bin.
- Low ΔR control regions: fit the MVA discriminant `mvaCRLow` trained for the low ΔR control regions.

The discriminant `mvaCRLow` is an MVA output trained specifically to separate W+bb events in the low ΔR control regions. More details are discussed in Section 4.3.

Boosted $VH(\to b\bar{b})$ categorization As shown in Figure 4.4, the boosted $VH(\to b\bar{b})$ signal regions have two p_T^V bins: 400-600 GeV and above 600 GeV.

There are top control regions in the 0-lepton and 1-lepton channels. The boosted top control region is defined by requiring at least one b-tagged track jet outside of the leading large-R jet. No top control region is needed in 2-lepton as the top background is negligible in boosted $VH(\to b\bar{b})$ 2-lepton.

4.2.3.1 Higgs candidate energy corrections

Lastly, after all events are selected and categorized into signal and control regions, the Higgs candidate jet energies are further corrected using analysis-specific methods before being used in the MVA training and likelihood fit. There are four jet energy correction methods: the muon-in-jet correction, the PtReco correction, the kinematic fit, and the FSR (final state radiation) recovery.

The muon-in-jet correction corrects the energy of b/c-hadrons that have muons in their decays. The muon four-momentum is added to the jet if the muon is inside the jet (that is $\Delta R(\text{jet}, \mu) < 0.2$). The PtReco correction factors are derived to correct the missing energy from the neutrinos in the b- and c-hadron semi-leptonic decays. The kinematic fit improves the jet energy resolution in the 2-lepton channel by balancing the momenta of the two leptons and two jets in the transverse plane. The two leptons from the Z boson decay tend have better energy resolutions than the jets. Lastly, the non-Higgs-candidate jets might come from the final state radiation. The FSR recovery identifies the potential FSR jets and corrects the Higgs candidate jet energy by adding the FSR jets back to the Higgs candidate jet. More details of the jet correction methods are discussed in [168].

The usage of all four Higgs candidate energy corrections in various phase spaces is listed in Table 4.12. The muon-in-jet correction is applied in all phase space and lepton channels. The PtReco correction is only applied in the resolved $VH(\to b\bar{b})$ phase space, as the improvement in the other phase spaces is negligible. The kinematic fit is applied in the 2-lepton channel for all three phase spaces. In the resolved $VH(\to b\bar{b})$ and the $VH(\to c\bar{c})$ phase space, the kinematic fit is only applied to events with two or three jets, as the improvement is negligible for events with four and more jets. The FSR recoveries are only used in 2-lepton to avoid $t\bar{t}$ migration to the signal regions in 0-lepton and 1-lepton. For n-jet ≥ 5, the improvement is negligible.

The final Higgs mass peak and resolution after all four corrections in the resolved $VH(\to b\bar{b})$ 2-lepton channel are shown in Figure 4.6. The Higgs mass peak is shifted by a few GeV and the resolution is improved by 37%.

Scheme	lepton channel	muon-in-jet	PtReco	kinematic fit	FSR recovery
Resolved $VH(\to b\bar{b})$	0-lepton	✓	✓		
	1-lepton	✓	✓		
	2-lepton	✓	✓(n-jet ≥ 4)	✓(n-jet ≤ 3)	✓(n-jet ≤ 4)
$VH(\to c\bar{c})$	0-lepton	✓			
	1-lepton	✓			
	2-lepton	✓		✓(n-jet ≤ 3)	✓(n-jet ≤ 4)
boosted $VH(\to b\bar{b})$	0-lepton	✓			
	1-lepton	✓			
	2-lepton	✓		✓	

Table 4.12: Higgs candidate jet energy correction used in different analysis phase space.

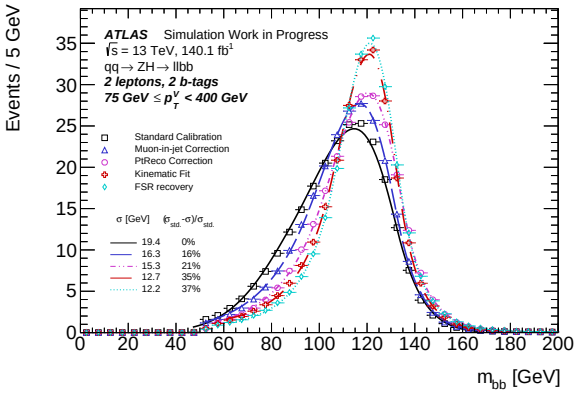

Figure 4.6: Corrected Higgs mass from the signal simulation in the resolved $VH(\to b\bar{b})$ 2-lepton channel [168].

4.3 Multivariate analysis

After discussing the objects and regions used in the analysis, a multivariate analysis is performed to differentiate the background and the signal events using the BDT. The MVA discriminant is used in the final likelihood fit. The MVA training variable is introduced

in Section 4.3.1. The final performance is discussed in Section 4.3.2. MVA is particularly important for the improved signal sensitivities of the $VH(\to b\bar{b}, c\bar{c})$ analysis.

The MVA training uses events that pass all event selections (Table 4.8-4.9) and after the jet energy corrections discussed in Section 4.2.3.1. In the resolved phase, the continuous ΔR cuts differentiating the ΔR control regions and the signal regions are not applied to improve the MVA training statistics.

The training uses nominal $VH(\to b\bar{b}, c\bar{c})$ signal samples as the signal and nominal V+jets, $t\bar{t}$, single-top, and diboson background samples as the background. The MVA training granularity is shown in Figure 4.7. Multiple trainings are conducted over subsets of analysis regions. For example, one training is performed for the 2-jet $VH(\to c\bar{c})$ 1tn-tagged region in 2-lepton in p_T^V 75-150 GeV. The fine training granularity ensures the MVA performance in each individual region. The MVA variable and performance are discussed in the following sections.

In addition to the trainings listed in Figure 4.7, a special BDT is trained over the $VH(\to b\bar{b})$ low ΔR control regions in 1-lepton. The BDT output is labeled `mvaCRLow`. The discriminant `mvaCRLow` separates the $W + bb$ events (signal) from other background events. The low ΔR control regions have enriched $W + bb$ events and use `mvaCRLow` discriminants in the final fit.

Figure 4.7: The $VH(\to b\bar{b}, c\bar{c})$ MVA training granularity [168].

4.3.1 MVA variables

The training variables used in the analysis are listed in Table 4.13. The variable selection is based on the experience of the previous resolved $VH(\to b\bar{b})$ analysis [155]. Some variables are tested but not used, due to their small impact on the final BDT output. Some variables were added in this analysis, such as the PCFT flavor tagging bins of jets. Extensive comparison and testing is performed between the $VH(\to b\bar{b}, c\bar{c})$ phase space across all lepton channels to optimize the variable selection. The resolved $VH(\to b\bar{b}, c\bar{c})$ phase space has the same set of variables, while the boosted $VH(\to b\bar{b})$ phase space uses a slightly different set of variables.

Resolved MVA variables There are 21 MVA variables used in the resolved phase space. 10 variables are used in all lepton channels, while 11 additional variables are only used in a subset of lepton channels. Those additional lepton-specific variables might not be defined in all lepton channels such as E_T^{miss}. They can also suppress backgrounds specific to the lepton channel, such as m_{top}.

- Variables used in all lepton channels:
  - $m_{j_1 j_2}$ or m_J: invariant mass of the Higgs candidate.
  - $m_{j_1 j_2 j_3}$ (resolved-only): the invariant mass of the three leading jets.
  - $p_T^{j_1}$ or $p_T^{j_1,\mathrm{trk}}$, $p_T^{j_2}$ or $p_T^{j_2,\mathrm{trk}}$: p_T of the leading and sub-leading jets;
  - $\sum_{i\neq 1,2} p_T^{j_i}$ (resolved-only): p_T sum of non-Higgs candidate jets;
  - $\Delta R(\vec{j_1}, \vec{j_2})$ or $\Delta R(j_{1,\mathbf{trk}}, j_{2,\mathbf{trk}})$: the angular distance between the two Higgs-candidate jets (resolved) or the two b-tagged track jets (boosted);
  - $\mathrm{bin}_{\mathrm{DL1r}}(j_1)$, $\mathrm{bin}_{\mathrm{DL1r}}(j_2)$: the variable shows the tagged bin of a jet among the five PCFT bins: the untagged, the 70% b-tag bin, the 60% b-tag bin, and the loose and tight c-tagged bins as shown in Figure 4.2. Here, j_1 and j_2 refer to the leading and sub-leading Higgs candidate jets. In the boosted phase space, there are four track jet tagging bins: 85%, 77%, 70%, 60% b-tag bins.
  - p_T^V: the transverse momentum of the vector boson.
  - $|\Delta\phi(\vec{V}, \vec{H_{cand}})|$: azimuthal distance between the reconstructed vector boson and the Higgs candidate.
- Variables used in some lepton channels:
  - $|\Delta\eta(\vec{j_1}, \vec{j_2})|$ (resolved-only, 0-lepton only): the pseudorapidity distances between the two Higgs-candidate jets.
  - E_T^{miss} (0-lepton+1-lepton): the missing transverse energy.

- $E_T^{miss}/\sqrt{S_T}$ (resolved-only, 2-lepton only): the quasi-significance of E_T^{miss} with S_T being the scalar sum of the p_T of the leptons and jets in the event (Equation 4.1).
- $|\Delta y(\vec{V}, \vec{H_{cand}})|$ (1-lepton+2-lepton): rapidity difference between the vector boson and Higgs boson candidate.
- $\min[\Delta\phi(\vec{\ell}, \vec{j_1} \text{ or } \vec{j_2})]$ (resolved-only, 1-lepton only): distance in ϕ between the lepton and the closest Higgs candidate jet.
- m_{eff} (resolved-only, 0-lepton only): the scalar sum of the p_T of all small-R jets and E_T^{miss} in the event.
- m_T^W (resolved-only, 1-lepton only): transverse mass of the W-boson candidate reconstructed from the lepton and E_T^{miss} (Equation 4.5).
- m_{top} (resolved-only, 1-lepton only): reconstructed mass of the leptonically decaying top quark. It can be determined using the longitudinal momentum of the neutrino.
- m_{ll} (resolved-only, 2-lepton only): the invariant mass of the 2 leptons system.
- $\cos\theta(\vec{l^-}, \vec{Z})$ (2-lepton only): the Z-boson polarization sensitive angle. It uses the polarization difference between the signal and the Z+jets background as suggested in [181].
- $\min\{\Delta R(b, j)\}$ (resolved-only, 0-lepton+1-lepton): the distance in ΔR between the closest Higgs-candidate jet and an additional jet.

	$VH(\to b\bar{b}, c\bar{c})$ Resolved			$VH(\to b\bar{b})$ Boosted		
Variable	0-lepton	1-lepton	2-lepton	0-lepton	1-lepton	2-lepton
$m_{j_1 j_2}$ or m_J	×	×	×	×	×	×
$m_{j_1 j_2 j_3}$	×	×	×			
$p_T^{j_1}$ or $p_T^{j_1,\mathrm{trk}}$	×	×	×	×	×	×
$p_T^{j_2}$ or $p_T^{j_2,\mathrm{trk}}$	×	×	×	×	×	×
$p_T^{\mathrm{j_3,trk}}$				×	×	×
$\sum_{i\neq 1,2} p_T^{j_i}$	×	×	×			
$\Delta R(\vec{j_1}, \vec{j_2})$ or $\Delta R(j_{1,\mathbf{trk}}, j_{2,\mathbf{trk}})$	×	×	×	×	×	×
$\lvert\Delta\eta(\vec{j_1}, \vec{j_2})\rvert$	×					
$\mathrm{bin}_{\mathrm{DL1r}}(j_1)$	×	×	×	×	×	×
$\mathrm{bin}_{\mathrm{DL1r}}(j_2)$	×	×	×	×	×	×
p_T^V	$\equiv E_T^{miss}$	×	×	$\equiv E_T^{miss}$	×	×
E_T^{miss}	×	×		×	×	
$E_T^{miss}/\sqrt{S_{\mathrm{T}}}$			×			
$\lvert\Delta y(\vec{V}, \vec{H_{cand}})\rvert$		×	×		×	×
$\lvert\Delta\phi(\vec{V}, \vec{H_{cand}})\rvert$	×	×	×	×	×	×
$\min[\Delta\phi(\vec{\ell}, \vec{j_1}$ or $\vec{j_2})]$		×				
m_{eff}	×					
m_T^W		×				
m_{top}		×				
m_{ll}			×			
$\cos\theta(\vec{l^-}, \vec{Z})$			×			×
$(p_T^{l_1} - E_T^{miss})/p_T^W$					×	
p_T^l					×	
N(track-jets in J)				×	×	×
N(add. small R-jets)				×	×	×
Color				×	×	×
$\min\{\Delta R(b,j)\}$	×	×				

Table 4.13: MVA variables used for the 0-, 1- and 2-lepton channels in the resolved $VH(\to b\bar{b}, c\bar{c})$ and boosted $VH(\to b\bar{b})$ analyses.

Boosted MVA variables There are 17 MVA variables used in the boosted phase space. Among them, eleven variables are also used in the resolved phase as introduced above. An additional six variables are specific to the boosted phase space.

- Variables used in all lepton channels:
  - $p_T^{j_3,\mathrm{trk}}$: p_T of the track jet inside the Higgs-candidate large-R jet. Here, j_3 refers to the leading no b-tagged track jet.
  - N(track-jets in J): the number of track-jets that are ghost-associated to the leading large-R jet (J).
  - N(add. small R-jets): the number of additional small-R jets that are not matched to the leading large-R jet (ΔR(small-R jet, large-R jet) > 1.0).
  - Color: a variable designed to exploit the difference in the color-flow between gluon splittings and decays from the QCD singlets [182]. The color is defined as:

$$\text{Color} = \frac{\theta^2_{j_1 j_3} + \theta^2_{j_2 j_3}}{\theta^2_{j_1 j_2}} \tag{4.7}$$

- Variables used in some lepton channels:
  - $(p_T^{l_1} - E_T^{miss})/p_T^W$ (1-lepton only): proxy for the p_T imbalance of the charged lepton and the neutrino of the W-boson.
  - p_T^l (1-lepton only): transverse momentum of the lepton.

For all input variables, when the variable is not defined in an event, a default value is assigned. The default value is chosen to be close to the distribution of the variable. For example, the default value of $\sum_{i\neq 1,2} p_T^{j_i}$ is set to zero. Some input variables have long tails. The range of each variable is limited to include 99% of the signal events. All variables above such limits are set to maximum values.

The most important variables in the BDT training tend to be $m_{j_1 j_2}$ (m_J) and $\Delta R(\vec{j_1}, \vec{j_2})$ ($\Delta R(\vec{j_{1,\mathbf{trk}}}, \vec{j_{2,\mathbf{trk}}})$). The distributions of the two variables are shown in Figure 4.8. For the reconstructed Higgs mass $m_{j_1 j_2}$ or m_H, there is a peak for the signal sample at around 120 GeV, while the background distribution is flat. Similarly, for $\Delta R(\vec{j_1}, \vec{j_2})$, the ΔR of the two jets from the Higgs boson in the signal tend to have a Gaussian distribution, whereas the background ΔR distribution is roughly flat. More details about the MVA variable ranking are discussed in [183].

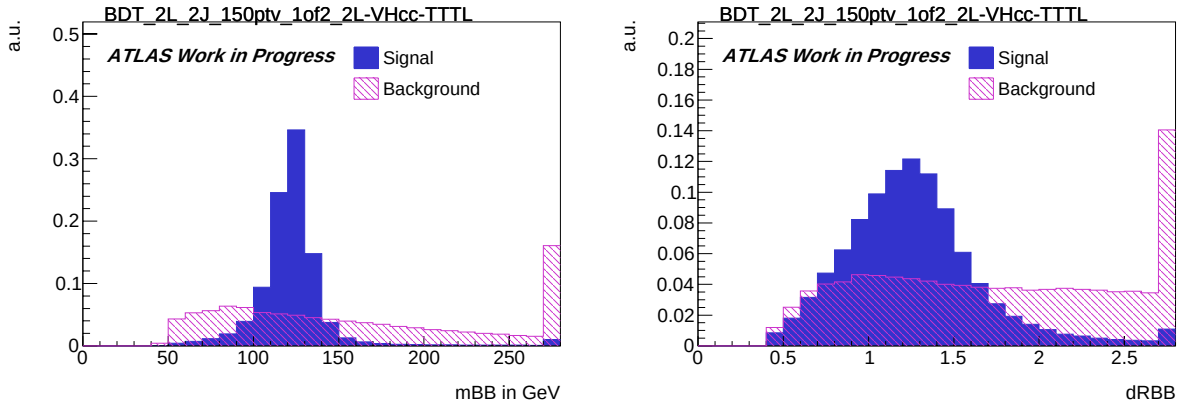

Figure 4.8: The $m_{j_1 j_2}$ and $\Delta R(\vec{j_1}, \vec{j_2})$ distribution in the $VH(\to c\bar{c})$ 2-lepton 2-jet training with $p_T^V > 150$ GeV for the 2tt+2lt regions [183]. Both the signal and the background distributions are normalized to unity and the last bin contains the overflow events.

4.3.2 MVA configuration and performance

Figure 4.9 shows that the final BDT output separates the signal and the background events in the $VH(\to c\bar{c})$ 2-lepton channel for the 2xt-tag, 2-jet, and $p_T^V > 150$ GeV region. The signal events have high BDT output scores near one, while the background events tend to have low BDT scores near -1. Other signal regions have similar MVA performance. In addition, over-training is checked by comparing the ROC (receiver operating characteristic) curves for the training (purple line) and test (pink dash line) data. The training and test data are assigned using even and odd events. At different signal efficiencies, the training and test data have similar values for 1-(background efficiency).

The default MVA binning is equidistant and fine with around 500 bins. The default binning does not have good sensitivities in the likelihood fit. Therefore, the binning of the BDT distributions is transformed to ensure $Z > 1$ in all bins before being used in the likelihood fit. The parameter Z is defined as follows:

$$Z = z_s \frac{n_s}{N_s} + z_b \frac{n_b}{N_b}. \tag{4.8}$$

Here, N_s and N_b are the total number of signal and background events respectively. The parameters n_s and n_b are the number of signals and background events in a certain bin. The transformation starts with 500 bins in the BDT distribution. The bins are merged from the highest to the lowest BDT output score until $Z > 1$. In addition, $n_s + n_b$ in a certain bin is required to be ≥ 3 to avoid empty bins.

The tunable parameters z_s and z_b reflect the number of desired bins with mostly signal events at high BDT scores and bins with mostly background events at low BDT scores. The parameters z_s and z_b are optimized in each analysis region to have fewer bins in regions with

fewer events and more bins in regions with more events. For example, in the $VH(\to c\bar{c})$ p_T^V > 250 GeV and 2tt-tag regions, $z_s = 2$ and $z_b = 2$, while $z_s = 5$ and $z_b = 3$ in the $VH(\to c\bar{c})$ $p_T^V > 250$ GeV and 2xt-tag regions.

The final BDT distribution before and after the re-binning is shown in Figure 4.10. The total number of bins in each region varies from 4 to 15. The significance of the BDT output can be approximated using [184]:

$$S = \sqrt{\sum_i 2\left[(s_i + b_i)\ln\left(1 + \frac{s_i}{b_i}\right) - s_i\right]} \tag{4.9}$$

Example MVA training hyperparameters are shown in Table 4.14 for $VH(\to c\bar{c})$. The hyperparameters are optimized per training channel by scanning parameters such as the number of trees, maximum depth, and minimum node size [183]. The number of trees refers to the number of decision trees to be trained. The maximum depth limits the nodes allowed in one tree. The minimum node size refers to the minimum number of samples required to split a node. Boosting enhances the BDT performance through sequential learning [185]. Most BDT trainings use the gradient boost method. However, in the boosted and $VH(\to c\bar{c})$ 2-lepton 3p-jet training, the adaptive boost method (`Adaboost`) is found to reduce over-training when the signal statistics are low [168].

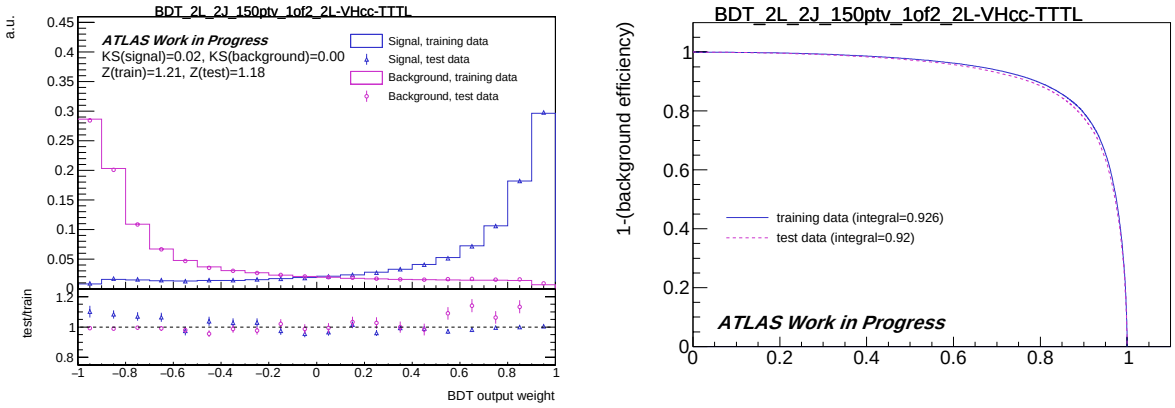

Figure 4.9: The final BDT output distribution (left) and efficiency distribution (right) in the $VH(\to c\bar{c})$ 2-lepton channel for the 2xt-tag, 2-jet and $p_T^V > 150$ GeV regions [168]. The efficiency distribution x-axis shows the signal efficiency from zero to one.

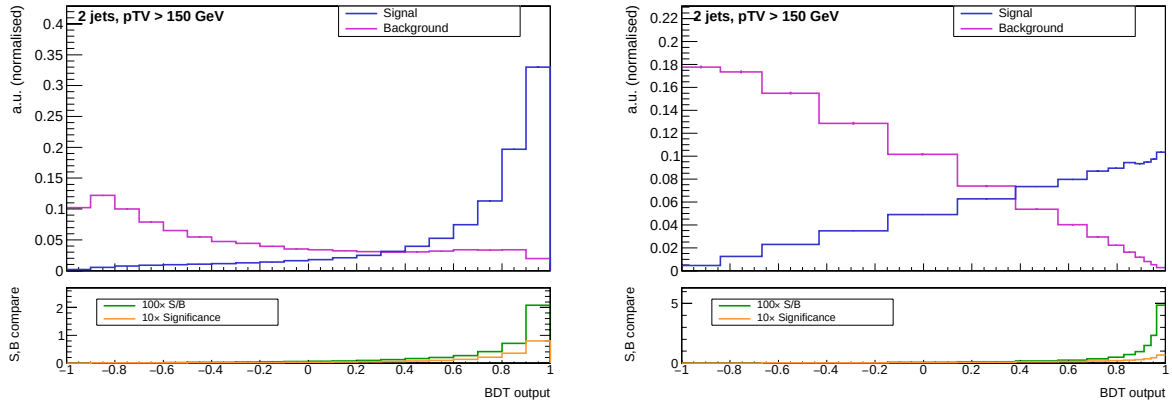

Figure 4.10: The BDT output transformation before (left) and after (right) [168]. The BDT output is shown for the $VH(\to c\bar{c})$ 2-lepton 2-jet, 2xt-tag and $p_T^V > 150$ GeV region.

	$VH(\to c\bar{c})$	
Settings	0-, 1- and most 2-lepton regions	2-leton, 3pJ, low pTV
Boost type	Gradient boost	Adaboost
Number of trees	600	200
Maximum depth	4	4
Learning rate (β)	0.5	0.15
Minimum node size	5%	5%

Table 4.14: Optimized BDT hyperparameters used for the 0-, 1- and 2-lepton channels for the $VH(\to c\bar{c})$ trainings.

4.4 Data and simulated samples

Both data and simulated samples are used in the $VH(\to b\bar{b}, c\bar{c})$ analysis. The data used were collected with the ATLAS detector during Run 2 at $\sqrt{s} = 13$ TeV. There are 140 fb^{-1} of data available [68]. All data events are recorded when the ATLAS detector was functioning correctly [186].

4.4.1 Simulated samples

Various MC generators are used to simulate the signal and background processes. The main components in MC simulations are discussed in Section 2.2.3. Accurate modeling of the

signal and background events and their uncertainties is crucial to determining the sensitivity of the analysis.

Table 4.15 lists the nominal samples of all simulated processes. The second, third and forth columns list the matrix element (ME) generators, parton distribution function (PDF), and parton shower (PS) versions. The listed PDF sets are used only for the ME calculations. For some samples, different PDF sets are used for the parton shower. Except for the Sherpa V+jets and diboson samples, all samples use the EvtGen package to describe the bottom and charm hadron decays along with the PYTHIA parton showering [187].

The last two columns of the table list the cross sections corresponding to each process and the order of the cross-section calculations for QCD or electroweak (EW) processes. NNLO refers to the next-to-next-to leading order and NNLL next-to-next-to leading logarithmic terms. The total number of events in all simulation samples are normalized to the cross sections listed.

During the event generation stage, various filtering techniques are used to enhance the statistics of samples of interest, such as the heavy-flavor jets. More details can be found in [188].

Data and nominal simulated samples are used in the event selection and the multivariate analysis. In addition to the nominal generators listed in Table 4.15, variations from the nominal generators are produced to assess the modeling uncertainties of the nominal samples. For the final statistical analysis, the nominal simulated samples are used as templates to fit the data, while the modeling uncertainties are added as nuisance parameters. Details of the samples used are discussed in Sections 4.4.1.1-4.4.1.5 for the signal process, V+jets, $t\bar{t}$, single top, and diboson.

The multi-jet background is negligible in the 0-lepton and 2-lepton channels and is not discussed in detail in this thesis. In the 1-lepton channel, a data-driven method is developed to estimate the multi-jet contribution and its uncertainties. The multijet template is derived from a region enriched with QCD events. The simulation cannot model this background well due to the limited sample size and the difficulties in modeling fake leptons.

Process	Matrix Element	PDF Set (ME)	Parton Shower	Tune	σ order	$\sigma\times$ Br [pb]
$qq \to WH \to \ell\nu b\bar{b}$	PowHeg-Box v2 + GoSam + MiNLO	NNPDF3.0NLO	Pythia-8.245	AZNLO	NNLO(QCD)+ NLO(EW)	2.69×10^{-1}
$qq \to ZH \to \nu\nu b\bar{b}$	PowHeg-Box v2 + GoSam + MiNLO	NNPDF3.0NLO	Pythia-8.245	AZNLO	NNLO(QCD)+ NLO(EW)	8.91×10^{-2}
$qq \to ZH \to \ell\ell b\bar{b}$	PowHeg-Box v2 + GoSam + MiNLO	NNPDF3.0NLO	Pythia-8.245	AZNLO	NNLO (QCD)+NLO(EW)	4.48×10^{-2}
$gg \to ZH \to \nu\nu b\bar{b}$	PowHeg-Box v2	NNPDF3.0NLO	Pythia-8.307	AZNLO	NLO+NLL	1.43×10^{-2}
$gg \to ZH \to \ell\ell b\bar{b}$	PowHeg-Box v2	NNPDF3.0NLO	Pythia-8.307	AZNLO	NLO+NLL	7.23×10^{-3}
$qq \to WH \to \ell\nu c\bar{c}$	PowHeg-Box v2 + GoSam + MiNLO	NNPDF3.0NLO	Pythia-8.245	AZNLO	NNLO(QCD)+ NLO(EW)	1.34×10^{-2}
$qq \to ZH \to \nu\nu c\bar{c}$	PowHeg-Box v2 + GoSam + MiNLO	NNPDF3.0NLO	Pythia-8.245	AZNLO	NNLO(QCD)+ NLO(EW)	4.42×10^{-3}
$qq \to ZH \to \ell\ell c\bar{c}$	PowHeg-Box v2 + GoSam + MiNLO	NNPDF3.0NLO	Pythia-8.245	AZNLO	NNLO (QCD)+NLO(EW)	2.23×10^{-3}
$gg \to ZH \to \nu\nu c\bar{c}$	PowHeg-Box v2	NNPDF3.0NLO	Pythia-8.307	AZNLO	NLO+NLL	7.10×10^{-4}
$gg \to ZH \to \ell\ell c\bar{c}$	PowHeg-Box v2	NNPDF3.0NLO	Pythia-8.307	AZNLO	NLO+NLL	3.59×10^{-4}
$Z \to \nu\nu$ + jets	Sherpa 2.2.11	NNPDF3.0nnlo	Sherpa 2.2.11	-	NNLO	416.05
$W \to \ell\nu$ + jets	Sherpa 2.2.11	NNPDF3.0nnlo	Sherpa 2.2.11	-	NNLO	60242
$Z \to \ell\ell$ + jets	Sherpa 2.2.11	NNPDF3.0nnlo	Sherpa 2.2.11	-	NNLO	6201
$t\bar{t}$	Powheg-Box v2	NNPDF3.0NLO	Pythia-8.230	A14	NNLO+NNLL	832
single-top (s)	Powheg-Box v2	NNPDF3.0NLO	Pythia-8.230	A14	NLO	3.35
single-top (t)	Powheg-Box v2	NNPDF3.0NLO	Pythia-8.230	A14	NLO	70.7
single-top (Wt)	Powheg-Box v2	NNPDF3.0NLO	Pythia-8.230	A14	Approx. NNLO	71.7
$qq \to WW$	Sherpa 2.2.11	NNPDF3.0nnlo	Sherpa 2.2.11	-	NLO	47.93
$qq \to WZ$	Sherpa 2.2.11	NNPDF3.0nnlo	Sherpa 2.2.11	-	NLO	20.85
$qq \to ZZ$	Sherpa 2.2.11	NNPDF3.0nnlo	Sherpa 2.2.11	-	NLO	6.33
$gg \to VV$	Sherpa 2.2.2	NNPDF3.0nnlo	Sherpa 2.2.2	-	NLO	2.78

Table 4.15: The nominal Monte Carlo samples used in the $VH(\to b\bar{b}, c\bar{c})$ analysis.

4.4.1.1 Signal

As shown in Table 4.15, there are 10 signal samples for $VH(\to b\bar{b})$ and $VH(\to c\bar{c})$ in different vector boson decay channels (0-lepton, 1-lepton, 2-lepton) from quark-initiated and gluon-initiated Higgs-strahlung events. Both WH and ZH events can be qq-initiated, while only the ZH events can be gg-initiated [189, 190]. Gluon-induced quark-loop WH processes are absent due to charge conservation. Examples of the quark-initiated and gluon-initiated Higgs-strahlung Feynman diagrams are shown in Figure 4.11.

As shown in Table 4.15, all qq-initiated Higgs-strahlung events, $qq \to ZH$ and $qq \to WH$, are simulated using the POWHEG generator [57]. MiNLO (Multiscale Improved NLO) is used for the choice of scales and the inclusion of Sudakov form factors [57]. The computation of the one-loop amplitudes is performed with the GoSam automated software [191]. POWHEG is interfaced to the PYTHIA MC generator (PYTHIA8.245 for the quark-induced processes, PYTHIA8.307 for the gluon-induced processes) for modeling parton shower (PS), hadronization, underlying event (UE) and multiple parton interactions (MPI) [192, 58]. The AZNLO tune is applied to POWHEG+PYTHIA [193]. The NNPDF3.0NLO PDF is used [194]. Additional electroweak corrections at NLO are applied to the qq-initiated processes using HAWK [195].

The signal cross sections are calculated for $m_H = 125$ GeV at NNLO QCD and NLO

electroweak (EW) accuracies [196, 28].

The gg-initiated quark-loop ZH events, $gg \to ZH$, are simulated similarly to the qq-initiated events, as shown in Table 4.15. The leading-order (LO) POWHEG is interfaced with PYTHIA.

Variations from the nominal sample In order to assess modeling uncertainties for the signal process, the nominal samples are compared to the following variations:

- POWHEG+HERWIG: these samples are used to assess the parton shower uncertainties as HERWIG7 is used to generate the parton shower instead of PYTHIA [197].
- **Final state radiation (FSR) variation**: the renormalization scale μ_r and the factorization scale μ_r take different values ($\pm$ 2 around the nominal value used in POWHEG and PYTHIA).

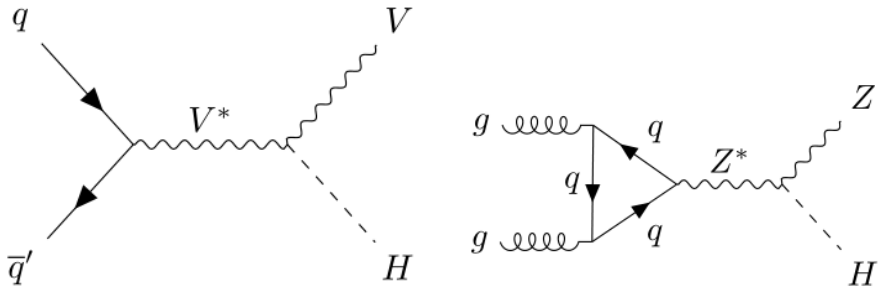

Figure 4.11: The lowest order Feynman diagrams of the $qq \to$VH and $gg \to$ZH processes.

4.4.1.2 V+jets

The production of V (V = W or Z) bosons in association with jets is one of the main backgrounds in $VH(\to b\bar{b}, c\bar{c})$. The tree-level Feynman diagrams of V+jets are shown in Figure 4.12. A vector boson is created along with two quarks. In the left plot, a vector boson and a gluon are produced when the two quarks scatter. The gluon radiates into two quarks subsequently. In the right plot, four quarks are emitted from the incoming gluons. Two intermediate quarks annihilate to create a vector boson.

The V+jets processes are simulated with SHERPA2.2.11 [56, 188]. The built-in Hessian NNPDF3.0nnlo PDF set is used [194, 198]. In SHERPA 2.2.11, Comix calculates NLO-accurate matrix elements for up to two jets and LO-accurate matrix elements for up to five jets [199]. The b- and c-quarks are treated as massless at the matrix-element level and massive in the parton shower. In SHERPA, the invariant mass of the charged leptons is

required to be larger than 40 GeV for Z+jets, while the invariant mass of the charged lepton plus neutrino is required to be larger than 2 GeV for W+jets final states.

The NLO matrix elements of a given jet multiplicity are matched to the parton shower using a color-exact variant of the MC@NLO algorithm [200]. Different jet multiplicities are then merged into an inclusive sample using an improved CKKW matching procedure [201]. It is extended to the NLO parton shower using the MEPS@NLO prescription [202]. The default SHERPA Catani–Seymour dipole parton shower scheme and the cluster hadronization model are used [203, 204].

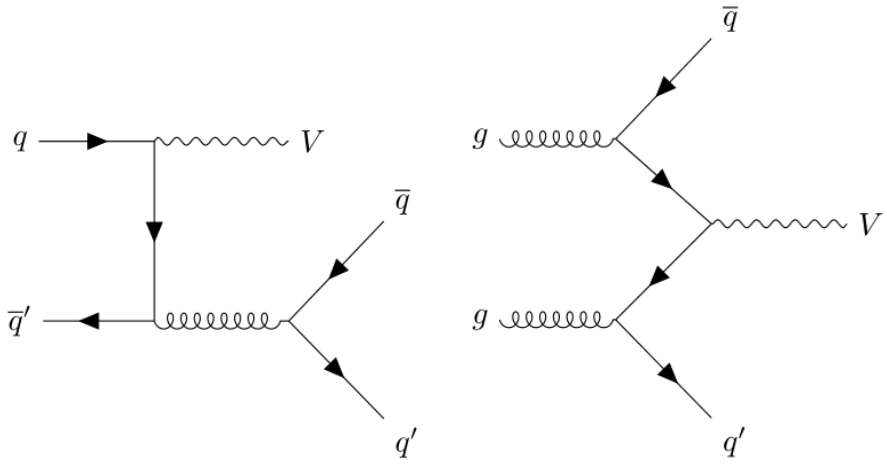

Figure 4.12: Tree-level Feynman diagrams of V+jets processes.

Electroweak corrections NLO EW corrections are available for SHERPA 2.2.11, with three different NLO QCD and NLO EW combination schemes: *additive* (Equation 4.10), *multiplicative* (Equation 4.11), and *exponentiated* (Equation 4.12) [188]. The NLO EW corrections include contributions from virtual loops and real emission of gauge bosons in the Feynman diagrams [188, 205]. The cross sections for a 2→n final state with the different combination schemes can be expressed as:

$$\sigma^{NLO}_{n,QCD+EW} = \sigma_{n,LO} + \Delta\sigma_{n,QCD} + \Delta\sigma_{n,EW} \tag{4.10}$$

$$\sigma^{NLO}_{n,QCD\times EW} = (\sigma_{n,LO} + \Delta\sigma_{n,QCD}) \times (1 + \Delta\sigma_{n,EW}) \tag{4.11}$$

$$\sigma^{NLO}_{n,QCD\times e^{EW}} = (\sigma_{n,LO} + \Delta\sigma_{n,QCD}) \times e^{\Delta\sigma_{n,EW}} \tag{4.12}$$

where $\sigma_{n,LO}$ denotes the Born-level cross-section and $\Delta\sigma_{n,QCD}$ the NLO QCD corrections to the Born process. And, $\Delta\sigma_{n,EW}$ contains the NLO EW corrections.

Figure 4.13 shows the differential cross sections of the V+jets processes with different EW correction schemes. The EW corrections are the largest at high p_T^V, as expected from the EW Sudakov logarithmic form [206]. In addition, the additive scheme has the smallest correction compared to the other schemes. The same trend is observed in the $VH(\rightarrow b\bar{b}, c\bar{c})$ analysis as shown in Figure 4.14. The *additive* scheme is chosen as the new SHERPA V+jets nominal, while the other two schemes are considered as variations for uncertainty calculations.

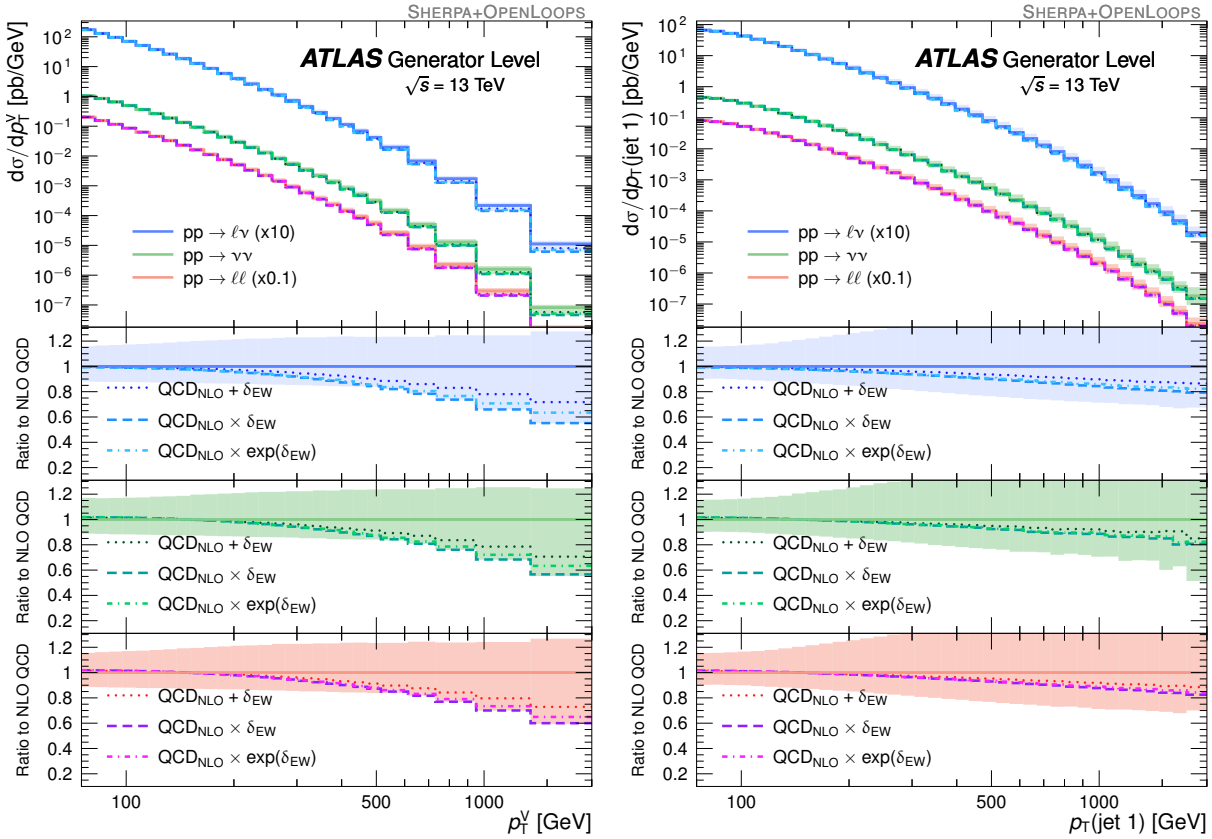

Figure 4.13: Electroweak corrections across p_T^V (left) and p_T of the highest transverse momentum jet (jet 1) (right) [188].

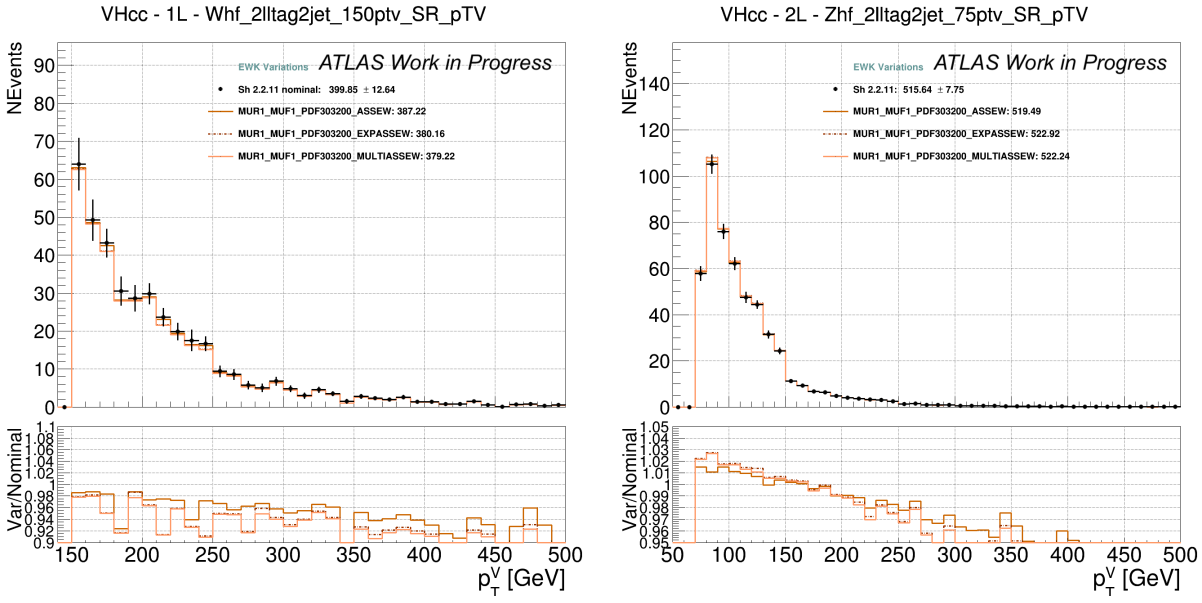

Figure 4.14: Electroweak corrections across p_T^V in $VH(\rightarrow c\bar{c})$ for W+jets (left) and Z+jets (right) [207]. In the legend, ASSEW, EXPASSEW, and MULTIASSEW refer to the *additive*, *multiplicative*, and *exponentiated* schemes respectively. The electroweak corrections are applied to both the matrix elements (ME) and the parton shower (PS).

Variations from the nominal samples There are five different variations to assess the modeling uncertainties of V+jets: the two electroweak corrections, the QCD scale variations, the parton distribution function variations, the alternative samples generated by MADGRAPH and SHERPA 2.2.1. When evaluating the modeling uncertainties, the largest variations from the electroweak corrections, QCD scale variations, and PDF variations respectively are typically considered. More details are discussed in Section 4.5.

- **Two of the three electroweak corrections:** The *multiplicative* and *exponentiated* electroweak corrections are used as variations of the nominal sample, while the *additive* electroweak correction is used as the nominal sample. All three electroweak corrections are presented in Equations 4.10-4.12.

- **QCD scale variations:** SHERPA 2.2.11 events have event weights corresponding to the 7-point variations of the factorization and renormalization scales (μ_f and μ_r). The scales are varied independently by factors of 0.5 and 2 while avoiding cases where μ_r and μ_f move in opposite directions. Figure 4.15 shows the 7-point variations in the analysis for Z+jets. When varying the QCD scales in both the matrix elements and the parton shower, the variations are the largest. However, the template is smoother with the matrix element only variation. As shown in the figure, the variations are

mainly driven by changing μ_r. The uncertainty is approximately 20% for the largest QCD variation across the Higgs mass bins from 50 to 200 GeV.

- **PDF variations:** The PDF variations for the nominal Hessian NNPDF3.0nnlo PDF set are evaluated using the Hessian eigenvector set and ± 0.001 shifts of α_s around the nominal value of 0.118 [188]. The LHAPDF tool combines all Hessian eigenvectors into an envelope and outputs the up and down PDF variations from the envelope [208]. Figure 4.16 shows the up and down PDF variations of the Higgs invariant mass in the $VH(\to b\bar{b}, c\bar{c})$ analysis for W+jets and Z+jets processes. The up and down variations tend to be symmetric. The PDF uncertainty size is small compared to the electroweak corrections and the QCD variations, less than 10% in most bins.

- **MADGRAPH FxFx:** MADGRAPH5_aMC@NLO 2.6.5 generates weak bosons with up to three additional partons at the NLO accuracy in QCD [60]. Showering and subsequent hadronization are performed using PYTHIA 8.240 [58]. The A14 tune is used [209]. The different jet multiplicities are merged using the FxFx NLO matrix element and the parton-shower merging prescription [210]. The FxFx cross sections are normalized to the same inclusive single boson cross sections as the nominal samples in Table 4.15. Figure 4.17 shows the differences between SHERPA 2.2.11 and MADGRAPH FxFx for the W+jets and Z+jets samples. The statistical uncertainties are smaller for the nominal sample due to a larger sample size. The uncertainties from MADGRAPH FxFx are approximately 20% in all bins.

- **SHERPA 2.2.1 p_T^V:** The SHERPA 2.2.11 p_T^V spectrum is different from that obtained from SHERPA 2.2.1, the nominal V+jets generator in the previous analysis [188]. There are several improvements from SHERPA 2.2.1 to SHERPA 2.2.11, such as the QCD accuracy for the matrix element. However, since SHERPA 2.2.1 recovers the data p_T^V spectrum better than SHERPA 2.2.11 in the di-lepton measurements, the SHERPA 2.2.1 V+jets sample is kept as an alternative sample. More details about the modeling uncertainties from SHERPA 2.2.1 are discussed in Section 4.5.

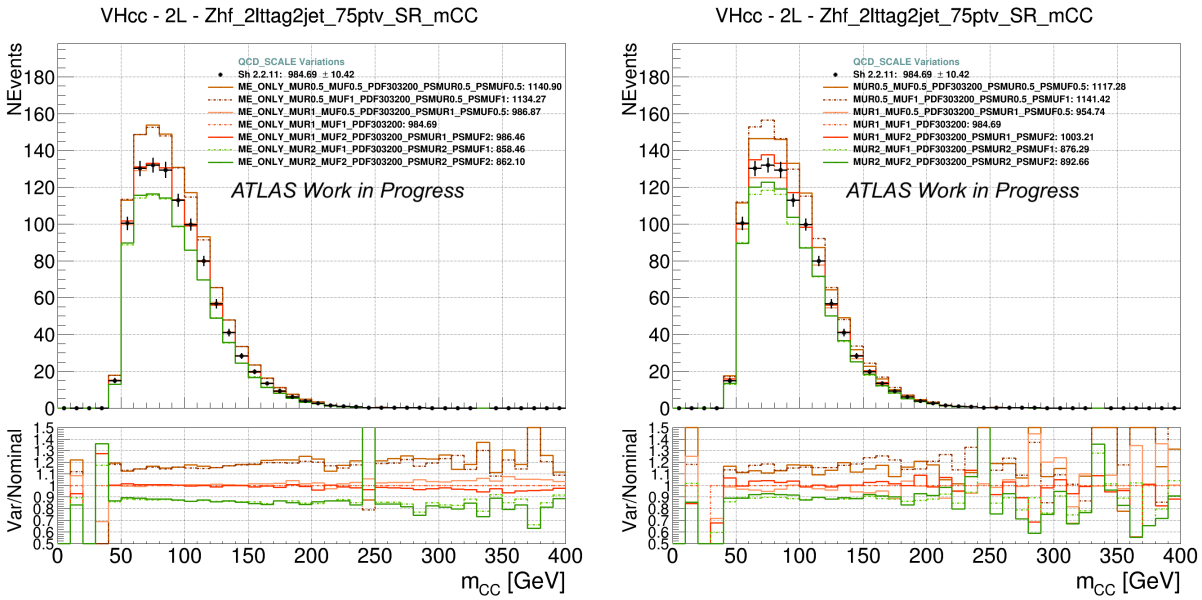

Figure 4.15: QCD variations across the Higgs invariant mass (m_{cc}) in $VH(\rightarrow c\bar{c})$ for the $Z+hf$ process in the 2-lepton 2lt-tag 2-jet signal region for p_T^V above 75 GeV. Six variations of the QCD scales were applied to the matrix elements only (left) and to both the matrix elements and the parton shower (right). The x-axis are in terms of the reconstructed Higgs mass from the two charm quarks, m_{cc}.

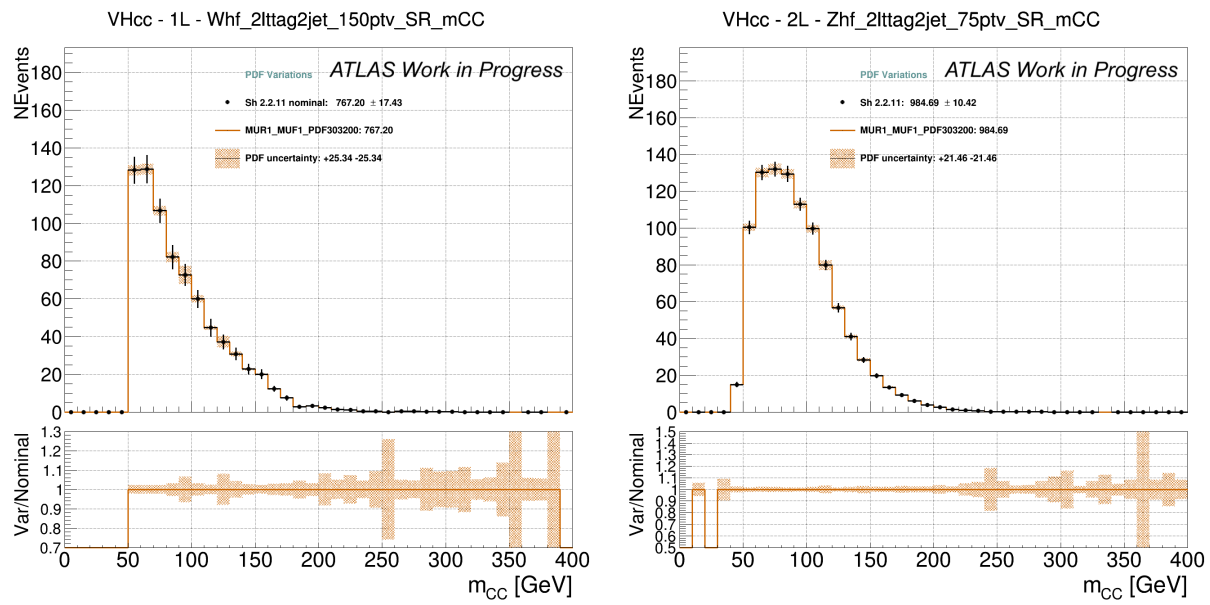

Figure 4.16: PDF up and down variations across the Higgs invariant mass (m_{cc}) in $VH(\rightarrow c\bar{c})$ for the W+jets (left) and Z+jets (right) samples [207].

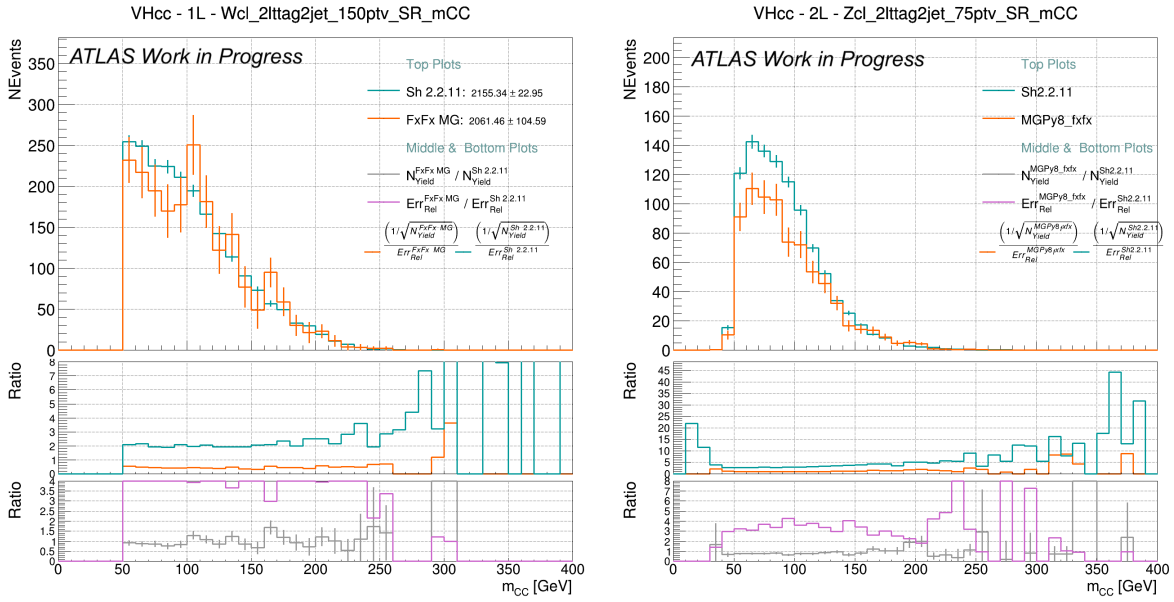

Figure 4.17: SHERPA 2.2.11 and MADGRAPH FxFx in $VH(\rightarrow c\bar{c})$ for W+jets (left) and Z+jets (right) [207]. The middle and bottom panels compare the relative uncertainties between the nominal sample and the alternative sample.

4.4.1.3 Top anti-top

Another important background is the $t\bar{t}$ decays. Example tree-level Feynman diagrams of $t\bar{t}$ decays are shown in Figure 4.18. A pair of top and anti-top quarks are produced from incoming gluons. In the left plot, two gluons annihilate and produce an intermediate gluon that radiates into the $t\bar{t}$ pair. In the right plot, two gluons scatter off, exchange an intermediate quark, and create a top quark and an anti-top quark each.

The $t\bar{t}$ events can be produced through high-energy gluon-gluon collisions. The top quark mostly decays to a W boson and a b quark. In the analysis, $t\bar{t}$ is a major background in 0-lepton and 1-lepton. For example, two b quarks can be tagged as b-jets or c-jets and one of the W bosons can be reconstructed in 0-lepton or 1-lepton.

As shown in Table 4.15, the default simulated sample for the $t\bar{t}$ process is generated with the POWHEG generator using an NLO calculation for the matrix element [211, 212]. PYTHIA 8.230 is used for the parton shower as in the case of the signal sample [192]. The PDF used in the ME calculation is NNPDF3.0 (NLO), while the parton shower utilises NNPDF2.3 (LO) [194]. A14 tune is used [209].

The cross section of producing $t\bar{t}$ events is calculated at NNLO in QCD including the resummation of NNLL soft gluon terms for a top-quark mass of 172.5 GeV [213, 214].

Variations from the nominal samples Similar to the signal and V+jets samples, there are four variations for the $t\bar{t}$ samples to assess the systematic uncertainties.

- **MADGRAPH+PYTHIA (ME)**: MADGRAPH5_aMC@NLO generates hard scattering at NLO precision instead of the nominal POWHEG [60]. This assesses the hard scattering generation uncertainties.
- **POWHEG+HERWIG (PS)**: HERWIG 7.04 generates the parton shower instead of the nominal PYTHIA [197, 59].
- **Initial state radiation (ISR) variation**: both μ_r and μ_f are varied and an A14 tuning variation is used to assess the ISR uncertainties [215]. There are two ISR variations: *RadHiPrime* and *RadLo*.
- **Final state radiation (FSR) variation**: μ_r is doubled or halved compared to the nominal value.

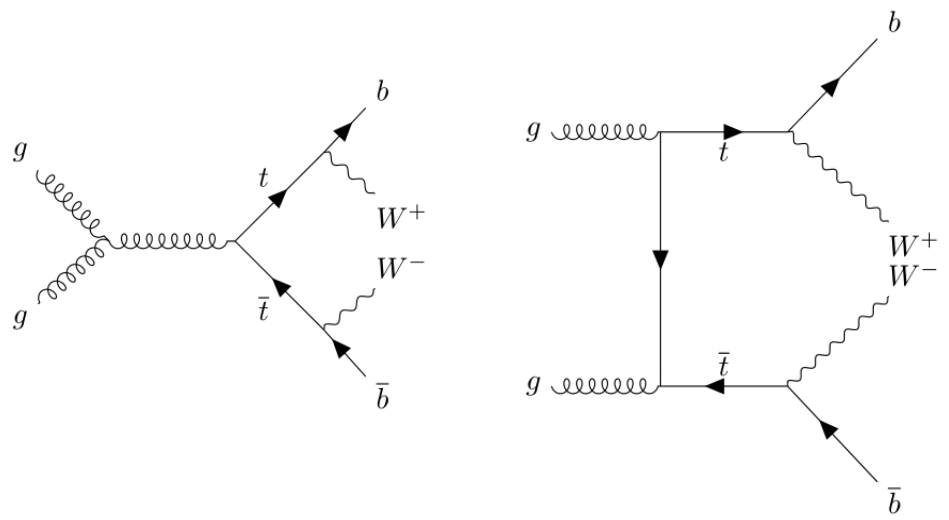

Figure 4.18: Tree-level $t\bar{t}$ Feynman diagrams.

4.4.1.4 Single top quark

The single top-quark production is a relatively minor background. Three single-top channels are generated separately: s-channel, t-channel, and Wt-channel. Example tree-level Feynman diagrams of the three single-top channels are shown in Figure 4.19.

Similar to the $t\bar{t}$ samples, POWHEG is used at the NLO accuracy for calculating the matrix element [212, 216, 217].

The cross-sections of the t- and s-channels are calculated at NLO while the cross-section of the Wt-channel is computed at NNLO [218, 219, 220]. The top mass used in the calculation is 172.5 GeV.

One particular issue of the Wt sample is that: at higher order, the definition of the Wt process can correspond to the leading order $t\bar{t}$ process [221, 222]. There are two approaches to resolve the overlap between the two samples:

- **Diagram subtraction (DS):** subtract local $t\bar{t}$ contribution from the NLO Wt cross section.
- **Diagram removal (DR):** remove all diagrams in the NLO Wt amplitudes that are doubly resonant.

The DS scheme is chosen as the nominal Wt sample, while the DR scheme is used as an alternative sample to assess the modeling uncertainties in the $t\bar{t}$ interference.

Variations from the nominal samples In addition to the DR scheme, similar to the variations used for the $t\bar{t}$ samples, four variations for the single-top processes are generated.

The variations are only generated for the t- and Wt-channels. The uncertainties of the s-channel is negligible.

- **MADGRAPH+PYTHIA (ME)**: MADGRAPH5_aMC@NLO
- **POWHEG+HERWIG (PS)**: HERWIG 7.04
- **Initial state radiation (ISR) variation**: RadHiPrime and RadLo.
- **Final state radiation (FSR) variation**: μ_r is doubled or halved compared to the nominal value.

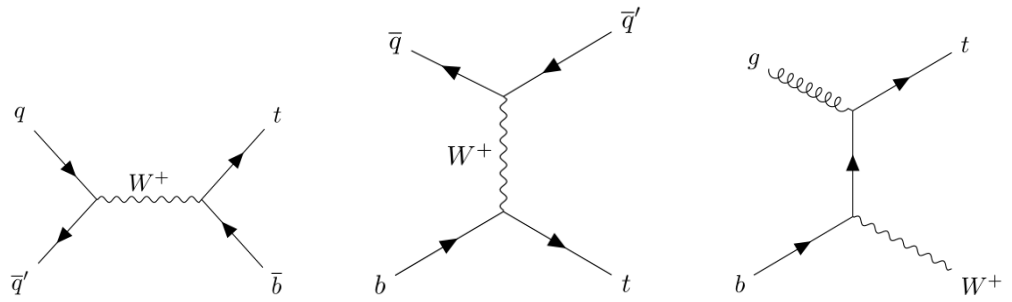

Figure 4.19: Tree-level single-top Feynman diagrams: s-channel (left), t-channel (center), Wt-channel (right).

4.4.1.5 Diboson

As shown in Table 4.15, there are four diboson samples. The quark-initiated $qqWW$, $qqWZ$ and $qqZZ$ samples and the gluon-initiated $ggVV$ processes are generated separately. The diboson processes are also a relatively minor background. However, the $VZ(\rightarrow b\bar{b}, c\bar{c})$ diboson processes resemble the signal $VH(\rightarrow b\bar{b}, c\bar{c})$ processes. The reconstructed Z boson mass from a pair of bottom or charm quarks has a peak similar to the reconstructed Higgs mass. Therefore, the $VZ(\rightarrow b\bar{b}, c\bar{c})$ processes are also used as signals in the diboson analysis validation. Here, the VZ process refers to the combination of qqWZ, qqZZ, ggWZ, and ggZZ samples. Example tree-level Feynman diagrams of the quark-initiated diboson processes are shown in Figure 4.20.

Similar to the V+jets samples, the quark-initiated diboson samples are generated using SHERPA 2.2.11. And, the *additive* scheme of the electroweak corrections (Equation 4.10) is used as the nominal sample. Gluon-initiated diboson processes are generated with SHERPA 2.2.2.

Variations from the nominal samples Similar to V+jets, there are four types of variations. In the case of the diboson samples, the PDF variations introduce negligible modeling uncertainties.

- **Two of the three electroweak corrections:** the *multiplicative* and *exponentiated* electroweak corrections.
- **QCD scale variations:** 7-point variations of the factorization and renormalization scales.
- **POWHEG+PYTHIA:** Instead of the MADGRAPH FxFx samples, the alternative diboson samples are generated using POWHEG for calculating the matrix elements and PYTHIA for generating the parton shower.
- **SHERPA 2.2.1:** The reconstructed Higgs mass peak shifts between the SHERPA 2.2.1 and 2.2.11 samples due to changes in the heavy flavor fragmentation function [168]. Therefore, the SHERPA 2.2.1 diboson sample is included as an alternative sample to assess the systematics from fragmentation. In addition, given the p_T^V spectrum differences observed in V+jets, it is recommended to include SHERPA 2.2.1 for potential p_T^V mismodeling in diboson as well.

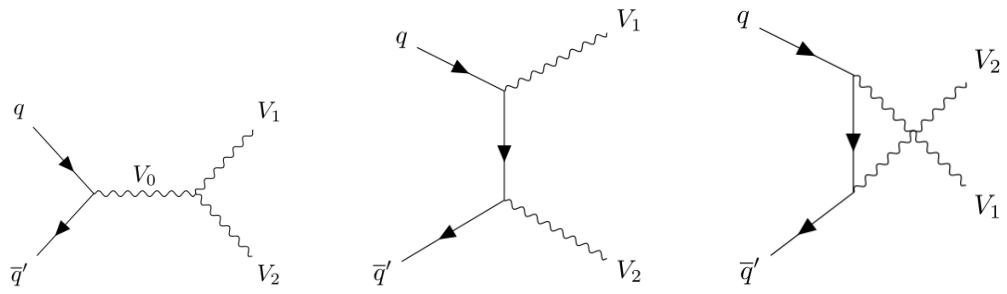

Figure 4.20: Diboson Feynman diagrams: s-channel (left), t-channel (center), u-channel (right).

4.5 Signal and background modeling

After all regions are specified and all MVA values derived, signal and background modeling uncertainties need to be assessed for the nominal samples using the alternative samples introduced in Section 4.4. The modeling uncertainty is an important piece in the final statistical analysis. The modeling uncertainties estimate how accurate the simulation is according to existing knowledge of the SM and thus indicate how to adjust the simulation according to data in the final statistical analysis.

The modeling uncertainties are assessed in three categories:

- **Normalization uncertainties:** address uncertainties for simulation yields in an inclusive region;
- **Acceptance ratio uncertainties:** address uncertainties for simulation yield ratios between two regions;
- **Shape uncertainties:** address uncertainties for simulation kinematic distribution in all regions;

The signal modeling uncertainty is first introduced. The uncertainties of the background samples are discussed in Sections 4.5.1-4.5.3.

Signal modeling The signal modeling considers all three kinds of uncertainties: normalization, acceptance ratio, and shape. The signal strengths $\mu_{VH(c\bar{c})}$ and $\mu_{VH(b\bar{b})}$ are floated in the fit and defined as follows:

$$\mu_{VH(c\bar{c})} = \frac{[\sigma_{VH} \times \mathrm{BR}(H \to c\bar{c})]_{\mathrm{measured}}}{[\sigma_{VH} \times \mathrm{BR}(H \to c\bar{c})]_{\mathrm{SM}}} \tag{4.13}$$

$$\mu_{VH(b\bar{b})} = \frac{[\sigma_{VH} \times \mathrm{BR}(H \to b\bar{b})]_{\mathrm{measured}}}{[\sigma_{VH} \times \mathrm{BR}(H \to b\bar{b})]_{\mathrm{SM}}} \tag{4.14}$$

The normalization uncertainties include uncertainties in the cross section of VH production and in the branching ratios of $H \to c\bar{c}$ and $H \to b\bar{b}$ [223, 224]. In addition, the uncertainties from the NLO electroweak corrections, PDF, and α_s are also included in the normalization uncertainties. Acceptance ratio uncertainties are included to account for different yield ratios between jet categories and lepton channels. The acceptance ratio uncertainties include contributions from the QCD scale variations and the POWHEG+HERWIG alternative sample.

Shape uncertainties include contributions from the QCD scale variations and POWHEG+HERWIG. Shape uncertainties from NLO electroweak corrections, PDF, and α_s are negligible. All normalization, acceptance ratio, and shape uncertainties are included separately for the $qq \to WH$, $qq \to ZH$, and $gg \to ZH$ samples. The signal samples are introduced in Section 4.4.1.1.

4.5.1 Normalization uncertainties

There are two types of normalization uncertainties: free floating normalization and fixed normalization uncertainties. The normalization is usually left to free float in the fit when the background statistics are large and dedicated control regions are implemented to constrain the backgrounds.

The fixed normalization uncertainties are calculated by comparing the nominal and alternative samples. The fixed normalization uncertainties are used when there are no control

regions to constrain the normalization or when the sample is small and the uncertainties have a small impact on the fit.

Resolved $VH(\to b\bar{b}, c\bar{c})$

- **Z+jets:** Z+jets is the main background in the 2-lepton and 0-lepton channels and negligible in 1-lepton. The Z+jets samples are categorized using the truth jet flavors that are used to reconstruct the Higgs candidates. Thus, the Z+jets sample is divided into six categories: $Z + bb$, $Z + cc$, $Z + bl$, $Z + cl$, $Z + bc$, and $Z + lf$. Categories with similar kinematic signatures are grouped together in the fit and for the modeling uncertainty calculations:
  - $Z + hf$ (heavy-flavor jets): Z+bb, Z+cc
  - $Z + mf$ (mixed-flavor jets): Z+bl, Z+cl, Z+bc
  - $Z + lf$ (light-flavor jets)

  The $Z+hf$, $Z+mf$, and $Z+lf$ samples are floated freely in the fit with decorrelation in n-jet and p_T^V in 2-lepton and 0-lepton in the resolved phase space. Decorrelation means that the floating normalizations can change independently in different n-jet and p_T^V categories. More details about the decorrelation scheme of all Z+jets nuisance parameters are discussed in Section 4.6.2.

- **W+jets:** W+jets is the main background in the 1-lepton and 0-lepton channels and negligible in 2-lepton. The W+jets samples with hadronically decayed τ-leptons contribute to the background in 0-lepton when the τ-leptons are not identified correctly. Similar to the Z+jets background, the W+jets samples are grouped into categories in the fit and for the modeling uncertainty calculations:
  - $W + hf$: W+bb, W+cc
  - $W + mf$: W+bl, W+cl, W+bc, W+bτ, W+cτ
  - $W + lf$: W+l, W+lτ

  The floating normalization for the $W+hf$, $W+mf$, and $W+lf$ processes is decorrelated in n-jet and p_T^V.

- **Top:** Top processes are the main background in the 1-lepton and 0-lepton channels. The $t\bar{t}$ and the single-top Wt channel are grouped together as a *top* process. The top backgrounds are further categorized according to the truth flavor compositions of the Higgs candidate jets in the resolved phase for 0-lepton and 1-lepton.
  - *top(bb)*
  - *top(bq/qq)*: bq includes bc+bl and qq includes cc+cl+ll

The top(bb) component is separated from the rest as the resolved $VH(\to b\bar{b})$ top background is dominated by top(bb). In the $VH(\to c\bar{c})$ phase space, the top background is dominated by top(bq/qq). In the resolved 2-lepton phase space, the top(bb) and top(bq/qq) categories are grouped together.

Floating normalizations for the top(bb) and top(bq/qq) processes are decorrelated in n-jet and p_T^V in the resolved 0-lepton and 1-lepton channels. The remaining single-top s- and t-channels have fixed normalization uncertainties of 5% and 17%. In the 2-lepton channel, as discussed in Section 4.2.3, the $VH(\to c\bar{c})$ top process is left free floating, constrained by the top-$e\mu$ control region. The $VH(\to b\bar{b})$ data-driven top template has a fixed uncertainty of 0.8%.

- **Diboson:** fixed normalization uncertainties are assigned to the qqZZ (17%), qqWW (16%), qqWZ (19%), and ggVV (30%) samples in all lepton channels.

Boosted $VH(\to b\bar{b})$ The boosted $VH(\to b\bar{b})$ normalization uncertainties are assigned differently from the resolved phase space, as there are fewer events in the boosted region. The grouping of individual background processes is also different in some cases.

- **Z+jets:** fixed normalization uncertainties are assigned to the $Z + mf$ (35%) and the $Z + lf$ (35%) processes in all lepton channels. The $Z + hf$ process is the dominant component and left free floating in the 2-lepton and 0-lepton channels.
- **W+jets:** fixed normalization uncertainties are assigned to the $W + mf$ (36%) and $W + lf$ (38%) processes in all lepton channels. The $W + hf$ process is the dominant component and left free floating in the 1-lepton and 0-lepton channels.
- **Top:** the top component ($t\bar{t}$ and single-top Wt) is left free floating in the 0-lepton and 1-lepton channels. In 2-lepton, a 20% normalization uncertainty is assigned. For the single-top s- and t-channels, fixed normalization uncertainties are 5% and 10%.
- **Diboson:** fixed normalization uncertainties are assigned to the qqZZ (17%) and qqWZ (27%) samples in all lepton channels.

The flavor composition for the Z+jets and W+jets processes in the signal regions is shown in Tables 4.16-4.17. For the Z+jets background, the $Z + hf$ component is dominated by the $Z + cc$ process, $Z + mf$ $Z + cl$ in the $VH(\to c\bar{c})$ phase space. The 1nt-tag regions have large $Z + mf$ contribution, while the 2tt-tag regions have large $Z + hf$ contribution.

Similarly for the W+jets background, the $W + hf$ process is dominated by $W + cc$ in the $VH(\to c\bar{c})$ phase space and $W + bb$ in $VH(\to b\bar{b})$. The $W + mf$ process is dominated by $W + cl$ in the $VH(\to c\bar{c})$ phase space. The $W + mf$ and $W + lf$ components have small contribution in $VH(\to b\bar{b})$ due to good flavor tagging rejections of c-jets and l-jets for b-jets.

The top process flavor composition is discussed in [207]. In the $VH(\to c\bar{c})$ 1-lepton channel, the top(bq/qq) component has large top(bc) contribution in the 2xt-tag signal regions and large top(bl) contribution in the 1nt-tag signal regions.

SR Sh2211, $p_T^V > 150$		1nttag		2lttag		2tttag	
Channel	Process	2jet	3pjet	2jet	3pjet	2jet	3pjet
2L	Z+bb	0.6%	0.5%	3.1%	2.4%	2.8%	2.6%
	Z+bc	0.5%	0.5%	2.5%	2.2%	3.5%	3.0%
	Z+bl	7.1%	6.0%	5.1%	4.7%	1.9%	1.9%
	Z+cc	8.8%	9.3%	33.4%	29.7%	73.5%	70.6%
	Z+cl	54.3%	52.6%	37.0%	39.8%	14.2%	16.6%
	Z+l	28.7%	31.1%	19.0%	21.2%	4.1%	5.4%
0L	Zbb	0.5%	0.5%	2.7%	2.5%	2.8%	2.6%
	Z+bc	0.5%	0.4%	2.3%	2.0%	2.8%	2.6%
	Z+bl	6.2%	5.7%	4.8%	4.5%	1.7%	1.5%
	Z+cc	8.7%	9.5%	34.1%	33.0%	74.2%	74.5%
	Z+cl	54.2%	52.8%	37.5%	38.8%	14.2%	14.6%
	Z+l	30.0%	31.0%	18.7%	19.1%	4.3%	4.1%

Table 4.16: Fractions of the individual Z+jets flavor components in the $VH(\to c\bar{c})$ signal regions in the $p_T^V > 150$ GeV category of the 2-lepton and 0-lepton channels. The fractions are calculated from the nominal SHERPA 2.2.11 Z+jets samples. The normalization uncertainties of each component are assessed through the flavor acceptance ratio uncertainties discussed in Section 4.5.2 and are not presented in this table.

SR, Sh2.2.11 $p_T^V > 150$ GeV		1nttag		2lttag		2tttag		2bbtag	
Channel	Process	2jet	3jet	2jet	3jet	2jet	3jet	2jet	3jet
0L	$W+bb$	0.2%	0.2%	1.1%	1.2%	1.3%	1.1%	90.7%	91.1%
	$W+bc$	0.2%	0.2%	1.1%	1.1%	1.3%	0.6%	3.8%	3.8%
	$W+bl$	2.1%	2.4%	1.8%	1.9%	0.7%	1.3%	1.4%	1.3%
	$W+b\tau$	0.0%	0.0%	0.1%	0.0%	0.1%	0.0%	-	-
	$W+cc$	4.8%	5.9%	19.8%	21.4%	60.6%	63.9%	3.0%	2.9%
	$W+cl$	55.2%	54.3%	44.9%	43.7%	25.4%	21.3%	1.0%	0.8%
	$W+c\tau$	0.9%	0.6%	2.7%	2.3%	2.9%	2.7%	-	-
	$W+l$	31.7%	31.7%	23.4%	24.6%	5.9%	7.7%	0.2%	0.1%
	$W+l\tau$	4.9%	4.6%	5.1%	3.7%	1.6%	1.3%	-	-
1L	$W+bb$	0.2%	0.2%	1.1%	1.2%	1.6%	1.5%	86.8%	88.3%
	$W+bc$	0.3%	0.3%	1.8%	1.6%	2.2%	2.5%	6.7%	5.8%
	$W+bl$	1.5%	1.9%	1.6%	1.9%	0.9%	0.9%	1.2%	1.2%
	$W+cc$	5.1%	5.9%	21.9%	23.9%	63.5%	63.5%	3.8%	3.5%
	$W+cl$	70.3%	67.6%	56.6%	52.3%	26.5%	25.4%	1.3%	1.1%
	$W+l$	22.6%	24.0%	17.0%	19.0%	5.3%	6.1%	0.1%	0.1%

Table 4.17: Fractions of the individual W+jets flavor components in the signal region in the $p_T^V > 150$ GeV category of the 0-lepton and 1-lepton channels.

4.5.2 Acceptance ratio uncertainties

As discussed in the previous section, when the background components are floated freely, templates in different regions are assigned one floating norm to change their normalization. For example, the Z+jets floating normalizations are only decorrelated in n-jet and p_T^V. The same floating normalizations are used for regions across tagging categories, lepton channels, and signal and control regions. The *acceptance ratio uncertainties* thus account for the possible change in the distribution of events across different regions in the analysis. The acceptance ratio uncertainties are calculated as double ratios:

$$\sqrt{\sum_i \left(\frac{\left(\frac{n_1}{n_2}\right)_{variation(i)}}{\left(\frac{n_1}{n_2}\right)_{nominal}} - 1 \right)} \tag{4.15}$$

The number of events in the two regions are denoted n_2 and n_1. The second region with n_2 events tends to have higher background purity and thus n_2 is the denominator in the acceptance ratio. The first region with n_1 events is where the acceptance ratio uncertainty is assigned and n_1 is the numerator in the ratio. As the acceptance ratio uncertainty is assigned to n_1, the uncertainty is extrapolated from n_2 to n_1.

Variation(i) refers to the variations from the nominal samples as discussed in Section 4.4. The final acceptance ratio uncertainties for region n_1 from region n_2 sum over all variations in quadrature. All variations for the acceptance ratio uncertainties for different background processes are listed in Table 4.18.

Depending on whether the background templates are floated together or whether the normalization uncertainties are inclusively assigned, the acceptance ratio uncertainties are calculated for the background processes.

The acceptance ratio uncertainties are calculated as inclusively as possible to minimize the number of nuisance parameters in the fit. For example, one acceptance ratio uncertainty is derived inclusively in all signal regions + ΔR control regions, lepton channels, n-jet, and p_T^V regions. However, when regions have large deviations from the inclusive uncertainty, the uncertainties are calculated individually in the regions. In the resolved phase space, the uncertainties are compared between the $VH(\rightarrow b\bar{b})$ and $VH(\rightarrow c\bar{c})$ phase spaces. In most cases, the same uncertainties are used in resolved $VH(\rightarrow b\bar{b}, c\bar{c})$. For Z+jets, W+jets, and diboson samples, the acceptance ratio uncertainties are usually calculated for different flavors such as $Z + hf$, $Z + mf$, and $Z + lf$ using the most dominant component such as $Z + cc$ (for $Z + hf$) and $Z + cl$ (for $Z + mf$).

Sample	Nominal samples	Sources of uncertainties
V+jets	SHERPA2.2.11	MADGRAPHFxFx Max of the 7-point QCD scale variations Max of the PDF up and down variations Max of the PDF $\alpha_s \pm 0.001$ variations Both EW corrections: multiplicative and exponentiated
$t\bar{t}$ and single top	POWHEG+PYTHIA8	POWHEG+HERWIG7 (PS) MADGRAPH5_aMC@NLO+PYTHIA8 (ME) Max of the ISR variations: RadHiPrime and RadLo Max of the FSR up and down variations
Diboson	SHERPA2.2.11	POWHEG+PYTHIA8 Max of the 7-point QCD scale variations Max of the PDF up and down variations Max of the PDF $\alpha_s \pm 0.001$ variations Both EW corrections: multiplicative and exponentiated

Table 4.18: Nominal samples and variations including the alternative generators for the acceptance ratio uncertainties for all background processes. The alternative generators are included in all uncertainties. For the SHERPA 2.2.11 samples, two of the EW corrections are included as well. The maximum uncertainties from other types of variations are included.

Resolved $VH(\to b\bar{b}, c\bar{c})$

- Z+**jets:** Three types of acceptance ratio uncertainties are used. All resolved $VH(\to b\bar{b}, c\bar{c})$ Z+jets acceptance ratio uncertainties are listed in Table 4.19. The first column lists all three types of acceptance ratio uncertainties derived. The second column lists if the uncertainty is derived in $VH(\to b\bar{b})$ only, $VH(\to c\bar{c})$ only, or in $VH(\to b\bar{b}, c\bar{c})$ inclusively. All the $Z+mf$ and $Z+lf$ uncertainties are only derived in the $VH(\to c\bar{c})$ phase space due to small contribution in $VH(\to b\bar{b})$. In the case of $Z+hf$ uncertainties, the $Z+cc/Z+bb$ ratio is derived inclusively in the $VH(\to b\bar{b}, c\bar{c})$ phase space, except for the $VH(\to b\bar{b})$ 2-jet regions. All other $Z+hf$ uncertainties are derived in either $VH(\to c\bar{c})$ only or $VH(\to b\bar{b})$ only. The numbers agree in all cases and the same numbers are used in both $VH(\to c\bar{c})$ and $VH(\to b\bar{b})$ phase spaces.

  The third column lists the sample and regions where the uncertainties are derived and applied. Most uncertainties are derived and applied inclusively in different regions. A few exceptions are the $Z+cc/Z+bb$ ratio in the 2-jet regions and the $Z+hf$ SR/CR ratio in 2-jet. The last column shows the values of all acceptance ratio uncertainties used in the likelihood fit.

  - **Flavor acceptance ratio uncertainties:** extrapolate from the $Z+bb$ process

(high purity n_2) to the Z+cc process (low purity n_1) (Z+cc/Z+bb), Z+bc/Z+cl, and Z+bl/Z+cl. The derivation of the Z+cc/Z+bb acceptance ratio uncertainty (12%) is shown in Table 4.20.

- **SR/CR acceptance ratio uncertainties:** extrapolate from the high ΔR control region (CRHigh) to the SR for the Z+hf and Z+mf processes (SR/CRHigh); extrapolate from SR to CRHigh for $Z + lf$ (CRHigh/SR). The derivation of the 2-lepton low p_T^V SR/CR acceptance ratio uncertainty (7%) is shown in Table 4.21.
- **Lepton channel acceptance ratio uncertainties:** extrapolate from the 2-lepton channel to the 0-lepton channel (0L/2L). The derivation of the lepton channel acceptance ratio uncertainties in the 2-jet regions is shown in Table 4.22.

- W+**jets:** Three types of acceptance ratio uncertainties are used as the Z+jets background. The values of the acceptance ratio uncertainties range from 4% to 33% in various regions.

  - **Flavor acceptance ratio uncertainties:** extrapolate from $W + bb$ to $W + cc$ (W+cc/W+bb), W+bc/W+cl, W+bl/W+cl, W+$q\tau$/W+cl, and W+$lf\tau$/W+lf.
  - **SR/CR acceptance ratio uncertainties:** extrapolate from the high ΔR control region (CRHigh) to SR for $W + mf$ (SR/CRHigh); extrapolate from SR to CRHigh for $W + lf$ (CRHigh/SR). For $W + hf$, as the low ΔR control region (CRLow) has high purity $W + hf$ events, the extrapolation is performed first from CRLow to SR (SR/CRLow) and then from SR+CRLow to CRHigh (CRHigh/(SR+CRLow)).
  - **Lepton channel acceptance ratio uncertainties:** extrapolate from 1-lepton to 0-lepton (0L/1L).

- **Top ($t\bar{t}$ + single-top Wt):** Four kinds of acceptance ratio uncertainties are used for flavor (top(bq/qq) and top(bl/bc)), lepton channel (0L/1L), between the signal and control regions, and from $t\bar{t}$ to Wt. The values of the uncertainties range from 2% to 10% in various regions.

- **Single-top t-channel:** Four kinds of acceptance ratio uncertainties are applied for the t-channel. For the s-channel, the contribution is negligible. There are acceptance ratio uncertainties for p_T^V (high pTV/low pTV), n-jet (2-jet/3-jet, 4-jet/3-jet), lepton channel and between the signal and control regions. The values of hte uncertainties range from 3% to 17% in various regions.

- **Diboson:** Similarly, four kinds of acceptance ratio uncertainties are applied for p_T^V (extrapolate from medium p_T^V), n-jet (extrapolate from 2-jet), lepton channel (extrapolate to 0-lepton) and from the signal to the control regions. The values of the uncertainties range from 2% to 23% in various regions.

Acceptance Ratio Uncertainty	**Phase space derived**	**Regions or processes derived**	**Value of the uncertainty**
$Z+cc/Z+bb$	$VH(\to b\bar{b}, c\bar{c})$ inclusive	$Z+cc$	12%
$Z+cc/Z+bb$	$VH(\to b\bar{b})$ only	$Z+cc$, $VH(\to b\bar{b})$, 2-jet	8%
$Z+bl/Z+cl$	$VH(\to c\bar{c})$ only	$Z+bl$	4%
$Z+bc/Z+cl$	$VH(\to c\bar{c})$ only	$Z+bc$	10%
$Z+hf$ SR/CR	$VH(\to c\bar{c})$ or $VH(\to b\bar{b})$ only	2L, SR, p_T^V 75-150 GeV	7%
$Z+hf$ SR/CR	$VH(\to c\bar{c})$ or $VH(\to b\bar{b})$ only	2L, SR, p_T^V>150 GeV	15%
$Z+hf$ SR/CR	$VH(\to c\bar{c})$ or $VH(\to b\bar{b})$ only	0L, SR, p_T^V>150 GeV	10%
$Z+hf$ SR/CR	$VH(\to c\bar{c})$ or $VH(\to b\bar{b})$ only	02L, SR, p_T^V>150 GeV, 2-jet	30%
$Z+mf$ SR/CR	$VH(\to c\bar{c})$ only	2L, SR, p_T^V 75-150 GeV	7%
$Z+lf$ CR/SR	$VH(\to c\bar{c})$ only	2L, SR, p_T^V 75-150 GeV	7%
$Z+mf$ SR/CR	$VH(\to c\bar{c})$ only	02L, SR, topCR, p_T^V>150 GeV	5%
$Z+lf$ CR/SR	$VH(\to c\bar{c})$ only	02L, SR, topCR, p_T^V>150 GeV	5%
$Z+hf$ 0L/2L	$VH(\to c\bar{c})$ or $VH(\to b\bar{b})$ only	0L, 2-jet	2%
$Z+hf$ 0L/2L	$VH(\to c\bar{c})$ or $VH(\to b\bar{b})$ only	0L, 3-jet	4%
$Z+mf$ 0L/2L	$VH(\to c\bar{c})$ only	0L, 2-jet	3%
$Z+mf$ 0L/2L	$VH(\to c\bar{c})$ only	0L, 3-jet	8%
$Z+lf$ 0L/2L	$VH(\to c\bar{c})$ only	0L, 2-jet	4%
$Z+lf$ 0L/2L	$VH(\to c\bar{c})$ only	0L, 3-jet	10%

Table 4.19: Summary of the Z+jets acceptance ratio uncertainties in the resolved phase space. The acceptance ratio uncertainties are calculated for different processes such as the $Z+hf$, $Z+mf$, and $Z+lf$ processes and for different regions such as the n-jet, p_T^V, and signal and control regions. The flavor acceptance ratio uncertainties are applied to processes including the $Z+cc$, $Z+bl$, and $Z+bc$ processes.

inclusiveReg	Categorisation	Variation	$Z + cc/Z + bb$
0L+2L	0bb+1nt+ 2lt+2tt tags, $p_T^V > 150$, 2+3jets	MG FxFx alternative	**-10.7**% $\pm$ 0.7%
		MUR0.5_MUF0.5	1.9%
		MUR0.5_MUF1	2.4%
		MUR1_MUF0.5	-0.7%
		MUR1_MUF1	0.0%
		MUR1_MUF2	-1.4%
		MUR2_MUF1	-3.5%
		MUR2_MUF2	**-4.8**%
		PDF303200_up	0.6%
		PDF303200_down	**-0.6**%
		PDF270000'	**1.1**%
		PDF269000	-1.0%
		PDF303200_ASSEW	0.0%
		PDF303200_EXPASSEW	**-0.2**%
		PDF303200_MULTIASSEW	**-0.1**%
		Total	**11.8**%

Table 4.20: Flavor acceptance ratio uncertainties $Z + cc/Z + bb$ in the resolved $VH(\rightarrow b\bar{b}, c\bar{c})$ phase space. MG FxFx alternative refers to the MADGRAPH FxFx alternative sample. MURx_MUFy labels refer to the 7-point QCD variations where μ_r is varied by a factor of x and μ_f by a factor of y. PDF303200_up and PDF303200_down refer to the PDF up and down variations. PDF270000 and PDF269000 refer to the PDF α_s variations of ± 0.001. PDF303200_ASSEW, PDF303200_EXPASSEW, and PDF303200_MULTIASSEW refer to three EW correction schemes. The PDF303200_ASSEW is chosen as the nominal sample and always has the acceptance ratio uncertainty at 0%. The uncertainty is derived by summing the largest contribution among QCD variations, PDF up and down variations, PDF α_s variations, and FxFx (bold) in quadrature. Two of the electroweak corrections, EXPASSEW and MULTIASSEW, are both summed in the final uncertainty. A final value of 12% is used in the fit.

Channel	Categorisation	Variation	$Z+cc$	$Z+cl$	$Z+lf$
2L	1nt+2lt+2tt tags, 2+3pjets, pTV $75-150$, SR/CRHigh	MG FxFx alternative	$0.3\% \pm \mathbf{1.0}\%$	$\mathbf{2.7}\% \pm 0.6\%$	$\mathbf{2.7}\% \pm 1.2\%$
		MUR0.5_MUF0.5	**-6.0**%	**-6.3**%	**-6.2**%
		MUR0.5_MUF1	-2.6%	-3.3%	-3.7%
		MUR1_MUF0.5	-4.0%	-3.2%	-2.9%
		MUR1_MUF1	0.0%	0.0%	0.0%
		MUR1_MUF2	2.5%	2.2%	2.6%
		MUR2_MUF1	2.0%	2.9%	3.0%
		MUR2_MUF2	4.8%	5.1%	5.9%
		PDF303200_up	-0.2%	0.3%	-0.0%
		PDF303200_down	**0.2**%	**-0.3**%	**0.0**%
		PDF270000'	**-0.5**%	**-0.5**%	**-0.4**%
		PDF269000	0.2%	0.2%	0.2%
		PDF303200_ASSEW	0.0%	0.0%	0.0%
		PDF303200_EXPASSEW	**-0.1**%	**0.1**%	**0.2**%
		PDF303200_MULTIASSEW	**-0.0**%	**0.1**%	**0.2**%
		Total	**6.1**%	**6.8**%	**6.8**%

Table 4.21: SR/CR acceptance ratio uncertainties in $75 < p_T^V < 150$ GeV in the $VH(\to c\bar{c})$ 2-lepton channel. The labels are the same as introduced in Table 4.20. The bold components are summed in quadrature for the total uncertainties as explained for Table 4.20. After comparing with the $VH(\to b\bar{b})$ equivalent, the $Z+hf$ (from $Z+cc$), $Z+mf$ (from $Z+cl$) and $Z+lf$ uncertainties are set to 7%. The $Z+lf$ CRHigh/SR uncertainty is around the same value after flipping the extrapolation direction.

inclusiveReg, 1nt+2lt+2tt tags, 2jets, $p_T^V > 150$, 0L/2L	$Z + cc$	$Z + cl$	$Z + lf$
MG FxFx alternative	$-0.7\% \pm$ **1.4**%	**-2.5**% $\pm$ 0.7%	**-4.0**% $\pm$ 1.2%
MUR0.5_MUF0.5	-0.8%	**-0.8**%	**-0.8**%
MUR0.5_MUF1	**-1.1**%	-0.6%	-0.7%
MUR1_MUF0.5	0.3%	-0.3%	0.0%
MUR1_MUF1	0.0%	0.0%	0.0%
MUR1_MUF2	-0.2%	-0.0%	-0.3%
MUR2_MUF1	0.4%	0.5%	0.2%
MUR2_MUF2	0.4%	0.4%	-0.1%
PDF303200_up	0.2%	0.1%	0.0%
PDF303200_down	**-0.2**%	**-0.1**%	**-0.0**%
PDF270000'	0.0%	**-0.1**%	**-0.1**%
PDF269000	**0.0**%	0.1%	0.1%
PDF303200_ASSEW	0.0%	0.0%	0.0%
PDF303200_EXPASSEW	**0.2**%	**0.1**%	**0.2**%
PDF303200_MULTIASSEW	**0.1**%	**0.1**%	**0.2**%
Total	**1.8**%	**2.6**%	**4.1**%

Table 4.22: Lepton acceptance ratio uncertainties for 2-jet in the $VH(\to c\bar{c})$ phase space. The bold components are summed in quadrature for the total uncertainties as explained for Table 4.20. After comparing with the $VH(\to b\bar{b})$ equivalent, the $Z + hf$ uncertainty is set to 2% in the fit for $VH(\to b\bar{b}, c\bar{c})$. The $Z + mf$ and $Z + lf$ uncertainties are set to 3% and 4% in the $VH(\to c\bar{c})$ phase space.

Boosted $VH(\to b\bar{b}, c\bar{c})$

- Z**+jets:** Four kinds of acceptance ratio uncertainties are applied for the flavors ($Z + cc/Z + bb$, $Z + cl/Z + bc$, $Z + bl/Z + bc$) ($\sim 6\%$), lepton channels ($\sim 3\%$), p_T^V (>600 GeV/400-600 GeV) ($\sim 15\%$), and top control regions (topCR/SR) ($\sim 20\%$).

- W**+jets:** Similar to Z+jets, four kinds of acceptance ratio uncertainties are applied for the flavors ($W + cc/W + bb$, $W + cl/W + bc$, $W + bl/W + bc$) ($\sim 10\%$), lepton channels ($\sim 20\%$), p_T^V ($\sim 3\%$), and top control regions ($\sim 30\%$).

- **Top ($t\bar{t}$ + single-top Wt):** Three kinds of acceptance ratio uncertainties are applied for the lepton channels ($\sim 15\%$), top control regions ($\sim 15\%$), and from the $t\bar{t}$ process to the Wt process ($\sim 30\%$). The single-top s- and t-channels have too small contribution to consider the acceptance ratio uncertainties in the boosted phase space.

- **Diboson:** Two kinds of acceptance ratio uncertainties are applied for the p_T^V ($\sim 30\%$) and lepton channels ($\sim 10\%$).

4.5.3 Shape uncertainties

In addition to the normalization and acceptance ratio uncertainties, the shape uncertainties are also included to account for bin-by-bin uncertainties in the kinematic distribution.

All shape uncertainties used for all samples for both the resolved and boosted phase space are summarized in Table 4.23. The PDF uncertainties are negligible as a shape uncertainty. For V+jets and diboson, the matrix element only (ME-only) QCD variation ($\mu_r = 2$ and $\mu_f = 2$) is included as a shape uncertainty. This variation tends to give the largest uncertainty among all QCD variations. The multiplicative EW correction is included as a shape uncertainty for the V+jets and diboson backgrounds as well. The Z+jets shape uncertainties are applied in all 0-lepton and 2-lepton regions.

Most shape uncertainties are used as a shape-only uncertainty. The normalization uncertainties are addressed separately by floating normalizations and acceptance ratio uncertainties. When calculating the shape uncertainties, the overall normalization in one region of the alternative generator is scaled to be the same as the nominal generator. The only exception is the DS-DR uncertainty for the single-top Wt sample. Diagram subtraction (DS) and diagram removal (DR) are two approaches to resolve the overlap between the $t\bar{t}$ and Wt processes, as introduced in Section 4.4.1.4. The DR (alternative) approach introduces a large normalization difference compared to the diagram subtraction method.

Most alternative generators are included as a shape uncertainty using CARL (calibrated likelihood ratio estimator) [169]. In the case of SHERPA 2.2.1 p_T^V uncertainty for V+jets, polynomial reweighting is used instead. More details of CARL and SHERPA 2.2.1 p_T^V reweighting are discussed below.

Sample	Variations	Uncertainty type
V+jets	CARL (MADGRAPHFxFx)	shape-only
	ME-only QCD $\mu_r = 2$ and $\mu_f = 2$	shape-only
	Electroweak correction multiplicative	shape-only
	SHERPA2.2.1 p_T^V	shape-only
$t\bar{t}$, single top	CARL (POWHEG+HERWIG7 (PS), MADGRAPH5_aMC@NLO+PYTHIA8 (ME))	shape-only
	ISR	shape-only
	FSR	shape-only
	DS-DR (single-top Wt)	shape+norm
Diboson	CARL (POWHEG+PYTHIA8, SHERPA2.2.1)	shape-only
	ME-only QCD $\mu_r = 2$ and $\mu_f = 2$	shape-only
	Electroweak correction multiplicative	shape-only

Table 4.23: Variations considered for the shape uncertainties for all background processes.

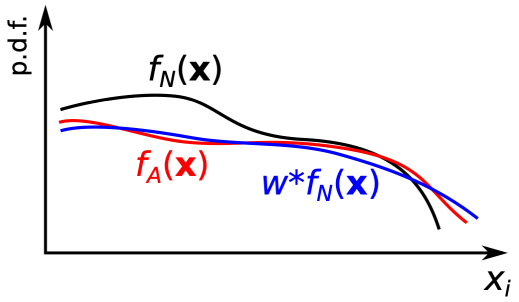

Figure 4.21: CARL (blue curve) reweights the nominal distribution ($y = 0$ in black) to be like the alternative distribution ($y = 1$ in red) [168].

CARL CARL is a machine learning package that can reweight the nominal generator samples to have the same kinematic distribution as the alternative samples as shown in Figure 4.21. The nominal distribution for the variable X_i is shown in the black curve. The alternative distribution is shown in the red curve. CARL reweights all events in the nominal sample and outputs a new distribution (the blue curve). Instead of using the difference between the red and black curves as the shape uncertainty, the difference between the blue and black curves is the CARL shape uncertainty.

The alternative samples tend to have a $\sim$ 50% smaller sample size compared to the

nominal sample. Instead of directly using the alternative sample as a shape uncertainty, the CARL approach removes large statistical fluctuations in the alternative samples. The $VH(\to b\bar{b}, c\bar{c})$ analysis is the first analysis that uses CARL to compute the shape uncertainties.

Compared to the traditional polynomial reweighting method, CARL can reweight the nominal samples in higher dimensions. Given the usage of MVA in the analysis, this is particularly important. CARL reweights the nominal sample to have the same distribution as the alternative sample for all MVA input invariables. This means that the final CARL MVA shape uncertainties can translate into meaningful uncertainties for all MVA input variables as well.

CARL training uses a deep neural network to reweight the nominal sample. The details of the training are listed below:

- **Input variables:** The CARL input variables include all MVA variables listed in Table 4.13 and some auxiliary variables. The auxiliary variables differentiate the regions of the events, such as the number of jets (n-jet), the PCFT bins of the two Higgs candidate jets, and the total number of loose and tight c-tags and b-tags in the event.

- **Training granularity:** unlike the fine granularity MVA trainings as shown in Figure 4.13, the CARL trainings are only performed once per lepton channel for the $VH(\to b\bar{b})$, $VH(\to c\bar{c})$ and boosted $VH(\to b\bar{b})$ phase spaces and for different alternative samples. The summary of all CARL trainings is shown in Table 4.24. While the MVA trainings need fine granularity to achieve good performance, CARL uses auxiliary variables to assist trainings across multiple regions and the CARL DNN can achieve good performance in all individual regions. Including a larger subset of regions also improves the DNN training statistics, which is important for its performance.

- **Hyperparameters:** the CARL deep neural network is simpler than the `DL1r` network shown in Table 3.8. There are only 3 layers. Each layer has the same number of neurons as the number of input variables (14 MVA variables and 5 auxiliary variables in the case of the $VH(\to c\bar{c})$ 2-lepton channel). There are 300 epochs. The loss function is categorical cross-entropy. The training sample in $VH(\to c\bar{c})$ 2-lepton has around 30 million events. Overall, the CARL DNN reweighting requires less differentiating power and thus shallower DNN to process all nominal and alternative samples.

- **Output:** the CARL training loops through all nominal and alternative events and outputs the probability for an event to be from the alternative generator ($y = 1$) given all input variable values, $P(y = 1|\mathbf{x})$.

The final CARL probability, $P(y = 1|\mathbf{x})$, is used to reweight the nominal events ($y = 0$):

$$w(\mathbf{x}) = \frac{f(\mathbf{x}|y=1)d\mathbf{x}}{f(\mathbf{x}|y=0)d\mathbf{x}} = \frac{P(y=1|\mathbf{x})}{P(y=0|\mathbf{x})} = \frac{P(y=1|\mathbf{x})}{1-P(y=1|\mathbf{x})} \tag{4.16}$$

How well the reweighted CARL distribution resembles the alternative distribution is evaluated closely before CARL is used to derive shape uncertainties from each sample and region.

The CARL closure is good in all cases. The difference between the CARL distribution and the alternative distribution is usually within 1σ. Figure 4.22 shows the V+jets CARL closure in $VH(\to c\bar{c})$.

Background	0-lepton	1-lepton	2-lepton
W+jets	×	×	
Z+jets	×		×
ttbar	×	×	
single-top Wt	×	×	
single-top t (only for resolved $VH(\to b\bar{b})$)		×	
ZZ	×		×
WW	×	×	
WZ (only for $VH(\to c\bar{c})$)	×	×	×

Table 4.24: Summary of all CARL trainings in different lepton channels for all background processes. All trainings are performed separately in the resolved $VH(\to b\bar{b})$, $VH(\to c\bar{c})$, and boosted $VH(\to b\bar{b})$ phase spaces. However, the single-top t-channel CARL shape is only needed for resolved $VH(\to b\bar{b})$. And, the WZ diboson CARL shape is only needed for $VH(\to c\bar{c})$. In addition, as noted in Table 4.23, for all $t\bar{t}$, single-top and diboson trainings, two sets of CARL trainings are performed for two different generators.

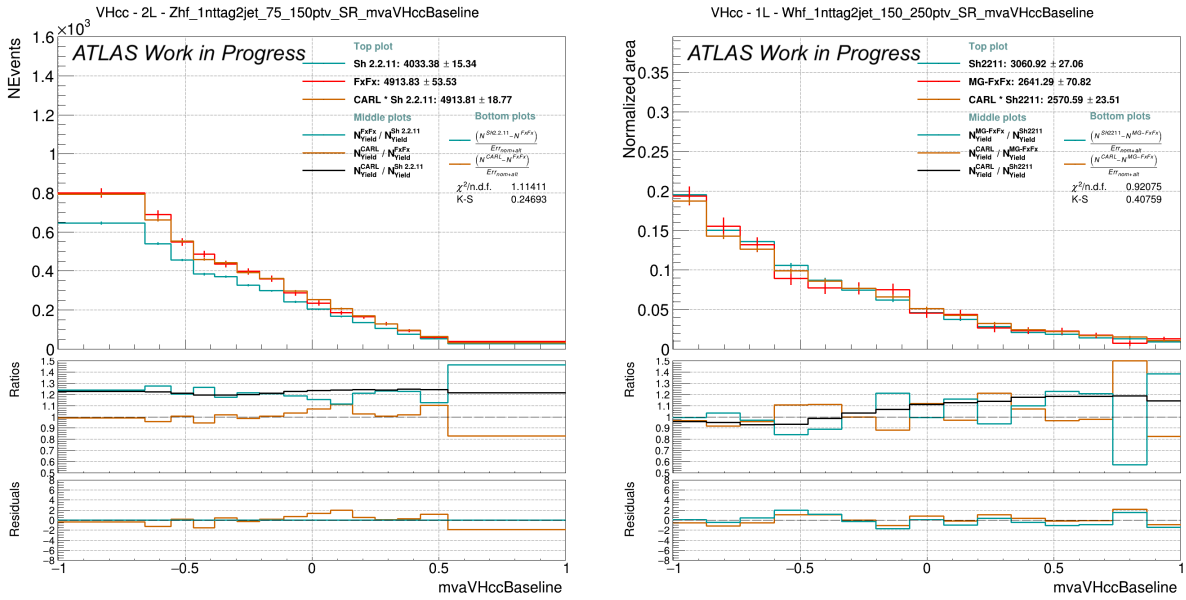

Figure 4.22: The CARL closure for the Z+jets (left) and W+jets (right) background in the $VH(\rightarrow c\bar{c})$ phase space [207]. The left plot is from the 1nt-tag 2-jet signal region at p_T^V 75-150 GeV for the $Z+hf$ process in 2-lepton. The right plot is from the 1nt-tag 2-jet signal region at p_T^V 150-250 GeV for the $W+hf$ process in 1-lepton. The CARL closure is good as the CARL distribution (brown curve) follows the alternative sample distribution (red). The black curve is the shape uncertainty introduced, roughly up to 10% in some bins.

SHERPA 2.2.1 p_T^V shape The SHERPA 2.2.11 p_T^V distribution is known to describe the data worse than SHERPA 2.2.1 over some p_T^V ranges, even though SHERPA 2.2.11 has many improvements compared to SHERPA 2.2.1 [188]. The comparison between SHERPA 2.2.11 and SHERPA 2.2.1 is shown in Figure 4.23. Similar trends are observed in the $VH(\rightarrow b\bar{b}, c\bar{c})$ analysis [168].

Given that p_T^V is an important MVA variable, the difference in p_T^V between SHERPA 2.2.1 and SHERPA2.2.11 is an important uncertainty on the final MVA distribution. Therefore, polynomials are used to reweight the SHERPA 2.2.11 p_T^V distribution to be like SHERPA 2.2.1 for the V+jets background to obtain the SHERPA 2.2.1 p_T^V shape uncertainty. Different polynomials are used for each lepton channel and flavor of the V+jets background (such as $Z+hf$). The polynomials are derived inclusively in all p_T^V bins. The polynomial reweighted SHERPA 2.2.11 p_T^V distribution is shown in Figure 4.24.

CARL is not used in the case of the V+jets SHERPA 2.2.1 p_T^V uncertainty, as machine learning reweighting is not necessary for the single variable reweighting. Some high ΔR control regions and the $Z+lf$ control regions use p_T^V as the fit variable to constrain this uncertainty. The uncertainties decrease by a factor of 3 when fitting p_T^V instead of m_{cc} in the control regions. The uncertainty is up to 20% in some p_T^V bins.

SHERPA 2.2.1 is also used as an alternative sample for the diboson background. However, CARL is used to assess the diboson SHERPA 2.2.1 shape uncertainty and reweights all the MVA variables including p_T^V. This is because diboson SHERPA 2.2.1 assesses the fragmentation systematics that affect the reconstructed Higgs mass peak in addition to any potential p_T^V mismodeling.

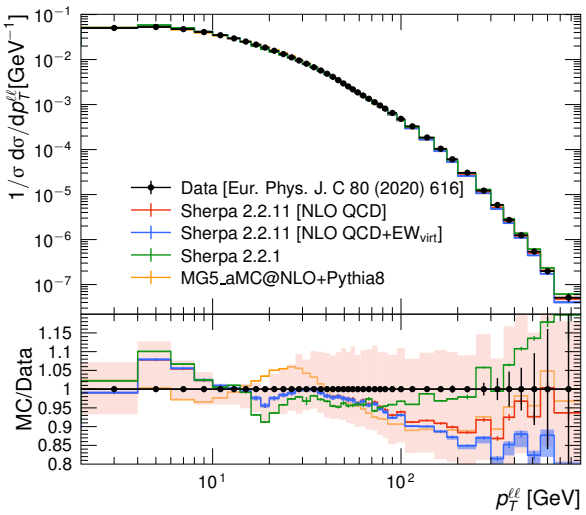

Figure 4.23: Data simulation comparison for di-lepton events [188]. SHERPA 2.2.1 (green) central values seem to agree with data better below 400 GeV than SHERPA 2.2.11 (blue). The red uncertainty band displays the QCD scale uncertainties of SHERPA 2.2.11. The blue uncertainty band displays the EW uncertainties of SHERPA 2.2.11.

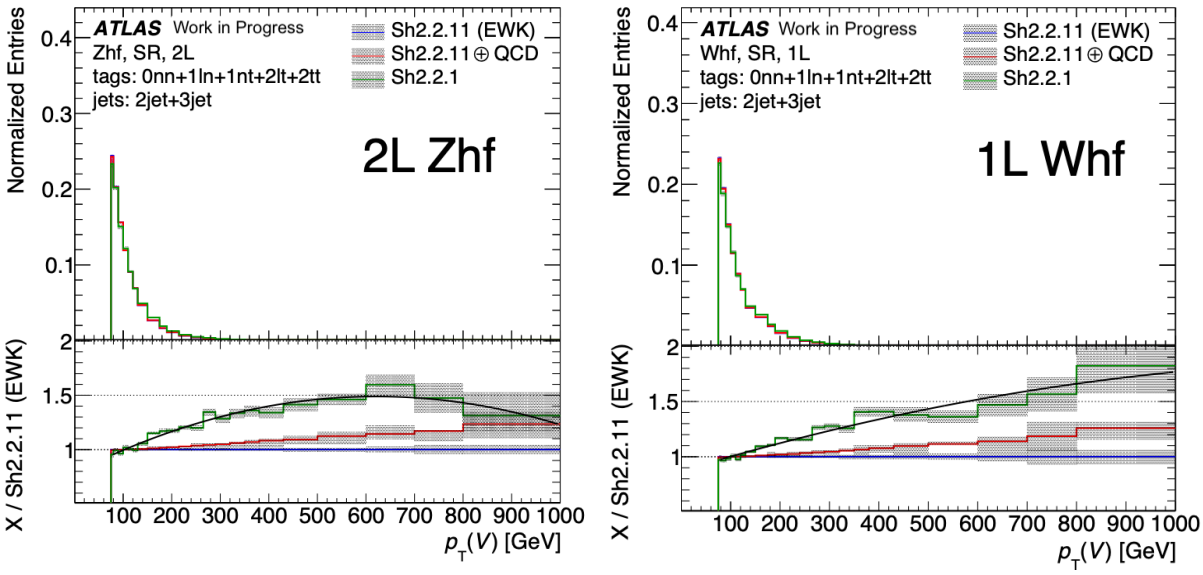

Figure 4.24: The Z+jets (left) and W+jets (right) SHERPA2.2.11 (blue) reweighting [168]. The reweighted polynomial (black) follows the SHERPA2.2.1 (green) p_T^V distribution.

4.6 Statistical analysis

After building all the regions, obtaining all the MVA distributions and calculating all the modeling uncertainties, the final $VH(\to b\bar{b}, c\bar{c})$ signal strengths can be extracted using the likelihood fit. In this section, the likelihood function and hypothesis testing are introduced in Section 4.6.1. Then, Section 4.6.2 discusses the fit performance checks. Lastly, Section 4.6.3 presents the fit results.

4.6.1 Likelihood function and hypothesis testing

The profile likelihood function is used in the statistical analysis of $VH(\to b\bar{b}, c\bar{c})$. The profile likelihood function is one of the most common statistical tools used in Higgs analyses at the LHC. It constrains the nuisance parameters given the collected data and computes the likelihood of the data given the theoretical predictions from the MC samples.

The full likelihood function is defined in Equation 4.17 [225, 184]:

$$\mathcal{L}(\vec{\mu}, \vec{\alpha_p}, \vec{\tau}, \vec{\gamma}) = \prod_{i \in \text{bins}} \text{Pois}(N_i | \vec{\mu} \cdot \vec{s_i} + b_i(\vec{\alpha_p}, \vec{\tau}, \gamma_i)) \times \prod_{a_p \in \vec{\alpha_p}} \frac{1}{\sqrt{2\pi\sigma^2_{\alpha_p}}} \exp\left[-\frac{(a_p - \alpha_p)^2}{2\sigma^2_{\alpha_p}}\right] \times \prod_{i \in \text{bins}} \text{Gauss}(n_p | \gamma_i \beta_i, \sqrt{\gamma_i \beta_i}) \tag{4.17}$$

It calculates the probability of observing N_i events in the data in bin i in all regions given the simulation predictions. The likelihood function has three main parts:

- **Poissonian physics term $\mathcal{L}_{phys}(\vec{\mu})$:** The physics term in Equation 4.18 uses a Poisson function to model the signal and background yields in all bins and regions. Here, $\vec{s_i}$ and b_i are the expected signal and background yields. The signal strengths, $\vec{\mu}$, are defined in Equations 4.13-4.14. The signal strengths are the modifications to the Standard Model predictions (i.e., the predicted production cross section times the branching ratios). The signal strengths are the parameters of interest. All other parameters are called nuisance parameters.

$$\mathcal{L}_{phys}(\vec{\mu}) = \prod_{i\in\text{bins}} \text{Pois}(N_i|\vec{\mu}\cdot\vec{s_i}+b_i) = \prod_{i\in\text{bins}} \frac{(\vec{\mu}\cdot\vec{s_i}+b_i)^{N_i}}{N_i!} e^{-(\vec{\mu}\cdot\vec{s_i}+b_i)} \tag{4.18}$$

- **Auxiliary measurements $\mathcal{L}_{aux}(\vec{a_p})$:** In addition to the physics measurements that encode the parameters of interest $\vec{\mu}$, auxiliary measurements a_p are made for various nuisance parameters as well. Auxiliary measurements use the Gaussian functions to accommodate the experimental and modeling uncertainties σ_{α_p} for certain process α_p, as shown in Equation 4.19. The auxiliary measurements are Poissonian and frequentist by nature as well. In this case, a Gaussian approximation is valid and it is convenient to model a_p by a mean α_p and a variance σ_{α_p}.

$$\mathcal{L}_{\text{aux}(\vec{a_p}|\alpha_p,\sigma_{\alpha_p})} = \prod_{a_p\in\vec{a_p}} \frac{1}{\sqrt{2\pi\sigma_{\alpha_p}^2}} \exp\left[-\frac{(a_p-\alpha_p)^2}{2\sigma_{\alpha_p}^2}\right] \tag{4.19}$$

  In addition, as discussed in Section 4.5.1, some large background processes are left free floating. In this case, the yields are modified by $\vec{\tau}$ without Gaussian constraints, similar to the signal strengths $\vec{\mu}$.

- **Simulation statistical error $\mathcal{L}_{bkgStat}(\vec{\gamma})$:** In addition to $\vec{\alpha_p}$ and $\vec{\tau}$, b_i can be changed by γ_i as well, $b_i(\vec{\alpha_p},\vec{\tau}) \to \gamma_i b_i(\vec{\alpha_p},\vec{\tau})$. The parameter γ_i accounts for the statistical uncertainties of the background simulation, while the data statistical uncertainties are accounted for in the Poissonian $\mathcal{L}_{phys}$ term. Similar to the $\vec{\alpha_p}$ parameters, the γ_i factor is also constrained by a Gaussian function, as shown in Equation 4.20.

$$\mathcal{L}_{\text{bkgStat}}(\vec{\gamma}) = \prod_{i\in\text{bins}} \text{Gauss}(n_p|\gamma_i\beta_i,\sigma_{\gamma_i\beta_i}) \tag{4.20}$$

  Here, $\beta_i = 1/\sigma_{rel}^2$ and σ_{rel} is the relative statistical uncertainty of the total background yields. The variance of the Gaussian function $\sigma_{\gamma_i\beta_i}$ is equal to $\sqrt{\gamma_i\beta_i}$. The statistical uncertainties are neglected for the signal MC, as the signal MC statistics are high.

Once the likelihood function is defined, the best-fit $\vec{\mu}$ are found by minimizing $-\ln\mathcal{L}(\vec{\mu},\vec{\alpha_p},\vec{\tau},\vec{\gamma})$ with respect to all the parameters $\vec{\mu}$, $\vec{\alpha_p}$, $\vec{\tau}$, and $\vec{\gamma}$. The best-fit likelihood can be expressed as $\mathcal{L}(\hat{\vec{\mu}},\hat{\vec{\alpha}_p},\hat{\vec{\tau}},\hat{\vec{\gamma}})$, where $\hat{\vec{\mu}}$, $\hat{\vec{\alpha}_p}$, $\hat{\vec{\tau}}$, and $\hat{\vec{\gamma}}$ are the best-fit values that minimize $-\ln\mathcal{L}(\vec{\mu},\vec{\alpha_p},\vec{\tau},\vec{\gamma})$.

Hypothesis testing After defining and fitting the likelihood function using data and simulations, a test statistic $q_{\vec{\mu}}$ is composed to evaluate a hypothesis for certain $\vec{\mu}$. The test statistic $q_{\vec{\mu}}$ is defined in terms of the likelihood ratio $\lambda(\vec{\mu})$.

$$\lambda(\vec{\mu}) = \frac{\mathcal{L}(\vec{\mu},\hat{\hat{\vec{\alpha}}}_p,\hat{\hat{\vec{\tau}}},\hat{\hat{\vec{\gamma}}})}{\mathcal{L}(\hat{\vec{\mu}},\hat{\vec{\alpha}}_p,\hat{\vec{\tau}},\hat{\vec{\gamma}})} \tag{4.21}$$

The parameter $\vec{\mu}$ is the parameter of interest value under evaluation. The likelihood $\mathcal{L}(\hat{\vec{\mu}},\hat{\vec{\alpha}}_p,\hat{\vec{\tau}},\hat{\vec{\gamma}})$ is the best-fit likelihood after minimization. The numerator likelihood $\mathcal{L}(\vec{\mu},\hat{\hat{\vec{\alpha}}}_p,\hat{\hat{\vec{\tau}}},\hat{\hat{\vec{\gamma}}})$ is the best-fit likelihood for the $\vec{\mu}$ under evaluation. Here, $\hat{\hat{\vec{\alpha}}}_p$, $\hat{\hat{\vec{\tau}}}$, and $\hat{\hat{\vec{\gamma}}}$ are best-fit values that minimize $-\ln\mathcal{L}$ when $\vec{\mu}$ is fixed to certain values. The likelihood ratio $\lambda(\vec{\mu})$ can vary in the range of $[0,1]$. The test statistics are defined differently for the $VH(\to b\bar{b})$ significance and the $VH(\to c\bar{c})$ upper limit:

- **Significance:** The test statistic for calculating the significance is defined as:

$$q_0 = \begin{cases} -2\ln\lambda(0) & \hat{\mu} \geq 0 \\ 0 & \hat{\mu} < 0 \end{cases} \tag{4.22}$$

  The significance test statistic aims to quantify the level of disagreement between the data and the null hypothesis ($\mu = 0$). This is achieved by defining the p-value:

$$p_0 = \int_{q_{0,\text{obs}}}^{\infty} f(q_0|0)dq_0 \tag{4.23}$$

  The function $f(q_0|0)$ is the probability density function of $q_{\vec{\mu}}$ under the assumption of $\mu = 0$. The function $f(q_0|0)$ approaches a chi-square distribution with a large sample size. The p_0 value can be converted to the significance:

$$Z = \Phi^{-1}(1 - p_0) \tag{4.24}$$

  Here, Φ^{-1} is the inverse of the cumulative distribution function of the standard Gaussian distribution. The conversion is conventional and does not assume $f(q_0|0)$ being Gaussian. In particle physics, conventionally, when the result significance reaches three standard deviations (3σ), the result is considered to be *evidence*. When the result significance reaches five standard deviations (5σ), the result is considered a *discovery*. At the 3σ (5σ) significance, the probability that the results are not due to statistical fluctuations is approximately 99.73% (99.99994%).

- **Upper limits:** When the significance is low, an upper limit is set as in the case of the $VH(\to c\bar{c})$ signal strength. The upper limit test statistic is similar to the significance case:

$$q_\mu = \begin{cases} -2\ln\lambda(\mu) & \hat{\mu} \leq \mu \\ 0 & \hat{\mu} > \mu \end{cases} \tag{4.25}$$

  When setting the upper limit, $\hat{\mu} > \mu$ does not represent less compatibility between the data and the μ hypothesis. Similarly, p_μ can be defined as:

$$p_\mu = \int_{q_{\mu,\text{obs}}}^{\infty} f(q_\mu|\mu)dq_\mu \tag{4.26}$$

  Here, $f(q_\mu|\mu)$ is defined from the CL_s method [226]. The upper limit μ can be found by solving for $p_\mu = 5\%$ at the 95% confidence level (CL).

4.6.2 Fit diagnostics

After minimizing $-\ln\mathcal{L}(\vec{\mu}, \vec{\alpha_p}, \vec{\gamma})$, various diagnostic tools are available to check the fitting performance. The diagnostic tools include: nuisance parameter *pulls and constraints*, nuisance parameter *correlation matrices*, nuisance parameter *rankings*, and *prefit and postfit plots*.

The nuisance parameter pulls and constraints are checked in two kinds of fit: the *data fit* and the *Asimov fit*. The data fit extracts the best-fit parameters given the data and the MC simulations. The Asimov fit uses the Asimov dataset instead of the actual data. The Asimov dataset is an artificial dataset with the same number of events as the simulation. The Asimov dataset is a good way to assess the expected nuisance parameter constraints in the data. The nuisance parameter correlation matrices and rankings are presented in the data fit below. All fit results are from the $VH(\to b\bar{b}, c\bar{c})$ fit over the entire $VH(\to b\bar{b}, c\bar{c})$ phase space.

In addition, all fit diagnostic results presented use unblinded *unconditional fits*. Unconditional fits mean that the signal strengths are free floating. Before unblinding, all fits were *conditional fits*. That is, the pulls of the signal strengths are fixed to one in the fits.

The analysis was *blinded* while the framework was being set up. Blinding intentionally hides the key analysis results such as the signal strengths from the analysis team during the analysis construction process. This ensures that the analysis decisions are not biased by the impact over the final results. In the $VH(\to b\bar{b}, c\bar{c})$ analysis, when blinded, only the conditional fits were performed. And, the MVA bins above zero were also hidden in the postfit plots before unblinding as well. The analysis was only unblinded when all event selections, MVA trainings, modeling uncertainties, and the fit framework had been finalized. The unblinding process proceeds in three steps: first check the unconditional nuisance parameter pulls with respect to the conditional nuisance parameter pulls, then study the $VZ(\to b\bar{b}, c\bar{c})$ diboson validation fit results, and lastly unblind all $VH(\to b\bar{b}, c\bar{c})$ results. At each step,

the results are studied in detail to ensure that the analysis framework behaves as expected. After unblinding, no changes are allowed in the analysis framework.

Nuisance parameter pull and constraint Equation 4.17 shows that there are three kinds of nuisance parameters (NPs) in the likelihood function: $\vec{\alpha_p}$, $\vec{\tau}$, and $\vec{\gamma}$. After minimization, all nuisance parameters can be pulled and constrained as shown in Figure 4.25. The pull value is defined as:

$$\text{pull} = \frac{\hat{\alpha_p} - \alpha_p}{\sigma_{\alpha_p}} \tag{4.27}$$

When the pull = 0, $\hat{\alpha_p}$ is the same as the default value. When the pull = 1, $\hat{\alpha_p}$ is one σ_{α_p} above α_p. The uncertainty σ of all nuisance parameters is evaluated using the second-order derivatives of the likelihood. When the error bar of the pull is equal to 1, $\sigma_{\hat{\alpha_p}}$ is the same as the prior uncertainty σ_{α_p}. When the error bar is less than 1, $\sigma_{\hat{\alpha_p}}$ is *constrained* and smaller than σ_{α_p}. When the error bar is larger than 1, $\sigma_{\hat{\alpha_p}}$ is *under-constrained* and augmented. This situation is unexpected and often means that the fit has issues in modeling the data. The nuisance parameters should only be pulled when $\sigma_{\hat{\alpha_p}}$ is constrained. Understanding and investigating the nuisance parameter pulls is a major part in diagnosing the performance of the fits.

In the case of a floating normalization τ, when the pull = 1, the $\hat{\tau}$ value is the same as the default normalization. When the pull = 1.2, for example, the $\hat{\tau}$ value increases by 20% from the default value. That is, the pull value is equal to $\hat{\tau}/\tau$. In the case of γ, the pull and error bar can be read the same as the α_p pulls and constraints.

Figure 4.25 shows the nuisance parameter pulls of the Z+jets SHERPA 2.2.1 p_T^V shape uncertainties. All pulls share the label of `Z_shape_Sh221_pTV` to differentiate the SHERPA 2.2.1 p_T^V shape uncertainty NPs from other NPs. The trailing labels such as `Zl_075-150ptv` denote the correlation scheme of the SHERPA 2.2.1 p_T^V shape uncertainty NPs. In the resolved phase space, the NPs are decorrelated in p_T^V bins. The NPs are also decorrelated for different Z+jets processes. The $Z + lf$ sample NPs (marked by `Zl`) are decorrelated from the $Z + hf$ and $Z + mf$ NPs (marked by `ZhfZmf`). In the boosted phase space, one NP is used for all regions and samples, `Z_shape_Sh221_pTV_Z_400+ptv`.

Overall, the modeling uncertainty pulls are decorrelated in different regions when the pulls are not compatible. The decorrelations of all Z+jets modeling uncertainties are shown in Tables 4.25-4.26. Some Z+jets nuisance parameters listed in the tables have significant impact on the $VH(\to c\bar{c})$ signal strength, such as the floating normalization NPs, the CARL shape uncertainties, and the SR/CR acceptance ratio uncertainties. More details about the nuisance parameter impact are discussed in the nuisance parameter ranking (Figure 4.27).

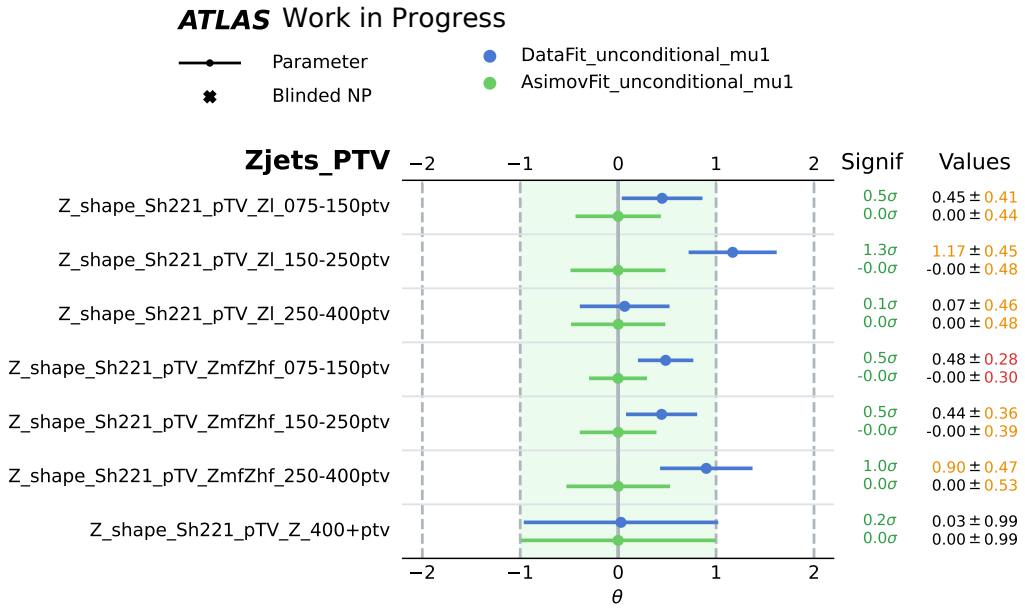

Figure 4.25: The pull plot for SHERPA 2.2.1 p_T^V shape uncertainties in the $VH(\to b\bar{b}, c\bar{c})$ fit [168]. Two kinds of pulls are presented for each nuisance parameters. The blue pulls correspond to the data unconditional fit, while the green pulls the Asimov unconditional fit. All Asimov pulls in green are zero as the Asimov dataset has the same yields as the MC simulation. The nuisance parameter constraints in the Asimov dataset are similar to the real data. The x-axis label θ refers to the nuisance parameter α_p.

Nuisance parameter names
Floating normalizations
NF_Zhf_J[2,3+]_[075-150, 150-250, 250-400]
NF_Zhf_J3_[075-150, 150-250, 250-400]
NF_Zmf_J[2,3+]_[075-150, 150-250, 250-400]
NF_Zl_J[2,3+]_[075-150, 150-250, 250-400]
Flavor acceptance ratio uncertainties
ZbbZccRatio_resolved
ZblZclRatio_resolved
ZbcZclRatio_resolved
SR/CR acceptance ratio uncertainties
Zhf_extrap_from_CRHigh_BMin_J[2,3,4]
Zmf_extrap_from_CRHigh
Zl_extrap_to_CRHigh
Lepton channel acceptance ratio uncertainties
Zhf_nLepAcc_L0_resolved
Zmf_nLepAcc_L0_resolved_[2,3]J
Zl_nLepAcc_L0_resolved_[2,3]J

Table 4.25: Nuisance parameters of the Z+jets modeling in the resolved phase space for floating normalizations and acceptance ratio uncertainties. All Z+jets categories such as $Z + hf$ are simplified to `Zhf`, omitting the plus sign for pull naming and plotting. The brackets `[]` displays the decorrelation of the nuisance parameters. For example, `norm_Zhf_J[2,3+]_[075-150, 150-250, 250-400]` means that the floating normalization for $Z + hf$ is decorrelated into 6 nuisance parameters for n-jet of 2-jet and 3p-jet and p_T^V of 75-150, 150-250, and 250-400 GeV. Note the $VH(\to c\bar{c})$ floating normalizations do not have an upper limit at 400 GeV as the $VH(\to c\bar{c})$ phase space does not have a stand-alone boosted region above 400 GeV. Most modeling uncertainties are correlated between the $VH(\to b\bar{b})$ and $VH(\to c\bar{c})$ phase spaces. All uncertainties are decorrelated between the resolved and boosted phase space. The SR/CR acceptance ratio uncertainties are only applied in the resolved phase space.

Nuisance parameter names
CARL Z+jets shape uncertainties
Carl_Z_Sh2211toFxFx_staticHighDR_[Zbb,Zcc]_[075-150ptv, 150-250ptv]
Carl_Z_Sh2211toFxFx_staticLowDR_[Zbb,Zcc]_[075-150ptv, 150-250ptv]
Carl_Z_Sh2211toFxFx_staticHighDR_[Zmf,Zl]_[075-150ptv, 150-250ptv]_[2,3+]J
Carl_Z_Sh2211toFxFx_staticLowDR_[Zmf,Zl]_[075-150ptv, 150-250ptv]
Carl_Z_Sh2211toFxFx_Zbb_250-400ptv
Carl_Z_Sh2211toFxFx_Zcc_250-400ptv
Carl_Z_Sh2211toFxFx_Zmf_250-400ptv_[2,3+]J
Carl_Z_Sh2211toFxFx_Zl_250-400ptv_[2,3+]
Carl_Z_Sh2211toFxFx_Z_400+ptv
SHERPA 2.2.1 p_T^V shape uncertainties
Z_shape_Sh221_pTV_ZmfZhf_[075-150,150-250, 250-400]ptv
Z_shape_Sh221_pTV_Zl_[075-150,150-250, 250-400]ptv
Z_shape_Sh221_pTV_Z_400+ptv
ME-only $\mu_r = 2$ and $\mu_f = 2$ QCD shape uncertainties
ME_ONLY_MUR2_MUF2_PDF303200_PSMUR2_PSMUF2_075-150ptv_[Zhf,Zmf,Zl]
ME_ONLY_MUR2_MUF2_PDF303200_PSMUR2_PSMUF2_150-400ptv_[Zhf,Zmf,Zl]
ME_ONLY_MUR2_MUF2_PDF303200_PSMUR2_PSMUF2_400+ptv_[Zhf,Zmf,Zl]
EW correction multiplicative scheme shape uncertainties
MUR1_MUF1_PDF303200_MULTIASSEW_[Zhf, Zmf, Zl]

Table 4.26: Nuisance parameters of Z+jets modeling in the resolved phase space for shape uncertainties. The naming convention is similar to Table 4.25. The CARL shape uncertainties are also decorrelated into high ΔR regions ($\Delta R > 1$) and low ΔR regions ($\Delta R < 1$) at $p_T^V < 250$ GeV, as the low ΔR regions suffer from mismodeling. The labels `staticHighDR` and `staticLowDR` refer to those regions, which are different from the ΔR control regions.

Nuisance parameter correlation matrix Similarly, the correlation between the signal strengths and nuisance parameters can be calculated using the second-order derivatives of the likelihood. When the parameters are positively correlated, the pulls tend to change in the same direction to maximize the likelihood. When they are negatively correlated, the pulls change in the opposite direction.

The correlation can shift events between regions, change signal strengths, and is thus important to understand. It is also important to verify whether the correlation is consistent between the data and the simulation. The correlation matrix of signal strengths in each lepton channel in the $VH(\to b\bar{b}, c\bar{c})$ phase space is shown in Figure 4.26. While the $VH(\to c\bar{c})$ signal strength does not have a strong correlation between the lepton channels (correlation coefficient < 0.15), the $VH(\to b\bar{b})$ signal strength tends to be correlated between the 0-lepton and 2-lepton channels (correlation coefficient $= 0.22$). The correlation between all nuisance parameters and the signal strengths is also studied.

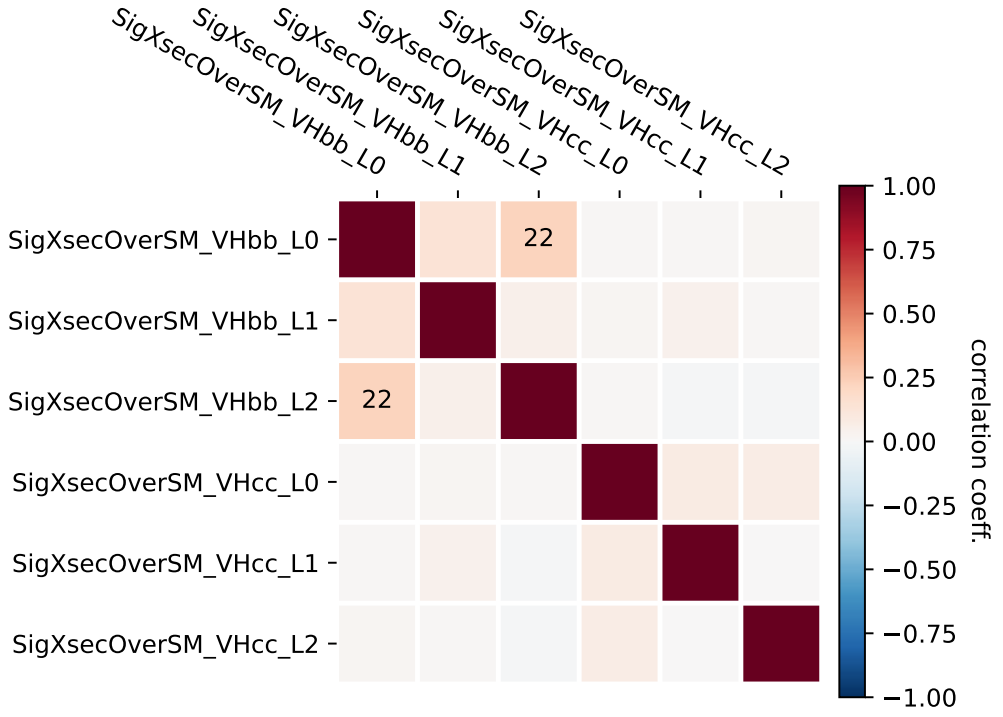

Figure 4.26: Correlation matrix for the signal strengths in the $VH(\to b\bar{b}, c\bar{c})$ fit [168]. The correlation coefficient is marked as percentages in the matrix, where 22 corresponds to a coefficient of 0.22.

Nuisance parameter ranking Given that there are approximately 2000 nuisance parameters in the fit, nuisance parameters are ranked according to their individual impact on the signal strengths $\mu_{VH(c\bar{c})}$ and $\mu_{VH(b\bar{b})}$ in the $VH(\to b\bar{b}, c\bar{c})$ fit. Figure 4.27 shows the ranking for $\mu_{VH(c\bar{c})}$ from the $VH(\to b\bar{b}, c\bar{c})$ fit. The color bars show the $\pm 1\sigma$ impact of the nuisance parameter on μ. The $\pm 1\sigma$ impact on μ is calculated as follows: first, set the nuisance parameter of interest α_p to the postfit value varied by the postfit constraint, i.e., $\hat{\alpha_p} \pm \sigma_{\hat{\alpha_p}}$; then, re-fit all other nuisance parameters to maximize the likelihood. The change in μ ($\Delta\mu$) is the $\pm 1\sigma$ impact of the nuisance parameter.

Figure 4.27 shows that the high-ranking nuisance parameters for the $VH(\to c\bar{c})$ signal strength tend to be the V+jets modeling uncertainties and floating normalizations. Some top modeling uncertainties and flavor tagging uncertainties are also highly ranked.

In addition to the nuisance parameter impact, the ranking plot also overlays the nuisance

parameter pulls and constraints, corresponding to the bottom axis. The floating normalization pulls are marked in pink dots. All other nuisance parameter pulls are marked in black dots. The floating normalization pulls tend to center around one, which correspond to the default MC normalizations.

Most high-ranking nuisance parameters are not pulled, such as `Carl_ShFxFx_staticHighDR_Zcc_150-250ptv`, and thus do not affect the observed signal strengths. Some high-ranking nuisance parameters are pulled and constrained, such as `Zhf_extrap_from_CRHigh_J2`. These pulled nuisance parameters have been carefully studied. For `Zhf_extrap_from_CRHigh_J2`, the SR/CR acceptance ratio uncertainties accommodate the difference of the $Z+hf$ yields in the signal regions and the high ΔR control regions. The $Z+hf$ process is a dominant background in the 0-lepton and 2-lepton channels. Comparing the data and MC yields in these regions, the correction needed between the data and the MC simulation is different in the SR versus the high ΔR CR. Therefore, the pull and constraint of the `Zhf_extrap_from_CRHigh_J2` nuisance parameter is reasonable.

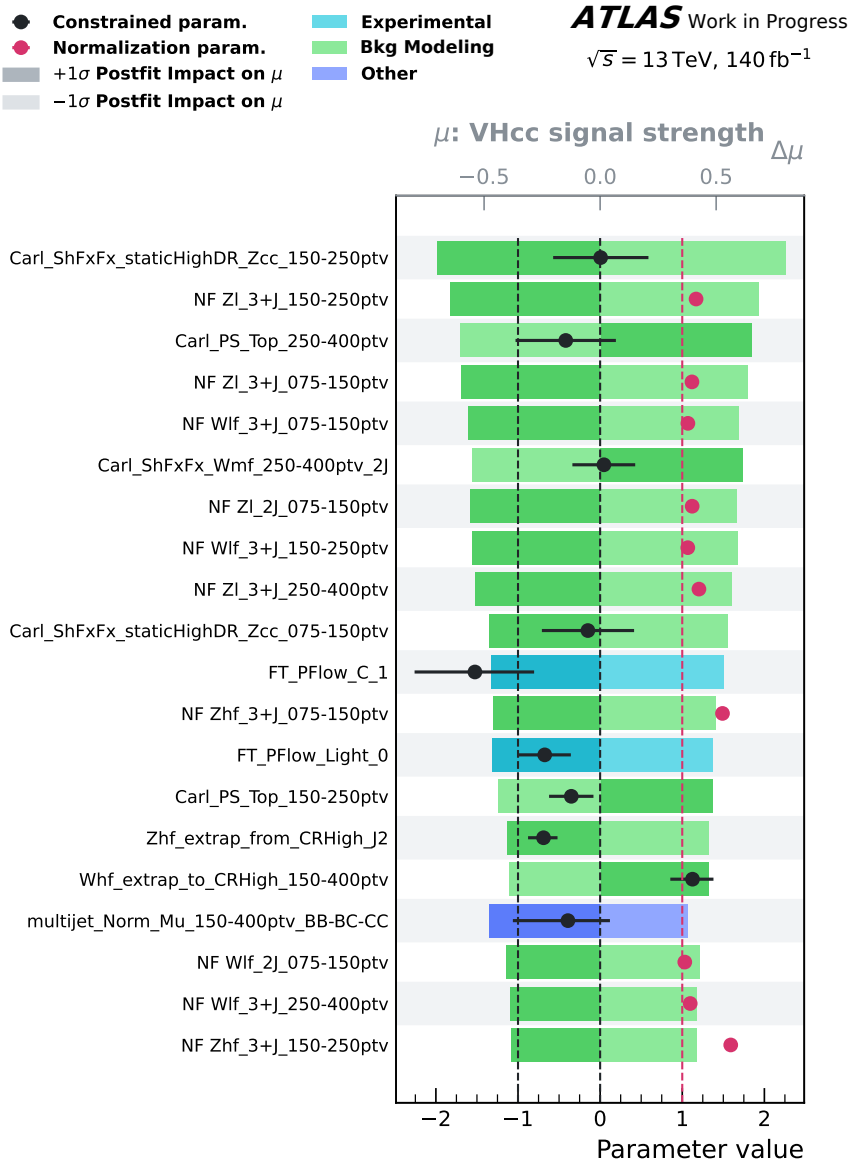

Figure 4.27: The nuisance parameter rankings for the $VH(\rightarrow c\bar{c})$ signal strength from the $VH(\rightarrow b\bar{b}, c\bar{c})$ fit [168]. For each nuisance parameter, the darker shades show the $+1\sigma$ impact on μ, while the lighter shades show the -1σ impact on μ. The nuisance parameter impact is marked in three different colors: blue for experimental uncertainty nuisance parameters, green for modeling uncertainty nuisance parameters, and purple for other nuisance parameters. In addition to the $\pm 1\sigma_{\hat{\alpha}_p}$ impact on μ, the pulls and constraints for the nuisance parameters are shown in black and pink dots with lines. The pink dots mark floating normalizations. The values of the pulls and constraints are measured by the bottom axis.

Prefit and postfit plots Lastly, examples of the prefit and postfit plots are shown in Figure 4.28 for the $VH(\rightarrow c\bar{c})$ 2-lepton regions. The 2-jet 2xt-tag signal and high ΔR control regions in the p_T^V 150-250 GeV bin are presented, along with the 2-jet top-$e\mu$ and V+light control regions in the same p_T^V range. The fit variable is the BDT output for the signal region, m_{cc} for the high ΔR control region, and p_T^V for the V+light control region. The top-$e\mu$ control region has one single bin. The high ΔR control regions in Figure 4.28 have a peak in m_{cc}. This peak is due to the ΔR-p_T^V cut and does not have physical meanings.

The prefit error bands tend to be large, and the postfit error bands are constrained due to the constraints of the nuisance parameters. The postfit data/simulation agreement is well around 1 as expected. The prefit simulation tends to underestimate the data. The prefit background yields tend to be smaller than the data. The postfit background composition for the 2-lepton channel is shown in Figure 4.29. The Z+jets process is the dominant background in the 2-lepton signal regions.

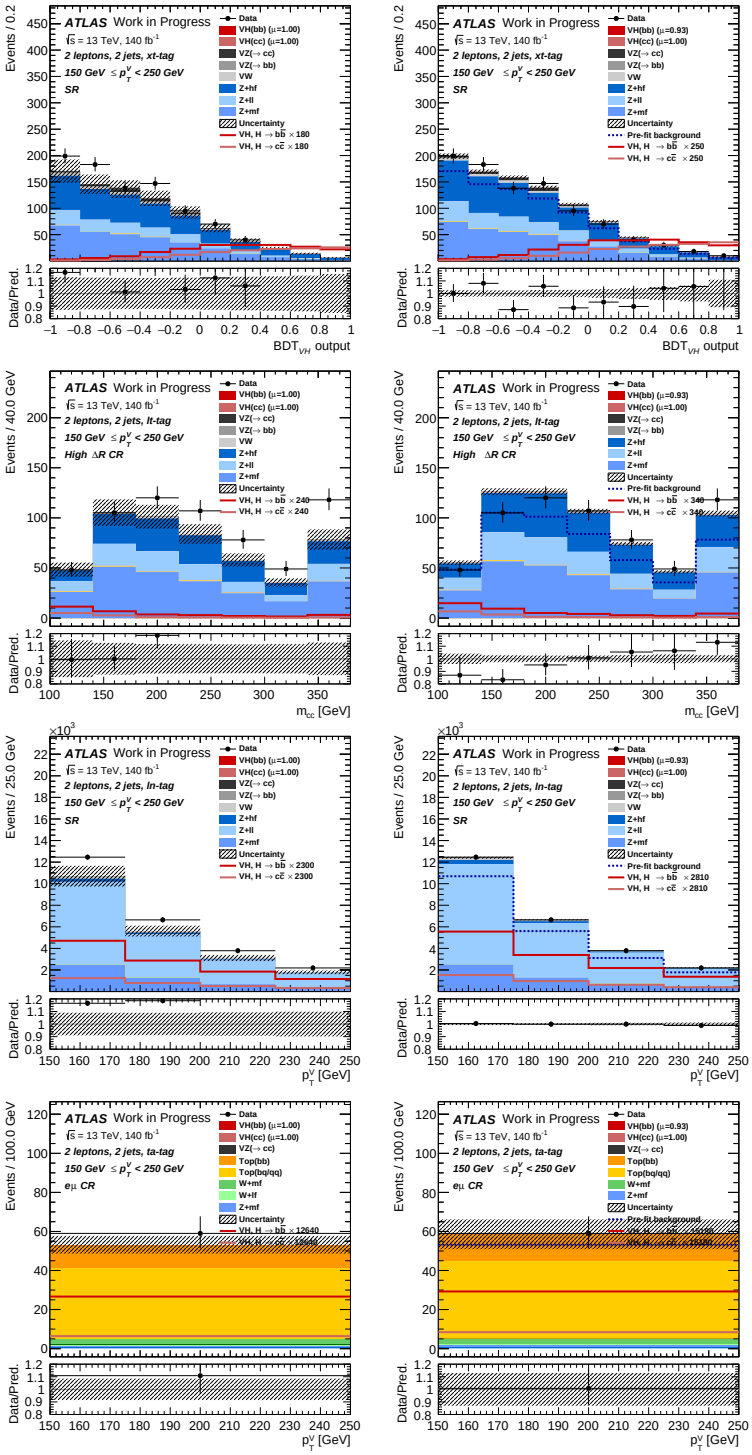

Figure 4.28: The prefit (left) and postfit (right) plots for the $VH(\rightarrow c\bar{c})$ 2-lepton channel in the signal region for 2-jet 2xt-tag at p_T^V 150-250 GeV (top row), the high ΔR control region for the 2lt-tag region (second row), the V+light control region with the 1ln-tag (third row), and the top-$e\mu$ control region (last row) [168].

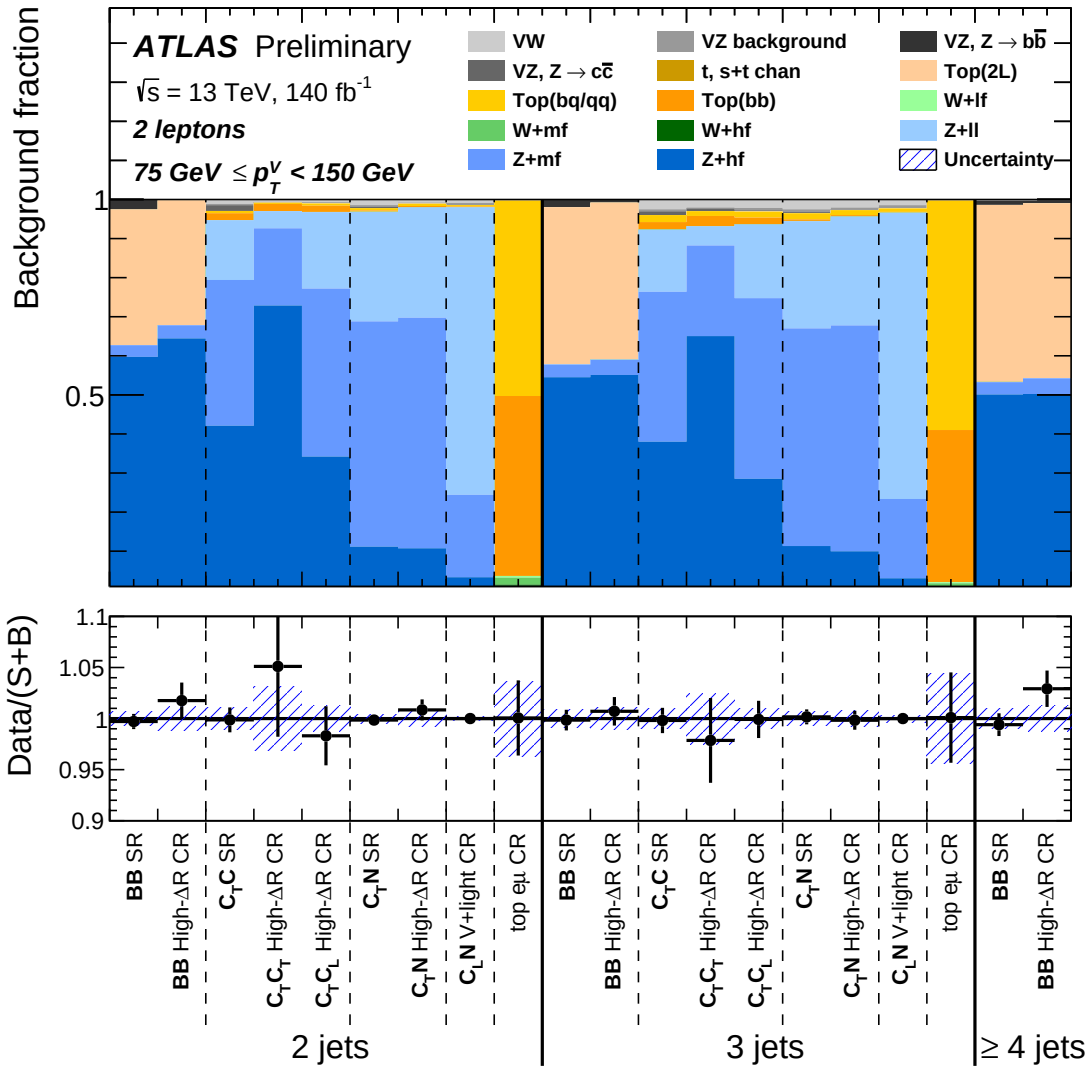

Figure 4.29: The postfit background composition in the $VH(\rightarrow b\bar{b}, c\bar{c})$ 2-lepton channel at the p_T^V of 75-150 GeV [1]. Here, BB stands for the 2b-tag regions in the $VH(\rightarrow b\bar{b})$ phase space. And, C_TC refers to the 2xt-tag $VH(\rightarrow c\bar{c})$ signal regions. C_TC_T and C_TC_L refer to the 2tt and 2lt-tag high ΔR regions. C_TN refers to the 1tn-tag regions. C_LN refers to the 1ln-tag V+light control regions. The top-$e\mu$ control regions consist of more than 90% top backgrounds.

4.6.3 Final results

After validating all fit diagnostic results, the final statistical analysis results are presented in this section. The final results are obtained from two kinds of fits: the $VZ(\to b\bar{b}, c\bar{c})$ fit and the $VH(\to b\bar{b}, c\bar{c})$ fit.

The diboson $VZ(\to b\bar{b}, c\bar{c})$ fit is used as a validation for the $VH(\to b\bar{b}, c\bar{c})$ results. In the $VZ(\to b\bar{b}, c\bar{c})$ diboson fit, the diboson samples are floated and treated as signals, while the VH samples are not floated. The modeling uncertainties are the same as in the default $VH(\to b\bar{b}, c\bar{c})$ fit. All pulls between the diboson fit and the $VH(\to b\bar{b}, c\bar{c})$ fit are similar. The diboson fit uses the diboson MVA. The diboson MVA, trained similarly to the default $VH(\to b\bar{b}, c\bar{c})$ MVA, uses the diboson samples as the signal and includes the VH signal samples as one of the backgrounds.

The $VZ(\to b\bar{b}, c\bar{c})$ and $VH(\to b\bar{b}, c\bar{c})$ results are presented in the following four sections. Section 4.6.3.1 presents the signal strengths from the $VZ(\to b\bar{b}, c\bar{c})$ and $VH(\to b\bar{b}, c\bar{c})$ fits. Section 4.6.3.2 presents the uncertainty breakdown of the $VZ(\to c\bar{c})$ and $VH(\to c\bar{c})$ signal strengths from the combined $VZ(\to b\bar{b}, c\bar{c})$ and $VH(\to b\bar{b}, c\bar{c})$ fits. Section 4.6.3.3 discusses the hypothesis testing results from the $VZ(\to b\bar{b}, c\bar{c})$ and $VH(\to b\bar{b}, c\bar{c})$ fits, including the $VZ(\to b\bar{b}, c\bar{c})$ and $VH(\to b\bar{b})$ significances and the $VH(\to c\bar{c})$ upper limits. Section 4.6.3.4 presents all $VH(\to b\bar{b}, c\bar{c})$ κ framework interpretations. All fit results presented in Sections 4.6.3.1-4.6.3.4 are obtained by fitting all three lepton channels. Section 4.6.3.5 presents additional results from the 2-lepton standalone fit. In general, the discussions focus on the $VH(\to c\bar{c})$ results.

4.6.3.1 VZ and VH signal strengths

The VH signal strengths $\mu_{VH(c\bar{c})}$ and $\mu_{VH(b\bar{b})}$ are defined in Equations 4.13-4.14. After minimizing the negative log likelihood function $(-\ln \mathcal{L}(\vec{\mu}, \vec{\alpha_p}, \vec{\tau}, \vec{\gamma}))$, the observed best-fit signal strengths $(\hat{\vec{\mu}})$ are extracted from the $VH(\to b\bar{b}, c\bar{c})$ fit:

$$\mu_{VH(c\bar{c})} = 1.0 \pm 5.3 \text{ (total)} = 1.0 \pm 4.0 \text{ (stat.)} \pm 3.6 \text{ (syst.)} \tag{4.28}$$

$$\mu_{VH(b\bar{b})} = 0.91 \pm 0.15 \text{ (total)} = 0.91 \pm 0.10 \text{ (stat.)} \pm 0.12 \text{ (syst.)} \tag{4.29}$$

The VZ signal strengths $\mu_{VZ(c\bar{c})}$ and $\mu_{VZ(b\bar{b})}$ are defined similarly as the VH signal strengths and extracted from the $VZ(\to b\bar{b}, c\bar{c})$ fit:

$$\mu_{VZ(c\bar{c})} = 0.97 \pm 0.13 \text{ (stat.)} \pm 0.20 \text{ (syst.)} \tag{4.30}$$

$$\mu_{VZ(b\bar{b})} = 0.91 \pm 0.05 \text{ (stat.)} \pm 0.11 \text{ (syst.)} \tag{4.31}$$

All VH and VZ signal strengths agree with the SM predictions (when $\mu = 1$) within uncertainties. The $VH(\to b\bar{b})$ and $VZ(\to b\bar{b}, c\bar{c})$ signal strength uncertainties are between 10 to 20%, while the $VH(\to c\bar{c})$ signal strength uncertainty is around five. Unlike $\mu_{VH(b\bar{b})}$, $\mu_{VZ(c\bar{c})}$, and $\mu_{VZ(b\bar{b})}$, the $\mu_{VH(c\bar{c})}$ statistical uncertainty (4.0) is larger than the systematic

uncertainty (3.6). More details about the $\mu_{VH(c\bar{c})}$ uncertainty breakdown are discussed in Section 4.6.3.2.

The signal strengths are obtained separately for each lepton channel in the combined $VH(\rightarrow b\bar{b}, c\bar{c})$ and $VZ(\rightarrow b\bar{b}, c\bar{c})$ fits. The signal strengths $\mu_{VH(c\bar{c})}$ and $\mu_{VZ(c\bar{c})}$ in 0-lepton, 1-lepton, and 2-lepton are shown in Figure 4.30. The 2-lepton $\mu_{VH(c\bar{c})}$ has larger statistical uncertainties compared to the other two channels while smaller systematic uncertainties. The 2-lepton, 1-lepton, and 0-lepton $\mu_{VH(c\bar{c})}$, statistical and systematic uncertainties are $4.3^{+7.6}_{-7.3}$ (stat.) $^{+5.1}_{-4.5}$ (syst.), $3.8^{+6.2}_{-6.1}$ (stat.) $^{+6.5}_{-6.1}$ (syst.), and $-5.7^{+6.8}_{-6.6}$ (stat.) $^{+5.3}_{-5.5}$ (syst.) respectively. The 2-lepton statistical uncertainties are roughly 20% (10%) larger than 1-lepton (0-lepton), while the 2-lepton systematic uncertainties are approximately 20% (10%) smaller. Overall, the total uncertainties are comparable for the 0-lepton, 1-lepton, and 2-lepton $VH(\rightarrow c\bar{c})$ signal strengths. The statistical uncertainties increase from 1-lepton, 0-lepton, to 2-lepton because for the VH events, the 1-lepton WH cross section is larger than the 0-lepton or 2-lepton ZH cross sections [196]. For the ZH process, the 0-lepton branching ratio is larger than the 2-lepton branching ratio [14]. The systematic uncertainties increase from 2-lepton, 0-lepton to 1-lepton as the signal-to-background ratio decreases from 2-lepton, 0-lepton to 1-lepton.

The 0-lepton $\mu_{VH(c\bar{c})}$ fluctuates downward compared to the other two channels. In general, the $\mu_{VH(c\bar{c})}$ values in all three lepton channels are consistent with the SM prediction within uncertainties. For the VZ fit, the 2-lepton $\mu_{VZ(c\bar{c})}$ fluctuates downward compared to the other two channels. The 0-lepton and 1-lepton $\mu_{VZ(c\bar{c})}$ values are consistent with the SM prediction within uncertainties.

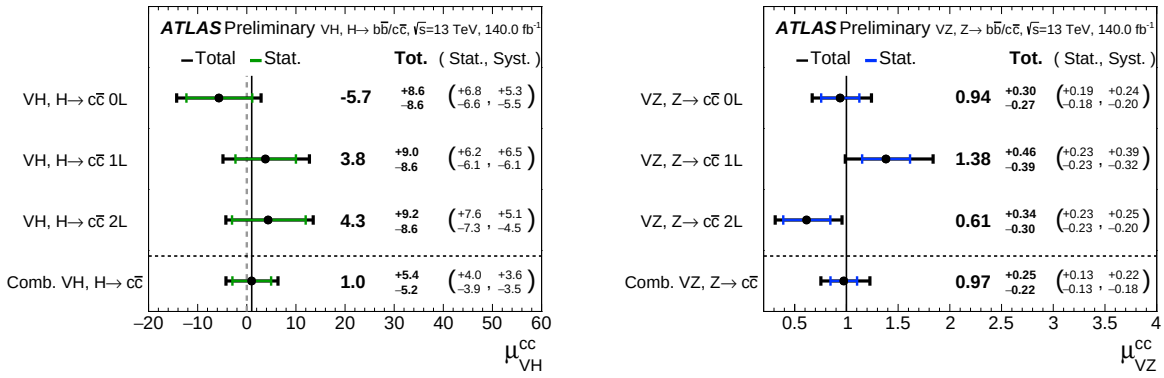

Figure 4.30: The signal strengths decorrelated in 0-lepton, 1-lepton, and 2-lepton channels for $\mu_{VH(c\bar{c})}$ (left) and $\mu_{VZ(c\bar{c})}$ (right) [1]. The statistical uncertainties are displayed in the green and blue bars.

4.6.3.2 VH(cc) signal strength uncertainty breakdowns

The uncertainty breakdown of the combined $\mu_{VH(c\bar{c})}$ signal strength in all lepton channels (Equation 4.28) is summarized in Table 4.27. For $\mu_{VH(c\bar{c})}$, the total uncertainty is 5.29. The statistical uncertainty (3.94) is around 10% larger than the systematic uncertainty (3.53). The systematic uncertainty is dominated by the V+jets background modeling uncertainties (1.76 for Z+jets and 1.41 for W+jets). The uncertainty of the limited simulation sample size (1.61) is also a major source of the systematic uncertainty. The experimental uncertainties from flavor tagging (such as 0.73 for c-jets) and jets (1.0) are other important sources. The flavor tagging uncertainties are reduced compared to the previous ATLAS $VH(\rightarrow c\bar{c})$ analysis due to improved calibration (such as 0.73 compared to 1.6 for c-jets) [2].

Source of uncertainty	$\mu_{VH(c\bar{c})}$
Total	5.29
Statistical	3.94
Systematic	3.53
Statistical uncertainties	
Data statistical uncertainties	3.70
Top-$e\mu$ control region	0.06
Background floating normalizations	1.23
Other VH floating normalizations	0.24
Simulation samples size	1.61
Theoretical and modeling uncertainties	
VH	0.56
Z+jets	1.76
W+jets	1.41
$t\bar{t}$ and single top Wt-channel	1.03
Single top s- and t-channel	0.15
Diboson	0.51
Multi-jet	0.57
Experimental uncertainties	
Jets	1.00
E_T^{miss}	0.24
Leptons	0.23
Pileup	0.24
Luminosity	0.08
Flavor tagging	
c-jets	0.73
l-jets	0.67
b-jets	0.30

Table 4.27: Sources of uncertainties for $\mu_{VH(c\bar{c})}$. The uncertainties are dimensionless. The mean of the absolute up and down uncertainties are listed.

4.6.3.3 VZ and VH hypothesis testing

Once the signal strengths are extracted, the significance of the diboson and $VH(\rightarrow b\bar{b})$ signals, and the $VH(\rightarrow c\bar{c})$ upper limit can be calculated following the hypothesis testing method discussed in Section 4.6.1. In the case of $VH(\rightarrow c\bar{c})$, as the significance is low, the

upper limit is presented instead. The observed and expected significance is listed below:

$$\text{Observed (expected) } VZ(b\bar{b}) \text{ significance: 13.8 (15.0) standard deviations} \tag{4.32}$$

$$\text{Observed (expected) } VZ(c\bar{c}) \text{ significance: 5.2 (5.3) standard deviations} \tag{4.33}$$

$$\text{Observed (expected) } VH(b\bar{b}) \text{ significance: 7.4 (8.0) standard deviations} \tag{4.34}$$

The expected results are calculated from the postfit Asimov fit. Both $VZ(\to b\bar{b})$ and $VZ(\to c\bar{c})$ have been observed, as the observed significances are larger than 5σ. This is the first observation of $VZ(\to c\bar{c})$ in ATLAS. The $VZ(\to c\bar{c})$ process was first observed in the CMS $VH(\to c\bar{c})$ analysis at the LHC last year [39].

The $VH(\to c\bar{c})$ upper limits are calculated for each lepton channel and for all three channels combined in the $VH(\to b\bar{b}, c\bar{c})$ fit. The observed (expected) $VH(\to c\bar{c})$ upper limit is 11.3 (10.4) times the SM prediction at the 95% confidence level (CL). Figure 4.31 shows the observed and expected upper limits in all lepton channels. The expected upper limit from all lepton channels is reduced by a factor of three compared to the previous ATLAS analysis using the same Run 2 dataset [2]. The observed upper limit improves around 20% compared to CMS [39]. This is driven primarily by the addition of MVA and the PCFT scheme. The 2-lepton expected upper limit improves around 60% compared to the previous analysis.

The 68% and 95% CL contours of the $VH(\to b\bar{b})$ and $VH(\to c\bar{c})$ signal strengths can be scanned over the 2D plane of $\mu_{VH(c\bar{c})}$ and $\mu_{VH(b\bar{b})}$, as shown in Figure 4.32. The 2D scan illustrates the signal sensitivities in two dimensions. The CL contours have a larger range in $\mu_{VH(c\bar{c})}$ as the $VH(\to c\bar{c})$ sensitivity is worse compared to $VH(\to b\bar{b})$. It also indicates the agreement between the measurement and the SM prediction in two dimensions.

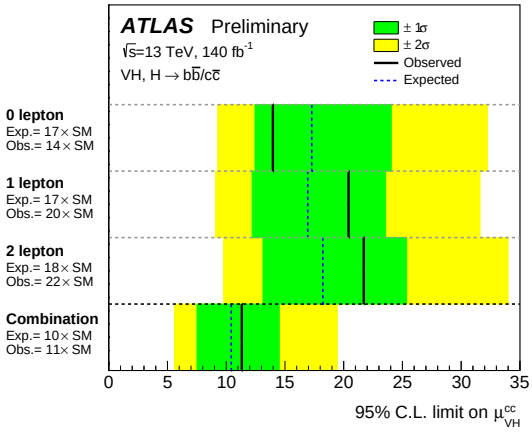

Figure 4.31: The $VH(\to c\bar{c})$ upper limits from the $VH(\to b\bar{b}, c\bar{c})$ fit [1].

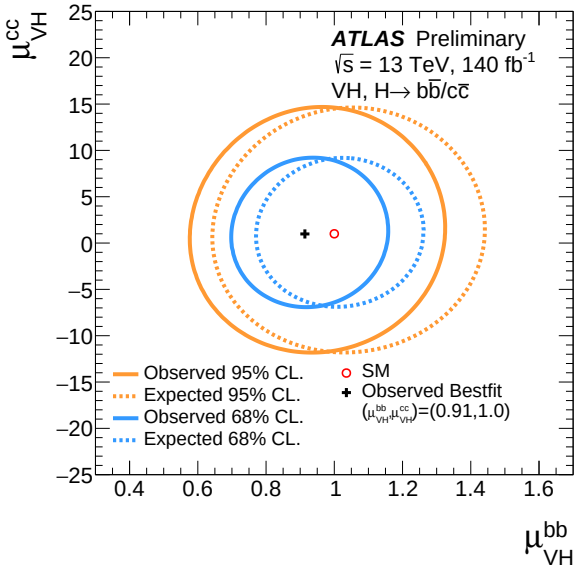

Figure 4.32: The 2D likelihood scans over $\mu_{VH(b\bar{b})}$ and $\mu_{VH(c\bar{c})}$ in the x and y axis [1]. The expected best-fit is marked by the blue cross at (1, 1), overlapping with the SM prediction marked by the red circle. The observed best-fit is marked by the black cross at (0.91, 1.0). The observed (expected) 68% and 95% CL contours are drawn in blue and orange solid lines (dash lines).

4.6.3.4 VH kappa interpretations

Lastly, the $VH(\rightarrow b\bar{b}, c\bar{c})$ signal strengths can be interpreted in the κ framework (introduced in Section 2.2.2). The SM Higgs-charm and Higgs-bottom Yukawa couplings (y_c and y_b) are modified as $\kappa_c y_c$ and $\kappa_b y_b$. Therefore, the $\mu_{VH(c\bar{c})}$ and $\mu_{VH(b\bar{b})}$ can be parameterized using κ_c and κ_b. A two-dimensional likelihood scan is performed over κ_b and κ_c. The parameterizations for the 2D κ scan are as follows:

$$\mu_{VH(c\bar{c})} = \frac{\kappa_c^2}{1 + (\kappa_b^2 - 1)BR(H \rightarrow b\bar{b}) + (\kappa_c^2 - 1)BR(H \rightarrow c\bar{c})} \tag{4.35}$$

$$\mu_{VH(b\bar{b})} = \frac{\kappa_b^2}{1 + (\kappa_b^2 - 1)BR(H \rightarrow b\bar{b}) + (\kappa_c^2 - 1)BR(H \rightarrow c\bar{c})} \tag{4.36}$$

The parameterizations only consider SM Higgs decays and all couplings are set to the SM predictions except κ_b and κ_c [2]. The branching ratios of the Higgs to bottom and charm quarks, $BR(H \rightarrow b\bar{b})$ and $BR(H \rightarrow c\bar{c})$, are set to the SM values of 58.2% and 2.9%. In these parameterizations, when defining the signal strengths in Equations 4.13-4.14, the measured cross section of the VH process ($[\sigma_{VH}]_{\text{measured}}$) is assumed to be the same as the SM prediction ($[\sigma_{VH}]_{\text{SM}}$). The parameters κ_c and κ_b modify the branching ratio $BR(H \rightarrow c\bar{c})$

and $BR(H \to b\bar{b})$ by changing the Higgs partial decay widths in the numerators ($\Gamma_H^{c\bar{c}}$ and $\Gamma_H^{b\bar{b}}$) and the Higgs total decay width in the denominators (Γ_H^{total}).

With the parameterizations, the expected and observed 68% and 95% CL contours are drawn for κ_b and κ_c as shown in Figure 4.33. The absolute value of κ_c ($|\kappa_c|$) tends to increase with increasing $|\kappa_b|$. There is good agreement between the expected and observed best-fit (κ_b, κ_c) and CL contours. While this analysis is not sensitive to the positive and negative signs of κ_c and κ_b, it is safe to assume that all κ modifiers have the positive signs as discussed in Section 2.2.2. The direct constraint on κ_c and κ_b from measuring the $VH(\to b\bar{b}, c\bar{c})$ process is complementary to the indirect constraint on κ_c and κ_b from the $H \to ZZ^*$ and $H \to \gamma\gamma$ combination [227]. The indirect constraints are set by considering the impact of κ_c and κ_b over the total Higgs width and the p_T^H distribution.

In addition to the 2D κ likelihood scans, 1D likelihood scans can also be performed to understand the κ_c constraints more carefully. The 1D scan over κ_c is performed without parameterizing $\mu_{VH(b\bar{b})}$ in terms of κ_b and setting κ_b equal to one for the κ_c parameterization. The $VH(\to b\bar{b})$ signal strength is left free floating in the fit. Therefore, the κ_c parameterization becomes:

$$\mu_{VH(c\bar{c})} = \frac{\kappa_c^2}{1 + (\kappa_c^2 - 1)BR(H \to c\bar{c})} \tag{4.37}$$

The 1D likelihood scan over κ_c is shown in Figure 4.34. The observed (expected) 95% CL upper limit is $|\kappa_c| < 4.2$ ($|\kappa_c| < 4.1$). This is the most stringent limit on κ_c to date. It improves by a factor of two compared to the previous ATLAS $VH(\to c\bar{c})$ analysis [2]. The latest CMS $VH(\to c\bar{c})$ analysis observes $1.1 < |\kappa_c| < 5.5$ at the 95% CL [39]. The $|\kappa_c|$ upper limit of 4.2 presented improves the CMS upper bound by around 20%.

Similarly, κ_c/κ_b upper limits can be extracted. The parameterization of the signal strengths to the ratio κ_c/κ_b is shown in Equation 4.38-4.39:

$$\mu_{VH(c\bar{c})} = \left(\frac{\kappa_c}{\kappa_b}\right)^2 \left(\frac{\kappa_b}{\kappa_H}\right)^2 \tag{4.38}$$

$$\mu_{VH(b\bar{b})} = \left(\frac{\kappa_b}{\kappa_H}\right)^2 \tag{4.39}$$

The parameterizations are different from the 2D κ scan parameterizations in Equations 4.35-4.36. While floating $\mu_{VH(b\bar{b})}$ and thus κ_b/κ_H, the ratio κ_c/κ_b is independent of BSM modifications to other Higgs production and decay channels and the Higgs total width, which makes it a powerful probe of the SM.

The 1D likelihood scan of κ_c/κ_b is shown in Figure 4.35. The observed (expected) κ_c/κ_b upper limit at 95% CL is $|\kappa_c/\kappa_b| < 3.6\,(3.5)$. The κ_c/κ_b parameterization is updated from the previous analysis. The observed κ_c/κ_b 95% CL upper limit is about 20% more stringent than before.

In Figure 4.35, the green lines show the κ_c/κ_b ratio at 4.578 when the Higgs-bottom and Higgs-charm coupling strengths are equal ($|\kappa_c y_c| = |\kappa_b y_b|$). The SM Yukawa coupling

strengths y_c and y_b are proportional to the masses of the charm and bottom quarks. Therefore, when $|\kappa_c y_c| = |\kappa_b y_b|$, $\kappa_c/\kappa_b = y_b/y_c = m_b/m_c = 4.578 \pm 0.008$ [228]. The observed (expected) κ_c/κ_b ratio of 3.6 (3.5) is smaller than 4.578. This means that the BSM scenario when the Higgs-charm coupling strength is the same as the Higgs-bottom coupling strength ($|\kappa_c y_c| = |\kappa_b y_b|$) is excluded at the 95% CL.

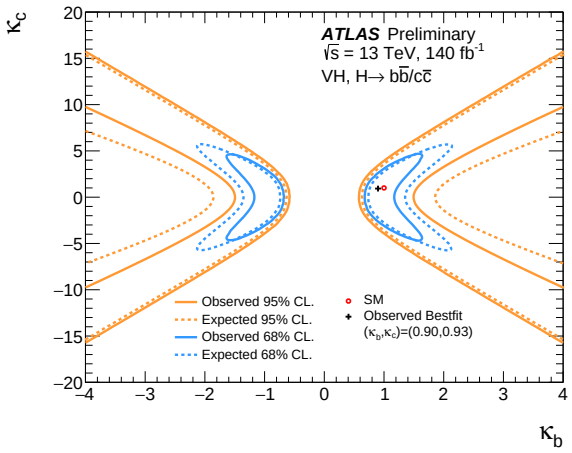

Figure 4.33: The 2D likelihood scans over κ_b and κ_c in the x and y axis [1]. The expected best-fit is marked by the blue cross at (1, 1), overlapping with the SM prediction. The observed best-fit is marked by the black cross at (0.90, 0.93). The observed (expected) 68% and 95% CL contours are drawn in blue and orange solid lines (dash lines).

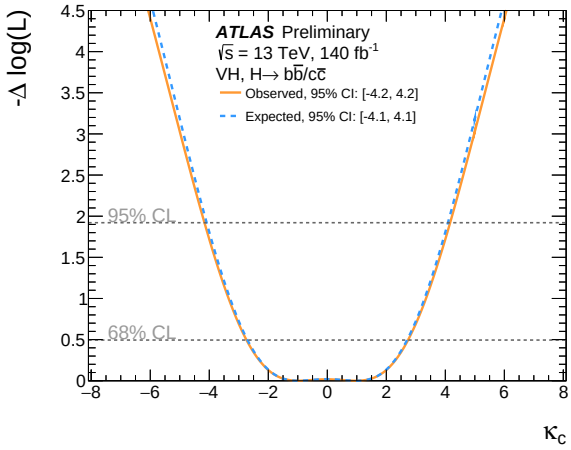

Figure 4.34: The 1D κ_c likelihood scan [1]. The observed and expected likelihood profiles are shown in orange solid and blue dash lines. The 68% and 95% CLs are drawn in grey dash lines. The observed κ_c likelihood agrees well with the expected. The likelihood scan is performed with κ_b fixed to one.

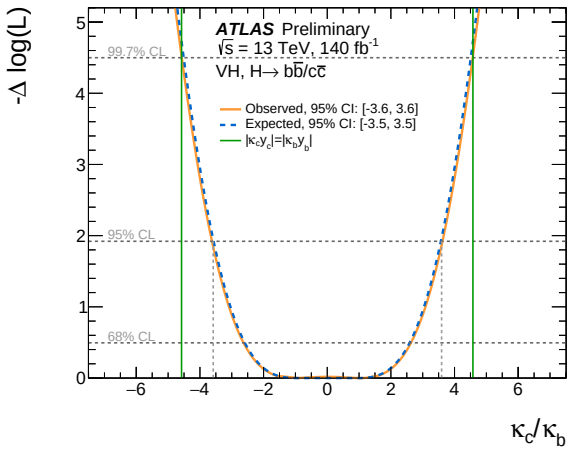

Figure 4.35: The 1D κ_c/κ_b likelihood scan [1]. The observed and expected likelihood profiles are shown in orange solid and blue dash lines. The 68% and 95% CLs are drawn in grey dash lines. Green lines are drawn at $\kappa_c/\kappa_b = 4.578$, at which $\kappa_c/\kappa_b = y_b/y_c = m_b/m_c$ [228].

4.6.3.5 2-lepton only results

In this thesis, the $VH(\rightarrow b\bar{b}, c\bar{c})$ signal strengths, upper limits, and κ interpretations are investigated in the 2-lepton standalone $VH(\rightarrow b\bar{b}, c\bar{c})$ fit to supplement the official results from fitting all three lepton channels. The 2-lepton standalone $VH(\rightarrow b\bar{b}, c\bar{c})$ signal strengths are:

$$\mu_{VH(c\bar{c})} = 5.9 \pm 9.4 \text{ (total)} \tag{4.40}$$

$$\mu_{VH(b\bar{b})} = 0.85 \pm 0.26 \text{ (total)} \tag{4.41}$$

The 2-lepton only $VH(\rightarrow c\bar{c})$ signal strength (signal strength uncertainty) is approximately 40% (6%) larger than the 2-lepton $VH(\rightarrow c\bar{c})$ signal strength and uncertainty obtained from fitting all three lepton channels in Figure 4.30. Although the 2-lepton only $VH(\rightarrow c\bar{c})$ signal strength (5.9) differs from the 2-lepton result when fitting all lepton channels (4.3), they agree within uncertainties (around 9). Most background modeling nuisance parameters are correlated between the lepton channels. The 2-lepton only fit background composition and signal strength are expected to be slightly different from the fit with all lepton channels.

The $VH(\rightarrow c\bar{c})$ upper limit and the $VH(\rightarrow b\bar{b})$ significance are:

Observed (expected) $VH(b\bar{b})$ significance: 3.6 (4.1) standard deviations (4.42)

Observed (expected) $VH(c\bar{c})$ upper limit: 24 (19) $\times$ SM prediction at the 95% CL (4.43)

The 2-lepton only observed (expected) $VH(\rightarrow c\bar{c})$ upper limit is approximately 10% (6%) larger than the 2-lepton upper limits from fitting all three lepton channels in Figure 4.31.

In Figure 4.36, the 68% and 95% CL contours are drawn over the 2D plane of $\mu_{VH(b\bar{b})}$ and $\mu_{VH(c\bar{c})}$ from the 2-lepton standalone fit. Compared to Figure 4.32, the $VH(\rightarrow c\bar{c})$ best-fit signal strength in the 2-lepton standalone fit (5.9) is larger than that in the fit with all three lepton channels (1.0). In Figure 4.36, the 2-lepton standalone fit observed and expected signal strengths agree within the contour of 68% CL.

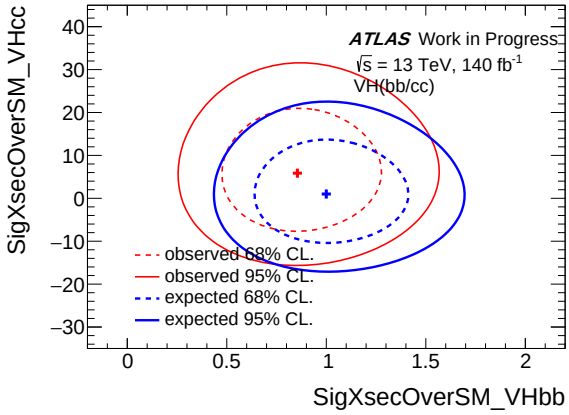

Figure 4.36: The 2D likelihood scans over $\mu_{VH(b\bar{b})}$ and $\mu_{VH(c\bar{c})}$ in the x and y axis in the 2-lepton standalone $VH(\rightarrow b\bar{b}, c\bar{c})$ fit. The expected best-fit is marked by the blue cross at (1, 1). The observed best-fit is marked by the red cross at (0.85, 5.9). The observed (expected) 68% and 95% CL contours are drawn in red (blue) dash and solid lines.

2-lepton only kappa interpretations Using Equations 4.35-4.36, the 68% and 95% CL contours are drawn over the 2D plane of κ_b and κ_c in Figure 4.37. Compared to Figure 4.33 from fitting all three lepton channels, the expected 68% and 95% CL contours enclose larger phase spaces in the 2-lepton standalone fit as the 2-lepton fit sensitivity is lower. For example, at $\kappa_b = 4$, approximately $|\kappa_c| \gtrsim 15$ ($|\kappa_c| \gtrsim 20$) at the 95% CL in Figure 4.33 (Figure 4.37). As the observed $VH(\rightarrow c\bar{c})$ signal strength (5.9) and upper limit (24) are larger than the expected signal strength (1.0) and upper limit (19) in the 2-lepton standalone fit, at the same κ_b, the observed $|\kappa_c|$ limits tend to be larger from the observed contours than the expected contours. For example, at $\kappa_b = 4$, approximately $|\kappa_c| \gtrsim 30$ ($|\kappa_c| \gtrsim 20$) at the observed (expected) 95% CL in Figure 4.37.

Using Equation 4.37, the 1D likelihood scan is performed over κ_c with $\mu_{VH(b\bar{b})}$ free floating in Figure 4.38. The observed κ_c likelihood profile (red curve) has a bump in the middle, favoring a higher value of $|\kappa_c|$ than zero. The observed (expected) 95% CL of κ_c is: $|\kappa_c| < 10.1$ ($|\kappa_c| < 6.0$). The observed κ_c upper limit is larger than the expected limit. Compared to Figure 4.34, the expected 2-lepton standalone $|\kappa_c|$ upper limit (6.0) is approximately 50% larger.

Using Equations 4.38-4.39, the 1D likelihood scan is performed over κ_c/κ_b with κ_b/κ_H floated in Figure 4.39. Similar to Figure 4.38, the observed κ_c/κ_b likelihood profile (red curve) also has a bump in the middle, favoring a higher value of κ_c/κ_b than zero. The observed (expected) 95% CL of κ_c/κ_b is: $|\kappa_c/\kappa_b| < 6.2$ ($|\kappa_c/\kappa_b| < 4.5$). Compared to Figure 4.35, the expected 2-lepton standalone $|\kappa_c/\kappa_b|$ upper limit is approximately 30% larger.

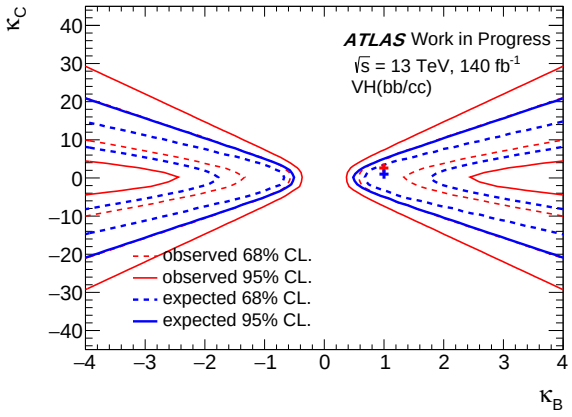

Figure 4.37: The 2D likelihood scans over κ_b and κ_c in the x and y axis from the 2-lepton standalone $VH(\rightarrow b\bar{b}, c\bar{c})$ fit. The expected best-fit is marked by the blue cross at (1, 1). The observed best-fit is marked by the red cross at (1.00, 2.61). The observed (expected) 68% and 95% CL contours are drawn in red (blue) dash and solid lines.

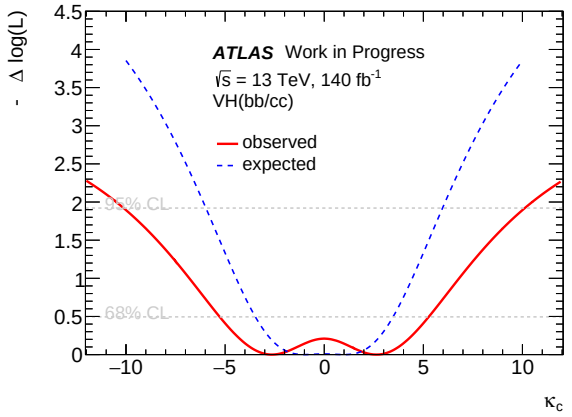

Figure 4.38: The 1D κ_c likelihood scan. The observed and expected likelihood profiles are shown in red solid and blue dash lines. The 68% and 95% CLs are drawn in grey dash lines. The observed (expected) 95% CL of κ_c is: $|\kappa_c| < 10.1$ ($|\kappa_c| < 6.0$). The likelihood scan is performed with $\mu_{VH(b\bar{b})}$ free floating.

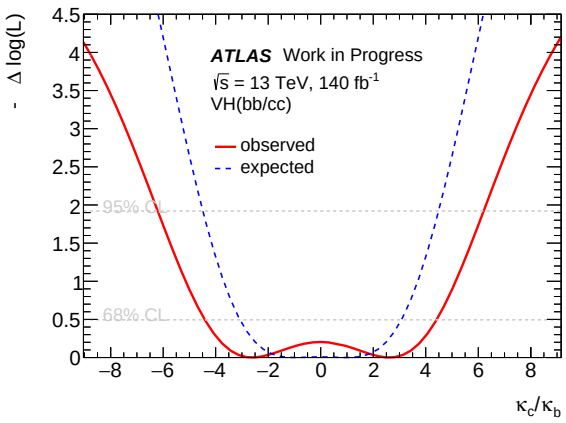

Figure 4.39: The 1D κ_c/κ_b likelihood scan. The observed and expected likelihood profiles are shown in red solid and blue dash lines. The 68% and 95% CLs are drawn in grey dash lines. The observed (expected) 95% CL of κ_c/κ_b is: $|\kappa_c/\kappa_b| < 6.2$ ($|\kappa_c/\kappa_b| < 4.5$). The likelihood scan is performed with κ_b/κ_H free floating.

4.7 Summary and outlook

In summary, this chapter discusses the Run 2 $VH(\to b\bar{b}, c\bar{c})$ analysis at ATLAS. Due to the focus of the thesis work, this chapter discusses in more detail the $VH(\to c\bar{c})$ phase space and results.

The analysis is validated through a diboson fit. The diboson measurements are consistent with the SM predictions. The observed (expected) significance is 13.8 (15.0) and 5.2 (5.3) standard deviations for $VZ(\to b\bar{b})$ and $VZ(\to c\bar{c})$. $VZ(\to c\bar{c})$ is observed for the first time in ATLAS.

The observed (expected) $VH(\to c\bar{c})$ upper limit is set to 11.3 (10.4) times the SM at the 95 % confidence level (CL). The expected upper limit is 3 times more stringent compared to the previous analysis [2]. There is good agreement between the expected and observed upper limit. The improvements mainly come from the use of the MVA and PCFT scheme. Most shape uncertainties from the alternative samples are derived using CARL, a machine learning package. CARL can reweight the nominal MC templates to resemble the alternative sample templates in all regions and for all MVA input variables and thus avoid large statistical fluctuations from directly using the alternative templates. The known mismodeling issue in SHERPA 2.2.11 is also addressed by including a SHERPA 2.2.1 p_T^V shape uncertainty constrained by control regions fitting p_T^V. The final statistical interpretation is fully harmonized between $VH(\to c\bar{c})$ and $VH(\to b\bar{b})$.

The $VH(\to b\bar{b}, c\bar{c})$ signal strengths are also parameterized in the κ framework. The observed (expected) κ_c upper limit at 95% CL is $|\kappa_c| < 4.2$ (4.1). This is the most stringent upper limit on κ_c to date. The observed (expected) κ_c/κ_b upper limit at 95% CL is $|\kappa_c/\kappa_b| < 3.6$ (3.5). This indicates that the Higgs-charm coupling strength is weaker than the Higgs-bottom coupling. In this thesis, the statistical interpretations of the 2-lepton standalone fit are also presented. In general, the 2-lepton only results, such as the upper limits of the $VH(\to c\bar{c})$ signal strength, κ_c, and κ_c/κ_b, are less stringent compared to the upper limits set by all three lepton channels.

More results, such as $VH(\to b\bar{b})$ interpretations in the simplified template cross section (STXS) framework, effective field theory interpretations, and combination with other Higgs measurements, can be extracted from the analysis. Looking ahead, the datasets from the ongoing LHC Run 3 could further decrease the statistical uncertainties of the $VH(\to c\bar{c})$ analysis. In addition, the previous HL-LHC $VH(\to c\bar{c})$ forecast needs to be updated to account for the latest analysis updates [229].

Chapter 5

High luminosity LHC upgrade and silicon detector

Higgs physics is entering a precision era at the high-luminosity LHC (HL-LHC). The HL-LHC is planned to start in 2029. In this chapter, an overview of the HL-LHC collider, the physics prospect, and the ATLAS detector upgrades is presented in Section 5.1. Section 5.1.1.1 discusses the ATLAS inner tracker pixel detector upgrade in more detail. The focus then shifts to the basic silicon detector mechanism in Section 5.2. Section 5.2.3 focuses on the radiation damage of the silicon detector and quantifies the HL-LHC expected radiation damage on the pixel detector. Lastly, the radiation testing of the pixel detector readout chip is discussed in Section 5.3.

5.1 HL-LHC upgrades and physics

The Run 2 peak luminosity of the LHC was approximately 21×10^{33} cm^{-2}s^{-1} at the center-of-mass energy $\sqrt{s} = 13$ TeV. In Run 3, the peak luminosity is approximately 24×10^{33} cm^{-2}s^{-1} at $\sqrt{s} = 13.6$ TeV [65]. The high luminosity LHC (HL-LHC) upgrade aims to increase the peak luminosity to 5×10^{34} cm^{-2}s^{-1} at $\sqrt{s} = 14$ TeV [230]. Figure 5.1 shows the planned HL-LHC timeline and luminosity target [231]. The Run 1, Run 2 and Run 3 total integrated luminosity goal is approximately 450 fb^{-1}. With the increased luminosity of the HL-LHC, the integrated luminosity aims to reach at least 3000 fb^{-1} (up to 4000 fb^{-1}) around the 2040s. The average pileup will increase from around 33 in Run 2 and roughly 48 in Run 3 to $140 - 200$ in the HL-LHC [65].

The HL-LHC upgrade is achieved through various collider upgrades [232]. For example, the beam β^*, as defined in Equation 3.3, is decreased by using stronger focusing Nb_3Sn quadrupoles. However, reducing β^* causes the beam crossing angle to increase. New crab cavities, tested at the e^+e^- Belle experiment, will be deployed at the LHC [230]. The crab cavities can rotate the beam and ensure head-on collisions.

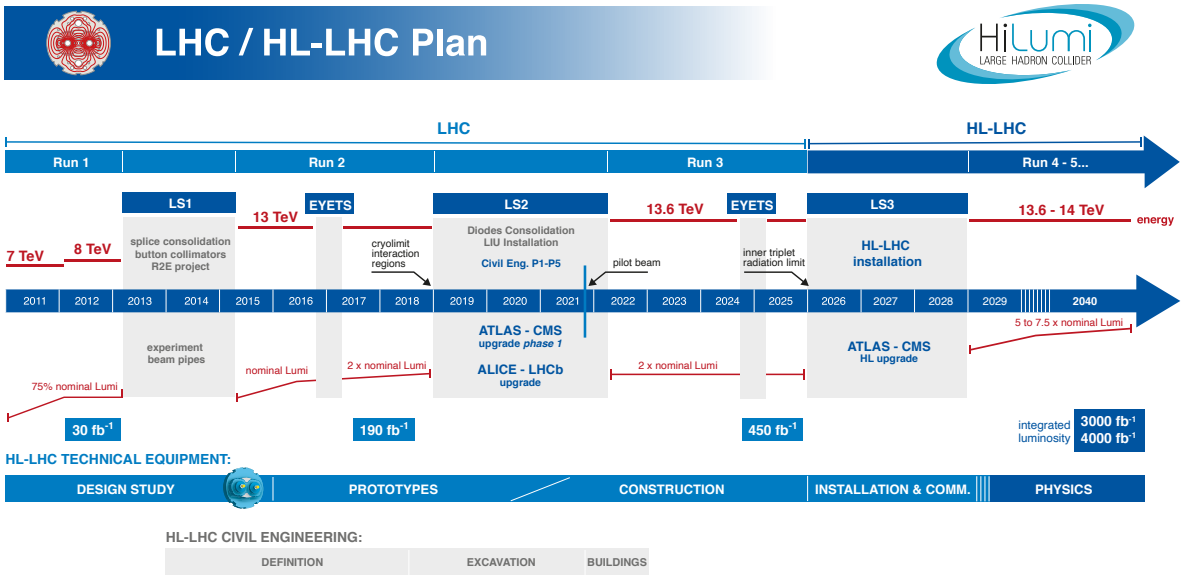

Figure 5.1: The LHC and HL-LHC data runs executed and planned till 2040s [231].

HL-LHC physics prospects As shown in Equation 3.2, the increased luminosities can directly increase the number of data events observed for physics processes of interest and decrease the statistical uncertainties of measurements. The HL-LHC can achieve promising precision results in various aspects.

The HL-LHC precision for the Higgs coupling κ modifiers can reach the % level from around 10% as shown in Figure 5.2. Specifically, for the Higgs-charm coupling, κ_c can be constrained to $\lesssim 3$ at 95% confidence level [229]. The extrapolation is based on the previous $VH(\rightarrow c\bar{c})$ analysis [2]. The signal and background yields are scaled up according to the HL-LHC luminosity and $\sqrt{s}$. The experimental and theoretical systematic uncertainties are scaled down according to the expected statistical and analysis technique improvements [233, 234]. Specifically, the flavor tagging uncertainties are scaled down by 50%, while some other experimental uncertainties, such as the jet and lepton uncertainties, are left unchanged. The modeling uncertainties are scaled down by 50% as well. The MC statistical uncertainties are considered negligible. The list of all systematic uncertainty scale factors used is available in [229]. With the analysis upgrades from the Run 2 $VH(\rightarrow b\bar{b}, c\bar{c})$ analysis, the next HL-LHC κ_c constraint forecast is expected to be significantly better.

More HL-LHC Higgs highlights include [235]: the invisible Higgs branching ratios such as Higgs decaying to dark matter can be limited to $\lesssim 3.8\%$; the di-Higgs measurement from ATLAS and CMS can reach 4σ; for the Higgs width, the uncertainties can be decreased from

$\sim$ 3 MeV to sub-MeV.

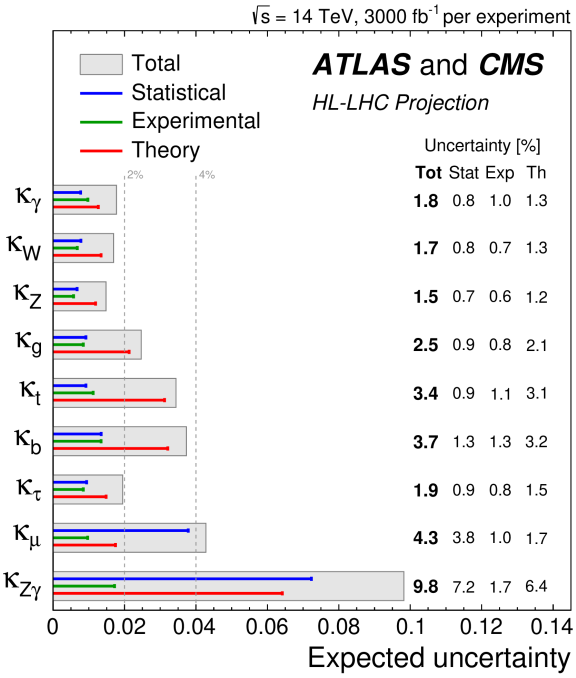

Figure 5.2: The HL-LHC projected κ modifier precisions [235].

5.1.1 ATLAS detector upgrades

While the HL-LHC can deliver precision Higgs physics, the detector environment is demanding. The main challenges are: 1) high event rate, 2) high pileup, and, 3) high radiation damage. The increased pileup will degrade the physics object resolution and increase uncertainties. To ensure precision physics performance in the HL-LHC environment, the ATLAS detector upgrades aim to have: 1) finer granularity, timing precision, and fast readout, and 2) high radiation tolerance. Section 5.1.1.1 focuses mainly on the inner tracker pixel detector upgrades, which is closely related to the work in Section 5.3. Section 5.1.1.2 gives a brief overview of the other sub-detector upgrades.

5.1.1.1 Inner tracker upgrades

The ATLAS inner detector, as discussed in Section 3.2, will be replaced by a new inner tracker for the HL-LHC [236, 237]. The current inner detector cannot handle data rates and radiation damage at the HL-LHC. The L1 trigger data rate will increase from $\sim$ 100 kHz to $\sim$ 1 MHz and the L1 latency time from $\sim$ 2 μs to $\sim$ 10 μs. The increased radiation damage from the HL-LHC on the inner tracker is discussed in more detail in Section 5.2.3.

The new inner tracker (ITk) design schematic is shown in Figure 4. Unlike the ATLAS inner detector, the inner tracker has only two components, the pixel detector and the strip detector. Both detectors use silicon as the sensor because of its radiation hardness. The inner tracker $|\eta|$ coverage increases from 2.5 to 4. This will allow higher η coverage for charged particle tracking and forward jet flavor tagging. For the pixel detector, the sensor pitch is 50×50 μm^2 for most sensors, finer than the IBL (Insertable B-Layer) 50×250 μm^2 pixel pitch. The sensor thickness is thinner as well, either 100 or 150 μm. In addition, the innermost layer of the pixel detector uses the *3D sensor* technology [238]. The 3D sensor technology arranges the *p-type* and *n-type* charge collecting electrodes in columns perpendicular to the sensor plane. For traditional *planar sensors*, the electrodes are parallel. The 3D arrangement decreases the electrode distance and improves the radiation hardness.

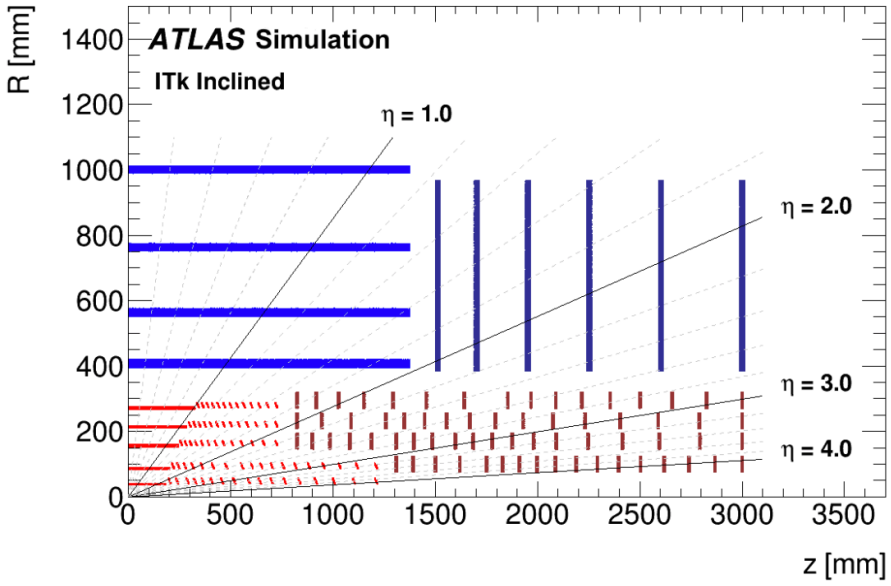

Figure 5.3: The ATLAS HL-LHC inner tracker schematic [236]. The pixel detector (red bars) and the strip detector (blue bars). The endcap detectors are shown in darker colors than the barrel detectors. The radial coverage is till $\sim$ 1 m from the beam pipe similar to the inner detector.

Pixel module upgrades Pixel modules are the building blocks of the ITk pixel detector. The modules are composed of the silicon sensors and the *readout chips*. Figure 5.4 shows the module schematic. The readout ASIC (application-specific integrated circuit) chip, also called the front-end chip, amplifies the charge particle signal, digitizes the signal, and sends the hit information to the DAQ (data acquisition) system.

The readout chip is connected to the pixel sensors through *hybridization*, also called bump bonding. While the bump bonding method has been developed for the current inner detector, the increased granularity requires a higher bump bonding density and is thus technologically challenging for the vendors. Given the challenges in assembling modules, there has been R&D towards a *monolithic* pixel detector as well. The monolithic pixel detector fabricates the sensor and the readout chip together on a single wafer. This would simplify the module production process and allow commercial module production. The idea has already been implemented in the ALICE detector but will not be implemented for the ATLAS inner tracker [239].

The readout chip is connected to the flexible printed circuit board (module *flex*) by wire bonds, as shown in Figure 5.4. The flex connects to the local electrical support. The readout chip uses CMOS (Complementary Metal-Oxide-Semiconductor) transistors, which are commonly used in building integrated circuit chips. A major improvement for the readout chip is to switch from the 130 nm CMOS technology to 65 nm. The smaller unit cell size allows more space for the digital architecture. The readout chip has been developed in collaboration with CMS within the RD53 collaboration [240]. More details on the RD53 chip, such as its improved data transmission speed and radiation testing, are presented in Section 5.3.

The strip detector upgrade extends the silicon detector coverage to radius up to 1000 mm, covering the radius originally covered by TRT before the HL-LHC [237]. The increased silicon coverage causes many challenges in the detector production, testing, and assembly [241].

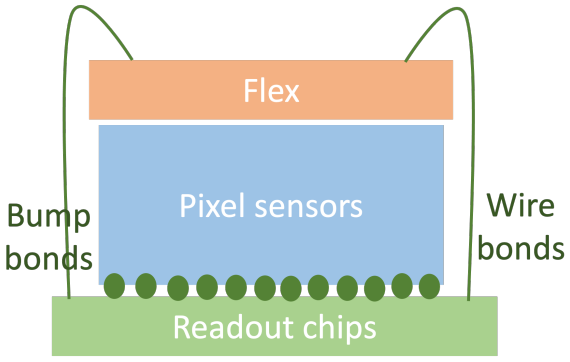

Figure 5.4: The ATLAS HL-LHC inner tracker pixel detector module schematic. The green dots are the bump bonds connecting the readout chip and the sensors. The green lines are the wire bonds connecting the readout chip and the flex.

5.1.1.2 Other detector upgrades

Similar to the inner tracker pixel and strip detector, the other sub-detectors need to be upgraded to cope with the increased radiation and data rates as well. Some upgrade highlights are discussed below:

- **Timing detector:** The High Granularity Timing Detector (HGTD) is a new detector that provides precision timing information at the HL-LHC [242]. HGTD will be installed at $z \sim \pm 3.5$ m with a radius from 120 mm to 640 mm. The timing resolution is ~ 50 ps. HGTD sensors use silicon-based Low Gain Avalanche Detectors (LGADs). The readout chip, ALTIROC, is similar to the RD53 chip used in the ITk pixel detector but with fewer channels.

- **TDAQ:** The TDAQ system will use a new TDAQ architecture [243]. The existing L1 (Level-1) and HLT (High Level Trigger) triggers will be replaced by the hardware-based L0 trigger system and the Event Filter (EF) system. Compared to the L1 triggers, the L0 system can perform offline-like algorithms over the full granularity of calorimeter data. The L0 system transmits data to DAQ at ~ 1 MHz. Events selected by the EF system will be sent to permanent storage at 60 GB/s, compared to 2 GB/s before. More trigger systems will utilize both flexible FPGA (Field Programmable Gate Arrays) technologies and custom ASICs.

- **Muon spectrometer:** The muon spectrometer upgrades mainly focus on the trigger chambers, RPC and TGC [244]. Solid angle coverage and granularity of trigger chambers will be improved. In addition to trigger chambers, the readout electronics of the MDT chamber will be upgraded to handle increased data rates and latency time requirements.

- **Calorimeters:** Similar to muon detector upgrades, the calorimeter upgrades focus on readout electronics to handle increased data rates, latency time, and radiation tolerance requirements [245, 246]. All calorimeter system readout electronics will be replaced except the FCal.

- **Computing:** Given the high data rates from the HL-LHC, the computation needs for MC simulation, object reconstruction, and data analysis and storage all increase [247]. For example, without more R&D, the CPU consumption per year is estimated to increase by 8 times during HL-LHC. The current computing frameworks cannot cope with the HL-LHC data increase and significant R&D is needed. There are various R&D approaches, such as enabling additional parallel-processing with hardware such as GPUs, adopting the columnar data format, and implementing fast detector simulation with parameterized models.

5.2 Silicon detectors

This section focuses on the basic working principles of silicon detectors [248]. Section 5.2.1 discusses the basics of semiconductors and their role in silicon sensors. Section 5.2.2 describes the interactions between charged particles and silicon sensors. Section 5.2.3 focuses on radiation damage in the silicon detector and briefly discusses the HL-LHC pixel detector expected radiation damage dosage.

5.2.1 Semiconductor and the silicon sensor

Silicon is a semiconductor, which means that its conductivity lies between insulators and metals. Its development as a semiconductor has revolutionized the field of electronics. Like *conductors* and *insulators*, *semiconductor* crystals can be described by energy bands [249, 250]. Electrons in crystals are arranged in *energy bands*. The bands are separated by *band gaps*, energy regions where no electron orbitals exist. Insulators tend to have filled or empty energy bands and no electrons can move in an external electric field. Metals have partly filled energy bands. The semiconductor energy band structure has been studied by solid state physicists for decades.

For semiconductors, there are two bands separated by an energy gap, the lower *valence band* and the higher energy *conduction band*. At room temperature, the semiconductors can conduct electricity, as there are electrons in the conduction band or unoccupied orbitals, called *holes*, in the valence band. In a pure semiconductor, at temperature T = 0 K, the conduction band is empty, the valence band is full, and the semiconductor becomes an insulator. The energy gaps E_g in semiconductors are:

$$E_g = E_c - E_v \tag{5.1}$$

E_c and E_v are the lowest energy of the conduction band and the highest energy of the valence band. In silicon, $E_g \approx 1.1$ eV. Insulators tend to have E_g greater than 2.5 eV.

In particle detectors, E_g is the minimum energy needed to generate an electron-hole pair [17]. Smaller band gaps generate larger signals and thus improve the energy resolution. The electron and hole concentration in semiconductors, n_e and n_d, can be calculated from Fermi-Dirac distribution:

$$f_e(E,T) = \frac{1}{\exp\left((E - E_f)/k_B T\right) + 1} \tag{5.2}$$

Here, E is the energy of the electrons, T is the temperature, and k_B is the Boltzmann constant. The parameter E_f is the electron chemical potential, also called the Fermi level.

Doping semiconductors In pure semiconductors, also called intrinsic semiconductors, the electron and hole concentrations are equal, $n_e = n_h$. In practice, most semiconductors are doped with impurities, also called *dopants* [251]. Dopants can introduce additional charge carriers and drastically increase the conductivity.

In the case of silicon, silicon has four valence electrons. It can be doped with an atom of 5 valence electrons such as phosphorus. In Figure 5.5, the schematic on the left shows the doping of silicon with phosphorus (red circle). There is one left-over electron after the 4 covalent bonds are established. The dopant that gives up an electron to the conduction band is called a *donor*. On the other hand, trivalent impurities, such as boron atoms, are called *acceptors*. In Figure 5.5, the schematic on the right shows the doping of silicon with boron (green circle). The acceptors accept electrons from the valence band and leave holes behind. Semiconductors with more conduction electrons than holes are called *n-type* (negative charge carriers). Semiconductors with more valence band holes than conduction electrons are called *p-type* (positive charge carriers). For the n-type (p-type) semiconductors, the Fermi level shifts to the conduction band (valence band) at low temperature.

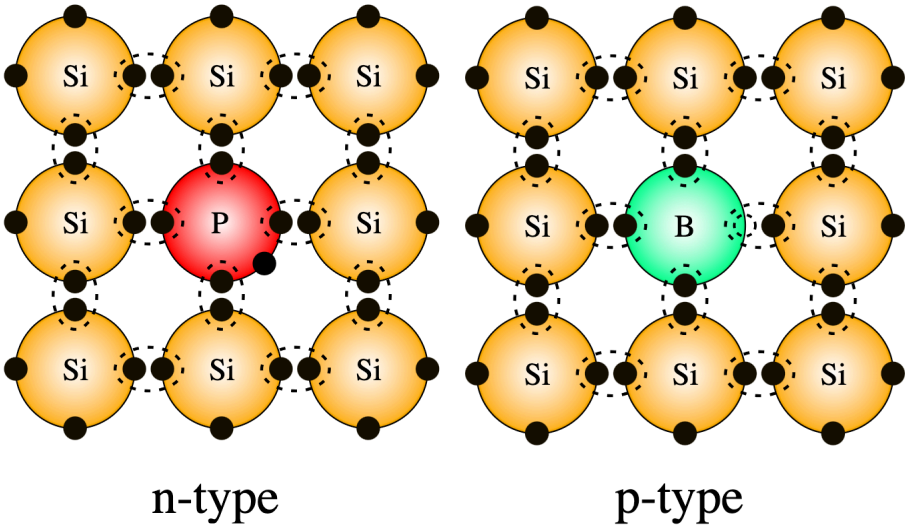

Figure 5.5: Doping for silicon [252]. Silicon (Si) doped by donor phosphorus atoms (P) (left) and acceptor boron atoms (B) (right).

p-n junctions P-type and n-type semiconductors can be placed together to form a p-n junction. In particle detectors, the sensors are made of fully depleted p-n junctions [248]. The depletion removes free charge carriers in semiconductors and allows detecting signals from ionizing particles.

An illustration of the p-n junctions is shown in Figure 5.6. A p-type semiconductor is placed at $x < 0$, while an n-type semiconductor is at $x > 0$. The intersection of the p-n junction is at $x = 0$. The Fermi level (ϵ_f) is lower for $x < 0$ and higher for $x > 0$. This causes electrons to move from the n-side to the p-side and holes from the p-side to the n-side until the Fermi level is the same throughout the system, as shown in the top row of Figure 5.6.

This redistribution also creates a space charge region or a depletion region. In the depletion region, the electrostatic potential is higher on the n-side as more positive space charges (from the fixed ions) are left. This is illustrated in the middle row of Figure 5.6. Lastly, electrons and holes annihilate in the depletion regions, causing unbound carrier densities to reduce significantly, as shown in the bottom row of Figure 5.6.

The electrostatic potential step $V_{\text{diffusion}}$ can be calculated from the shift in the conduction band energies on the p-side (E_{cp}) and on the n-side (E_{cn}).

$$V_{\text{diffusion}} = E_{cp} - E_{cn} = \frac{k_B T}{e} \ln(\frac{n_a n_d}{n_i^2}) \tag{5.3}$$

Here, n_a and n_d are the doping concentrations. The symbol n_i is the intrinsic carrier concentration. The electrostatic potential step is a function of the depletion width w.

$$w = \sqrt{\frac{2\epsilon}{e} \frac{n_a + n_d}{n_a n_d} (V_{\text{diffusion}} - 2k_B T/e)} \tag{5.4}$$

ϵ is the semiconductor permittivity.

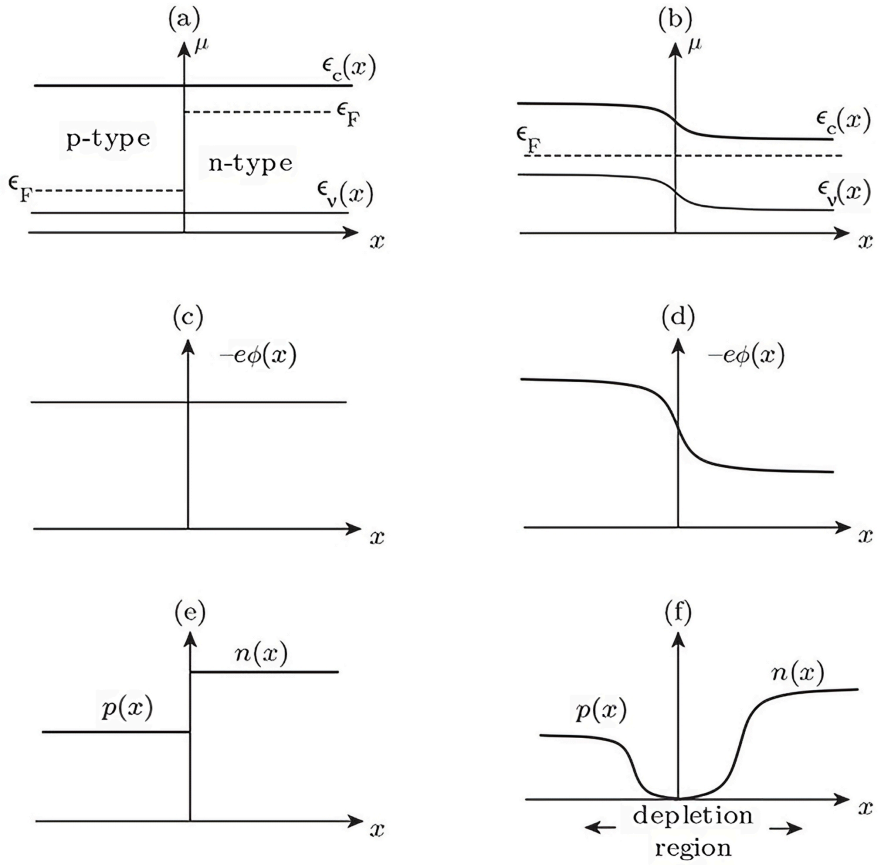

Figure 5.6: The p-n junction illustration before (left column) and after equilibrium (right column) [251]. (Top) chemical potential as a function of position x. Here, ϵ_F stands for the level. And, $\epsilon_c(x)$ ($\epsilon_v(x)$) stands for the conduction (valence) band energies. (Middle) electrostatic potential ϕ. Here, e is the charge. (Bottom) density of free carriers. p(x) is the number density of valence band holes and n(x) conduction electrons.

Reverse biasing The depletion region in p-n junctions exists without any external voltage. However, in particle detectors, the depletion regions are often extended to the full sensor thickness to maximize the detector sensitivity to ionizing signals. Sensors can be fully depleted using *reverse biasing*. The schematic of reverse biasing is shown in Figure 5.7. When a positive voltage is connected to the n-type semiconductor, electrons from the external circuit fill the holes in p-type semiconductors. Electrons from the n-type semiconductors are displaced towards the positive external potential and the depletion region increases. The forward biasing works in the opposite way and the depletion region shrinks.

Assuming the external field $V_{\text{bias}} \gg V_{\text{diffusion}}$, the depletion region width in Equation 5.4

simplifies to:

$$w \approx \sqrt{\frac{2\epsilon}{e}\frac{n_a + n_d}{n_a n_d}V_{\text{bias}}} \tag{5.5}$$

Given the sensor thickness, the bias voltage needed to fully deplete the sensor can be estimated. When the bias voltage is too high and the sensor is over-depleted, a *breakdown* can occur and the current through the semiconductor increases dramatically [248]. Before the breakdown, the semiconductor still has some leakage current.

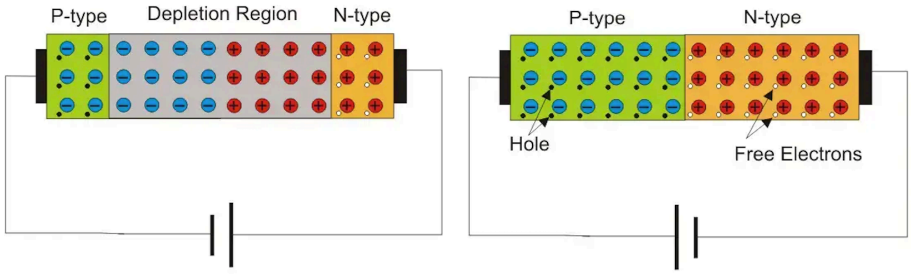

Figure 5.7: Reverse biasing (left) and forward biasing (right) of p-n junctions [253].

5.2.2 Silicon sensor signals

When charge particles transverse silicon sensors, the ionized charge generated Q is proportional to the ionization energy loss of the particles, dE/dx. A schematic is shown in Figure 5.8.

$$Q = \frac{dE/dx}{E_{eh}}d \tag{5.6}$$

Here, d is the silicon sensor thickness. And, $E_{eh} \approx 3.65$ eV is the average energy for creating an electron-hole (e-h) pair [17].

The ionization energy loss of particles is described by the Bethe-Bloch equation [17]. The ionization energy loss dE/dx of muons on copper is shown in Figure 5.9. The ionization energy loss is at its minimum around $\beta\gamma \approx 3$. Silicon sensors need to have noise below the minimum ionization energy to detect the minimum ionizing particles (MIP). The mean loss of a MIP in silicon is:

$$\left\langle \frac{dE}{dx} \right\rangle = 388\,\text{eV}/\mu\text{m} \tag{5.7}$$

When describing individual particles, the mean loss as shown in Equation 5.7 is not effective because the probability distribution function (pdf) of the loss is highly skewed. The pdf describing the energy loss is called the Landau distribution [17]. An example of the Landau distribution for silicon is shown in Figure 5.10. The most probable value (MPV) tends to be 30% lower than the mean energy loss. Therefore, taking a sensor thickness d =

100 μm, the sensor thickness of the inner tracker pixel detector, the charge generated is as follows:

$$Q \approx \frac{388\,\text{eV}/\mu\text{m} \times 0.7}{3.65\,\text{eV}} \times 100\,\mu\text{m} \approx 7433 \tag{5.8}$$

This means that typically 7433 e-h pairs are created by a MIP transversing the pixel sensor. In addition, the charge collection time and signal current pulse shape can be estimated from the Shockley-Ramo theorem [17].

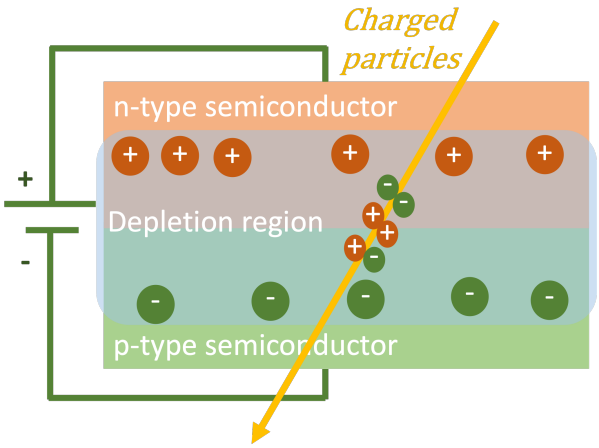

Figure 5.8: The schematic of ionizing signals from charge particles in silicon sensors.

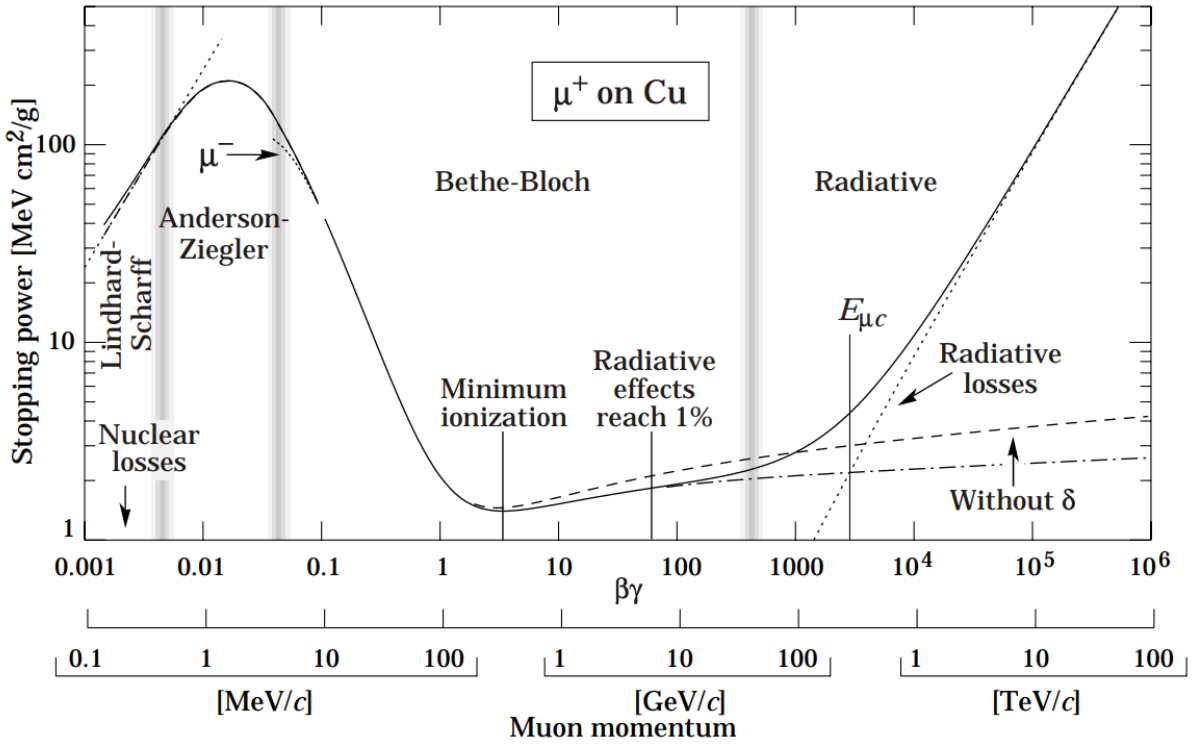

Figure 5.9: The ionization energy loss of muons in copper [17].

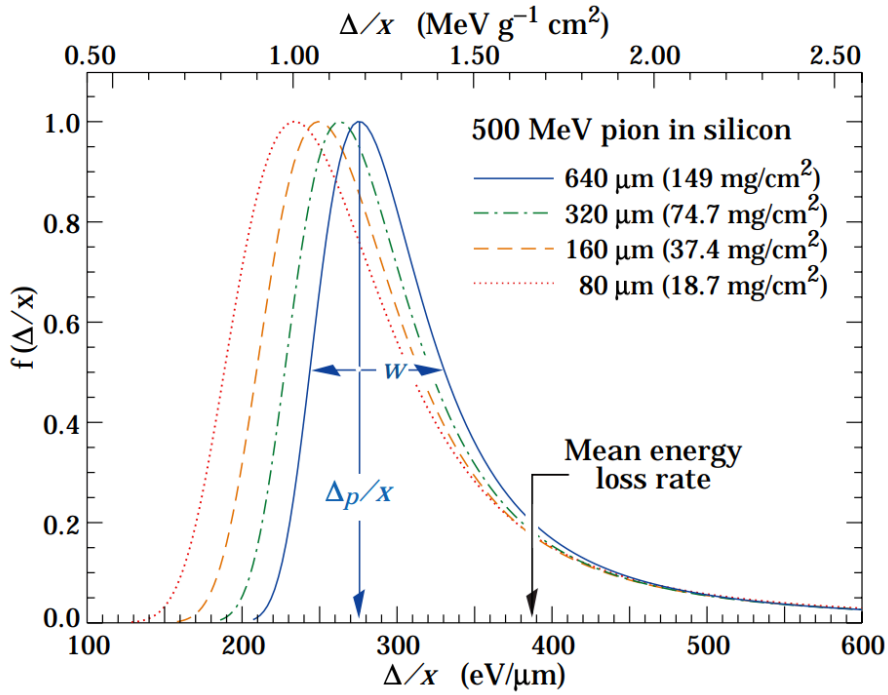

Figure 5.10: The Landau distribution of 500 MeV pion in silicon [17]. The ionization loss Δ/x is normalized to unity at the most probable value Δ_p/x. The different curves correspond to different silicon sensor thickness, d. The value of $d\rho$ is shown in the bracket with $\rho \approx 2.33\,\mathrm{g/cm^3}$ for silicon density. The ionization loss Δ/x can be expressed in the units of $\mathrm{MeV\,g^{-1}\,cm^2}$ and $\mathrm{eV}/\mu\mathrm{m}$. The two expressions differ by a factor of ρ.

5.2.3 Silicon detector radiation damage

One of the main challenges of the HL-LHC ATLAS upgrade is the high radiation damage. The silicon sensors and readout chips tend to suffer two kinds of radiation damage: *bulk damage* and *surface damage*:

- **Bulk damage:** The sensors mostly suffer from the bulk damage, where the atoms are displaced. Atoms can be replaced and create interstitials, vacancies, and more complex structures. The displacements change the band gap energy levels and the initial silicon properties. Such as increasing the leakage currents, changing depletion voltages, and trapping charge carriers. The bulk damage can be quantified in terms of NIEL, non-ionizing energy loss, in the unit of 1 MeV neutron equivalent fluence (n_{eq}/cm^2). The reference value corresponds to 95 MeV mb/cm^2.

- **Surface damage:** Surface damage is introduced by ionization instead of atom displacement. Thus, the surface damage is measured by the total ionizing dose (TID) in the unit of rad. It is most prominent in the transistors of the readout chip. The 65 nm CMOS technology allows sufficiently thin gate oxide to be insensitive to the TID. However, the size of other insulating oxides such as the spacer and shallow trench isolation oxide (STI) does not scale down [254, 255]. Spacers are thin insulating layers between transistor components that prevent leakage. STI isolate adjacent transistors.

  Surface damage causes charge build-up in the silicon oxide and silicon interface. Ionizing radiation generates electron-hole pairs in the oxides. Electrons in oxides are more mobile and quickly drift to the metal electrode, while holes are trapped in the interface region [248]. This causes the threshold voltage of transistors to shift and the leakage current and noise to increase. Irradiation studies also show worse damage for smaller transistors, lower dose rate, and, higher temperature [256, 257].

- **Annealing:** After irradiation, two types of annealing process can happen: *beneficial* and *reverse* annealing. In beneficial annealing, radiation defects can diffuse and reverse the macroscopic damage. On the other hand, reverse annealing degrades the macroscopic damage. Annealing can be frozen out at low temperatures. Therefore, the readout chips are always kept at low temperatures after irradiation to avoid reverse annealing [248].

The expected radiation damage in the ATLAS inner tracker pixel detector at the end of HL-LHC is quantified in Figure 5.11. At the left of Figure 5.11, the fluence distribution quantifies the bulk damage on sensors in the unit of 1 MeV neutron equivalent fluence (n_{eq}/cm^2). At the right of Figure 5.11, the surface damage on the chip is quantified in TID. Here, the TID is measured in the unit of Gray (Gy), where 1 Gray = 100 rad. The radiation dose is highest in the central region of the detector where the radius $r = 0$ and decreases as r increases. At smaller radii, the radiation damage is roughly homogeneous in z. At larger radii, the radiation dose is higher at smaller z.

Various radiation tests have been performed on pixel detector sensors and readout chips to validate the inner tracker performance at the end of HL-LHC [236, 258]. Sensors have shown good hit efficiency after $1 \times 10^{16} n_{eq}/cm^2$ [259]. The readout chip has been shown to withstand up to 1 Grad [258]. The readout chip radiation tolerance testing is discussed in more detail in Section 5.3.2. Currently, the inner barrel and endcaps are planned to be replaced after 2000 fb^{-1} of irradiation with roughly 1 Grad of TID.

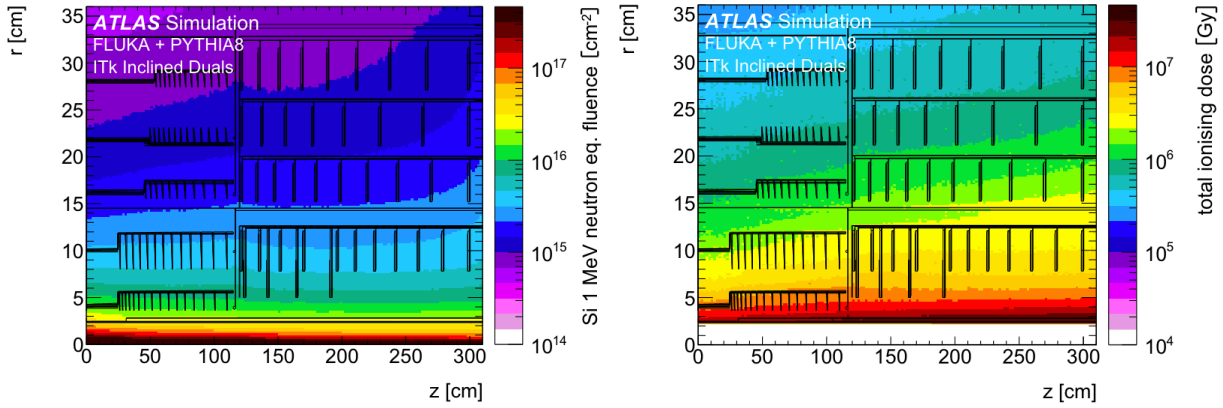

Figure 5.11: The fluence (left) and TID (right) distribution in the inner tracker pixel detector after 4000 fb^{-1} [236]. The ITk pixel detector schematic is marked in black lines. The y-axis covers the radius from the beam pipe ($r \sim 0$ cm) to the last layer of the ITk pixel detector ($r \sim 30$ cm). The x-axis covers the from $z = 0$ cm to $z = 300$ cm (the end of the ITk pixel detector).

5.3 Radiation tolerance of the inner tracker readout chip

The RD53 readout chip is an important component in building the ATLAS HL-LHC pixel detector [240]. As mentioned above, the ATLAS HL-LHC pixel detector readout chip has many improvements, such as the 65 nm technology and the improved data transmission speed from $\sim$ 100 Mb/s to $\sim$ 5 Gb/s [260, 236]. The readout chip, along with the pixel silicon sensors, also suffers a high dose of radiation. It is thus important to characterize the readout chip performance after the radiation. In this section, Section 5.3.1 introduces the basic circuitry of the RD53B ASIC. Section 5.3.2 discusses the results from the RD53B radiation testing campaign.

5.3.1 RD53B readout chip

The RD53 readout chip amplifies the current pulse from the pixel detector silicon sensor, digitizes the signal, and sends the signal to the DAQ [240]. The RD53 readout chip three two generations, RD53A [261], RD53B [240], and RD53C [262]. The RD53 chip framework is used by both ATLAS and CMS HL-LHC upgrades. The ATLAS and CMS versions mostly differ in the pixel matrix size. The ATLAS chip version is called ITkPix. ITkPixV2, developed for ATLAS under the RD53C framework, is the final chip version for the ATLAS pixel detector. ITkPixV1, based on RD53B, is the chip tested in this section as the ITkPixV2 chip was not available at the time.

There are minor updates from RD53B to RD53C, such as power stability. Both RD53B and RD53C satisfy all HL-LHC upgrade requirements [263]. Most functionalities discussed below about RD53B are valid for RD53C. The radiation tests on ITkPixV1 are informative for ITkPixV2 as the basic digital logic cells stay the same in both versions [258].

The ITkPixV1 chip consists of a *pixel matrix* and a *chip bottom*. The chip schematic is illustrated at the left of Figure 5.12. The pixel matrix is built from *cores* with 8×8 pixels. Since each pixel is 50 $\mu m \times$ 50 μm, each core is 400 μm $\times$ 400 μm. ITkPixV1 has 48×50 pixel cores. Each core has 64 *analog front ends* for shaping the signal pulse and comparing it to a threshold. 64 pixels are controlled by one *digital core*. The digital core digitizes the signal from the analog front end and stores the signal and its timestamp while retrieving the trigger decision. The digital and analog circuitry layout view is presented at the right of Figure 5.12.

The chip bottom contains many analog and digital functionalities. For example, it generates the analog front end threshold bias voltage through a 10-bit digital analog converter (DAC). It also implements readout, configuration, monitoring, and powering. The wire bond pads to the module flex are located below the chip bottom.

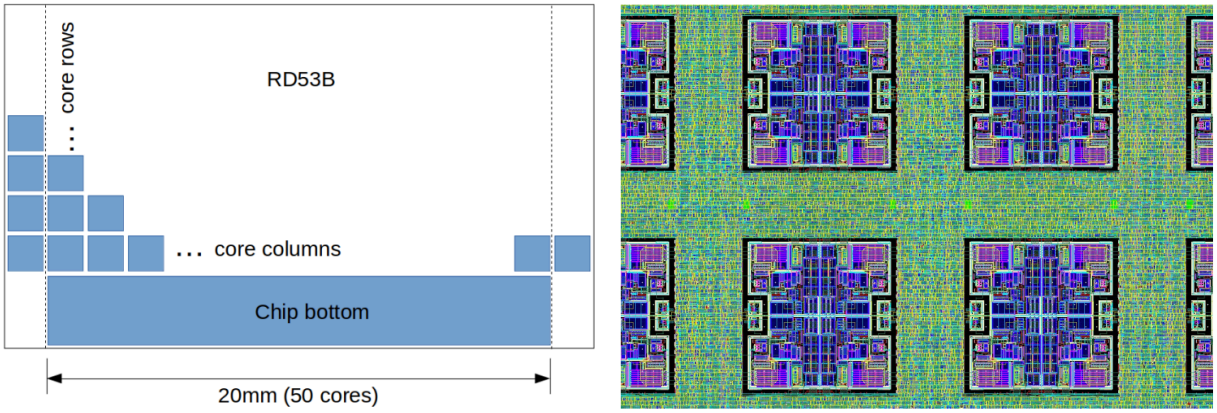

Figure 5.12: The RD53B chip schematic (left) and the analog front end in digital sea layout view (right) [240]. The chip schematic shows a small fraction of all cores in RD53B. For ITkPixV1, there are 48 × 50 cores and thus 384 × 400 pixels. Thus, the chip size is around 2 × 2 cm. On the right, the analog front ends are the purple squares. The digital "sea" is the green portion surrounding the purple squares. The digital sea refers to the digital cores on the chip.

Chip settings There are various configurations that govern chip operations. The chip *powering* is performed through a combination of a linear low dropout regulator with a shunt element (SLDO). The schematic is shown in Figure 5.13. The SLDO provides constant current and voltage to chips connected in serial powering. That is,

$$I_{in} = I_S + I_L = \text{const} \tag{5.9}$$

Here, I_{in} is the input current to the SLDO, I_S is the shunt current, and I_L is the load current of the chip. The main settings related to the SLDO powering are:

- `VINA`: the SLDO input voltage for the analog front end; default: 1.6 V.
- `VIND`: the SLDO input voltage for the digital core; default: 1.6 V.
- `VDDA`: the SLDO output voltage for the analog front end; default: 1.2 V.
- `VDDD`: the SLDO output voltage for the digital core; default: 1.2 V.
- `VREFA` or `SldoTrimA`: the SLDO reference voltage for the analog front end, adjustable by a 4-bit DAC; default: 0, 1, ... 14, 15.
- `VREFD` or `SldoTrimD`: the SLDO reference voltage for the digital core, adjustable by a 4-bit DAC; default: 0, 1, ... 14, 15.

In addition, RD53B has an external reference current independent of the SLDO circuits:

- `IREF`: the main reference current; default: 20 μA and can be adjusted through wire bonds.
- `VREF_ADC`: the reference voltage for the ADC; default: 0.8 V.

`IREF` sets the reference voltage for other chip functions such as the SLDO powering and the ADC (analog-to-digital converter) for digitizing the analog signal and timing information. `VREF_ADC` sets the analog front end injection voltages and is determined by `IREF`.

In addition to the powering settings, the analog front end settings can be adjusted as well. The analog front end has three main parts: *pre-amplifier* (preamp), *pre-comparator* (precomp), and *comparator* (comp). The schematic is shown in Figure 5.14.

The preamp amplifies and integrates the signal current into a voltage pulse using an op-amp with a continuous reset feedback current. The preamp outputs can be adjusted through three different settings:

- `DiffPreamp`: the DAC bias voltage for preamp; default: 900 or 400 [DAC units];
- `DiffVff`: the continuous reset feedback current; default: 150 or 60 [DAC units];
- `LCC`: additional leakage current compensation circuit; default: enabled (1) or disabled (0);

The precomp stage introduces the global *threshold* by offsetting the signal voltage with two voltages, `DiffVth1` and `DiffVth2`. In addition, each pixel threshold can be trimmed through 5-bit `TDAC`.

- `DiffVth1`: main global threshold voltage; default: tuned for the chip to allow thresholds of 1000 or 2000e, much lower than the typical MIP charge signal around 7000 electrons in Equation 5.8.
- `DiffVth2`: secondary global threshold voltage; default: 0 [DAC units];
- `TDAC`: individual pixel threshold tuning voltage, adjustable by 5-bit DAC; default: -15, -14, ... 14, 15;

The last comp stage outputs the voltage over the threshold as a step function. The analog voltage signal is then sent to the digital domain and digitized as *time-over-threshold* (ToT). ToT is proportional to the charge deposited by the charged particles. Similar to the previous stages, the bias voltage can be set:

- `DiffComp`: the DAC bias voltage for comp; default: 500 [DAC units];

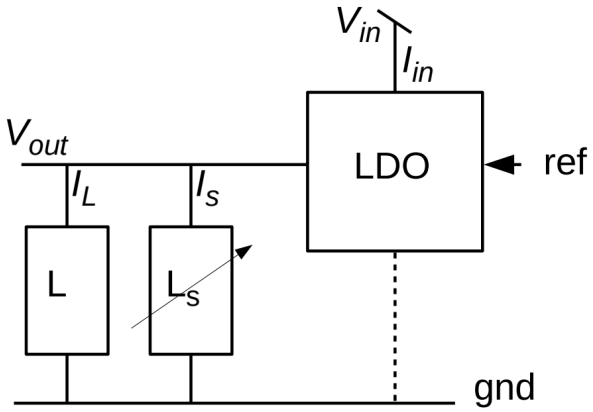

Figure 5.13: The ITkPixV1 SLDO conceptual diagram [240].

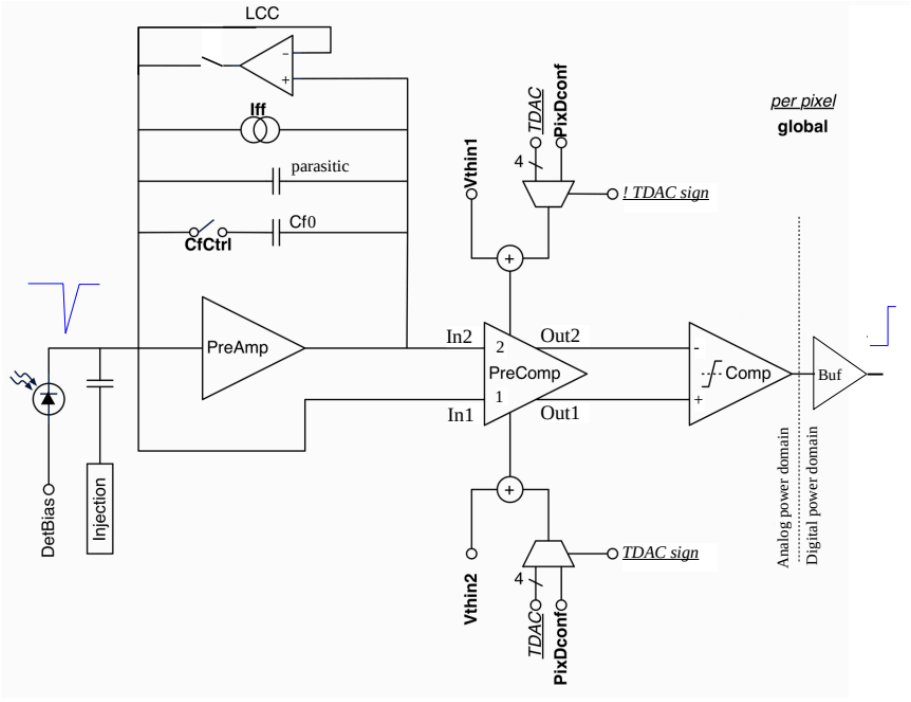

Figure 5.14: The ITkPixV1 analog front end schematic [240].

Chip scans The chip is configured, operated and read out through YARR (Yet Another Rapid Readout) [264]. YARR is a DAQ system for reading out the ITkPixV1 chip. It uses a PCIe card with an FPGA for reconfigurable fast processing. It was first developed for the Run 2 inner detector IBL layer. There are several types of scans in YARR to test the chip performance at the per pixel level:

- **Digital scan:** In digital scans, a fixed length of pulse is injected into the digital domain of the chip for every pixel bypassing the analog domain for a fixed number of times. Ideally, each pixel should see the same number of pulses (*hits*) injected in the occupancy map. This scan is usually run first to configure the chip and ensure chip communications. A *noise scan* is similar to a digital scan. No injections are made, but the chip is read out for a fixed amount of time.
- **Threshold tuning:** The threshold determines whether a pixel registers a hit when a charged particle passes through and affects the ToT values of the hits. Ideally, all pixels should have the same thresholds at 1000 or 2000e. This is achieve by threshold tuning. A desired amount of charge is directly injected to the analog front end using a capacitor and injection voltages. In the case of 2000e threshold tuning, the global threshold setting `DiffVth1` is varied in the range from 600 to 0 [DAC units] until 50% of the pixels register a hit. Once the global threshold `DiffVth1` is tuned, the per pixel threshold is further fine tuned by adjusting the `TDAC`.
- **Threshold scan:** After tuning, the threshold of each pixel can be measured through the threshold scan. Various analog signals are injected by varying `VCAL` multiple times and the occupancy of pixels is measured each time. The occupancy for pixels increases as a function of injection charges, resulting in an S-curve. The 50% occupancy point for the pixel is defined as the pixel threshold. Consequently, the chip threshold distribution for all pixels can be derived.

5.3.2 RD53B radiation tolerance testing

The irradiation testing of the ITkPixV1 chip presented in this thesis is carried out at Berkeley Lab using a commercial X-ray machine that has been recently installed in the lab [265]. Section 5.3.2.1 discusses how to calibrate the X-ray machine in the lab. Section 5.3.2.2 discusses the X-ray radiation campaign on ITkPixV1.

5.3.2.1 X-ray and irradiation calibration

The X-rays are generated in the X-ray tube using a tungsten anode and sealed off with beryllium windows. The empty X-ray machine cabinet is shown at the left of Figure 5.15.

The X-ray generation schematic is shown at the right of Figure 5.15. Inside the X-ray tube, X-rays are emitted when high voltage accelerates electrons from the cathode to the tungsten anode. X-rays are generated from both *bremsstrahlung* and *characteristic* radiation.

In bremsstrahlung, the energy spectrum of the X-rays is continuous. The electrons lose kinematic energy, which is then converted to X-ray photon energy. In characteristic radiation, the electrons eject bound inner shell electrons from the atom. Outer shell electrons emit X-ray photons and fill the inner shell. The X-ray energy spectrum was measured in an earlier irradiation campaign using a similar X-ray machine at Oxford University [266]. The results show that 150 μm aluminum foil can filter low-energy X-rays below 8 keV. As shown in Figure 5.15, the aluminum foil is always installed during X-ray calibration and chip irradiation.

The X-ray tube is operated at 40 kV. The tube current can increase from 20 mA to 55 mA. The maximum power is 3 kW. The X-ray dose rate is calibrated using the AXUVHS5 photodiode. The photodiode has an active area of 1 mm^2. The photodiode is reverse biased to -50 V using a Keithley oscilloscope and measures the X-ray dose rate in terms of the photocurrent produced. The diode outputs roughly 657 nA when the dose rate is 2 Mrad/h. The diodes are calibrated using the Oxford X-ray machine as shown in Figure 5.16 [266].

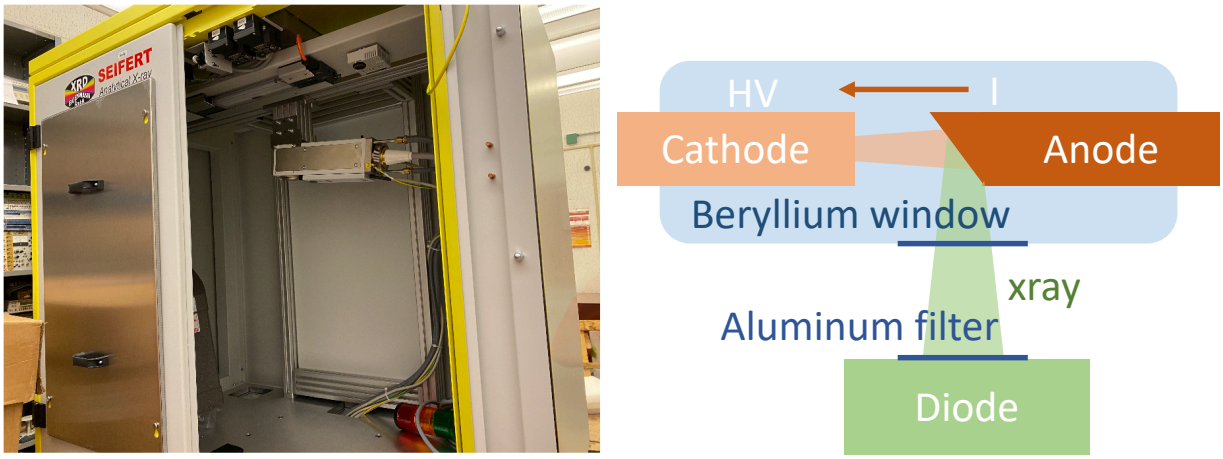

Figure 5.15: The empty X-ray machine (left) and calibration schematic (right). In the schematic, HV stands for high voltage and I current. The X-ray machine is well-shielded during irradiation.

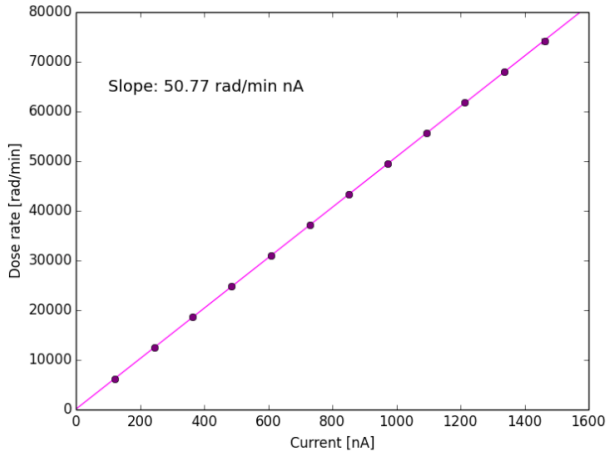

Figure 5.16: The diode calibration curve from the Oxford X-ray machine [266]. The diode current readings can be converted to the X-ray dose rate using the slope of 50.77 rad/min nA.

Calibration setup The calibration setup is shown in more detail in Figure 5.17. The photodiode is installed on a customized metal plate. The metal plate is then mounted inside a plastic calibration box. The calibration box is installed on a breadboard platform connected to the *xyz* stage. The *z* stage is manual and has a load of 15 kg and 30 cm range. The *xy* stage is composed of two NLE series high-precision linear stages from Newmark in the orthogonal directions. The *xy* stage range is 30 cm with a 0.1 μm resolution. The load is 22.6 kg. The *xy* stage is programmed in a `c++ xrayCtrl` package using the Newmark NSC-A2L Two Axis USB Stepper Motor Controller to scan a grid of *xy* coordinates or move to one coordinate in the *xy* plane. The *xyz* stage allows scanning a 2D X-ray dose rate map near the beryllium window at different *z* positions from the X-ray platform.

The `c++ xrayCtrl` package controls the *xy* stage, the Keithley oscilloscope, and the X-ray machine shutter to measure the X-ray dose rate in a 2D plane. The program moves the *xy* stage to the position of interest. X-ray shutter opens for 1 second to allow the Keithley oscilloscope to read out the photodiode current. At the same position, a second measurement is made with the X-ray shutter closed for 1 second. The *xy* scan range and X-ray wait time are adjustable through a configuration file. The final photodiode current subtracts the dark current. It is necessary to conduct dark current measurements at each scanned point as the dark current increases with the irradiation time, as shown in Figure 5.18. As shown in the figure, the beam spot is not uniform with higher dose rates in an eclipse shape, due to the X-ray heel effect [267].

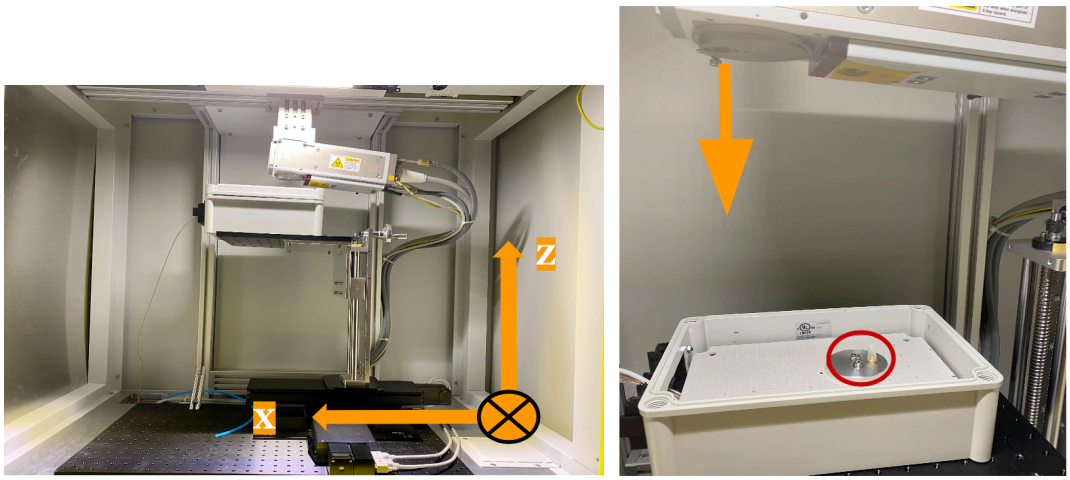

Figure 5.17: The diode calibration box on the *xyz* motion stage (left) and the calibration photodiode inside the box (right). On the left, the yellow arrows show the coordinate system defined in the *xyz* stage. The *y*-axis points into the X-ray machine. On the right, the yellow arrow marks the X-ray emission point and direction from the tube.

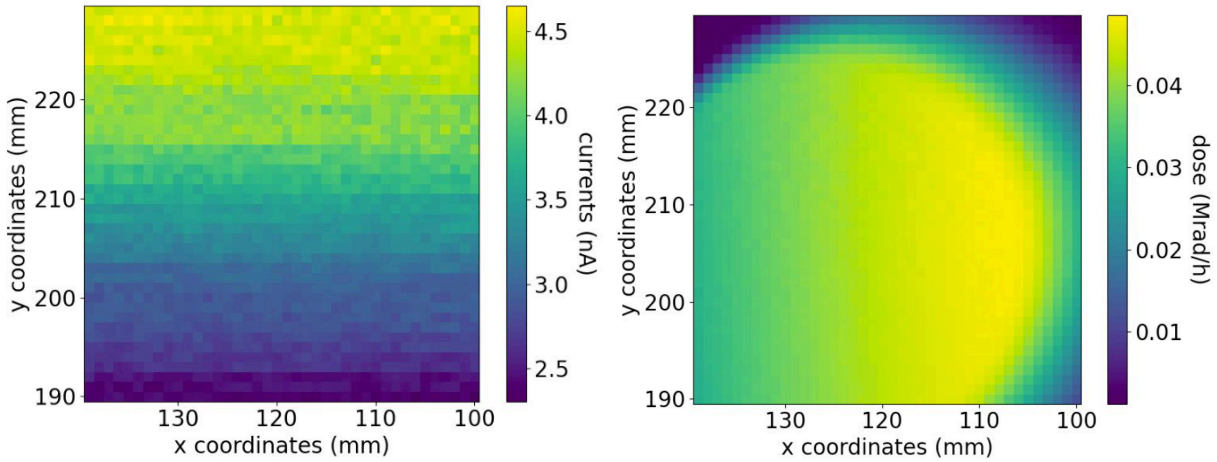

Figure 5.18: The X-ray calibration dark current (left) and dose rate (right) measured in a 40 mm x 40 mm grid with 1 mm step size. The measurements are performed at z = 0 and X-ray current = 20 mA. The xyz coordinate is shown in Figure 5.17. The origin in the xy plane follows from that of the xy motion stage. The dark current increases with y coordinates due to larger irradiation time. Dark currents are subtracted from the dose rate on the right. The current and dose rate conversion is shown in Figure 5.16.

Calibration results Detailed calibration measurements are made at z = 23, 17.25, 11.5, 5.75, 0 cm and X-ray current = 20, 40, 55 mA. At each z and X-ray current setting, a 90 mm x 90 mm scan with 10 mm step size is performed to locate the beam spot. Then, 1 mm step size fine scan is performed around the beam spot. The beam intensity increases with the X-ray current and the beam size decreases closer to the beam spot as shown in Figure 5.19.

After understanding the X-ray beam profiles, the 2D calibration scans help determine the final irradiation settings. The z position is set to 5.75 cm to ensure a uniform beam across the chip as shown in Figure 5.20. The beam current is set at 55 mA to maximize the dose rate. During the ITkPixV1 irradiation campaign, the chip is carefully positioned in the plastic irradiation box similar to the calibration box such that the dose rates on the chip are the same as shown in Figure 5.20. With these irradiation settings, the radiation dose rate on the chip is taken as the maximum dose rate in the 2D plane in Figure 5.20: 0.48 Mrad/h.

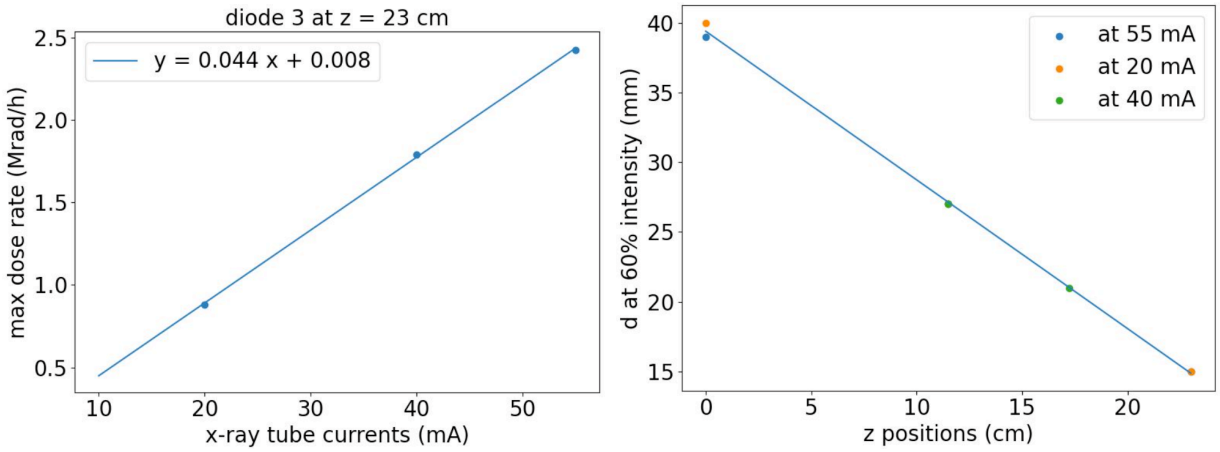

Figure 5.19: The X-ray maximum dose rate with respect to the tube currents (left) and the X-ray beam size as a function of the distance to the beam spot (right). (left) The maximum dose rate increases from around 1 Mrad/h at 20 mA to 2.5 Mrad/h at 55 mA. The maximum dose rate are measured at z = 23 cm. (right) The diameter of the beam spot at 60% of the maximum dose rate decreases from 40 mm at z = 0 to around 15 mm to z = 23 cm closest to the beam. The beam size is consistent at different X-ray currents.

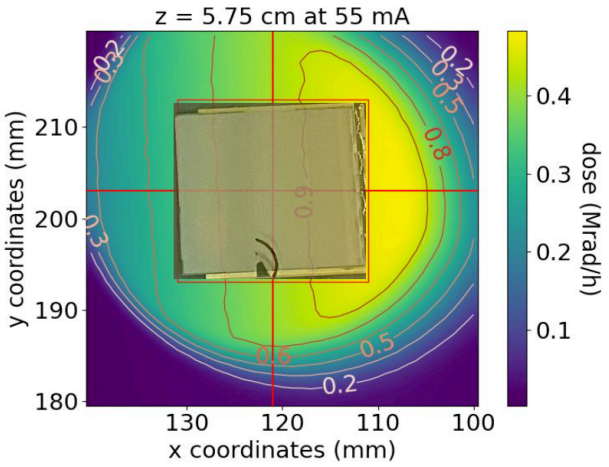

Figure 5.20: The X-ray beam spot for irradiating the ITkPixV1 chip. A 2×2 cm square is drawn around the beam center with the ITkPixV1 chip overlaid. The chip bottom with the wire bonds connected to the single chip card is placed at the maximum dose rate regions.

5.3.2.2 Irradiation setup and damage to the chip

The final irradiation dose rate is measured to be 0.48 Mrad/h. To irradiate the chip, the ITkPixV1 chip is connected to a single chip card and irradiated at the position shown in Figure 5.20. The dose rate is 0.48 Mrad/h. The single chip card (SCC) is a printed circuit board (PCB) for operating and reading out the chip in the lab. The irradiation box is shown in Figure 5.21. Unlike the calibration box, the chip irradiation box cools and stabilizes the readout chip temperature to approximately -7 °C. This irradiation temperature is similar to the ITk operation temperature at -10 °C. The cooling is performed with a CP60231H Peltier. The Peltier schematic is shown in Figure 5.21. Nitrogen is constantly flushed into the box to avoid condensation. The temperature is stabilized at ±1°C through a PID loop in the `rd53b_anamon` package by adjusting the Peltier voltage [268]. The temperature is an important parameter to control during irradiation as the radiation damage is temperature dependent.

The temperature and humidity inside the box are constantly monitored through a humidity sensor, the SCC Negative Temperature Coefficient (NTC) thermistor and the `rd53b_anamon` package and displayed in `Grafana` [269]. Peltier cooling is adjusted when the temperature is below the condensation point. In addition, `rd53b_anamon` and `Grafana` also monitors: the chip `VINA`, `VIND`, `VDDA`, `VDDD`, and `VREF_ADC` read out through the SCC. Most settings are stable throughout the month-long irradiation campaign. The X-ray operation status, high voltage, shutter status, and dose irradiated are also monitored in `xrayCtrl` and `Grafana`. If any value deviates outside the expected range, `Grafana` will send a message alarm. To minimize the radiation exposure, most electronic equipment, such as the chip power supply,

the Peltier power supply, and the YARR readout, is placed on the rack next to the X-ray machine, as shown in Figure 5.22. The cables are fed through the cable chase inside the X-ray machine.

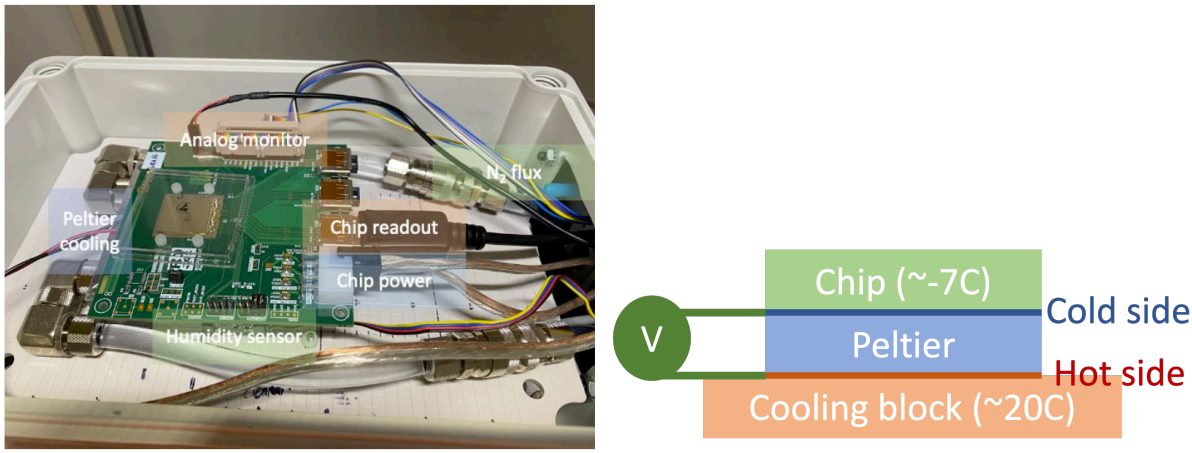

Figure 5.21: The ITkPixV1 irradiation box (left) and Peltier cooling schematic (right).

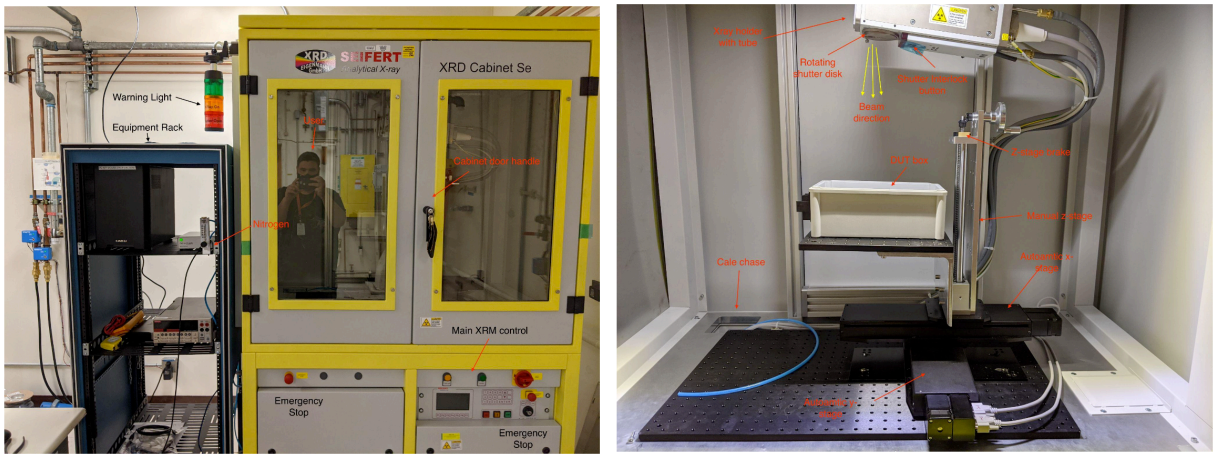

Figure 5.22: The X-ray irradiation campaign equipment rack (left) and cable chase inside the X-ray machine (right).

Ring oscillator radiation damage The readout chip transistor radiation damage is quantified by measuring the ring oscillator gate delays. There are 42 ring oscillators at the chip bottom of ITkPixV1 near the SCC wire bonds. Each ring oscillator drives a 12-bit

counter enabled for a given amount of time. During this time, the ring oscillator outputs oscillate between 0 and 1 at specific frequencies. The frequencies f are related to the ring oscillator gate delay T as:

$$T = 1/f \tag{5.10}$$

After irradiation, the ring oscillator frequencies decrease, which means that the gate delays increase. When the gate delay increases by 200%, the ITkPixV1 digital logic performance is degraded.

The ring oscillators are separated into two banks; bank A contains the same oscillators as RD53A, allowing direct comparison with previous radiation studies. Bank B ring oscillators are separated into 4 groups and each group shares the same enable signal. The ring oscillators are made of different logic cells. The numbers of cells (lengths) are chosen to allow typical frequencies of 600 MHz for Bank A and 800 MHz for Bank B. The ring oscillators also use different transistor drive strengths. The transistor drive strength is proportional to the transistor size. As discussed above, smaller transistors with strength 0 tend to suffer more radiation damage. All ring oscillator types, strengths, and lengths are summarized in Table 5.1.

The ring oscillator frequencies depend on the `VDDD` settings. The `VDDD` can be adjusted using `SldoTrimD`. The ring oscillator frequencies are read out at different `VDDD` settings as shown in Figure 5.23. The ring oscillator frequencies with respect to temperature changes are also measured. The frequency dependence on temperature is negligible within $\pm 1^{\circ}$C.

During irradiation, in addition to the environment and chip monitoring discussed above, YARR reads out the ring oscillator frequencies every 0.1 Mrad, scans the ring oscillator frequencies with respect to `VDDD` every 50 Mrad, and performs noise scans on the chip otherwise. The final ring oscillator gate delay changes with respect to the radiation dose are shown in Figure 5.24. The frequencies are corrected for the drifting of `VDDD` using the scans done every 50 Mrad. The dose is also corrected by 20% due to the attenuation from a thin copper layer covering the ring oscillators on the chip.

Up to 415 Mrad, the bank B ring oscillators gate delay increases by less than 25%. As shown in Figure 5.24, the strength 0 ring oscillators tend to suffer more radiation damage compared to strength 4 as discussed above. Different logic cell ring oscillators also tend to have different radiation damage.

Similar ring oscillator irradiation tests were also performed at Oxford university. The ring oscillator radiation damage results at Berkeley are compared with the Oxford results and found to be consistent [266]. The slopes of the gate delay change with respect to the dose are similar independent of the measurement sites.

Lastly, in addition to the ring oscillator radiation damage, the radiation damage to the chip threshold can be assessed by comparing the threshold distribution before and after irradiation as shown in Figure 5.25. The threshold distribution broadens after irradiation, which means that the chip threshold tuning will be required during operation to mitigate the radiation damage.

Ring oscillator	**Type**	**Strength**	**Length**
	Bank A		
0	Inv. CLK driver	0	55
1	Inv. CLK driver	4	51
2	Inverter	0	55
3	Inverter	4	55
4	4-input NAND	0	19
5	4-input NAND	4	19
6	4-input NOR	0	19
7	4-input NOR	4	19
	Bank B left & right		
0 & 1	Inv. CLK driver	0	38.2
2 & 3	Inv. CLK driver	4	44.5
4 & 5	Inverter	0	38.1
6 & 7	Inverter	4	44.3
8 & 9	4-input NAND	0	12.6
10 & 11	4-input NAND	4	16
12 & 13	4-input NOR	0	14.5
14 & 15	4-input NOR	4	14.5
	Bank B FF		
16 & 17	Scan D-flip-flop	0	6.1
18 & 19	D-flip-flop	1	6.2
20 & 21	Neg. edge D-flip-flop	1	5
	Bank B LVT		
22	LVT inverter	0	40.6
23	LVT inverter	4	56
24	LVT 4-input NAND	0	16.5
25	LVT 4-input NAND	4	22.8
	Bank B CAPA		
26-33	Inj-cap loaded 4-input NAND	4	16.8

Table 5.1: ITkPixV1 ring oscillator summary [240].

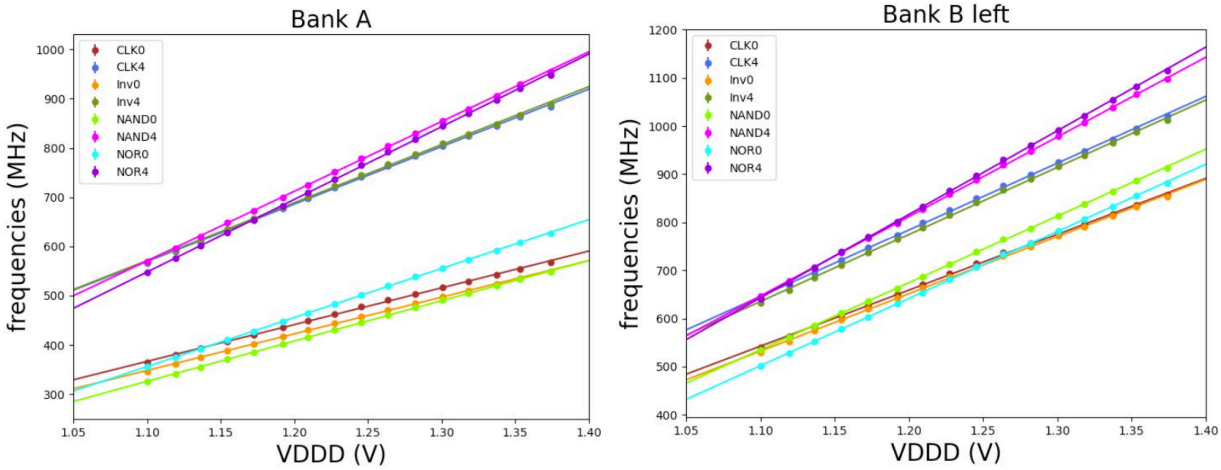

Figure 5.23: The ring oscillator frequencies with respect to VDDD for bank A (left) and bank B left (right) ring oscillators.

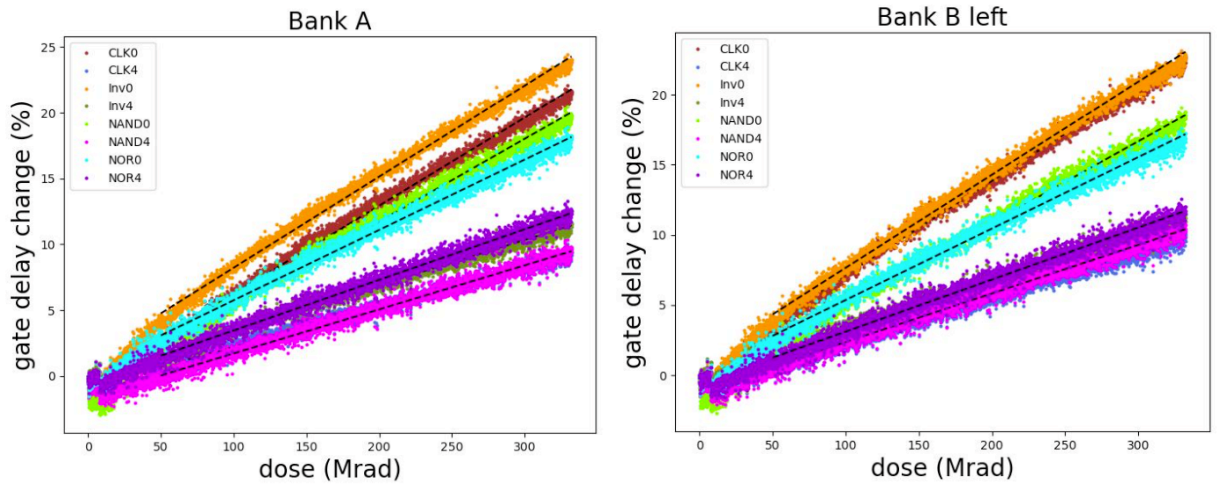

Figure 5.24: The ring oscillator gate delay changes with respect to radiation dose up to 415 Mrad for bank A (left) and bank B left (right) ring oscillators. The gate delays are calculated from the frequencies using Equation 5.10.

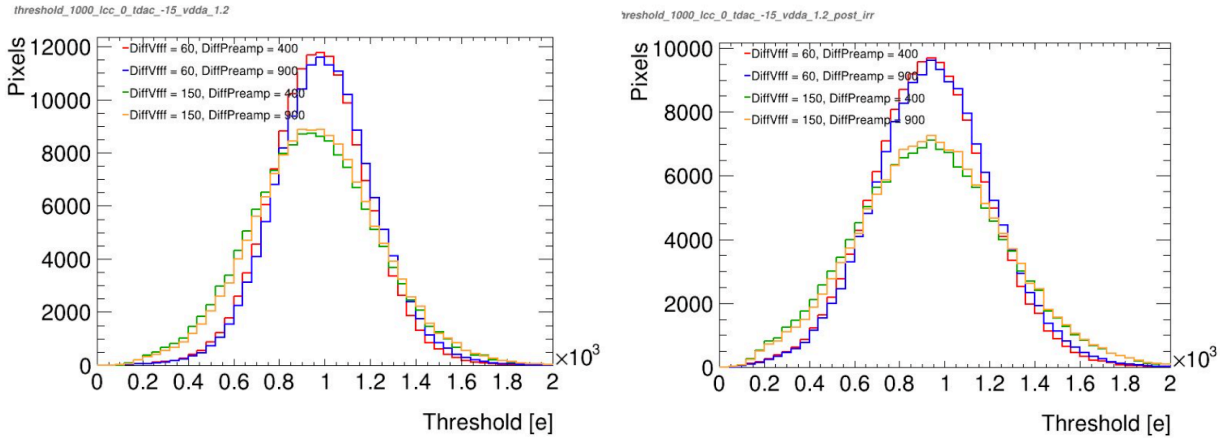

Figure 5.25: The threshold distribution before (left) and after (right) irradiation. The chip threshold was tuned to 1000 e before irradiation with `DiffVff`, `DiffPreamp`, `LCC`, `TDAC`, and `VDDA` fixed at specific settings.

5.4 Summary and outlook

In summary, the HL-LHC upgrade has the potential to probe the Higgs boson more precisely. However, the ATLAS detector needs significant upgrades in order to cope with the HL-LHC environment. The ATLAS HL-LHC inner tracker uses mature silicon detector technology to record charged particle tracks. However, radiation damage during HL-LHC poses new challenges to the sensor and readout chip radiation tolerance.

The first X-ray radiation campaign on the ATLAS ITkPixV1 chip was conducted successfully at Berkeley Lab, paving ways for future irradiation measurements on site. The X-ray machine dose rates are well understood and the ring oscillator radiation damage matches expectations. However, much more work is needed to understand the ITkPixV2 and pixel sensor performance under the HL-LHC radiation environment and ensure that they meet the inner tracker performance requirements.

The X-ray radiation dose rate is high compared to the actual radiation environment. The radiation damage on chips depends on the dose rate. Slower dose rates tend to cause more damage. SLIPPER (SLow Irradiation of Phase-II Pixel Readout) intends to understand this issue with the low dose rate Kryton source [270]. The radiation damage on a bare chip without sensors might be different compared to ITk modules. Irradiating the module requires a proton source with both bulk and surface damage to the sensor and the chip [266]. Both the slow dose rate and the proton irradiation campaigns show promising radiation tolerance of the ITkPixV1 chip. While the ITkPixV2 chip is finalized and ready for production, more realistic testings of the ITkPixV2 chip are crucial to characterize the detector performance and inform the detector operation.

Chapter 6

Summary and outlook

The Standard Model of particle physics has successfully predicted many Higgs boson properties. However, many beyond the Standard Model theories offer compatible predictions with the existing measurements and deviations in uncharted regimes. The Higgs coupling to charm is one example where potential new physics can hide as the Higgs-charm coupling has not been measured yet.

This thesis presented the results from the ATLAS $VH(\to b\bar{b}, c\bar{c})$ analysis using the full Run 2 dataset. In the analysis, most object are reconstructed using the standard ATLAS reconstruction techniques. The Higgs to bottom and charm couplings are measured using Higgs bosons produced in association with the vector bosons. The analysis regions are further divided into three lepton channels given the decay signature of the vector bosons. The signal and background modeling uses various Monte Carlo generators. The modeling uncertainties are assessed in terms of the normalization uncertainties and shape uncertainties. Profile likelihood fits are performed to correct the background simulation given data and extract the final signal strength and upper limits. The results presented in the thesis primarily focus on the $VH(\to c\bar{c})$ 2-lepton channel, which probes the $ZH(\to c\bar{c})$ process.

In the $VH(\to b\bar{b}, c\bar{c})$ analysis, the `DL1r` flavor tagging algorithm is used, which improves the c-tagging performance compared to the previous `DL1` algorithm [2]. In addition, the flavor tagging working points are customized using the pseudo-continuous flavor tagging scheme. This ensures orthogonality between the $VH(\to b\bar{b})$ and $VH(\to c\bar{c})$ phase spaces and enhances the signal sensitivities with more flavor tagging bins available. The multivariate analysis method significantly improves the signal sensitivities by separating signal and background events using boosted decision trees. Lastly, CARL, the neural network reweighting package, enables assessing the MVA shape uncertainties in all phase space.

The $VH(\to b\bar{b}, c\bar{c})$ analysis sets the most stringent upper limits on $\mu_{VH(c\bar{c})}$, κ_c, and κ_c/κ_b to date. The observed (expected) $\mu_{VH(c\bar{c})}$ upper limit is set to 11.3 (10.4) times the SM at the 95% confidence level (CL). The observed κ_c upper limit at the 95% CL is $|\kappa_c| < 4.2$. The observed (expected) κ_c/κ_b upper limit at the 95% CL is $|\kappa_c/\kappa_b| < 3.6$ (3.5). The observed upper limits agree well with the expected values and are consistent with the Standard Model expectations. Looking ahead, the Higgs charm coupling sensitivities can be further improved

with the latest ATLAS flavor tagging algorithm, GN1 and GN2 [133, 271]. GN1 has 50% better light jet rejections using graph neural networks, while GN2 has two times better light jet rejections using transformer neural networks. There is also ongoing work to further improve the GN1 and GN2 performance by adding soft leptons. The boosted phase space with vector boson p_T^V above 400 GeV also shows promising sensitivities [272]. There is now a dedicated large-R jet tagger for identifying boosted Higgs decaying to bottom and charm quarks based on a transformer neural network [273]. In addition, various other Higgs production channels could also be explored to enhance the Higgs-charm sensitivity [274].

In addition, this thesis discusses the ATLAS high luminosity upgrades and the first X-ray irradiation campaign at Berkeley Lab on ITkPixV1, the prototype inner tracker pixel detector readout chip. The inner tracker will replace the current ATLAS inner detector in the HL-LHC. To perform irradiation testing, the X-ray dose rates are first calibrated carefully. The maximum dose rate during the month-long irradiation campaign is 0.48 Mrad/h. The ITkPixV1 ring oscillator radiation damage agrees with the observation from other sites up to a dose of 415 Mrad.

The RD53C collaboration has delivered the final version of the ATLAS inner tracker pixel detector readout chip, ITkPixV2. Production and extensive testing are currently ongoing. Beyond HL-LHC, many future collider proposals are being developed and reviewed such as the CERN Future Circular Collider [275], Chinese Circular Electron Positron Collider [276], and the Muon Collider [277]. The proposed future lepton colliders tend to have high precision in measuring the Higgs-charm coupling with around a few % of the total uncertainties [278, 279, 280]. The lepton colliders offer a clean environment for detecting hadronic final states. All future colliders continue to need silicon trackers. Many silicon tracker R&D programs are being explored to extend the current signal sensitivities such as 4D tracking [281] and monolithic detectors [282].

Further down the road, while the Standard Model of particle physics successfully predicts many properties of the Higgs boson, there are still many open questions beyond the current Standard Model framework. What is the shape of the Higgs potential [283]? What is the mass of neutrinos [10]? What can explain the observed matter-antimatter asymmetry in the universe [284]? What is the nature of dark matter and dark energy [285]? Can gravity be quantum as well [286]? Answering these challenging questions requires many more groundbreaking experiments yet to come.

Bibliography

[1] The ATLAS Collaboration. *Measurements of W H and Z H Higgs production with decays into bottom quarks and direct constraints on the charm Yukawa coupling with 13 TeV collisions in the ATLAS detector.* Tech. rep. Geneva: CERN, 2024. URL: http://cds.cern.ch/record/2905263.

[2] G. Aad, B. Abbott, et al. "Direct constraint on the Higgs–charm coupling from a search for Higgs boson decays into charm quarks with the ATLAS detector". In: *The European Physical Journal C* 82.8 (Aug. 2022). ISSN: 1434-6052. DOI: 10.1140/epjc/s10052-022-10588-3.

[3] A. Pais and S. B. Treiman. "How Many Charm Quantum Numbers are There?" In: *Phys. Rev. Lett.* 35 (23 Dec. 1975), pp. 1556–1559. DOI: 10.1103/PhysRevLett.35.1556.

[4] Mark Thomson. *Modern particle physics*. New York: Cambridge University Press, 2013. ISBN: 978-1-107-03426-6. DOI: 10.1017/CBO9781139525367.

[5] Michael E. Peskin and Daniel V. Schroeder. *An Introduction to quantum field theory*. Reading, USA: Addison-Wesley, 1995. ISBN: 978-0-201-50397-5. DOI: 10.1201/9780429503559.

[6] Matthew D. Schwartz. *Quantum Field Theory and the Standard Model*. Cambridge University Press, 2013.

[7] A. Salam and J.C. Ward. "Electromagnetic and weak interactions". In: *Physics Letters* 13.2 (1964), pp. 168–171. ISSN: 0031-9163. DOI: https://doi.org/10.1016/0031-9163(64)90711-5. URL: https://www.sciencedirect.com/science/article/pii/0031916364907115.

[8] Howard Georgi. *Lie Algebras In Particle Physics : from Isospin To Unified Theories*. Boca Raton: Taylor & Francis, 2000. ISBN: 978-0-7382-0233-4. DOI: 10.1201/9780429499210.

[9] Peter W. Higgs. "Broken Symmetries and the Masses of Gauge Bosons". In: *Phys. Rev. Lett.* 13 (16 Oct. 1964), pp. 508–509. DOI: 10.1103/PhysRevLett.13.508.

[10] M Aker et al. "Direct neutrino-mass measurement with sub-electronvolt sensitivity". In: *Nature Physics* 18.2 (2022), pp. 160–166. DOI: 10.1038/s41567-021-01463-1. URL: https://www.nature.com/articles/s41567-021-01463-1.

[11] D. Q. Adams et al. "New Direct Limit on Neutrinoless Double Beta Decay Half-Life of ^{128}Te with CUORE". In: *Phys. Rev. Lett.* 129 (22 Nov. 2022), p. 222501. DOI: 10.1103/PhysRevLett.129.222501.

[12] Carsten Burgard. *Standard model graphics*. Mar. 2024. URL: https://texample.net/tikz/examples/model-physics/.

[13] Basudeb Dasgupta and Joachim Kopp. "Sterile neutrinos". In: *Physics Reports* 928 (Sept. 2021), pp. 1–63. ISSN: 0370-1573. DOI: 10.1016/j.physrep.2021.06.002.

[14] Matthew D. Schwartz. *TASI Lectures on Collider Physics*. 2017. arXiv: 1709.04533 [hep-ph].

[15] Lorenz Willmann and Klaus Jungmann. "Matter-antimatter asymmetry - aspects at low energy". In: *Annalen der Physik* 528.1-2 (2016), pp. 108–114. DOI: https://doi.org/10.1002/andp.201500008.

[16] John Ellis, Mary K. Gaillard, and Dimitri V. Nanopoulos. "An Updated Historical Profile of the Higgs Boson". In: (2016), pp. 255–274. DOI: 10.1142/9789814733519_0014. arXiv: 1504.07217. URL: https://cds.cern.ch/record/2012465.

[17] Particle Data Group. "Review of Particle Physics". In: *Progress of Theoretical and Experimental Physics* 2020.8 (Aug. 2020), p. 083C01. ISSN: 2050-3911. DOI: 10.1093/ptep/ptaa104. eprint: https://academic.oup.com/ptep/article-pdf/2020/8/083C01/34673722/ptaa104.pdf.

[18] G. Aad et al. "Combined Measurement of the Higgs Boson Mass from the $H \to \gamma\gamma$ and $H \to ZZ^* \to 4\ell$ Decay Channels with the ATLAS Detector Using $\sqrt{s} = 7$, 8, and 13 TeV *pp* Collision Data". In: *Phys. Rev. Lett.* 131 (25 Dec. 2023), p. 251802. DOI: 10.1103/PhysRevLett.131.251802.

[19] Anwar A. Bhatti and Don Lincoln. "Jet Physics at the Tevatron". In: *Annual Review of Nuclear and Particle Science* 60.1 (Nov. 2010), pp. 267–297. ISSN: 1545-4134. DOI: 10.1146/annurev.nucl.012809.104430.

[20] Emanuele R. Nocera. "Unbiased polarized PDFs upgraded with new inclusive DIS data". In: *Journal of Physics: Conference Series* 678.1 (Jan. 2016), p. 012030. DOI: 10.1088/1742-6596/678/1/012030.

[21] Richard D. Ball et al. "Parton distributions from high-precision collider data: NNPDF Collaboration". In: *The European Physical Journal C* 77.10 (Oct. 2017). ISSN: 1434-6052. DOI: 10.1140/epjc/s10052-017-5199-5.

[22] Steven D. Bass, Albert De Roeck, and Marumi Kado. "The Higgs boson implications and prospects for future discoveries". In: *Nature Reviews Physics* 3.9 (July 2021), pp. 608–624. ISSN: 2522-5820. DOI: 10.1038/s42254-021-00341-2.

[23] A. V. Bednyakov et al. "Stability of the Electroweak Vacuum: Gauge Independence and Advanced Precision". In: *Phys. Rev. Lett.* 115 (20 Nov. 2015), p. 201802. DOI: 10.1103/PhysRevLett.115.201802.

[24] M. Reichert et al. "Probing baryogenesis through the Higgs boson self-coupling". In: *Phys. Rev. D* 97 (7 Apr. 2018), p. 075008. DOI: 10.1103/PhysRevD.97.075008.

[25] Brian Patt and Frank Wilczek. *Higgs-field Portal into Hidden Sectors*. 2006. arXiv: hep-ph/0605188 [hep-ph].

[26] Paolo Bolzoni et al. "Vector boson fusion at next-to-next-to-leading order in QCD: Standard model Higgs boson and beyond". In: *Phys. Rev. D* 85 (3 Feb. 2012), p. 035002. DOI: 10.1103/PhysRevD.85.035002.

[27] M. Aaboud et al. "Observation of Higgs boson production in association with a top quark pair at the LHC with the ATLAS detector". In: *Physics Letters B* 784 (2018), pp. 173–191. ISSN: 0370-2693. DOI: https://doi.org/10.1016/j.physletb.2018.07.035. URL: https://www.sciencedirect.com/science/article/pii/S0370269318305732.

[28] D. de Florian et al. *Handbook of LHC Higgs Cross Sections: 4. Deciphering the Nature of the Higgs Sector*. CERN Yellow Reports: Monographs. Geneva: CERN, 2017. DOI: 10.23731/CYRM-2017-002. URL: https://cds.cern.ch/record/2227475.

[29] G. Aad et al. "Observation of a new particle in the search for the Standard Model Higgs boson with the ATLAS detector at the LHC". In: *Physics Letters B* 716.1 (Sept. 2012), pp. 1–29. ISSN: 0370-2693. DOI: 10.1016/j.physletb.2012.08.020.

[30] S. Chatrchyan et al. "Observation of a new boson at a mass of 125 GeV with the CMS experiment at the LHC". In: *Physics Letters B* 716.1 (Sept. 2012), pp. 30–61. ISSN: 0370-2693. DOI: 10.1016/j.physletb.2012.08.021.

[31] The ATLAS Collaboration. "A detailed map of Higgs boson interactions by the ATLAS experiment ten years after the discovery". In: *Nature* 607.7917 (July 2022), pp. 52–59. ISSN: 1476-4687. DOI: 10.1038/s41586-022-04893-w.

[32] The CMS Collaboration. "A portrait of the Higgs boson by the CMS experiment ten years after the discovery". In: *Nature* 607.7917 (July 2022), pp. 60–68. ISSN: 1476-4687. DOI: 10.1038/s41586-022-04892-x.

[33] A.M. Sirunyan et al. "A measurement of the Higgs boson mass in the diphoton decay channel". In: *Physics Letters B* 805 (2020), p. 135425. ISSN: 0370-2693. DOI: https://doi.org/10.1016/j.physletb.2020.135425. URL: https://www.sciencedirect.com/science/article/pii/S037026932030229X.

[34] G. Aad and others (ATLAS Collaboration). "Constraints on the Higgs boson width from off-shell production and decay to ZZ to 4l and 2l2v with the ATLAS detector". In: *PoS* EPS-HEP2013 (2013). [Proceedings, 2013 European Physical Society Conference on High Energy Physics (EPS-HEP 2013), Stockholm, Sweden, July 18-24, 2013], p. 114. arXiv: 1403.4427 [hep-ex].

[35] Philip Coleman Harris, Dylan Sheldon Rankin, and Cristina Mantilla Suarez. *An approach to constraining the Higgs width at the LHC and HL-LHC*. 2019. arXiv: 1910.02082 [hep-ph]. URL: https://arxiv.org/abs/1910.02082.

[36] The CMS Collaboration. "Measurement of the Higgs boson width and evidence of its off-shell contributions to ZZ production". In: *Nature Physics* 18.11 (Nov. 2022), pp. 1329–1334. ISSN: 1745-2481. DOI: 10.1038/s41567-022-01682-0.

[37] G. Aad et al. "Evidence of off-shell Higgs boson production from ZZ leptonic decay channels and constraints on its total width with the ATLAS detector". In: *Physics Letters B* 846 (Nov. 2023), p. 138223. ISSN: 0370-2693. DOI: 10.1016/j.physletb.2023.138223.

[38] C T Potter et al. *Handbook of LHC Higgs Cross Sections: 3. Higgs Properties: Report of the LHC Higgs Cross Section Working Group*. en. 2013. DOI: 10.5170/CERN-2013-004. URL: http://cds.cern.ch/record/1559921.

[39] A. Tumasyan et al. "Search for Higgs boson decay to a charm quark-antiquark pair in proton-proton collisions at $\sqrt{s} = 13$ TeV". In: *Physical Review Letters* 131.6 (Aug. 2023). ISSN: 1079-7114. DOI: 10.1103/physrevlett.131.061801.

[40] G. Aad et al. "Search for invisible Higgs-boson decays in events with vector-boson fusion signatures using 139 fb−1 of proton-proton data recorded by the ATLAS experiment". In: *Journal of High Energy Physics* 2022.8 (Aug. 2022). ISSN: 1029-8479. DOI: 10.1007/jhep08(2022)104.

[41] Michaela Mlynarikova. *Higgs Physics at HL-LHC*. Tech. rep. Presented at DIS2023. Geneva: CERN, 2023. arXiv: 2307.07772. URL: https://cds.cern.ch/record/2865117.

[42] The ATLAS Collaboration. *Combination of searches for Higgs boson pair production in pp collisions at $\sqrt{s} = 13$ TeV with the ATLAS detector*. 2024. arXiv: 2406.09971 [hep-ex]. URL: https://arxiv.org/abs/2406.09971.

[43] The ATLAS Collaboration. *Interpretations of the ATLAS measurements of Higgs boson production and decay rates and differential cross-sections in pp collisions at $\sqrt{s} = 13$ TeV*. 2024. arXiv: 2402.05742 [hep-ex].

[44] Admir Greljo and Ajdin Palavrić. *Leading directions in the SMEFT*. 2023. arXiv: 2305.08898 [hep-ph]. URL: https://arxiv.org/abs/2305.08898.

[45] S. Bar-Shalom and A. Soni. "Universally enhanced light-quarks Yukawa couplings paradigm". In: *Phys. Rev. D* 98 (5 2018), p. 055001. DOI: 10.1103/PhysRevD.98.055001.

[46] C. Delaunay et al. "Enhanced Higgs boson coupling to charm pairs". In: *Phys. Rev. D* 89 (3 2014), p. 033014. DOI: 10.1103/PhysRevD.89.033014.

[47] F.J. Botella et al. "What if the masses of the first two quark families are not generated by the standard model Higgs boson?" In: *Phys. Rev. D* 94.11 (2016), p. 115031. DOI: 10.1103/PhysRevD.94.115031. arXiv: 1602.08011 [hep-ph].

[48] D. Egana-Ugrinovic, S. Homiller, and P. R. Meade. "Higgs bosons with large couplings to light quarks". In: *Phys. Rev. D* 100.11 (2019), p. 115041. DOI: 10.1103/PhysRevD.100.115041. arXiv: 1908.11376 [hep-ph].

[49] D. Egana-Ugrinovic, S. Homiller, and P. R. Meade. "Aligned and Spontaneous Flavor Violation". In: *Phys. Rev. Lett.* 123.3 (2019), p. 031802. DOI: 10.1103/PhysRevLett.123.031802. arXiv: 1811.00017 [hep-ph].

[50] D. Ghosh, R. S. Gupta, and G. Perez. "Is the Higgs mechanism of fermion mass generation a fact? A Yukawa-less first-two-generation model". In: *Physics Letters B* 755 (2016), pp. 504–508. ISSN: 0370-2693. DOI: 10.1016/j.physletb.2016.02.059.

[51] Florin Pop. "High Performance Numerical Computing for High Energy Physics: A New Challenge for Big Data Science". In: *Adv. High Energy Phys.* 2014 (2014), p. 507690. DOI: 10.1155/2014/507690.

[52] G. Aad et al. "The ATLAS Simulation Infrastructure". In: *The European Physical Journal C* 70.3 (Sept. 2010), pp. 823–874. ISSN: 1434-6052. DOI: 10.1140/epjc/s10052-010-1429-9.

[53] Zachary Marshall and the ATLAS Collaboration. "Simulation of Pile-up in the ATLAS Experiment". In: *Journal of Physics: Conference Series* 513.2 (June 2014), p. 022024. DOI: 10.1088/1742-6596/513/2/022024.

[54] S. Agostinelli et al. "Geant4 a simulation toolkit". In: *Nuclear Instruments and Methods in Physics Research Section A: Accelerators, Spectrometers, Detectors and Associated Equipment* 506.3 (2003), pp. 250–303. ISSN: 0168-9002. DOI: https://doi.org/10.1016/S0168-9002(03)01368-8. URL: http://www.sciencedirect.com/science/article/pii/S0168900203013688.

[55] G. Aad et al. "AtlFast3: The Next Generation of Fast Simulation in ATLAS". In: *Computing and Software for Big Science* 6.1 (Mar. 2022). ISSN: 2510-2044. DOI: 10.1007/s41781-021-00079-7.

[56] Enrico Bothmann et al. "Event generation with Sherpa 2.2". In: *SciPost Phys.* 7.3 (2019), p. 034. DOI: 10.21468/SciPostPhys.7.3.034. arXiv: 1905.09127 [hep-ph].

[57] Nason P. Luisoni G. et al. "HW ±/HZ + 0 and 1 jet at NLO with the POWHEG BOX interfaced to GoSam and their merging within MiNLO". In: *J. High Energ. Phys. 2013: 83* (2013). DOI: https://doi.org/10.1007/JHEP10(2013)083. URL: https://link.springer.com/article/10.1007%2FJHEP10%282013%29083.

[58] Sjostrand T., S. Mrenna, and P. Skands. "A brief introduction to PYTHIA 8.1". In: *Computer Physics Communications* 178.11 (2008), pp. 852–867. ISSN: 0010-4655. DOI: https://doi.org/10.1016/j.cpc.2008.01.036. URL: http://www.sciencedirect.com/science/article/pii/S0010465508000441.

[59] Johannes Bellm et al. "Herwig 7.0/Herwig++ 3.0 release note". In: *Eur. Phys. J. C* 76.4 (2016), p. 196. DOI: 10.1140/epjc/s10052-016-4018-8. arXiv: 1512.01178 [hep-ph].

[60] J. Alwall et al. "The automated computation of tree-level and next-to-leading order differential cross sections, and their matching to parton shower simulations". In: *JHEP* 07 (2014). Comments: 158 pages, 27 figures; a few references have been added, p. 079. DOI: 10.1007/JHEP07(2014)079. arXiv: 1405.0301. URL: https://cds.cern.ch/record/1699128.

[61] Lyndon Evans and Philip Bryant. "LHC Machine". In: *Journal of Instrumentation* 3.08 (Aug. 2008), S08001. DOI: 10.1088/1748-0221/3/08/S08001.

[62] *Facts and Figures about LHC*. CERN. 2024. URL: https://home.cern/resources/faqs/facts-and-figures-about-lhc.

[63] The ATLAS Collaboration. *ATLAS Luminosity Public Results for Run 1*. Accessed on Jun 10th 2024. 2024. URL: https://twiki.cern.ch/twiki/bin/view/AtlasPublic/LuminosityPublicResultsRun1.

[64] ATLAS Collaboration. *ATLAS Luminosity Public Results for Run 2*. Accessed on Jun 10th 2024. 2024. URL: https://twiki.cern.ch/twiki/bin/view/AtlasPublic/LuminosityPublicResultsRun2.

[65] The ATLAS Collaboration. *ATLAS Luminosity Public Results for Run 3*. Accessed on Jun 10th 2024. 2024. URL: https://twiki.cern.ch/twiki/bin/view/AtlasPublic/LuminosityPublicResultsRun3.

[66] Michael Benedikt and Frank Zimmermann. "Proton colliders at the energy frontier". In: *Nuclear Instruments and Methods in Physics Research Section A: Accelerators, Spectrometers, Detectors and Associated Equipment* 907 (Nov. 2018), pp. 200–208. ISSN: 0168-9002. DOI: 10.1016/j.nima.2018.03.021.

[67] Esma Mobs. "The CERN accelerator complex in 2019. Complexe des accélérateurs du CERN en 2019". In: (2019). General Photo. URL: https://cds.cern.ch/record/2684277.

[68] The ATLAS Collaboration. "Luminosity determination in pp collisions at 13 TeV using the ATLAS detector at the LHC". In: *The European Physical Journal C* 83.10 (Oct. 2023), p. 982. ISSN: 1434-6052. DOI: 10.1140/epjc/s10052-023-11747-w.

[69] The CMS Collaboration. "The CMS experiment at the CERN LHC". In: *Journal of Instrumentation* 3.08 (Aug. 2008), S08004. DOI: 10.1088/1748-0221/3/08/S08004.

[70] The ATLAS Collaboration. "The ATLAS Experiment at the CERN Large Hadron Collider". In: *Journal of Instrumentation* 3.08 (Aug. 2008), S08003. DOI: 10.1088/1748-0221/3/08/S08003.

[71] The LHCb Collaboration. "The LHCb Detector at the LHC". In: *Journal of Instrumentation* 3.08 (Aug. 2008), S08005. DOI: 10.1088/1748-0221/3/08/S08005.

[72] Elena Graverini. *Luminosity at LHCb in Run 3*. 2022. arXiv: 2211.12405 [hep-ex].

[73] The ALICE Collaboration. "The ALICE experiment at the CERN LHC". In: *Journal of Instrumentation* 3.08 (Aug. 2008), S08002. DOI: 10.1088/1748-0221/3/08/S08002.

[74] Henso Abreu et al. "The FASER detector". In: *Journal of Instrumentation* 19.05 (May 2024), P05066. ISSN: 1748-0221. DOI: 10.1088/1748-0221/19/05/p05066.

[75] Claudio Luci. "The ATLAS experiment Phase-I upgrades for the LHC Run-3". In: (2023). URL: https://cds.cern.ch/record/2871857.

[76] G. Aad et al. "Electron and photon performance measurements with the ATLAS detector using the 2015–2017 LHC proton-proton collision data". In: *Journal of Instrumentation* 14.12 (Dec. 2019), P12006. DOI: 10.1088/1748-0221/14/12/P12006.

[77] Giles Chatham Strong. "On the impact of selected modern deep-learning techniques to the performance and celerity of classification models in an experimental high-energy physics use case". In: *Machine Learning: Science and Technology* 1.4 (Sept. 2020), p. 045006. DOI: 10.1088/2632-2153/ab983a.

[78] Karolos Potamianos. *The upgraded Pixel detector and the commissioning of the Inner Detector tracking of the ATLAS experiment for Run-2 at the Large Hadron Collider*. 2016. arXiv: 1608.07850 [physics.ins-det].

[79] M. Aaboud et al. "Study of the material of the ATLAS inner detector for Run 2 of the LHC". In: *Journal of Instrumentation* 12.12 (Dec. 2017), P12009. DOI: 10.1088/1748-0221/12/12/P12009.

[80] ATLAS Collaboration. *IBL Efficiency and Single Point Resolution in Collision Events*. Tech. rep. Geneva: CERN, 2016. URL: https://cds.cern.ch/record/2203893.

[81] A Abdesselam and T Akimoto. *The Barrel Modules of the ATLAS SemiConductor Tracker*. Tech. rep. Geneva: CERN, 2006. DOI: 10.1016/j.nima.2006.08.036. URL: https://cds.cern.ch/record/974073.

[82] Bartosz Mindur. "ATLAS Transition Radiation Tracker (TRT): Straw tubes for tracking and particle identification at the Large Hadron Collider". In: *Nuclear Instruments and Methods in Physics Research Section A: Accelerators, Spectrometers, Detectors and Associated Equipment* 845 (2017). Proceedings of the Vienna Conference on Instrumentation 2016, pp. 257–261. ISSN: 0168-9002. DOI: https://doi.org/10.1016/j.nima.2016.04.026. URL: https://www.sciencedirect.com/science/article/pii/S0168900216301905.

[83] A Vogel. *ATLAS Transition Radiation Tracker (TRT): Straw Tube Gaseous Detectors at High Rates*. Tech. rep. Geneva: CERN, 2013. URL: https://cds.cern.ch/record/1537991.

[84] R.L. Gluckstern. "Uncertainties in track momentum and direction, due to multiple scattering and measurement errors". In: *Nuclear Instruments and Methods* 24 (1963), pp. 381–389. ISSN: 0029-554X. DOI: https://doi.org/10.1016/0029-554X(63)90347-1. URL: https://www.sciencedirect.com/science/article/pii/0029554X63903471.

[85] Dag Gillberg et al. "Performance of the ATLAS Forward Calorimeters in First LHC Data". In: *Journal of Physics: Conference Series* 293.1 (Apr. 2011), p. 012041. DOI: 10.1088/1742-6596/293/1/012041.

[86] D M Gingrich et al. "Construction, assembly and testing of the ATLAS hadronic end-cap calorimeter". In: *Journal of Instrumentation* 2.05 (May 2007), P05005. DOI: 10.1088/1748-0221/2/05/P05005.

[87] Michele Livan and Richard Wigmans. *Misconceptions about Calorimetry*. 2017. arXiv: 1704.00661 [physics.ins-det].

[88] The ATLAS collaboration. "ATLAS liquid argon calorimeter: Technical design report". In: (Dec. 1996).

[89] J Wotschack. *ATLAS Muon Chamber Construction Parameters for CSC, MDT, and RPC chambers*. Tech. rep. Back-up document for the ATLAS Detector Paper. Geneva: CERN, 2008. URL: https://cds.cern.ch/record/1099400.

[90] Giordano Cattani and the ATLAS Collaboration. "The Resistive Plate Chambers of the ATLAS experiment: performance studies". In: *Journal of Physics: Conference Series* 280.1 (Feb. 2011), p. 012001. DOI: 10.1088/1742-6596/280/1/012001.

[91] The ATLAS collaboration. "Operation of the ATLAS trigger system in Run 2". In: *Journal of Instrumentation* 15.10 (Oct. 2020), P10004. DOI: 10.1088/1748-0221/15/10/P10004.

[92] G. Aad et al. "The ATLAS Fast TracKer system". In: *Journal of Instrumentation* 16.07 (July 2021), P07006. ISSN: 1748-0221. DOI: 10.1088/1748-0221/16/07/p07006.

[93] R Achenbach et al. *The ATLAS Level-1 Calorimeter Trigger*. Tech. rep. Geneva: CERN, 2008. DOI: 10.1088/1748-0221/3/03/P03001. URL: https://cds.cern.ch/record/1080560.

[94] Julian Glatzer and the ATLAS Collaboration. "Operation of the Upgraded ATLAS Level-1 Central Trigger System". In: *Journal of Physics: Conference Series* 664.8 (Dec. 2015), p. 082013. DOI: 10.1088/1742-6596/664/8/082013.

[95] The ATLAS Collaboration. *ATLAS Trigger Operation Public Results*. Accessed on July 15th 2024. Jan. 2024. URL: https://twiki.cern.ch/twiki/bin/view/AtlasPublic/TriggerOperationPublicResults.

[96] Joao Pequenao and Paul Schaffner. "How ATLAS detects particles: diagram of particle paths in the detector". 2013. URL: https://cds.cern.ch/record/1505342.

[97] Andreas Salzburger and the ATLAS Collaboration. "Optimisation of the ATLAS Track Reconstruction Software for Run-2". In: *Journal of Physics: Conference Series* 664.7 (Dec. 2015), p. 072042. DOI: 10.1088/1742-6596/664/7/072042.

[98] M. Aaboud et al. "Performance of the ATLAS track reconstruction algorithms in dense environments in LHC Run 2". In: *The European Physical Journal C* 77.10 (Oct. 2017). ISSN: 1434-6052. DOI: 10.1140/epjc/s10052-017-5225-7.

[99] Wolfgang Lukas. "ATLAS inner tracking detectors: Run 1 performance and developments for Run 2". In: *Nuclear and Particle Physics Proceedings* 273-275 (2016). 37th International Conference on High Energy Physics (ICHEP), pp. 1134–1140. ISSN: 2405-6014. DOI: https://doi.org/10.1016/j.nuclphysbps.2015.09.178. URL: https://www.sciencedirect.com/science/article/pii/S2405601415006677.

[100] T G Cornelissen et al. *Updates of the ATLAS Tracking Event Data Model (Release 13)*. Tech. rep. Geneva: CERN, 2007. URL: https://cds.cern.ch/record/1038095.

[101] S Boutle et al. "Primary vertex reconstruction at the ATLAS experiment". In: *Journal of Physics: Conference Series* 898.4 (Oct. 2017), p. 042056. DOI: 10.1088/1742-6596/898/4/042056.

[102] Paul Laycock et al. *ATLAS data preparation in run 2*. Tech. rep. 4. Geneva: CERN, 2017. DOI: 10.1088/1742-6596/898/4/042050. URL: https://cds.cern.ch/record/2253427.

[103] *ATLAS Beam Spot Public Results*. Jan. 2024. URL: https://twiki.cern.ch/twiki/bin/view/AtlasPublic/BeamSpotPublicResults#Run_2_25ns_pp_Collisions_s_13_Te.

[104] G. Aad et al. "Electron and photon performance measurements with the ATLAS detector using the 2015–2017 LHC proton-proton collision data". In: *Journal of Instrumentation* 14.12 (Dec. 2019), P12006–P12006. ISSN: 1748-0221. DOI: 10.1088/1748-0221/14/12/p12006.

[105] W Lampl et al. *Calorimeter Clustering Algorithms: Description and Performance*. Tech. rep. Geneva: CERN, 2008. URL: https://cds.cern.ch/record/1099735.

[106] The ATLAS Collaboration. *Improved electron reconstruction in ATLAS using the Gaussian Sum Filter-based model for bremsstrahlung*. Tech. rep. Geneva: CERN, 2012. URL: https://cds.cern.ch/record/1449796.

[107] G. Aad et al. "Electron and photon energy calibration with the ATLAS detector using LHC Run 1 data". In: *The European Physical Journal C* 74.10 (Oct. 2014). ISSN: 1434-6052. DOI: 10.1140/epjc/s10052-014-3071-4.

[108] The ATLAS Collaboration. "Muon reconstruction and identification efficiency in ATLAS using the full Run 2 pp collision data set at 13 TeV". In: *The European Physical Journal C* 81.7 (July 2021), p. 578. ISSN: 1434-6052. DOI: 10.1140/epjc/s10052-021-09233-2.

[109] G. Aad et al. "Topological cell clustering in the ATLAS calorimeters and its performance in LHC Run 1". In: *The European Physical Journal C* 77.7 (July 2017). ISSN: 1434-6052. DOI: 10.1140/epjc/s10052-017-5004-5.

[110] The ATLAS Collaboration. *Measurement of the tau lepton reconstruction and identification performance in the ATLAS experiment using pp collisions at 13 TeV*. Tech. rep. Geneva: CERN, 2017. URL: https://cds.cern.ch/record/2261772.

[111] The ATLAS Collaboration. *Identification of hadronic tau lepton decays using neural networks in the ATLAS experiment*. ATL-PHYS-PUB-2019-033. 2019. URL: https://cds.cern.ch/record/2688062.

[112] Gavin P. Salam. "Towards jetography". In: *The European Physical Journal C* 67.3 (June 2010), pp. 637–686. ISSN: 1434-6052. DOI: 10.1140/epjc/s10052-010-1314-6.

[113] M. Aaboud et al. "Jet reconstruction and performance using particle flow with the ATLAS Detector". In: *The European Physical Journal C* 77.7 (July 2017). ISSN: 1434-6052. DOI: 10.1140/epjc/s10052-017-5031-2.

[114] Matteo Cacciari, Gavin P. Salam, and Gregory Soyez. "The anti-kt jet clustering algorithm". In: *Journal of High Energy Physics* 2008.04 (Apr. 2008), p. 063. DOI: 10.1088/1126-6708/2008/04/063.

[115] G. Aad et al. "Optimisation of large-radius jet reconstruction for the ATLAS detector in 13 TeV proton–proton collisions". In: *The European Physical Journal C* 81.4 (Apr. 2021), p. 334. ISSN: 1434-6052. DOI: 10.1140/epjc/s10052-021-09054-3.

[116] The ATLAS Collaboration. "Jet energy scale and resolution measured in proton–proton collisions at 13 TeV with the ATLAS detector". In: *The European Physical Journal C* 81.8 (Aug. 2021), p. 689. ISSN: 1434-6052. DOI: 10.1140/epjc/s10052-021-09402-3.

[117] The ATLAS Collaboration. "In situ calibration of large-radius jet energy and mass in 13 TeV proton–proton collisions with the ATLAS detector". In: *Eur. Phys. J. C* 79 (2019), p. 135. DOI: 10.1140/epjc/s10052-019-6632-8. arXiv: 1807.09477 [hep-ex].

[118] The ATLAS Collaboration. *Tagging and suppression of pileup jets with the ATLAS detector*. Tech. rep. Geneva: CERN, 2014. URL: https://cds.cern.ch/record/1700870.

[119] The ATLAS Collaboration. *Forward jet vertex tagging using the particle flow algorithm*. Tech. rep. Geneva: CERN, 2019. URL: https://cds.cern.ch/record/2683100.

[120] The ATLAS Collaboration. *Selection of jets produced in 13TeV proton-proton collisions with the ATLAS detector*. Tech. rep. Geneva: CERN, 2015. URL: https://cds.cern.ch/record/2037702.

[121] The ATLAS collaboration. "Monitoring and data quality assessment of the ATLAS liquid argon calorimeter". In: *Journal of Instrumentation* 9.07 (July 2014), P07024–P07024. ISSN: 1748-0221. DOI: 10.1088/1748-0221/9/07/p07024.

[122] Morad Aaboud et al. "Performance of missing transverse momentum reconstruction with the ATLAS detector using proton-proton collisions at $\sqrt{s} = 13$ TeV". In: *Eur. Phys. J. C* 78.11 (2018), p. 903. DOI: 10.1140/epjc/s10052-018-6288-9. arXiv: 1802.08168. URL: https://cds.cern.ch/record/2305380.

[123] The ATLAS Collaboration. *Quark versus Gluon Jet Tagging Using Jet Images with the ATLAS Detector*. Tech. rep. Geneva: CERN, 2017. URL: https://cds.cern.ch/record/2275641.

[124] Georges Aad et al. "ATLAS flavour-tagging algorithms for the LHC Run 2 pp collision dataset". In: *Eur. Phys. J. C* 83.7 (2023), p. 681. DOI: 10.1140/epjc/s10052-023-11699-1. arXiv: 2211.16345 [physics.data-an].

[125] The ATLAS Collaboration. *Expected performance of the ATLAS b-tagging algorithms in Run-2*. Tech. rep. Geneva: CERN, 2015. URL: https://cds.cern.ch/record/2037697.

[126] The ATLAS Collaboration. *Measuring the b-jet identification efficiency for high p_T jets using multijet events in proton−proton collisions at $\sqrt{s} = 13$ TeV recorded with the ATLAS detector*. Tech. rep. Geneva: CERN, 2022. URL: https://cds.cern.ch/record/2804062.

[127] ALICE Collaboration. "Direct observation of the dead-cone effect in quantum chromodynamics". In: *Nature* 605.7910 (May 2022), pp. 440–446. ISSN: 1476-4687. DOI: 10.1038/s41586-022-04572-w.

[128] Diederik P. Kingma and Jimmy Ba. *Adam: A Method for Stochastic Optimization*. 2017. arXiv: 1412.6980 [cs.LG].

[129] *Keras*. Feb. 2024. URL: https://keras.io/.

[130] The ATLAS Collaboration. "ATLAS b-jet identification performance and efficiency measurement with $t\bar{t}$ events in pp collisions at $\sqrt{s} = 13$ TeV". In: *Eur. Phys. J. C* 79 (2019), p. 970. DOI: 10.1140/epjc/s10052-019-7450-8. arXiv: 1907.05120 [hep-ex].

[131] Georges Aad et al. "Calibration of the light-flavour jet mistagging efficiency of the b-tagging algorithms with Z+jets events using 139 fb^{-1} of ATLAS proton-proton collision data at $\sqrt{s} = 13$ TeV". In: *Eur. Phys. J. C* 83 (2023), p. 728. DOI: 10.1140/epjc/s10052-023-11736-z. arXiv: 2301.06319. URL: https://cds.cern.ch/record/2846342.

[132] The ATLAS Collaboration. "Measurement of the c-jet mistagging efficiency in $t\bar{t}$ events using pp collision data at $\sqrt{s} = 13$ TeV collected with the ATLAS detector". In: *Eur. Phys. J. C* 82 (2021), p. 95. DOI: 10.1140/epjc/s10052-021-09843-w. arXiv: 2109.10627 [hep-ex].

[133] The ATLAS Collaboration. *Graph Neural Network Jet Flavour Tagging with the ATLAS Detector*. Tech. rep. Geneva: CERN, 2022. URL: https://cds.cern.ch/record/2811135.

[134] Kim Albertsson et al. *Machine Learning in High Energy Physics Community White Paper*. 2019. arXiv: 1807.02876 [physics.comp-ph].

[135] The ATLAS Collaboration. *Machine Learning*. https://atlas.cern/Updates/Feature/Machine-Learning. 2024.

[136] François Chollet. *Deep Learning with Python*. Manning Publications, 2017.

[137] Yann Coadou. "Boosted Decision Trees". In: *Artificial Intelligence for High Energy Physics*. WORLD SCIENTIFIC, Feb. 2022, pp. 9–58. ISBN: 9789811234033. DOI: 10.1142/9789811234033_0002.

[138] Jie Zhou et al. *Graph Neural Networks: A Review of Methods and Applications*. 2021. arXiv: 1812.08434 [cs.LG].

[139] Saidul Islam et al. *A Comprehensive Survey on Applications of Transformers for Deep Learning Tasks*. 2023. arXiv: 2306.07303 [cs.LG].

[140] John J. Hopfield. "Neural networks and physical systems with emergent collective computational abilities". In: *Proceedings of the National Academy of Sciences* 79.8 (1982), pp. 2554–2558.

[141] *Rectifier (neural networks)*. https://en.wikipedia.org/wiki/Rectifier_(neural_networks). Accessed: 2024-06-03. 2024.

[142] *Softmax function*. https://en.wikipedia.org/wiki/Softmax_function. Accessed: 2024-06-03. 2024.

[143] *Cross-entropy*. https://en.wikipedia.org/wiki/Cross-entropy. Accessed: 2024-06-03. 2024.

[144] David E. Rumelhart, Geoffrey E. Hinton, and Ronald J. Williams. "Learning representations by back-propagating errors". In: *Nature* 323.6088 (Oct. 1986), pp. 533–536. ISSN: 1476-4687. DOI: 10.1038/323533a0.

[145] *DL4Sci Workshop*. https://dl4sci-school.lbl.gov/. Accessed: 2024-06-03. 2019.

[146] The ATLAS Collaboration. *Electron Identification with a Convolutional Neural Network in the ATLAS Experiment*. Tech. rep. Geneva: CERN, 2023. URL: https://cds.cern.ch/record/2850666.

[147] M. Aaboud et al. "Electron reconstruction and identification in the ATLAS experiment using the 2015 and 2016 LHC proton–proton collision data at $\sqrt{s} = 13$ TeV". In: *The European Physical Journal C* 79.8 (Aug. 2019). ISSN: 1434-6052. DOI: 10.1140/epjc/s10052-019-7140-6.

[148] Takuya Akiba et al. "Optuna: A Next-generation Hyperparameter Optimization Framework". In: *Proceedings of the 25th ACM SIGKDD International Conference on Knowledge Discovery and Data Mining*. 2019.

[149] M. Aaboud et al. "Observation of Higgs boson production in association with a top quark pair at the LHC with the ATLAS detector". In: *Physics Letters B* 784 (Sept. 2018), pp. 173–191. ISSN: 0370-2693. DOI: 10.1016/j.physletb.2018.07.035.

[150] A. M. Sirunyan et al. "Observation of ttH Production". In: *Physical Review Letters* 120.23 (June 2018). ISSN: 1079-7114. DOI: 10.1103/physrevlett.120.231801.

[151] M. Aaboud et al. "Observation of Hbb decays and VH production with the ATLAS detector". In: *Physics Letters B* 786 (Nov. 2018), pp. 59–86. ISSN: 0370-2693. DOI: 10.1016/j.physletb.2018.09.013.

[152] A. M. Sirunyan et al. "Observation of Higgs Boson Decay to Bottom Quarks". In: *Physical Review Letters* 121.12 (Sept. 2018). ISSN: 1079-7114. DOI: 10.1103/physrevlett.121.121801.

[153] G. Aad et al. "Measurements of Higgs bosons decaying to bottom quarks from vector boson fusion production with the ATLAS experiment at $\sqrt{s} = 13$ TeV". In: *The European Physical Journal C* 81.6 (June 2021). ISSN: 1434-6052. DOI: 10.1140/epjc/s10052-021-09192-8.

[154] A. Hayrapetyan et al. "Measurement of the Higgs boson production via vector boson fusion and its decay into bottom quarks in proton-proton collisions at $\sqrt{s} = 13$ TeV". In: *Journal of High Energy Physics* 2024.1 (Jan. 2024). ISSN: 1029-8479. DOI: 10.1007/jhep01(2024)173.

[155] The ATLAS Collaboration. "Measurements of WH and ZH production in the VHbb decay channel in pp collisions with the ATLAS detector". In: *The European Physical Journal C* 81.2 (Feb. 2021), p. 178. ISSN: 1434-6052. DOI: 10.1140/epjc/s10052-020-08677-2.

[156] G. Aad et al. "Measurement of the associated production of a Higgs boson decaying into b-quarks with a vector boson at high transverse momentum in pp collisions with the ATLAS detector". In: *Physics Letters B* 816 (May 2021), p. 136204. ISSN: 0370-2693. DOI: 10.1016/j.physletb.2021.136204.

[157] The ATLAS Collaboration. *Combination of measurements of Higgs boson production in association with a W or Z boson in the $b\bar{b}$ decay channel with the ATLAS experiment at $\sqrt{s} = 13$ TeV*. Tech. rep. Geneva: CERN, 2021. URL: https://cds.cern.ch/record/2782535.

[158] A. M. Sirunyan et al. "Evidence for Higgs boson decay to a pair of muons". In: *Journal of High Energy Physics* 2021.1 (Jan. 2021). ISSN: 1029-8479. DOI: 10.1007/jhep01(2021)148.

[159] G. Aad et al. "A search for the dimuon decay of the Standard Model Higgs boson with the ATLAS detector". In: *Physics Letters B* 812 (Jan. 2021), p. 135980. ISSN: 0370-2693. DOI: 10.1016/j.physletb.2020.135980.

[160] G. Aad et al. "Search for the Higgs boson decays Hee and Hemu in pp collisions with the ATLAS detector". In: *Physics Letters B* 801 (Feb. 2020), p. 135148. ISSN: 0370-2693. DOI: 10.1016/j.physletb.2019.135148.

[161] V. Khachatryan et al. "Search for a standard model-like Higgs boson in the mumu and ee decay channels at the LHC". In: *Physics Letters B* 744 (May 2015), pp. 184–207. ISSN: 0370-2693. DOI: 10.1016/j.physletb.2015.03.048.

[162] M. Aaboud et al. "Searches for exclusive Higgs and Z boson decays into J/psi with the ATLAS detector". In: *Physics Letters B* 786 (Nov. 2018), pp. 134–155. ISSN: 0370-2693. DOI: 10.1016/j.physletb.2018.09.024.

[163] A. M. Sirunyan et al. "Search for rare decays of Z/H to J/psi and a photon in proton-proton collisions". In: *The European Physical Journal C* 79.2 (Jan. 2019). ISSN: 1434-6052. DOI: 10.1140/epjc/s10052-019-6562-5.

[164] M. Aaboud et al. "Search for exclusive Higgs and Z boson decays to phipsi and phipsi with the ATLAS detector". In: *Journal of High Energy Physics* 2018.7 (July 2018). ISSN: 1029-8479. DOI: 10.1007/jhep07(2018)127.

[165] A. M. Sirunyan et al. "Search for decays of the 125 GeV Higgs boson into a Z boson and a rho or phi meson". In: *Journal of High Energy Physics* 2020.11 (Nov. 2020). ISSN: 1029-8479. DOI: 10.1007/jhep11(2020)039.

[166] Ben Carlson, Tao Han, and Sze Ching Iris Leung. "Higgs boson to charm quark decay in vector boson fusion plus a photon". In: *Phys. Rev. D* 104 (7 Oct. 2021), p. 073006. DOI: 10.1103/PhysRevD.104.073006.

[167] A. Tumasyan et al. "Search for Higgs Boson and Observation of Z Boson through Their Decay into a Charm Quark-Antiquark Pair in Boosted Topologies in Proton-Proton Collisions at $\sqrt{s} = 13$ TeV". In: *Phys. Rev. Lett.* 131 (4 July 2023), p. 041801. DOI: 10.1103/PhysRevLett.131.041801.

[168] Andrew Chisholm et al. *VH(bb/cc) Legacy Analysis main internal note*. Tech. rep. Geneva: CERN, 2020. URL: https://cds.cern.ch/record/2743096.

[169] *CARL github*. Mar. 2024. URL: https://github.com/sjiggins/carl-torch/tree/master.

[170] M. Aaboud et al. "Electron and photon energy calibration with the ATLAS detector using 2015–2016 LHC proton-proton collision data". In: *Journal of Instrumentation* 14.03 (Mar. 2019), P03017–P03017. ISSN: 1748-0221. DOI: 10.1088/1748-0221/14/03/p03017.

[171] The ATLAS Collaboration. *Variable Radius, Exclusive-k_T, and Center-of-Mass Subjet Reconstruction for Higgs($\to b\bar{b}$) Tagging in ATLAS*. Tech. rep. ATL-PHYS-PUB-2017-010. Geneva: CERN, June 2017. URL: https://cds.cern.ch/record/2268678.

[172] The ATLAS Collaboration, Hannah Arnold, et al. *Object definition of VH(bb/cc) Legacy Analysis*. Tech. rep. Geneva: CERN, 2022. URL: https://cds.cern.ch/record/2843084.

[173] The ATLAS Collaboration. *Flavor Tagging Efficiency Parametrisations with Graph Neural Networks*. Tech. rep. Geneva: CERN, 2022. URL: https://cds.cern.ch/record/2825433.

[174] The ATLAS Collaboration. *Monte Carlo to Monte Carlo scale factors for flavour tagging efficiency calibration*. ATL-PHYS-PUB-2020-009. 2020. URL: https://cds.cern.ch/record/2718610.

[175] The ATLAS Collaboration. *LuminosityForPhysics*. https://twiki.cern.ch/twiki/bin/view/Atlas/LuminosityForPhysics. Accessed: 2024-06-17.

[176] The ATLAS Collaboration. *ExtendedPileupReweighting*. https://twiki.cern.ch/twiki/bin/view/AtlasProtected/ExtendedPileupReweighting#Prescaling_MC. Accessed: 2024-06-17.

[177] The ATLAS Collaboration. *EGammaRecommendationsR21*. https://twiki.cern.ch/twiki/bin/viewauth/AtlasProtected/EGammaRecommendationsR21. Accessed: 2024-06-17.

[178] The ATLAS Collaboration. *MCPAnalysisGuidelinesMC16*. https://twiki.cern.ch/twiki/bin/viewauth/AtlasProtected/MCPAnalysisGuidelinesMC16. Accessed: 2024-06-17.

[179] Matteo Cacciari, Gavin P. Salam, and Gregory Soyez. "The Catchment Area of Jets". In: *JHEP* 04 (2008), p. 005. DOI: 10.1088/1126-6708/2008/04/005. arXiv: 0802.1188 [hep-ph].

[180] G. Aad et al. "Identification of boosted Higgs bosons decaying into b-quark pairs with the ATLAS detector at $\sqrt{s} = 13$ TeV". In: *The European Physical Journal C* 79.10 (Oct. 2019). ISSN: 1434-6052. DOI: 10.1140/epjc/s10052-019-7335-x.

[181] Dorival Goncalves and Junya Nakamura. "Role of the Z polarization in the $H \to b\bar{b}$ measurement". In: *Phys. Rev.* D98.9 (2018), p. 093005. DOI: 10.1103/PhysRevD.98.093005. arXiv: 1805.06385 [hep-ph].

[182] Andy Buckley et al. "An Optimal Observable for Color Singlet Identification". In: *SciPost Phys.* 9 (2020), p. 026. DOI: 10.21468/SciPostPhys.9.2.026. arXiv: 2006.10480 [hep-ph].

[183] Andrew Chisholm et al. *VH(bb/cc) MVA internal note*. Tech. rep. Geneva: CERN, 2022. URL: https://cds.cern.ch/record/2843143/.

[184] Glen Cowan et al. "Asymptotic formulae for likelihood-based tests of new physics". In: *The European Physical Journal C* 71.2 (Feb. 2011). ISSN: 1434-6052. DOI: 10.1140/epjc/s10052-011-1554-0.

[185] A. Hoecker et al. *TMVA - Toolkit for Multivariate Data Analysis*. 2009. arXiv: physics/0703039 [physics.data-an]. URL: https://arxiv.org/abs/physics/0703039.

[186] Georges Aad et al. "ATLAS data quality operations and performance for 2015-2018 data-taking". In: *JINST* 15.04 (2020), P04003. DOI: 10.1088/1748-0221/15/04/P04003. arXiv: 1911.04632. URL: https://cds.cern.ch/record/2700249.

[187] D. Lange. "The EvtGen particle decay simulation package". In: *Nuclear Instruments and Methods in Physics Research Section A: Accelerators, Spectrometers, Detectors and Associated Equipment* 462.1 (2001). BEAUTY2000, Proceedings, pp. 152–155. ISSN: 0168-9002. DOI: https://doi.org/10.1016/S0168-9002(01)00089-4. URL: http://www.sciencedirect.com/science/article/pii/S0168900201000894.

[188] The ATLAS Collaboration. "Modelling and computational improvements to the simulation of single vector-boson plus jet processes for the ATLAS experiment". In: (2021). arXiv: 2112.09588 [hep-ex].

[189] Lukas Altenkamp et al. "Gluon-induced Higgs-strahlung at next-to-leading order QCD". In: *Journal of High Energy Physics* 2013.2 (Feb. 2013). ISSN: 1029-8479. DOI: 10.1007/jhep02(2013)078.

[190] Robert V. Harlander et al. "Soft gluon resummation for gluon-induced Higgs Strahlung". In: *Journal of High Energy Physics* 2014.11 (Nov. 2014). ISSN: 1029-8479. DOI: 10.1007/jhep11(2014)082.

[191] Gavin Cullen et al. "Automated One-Loop Calculations with GoSam". In: *Eur. Phys. J.* C72 (2012), p. 1889. DOI: 10.1140/epjc/s10052-012-1889-1. arXiv: 1111.2034 [hep-ph].

[192] Sjostrand T., S. Ask, J. Christiansen, et al. "An Introduction to PYTHIA 8.2". In: *Comput. Phys. Commun.* 191 (2015), pp. 159–177. DOI: 10.1016/j.cpc.2015.01.024. arXiv: 1410.3012 [hep-ph].

[193] G. Aad et al. "Measurement of the Z/γ^* boson transverse momentum distribution in pp collisions at $\sqrt{s} = 7$ TeV with the ATLAS detector". In: *JHEP* 09 (2014), p. 145. DOI: 10.1007/JHEP09(2014)145. arXiv: 1406.3660 [hep-ex].

[194] R. D. Ball et al. "Parton distributions for the LHC Run II". In: *JHEP* 04 (2015), p. 040. DOI: 10.1007/JHEP04(2015)040. arXiv: 1410.8849 [hep-ph].

[195] Ansgar Denner et al. "HAWK 2.0: A Monte Carlo program for Higgs production in vector-boson fusion and Higgs strahlung at hadron colliders". In: *Comput. Phys. Commun.* 195 (2015), pp. 161–171. DOI: 10.1016/j.cpc.2015.04.021. arXiv: 1412.5390 [hep-ph].

[196] *SM Higgs production cross sections at 13 TeV*. Feb. 2024. URL: https://twiki.cern.ch/twiki/bin/view/LHCPhysics/CERNYellowReportPageAt13TeV.

[197] M. Bahr et al. "Herwig++ Physics and Manual". In: *Eur. Phys. J.* C58 (2008), pp. 639–707. DOI: 10.1140/epjc/s10052-008-0798-9. arXiv: 0803.0883 [hep-ph].

[198] Stefano Carrazza et al. "An Unbiased Hessian Representation for Monte Carlo PDFs". In: *Eur. Phys. J. C* 75.8 (2015), p. 369. DOI: 10.1140/epjc/s10052-015-3590-7. arXiv: 1505.06736 [hep-ph].

[199] Tanju Gleisberg and Stefan Höche. "Comix, a new matrix element generator". In: *JHEP* 12 (2008), p. 039. DOI: 10.1088/1126-6708/2008/12/039. arXiv: 0808.3674 [hep-ph].

[200] Stefan Höche et al. "A critical appraisal of NLO+PS matching methods". In: *JHEP* 09 (2012), p. 049. DOI: 10.1007/JHEP09(2012)049. arXiv: 1111.1220 [hep-ph].

[201] Stefan Höche et al. "QCD matrix elements and truncated showers". In: *JHEP* 05 (2009), p. 053. DOI: 10.1088/1126-6708/2009/05/053. arXiv: 0903.1219 [hep-ph].

[202] Stefan Höche et al. "QCD matrix elements + parton showers. The NLO case". In: *JHEP* 04 (2013), p. 027. DOI: 10.1007/JHEP04(2013)027. arXiv: 1207.5030 [hep-ph].

[203] Steffen Schumann and Frank Krauss. "A parton shower algorithm based on Catani–Seymour dipole factorisation". In: *JHEP* 03 (2008), p. 038. DOI: 10.1088/1126-6708/2008/03/038. arXiv: 0709.1027 [hep-ph].

[204] Jan-Christopher Winter, Frank Krauss, and Gerhard Soff. "A modified cluster hadronization model". In: *Eur. Phys. J. C* 36 (2004), pp. 381–395. DOI: 10.1140/epjc/s2004-01960-8. arXiv: hep-ph/0311085.

[205] S. Kallweit et al. "NLO QCD+EW predictions for V + jets including off-shell vector-boson decays and multijet merging". In: *Journal of High Energy Physics* 2016.4 (Apr. 2016), pp. 1–51. ISSN: 1029-8479. DOI: 10.1007/jhep04(2016)021.

[206] Stefan Kallweit et al. "NLO QCD+EW predictions for V + jets including off-shell vector-boson decays and multijet merging". In: *JHEP* 04 (2016), p. 021. DOI: 10.1007/JHEP04(2016)021. arXiv: 1511.08692 [hep-ph].

[207] Andrew Chisholm et al. *VH(bb/cc) modeling internal note*. Tech. rep. Geneva: CERN, 2022. URL: https://cds.cern.ch/record/2843072.

[208] Andy Buckley et al. "LHAPDF6: parton density access in the LHC precision era". In: *Eur. Phys. J. C* 75 (2015), p. 132. DOI: 10.1140/epjc/s10052-015-3318-8.

[209] The ATLAS Collaboration. *ATLAS Pythia 8 tunes to 7 TeV data*. Tech. rep. Geneva: CERN, 2014. URL: https://cds.cern.ch/record/1966419.

[210] Rikkert Frederix and Stefano Frixione. "Merging meets matching in MC@NLO". In: *JHEP* 12 (2012), p. 061. DOI: 10.1007/JHEP12(2012)061. arXiv: 1209.6215 [hep-ph].

[211] S. Frixione, P. Nason, and G. Ridolfi. "A Positive-weight next-to-leading-order Monte Carlo for heavy flavour hadroproduction". In: *JHEP* 09 (2007), p. 126. DOI: 10.1088/1126-6708/2007/09/126. arXiv: 0707.3088 [hep-ph].

[212] P. Nason. "A New method for combining NLO QCD with shower Monte Carlo algorithms". In: *JHEP* 11 (2004), p. 040. DOI: 10.1088/1126-6708/2004/11/040. arXiv: hep-ph/0409146 [hep-ph].

[213] M. Beneke et al. "Hadronic top-quark pair production with NNLL threshold resummation". In: *Nucl. Phys. B* 855 (2012), pp. 695–741. DOI: 10.1016/j.nuclphysb.2011.10.021. arXiv: 1109.1536 [hep-ph].

[214] M. Czakon and A. Mitov. "Top++: A Program for the Calculation of the Top-Pair Cross-Section at Hadron Colliders". In: *Comput. Phys. Commun.* 185 (2014), p. 2930. DOI: 10.1016/j.cpc.2014.06.021. arXiv: 1112.5675 [hep-ph].

[215] The ATLAS Collaboration. *Studies on top-quark Monte Carlo modelling with Sherpa and MG5_aMC@NLO*. ATL-PHYS-PUB-2017-007. 2017. URL: https://cds.cern.ch/record/2261938.

[216] Simone Alioli et al. "A general framework for implementing NLO calculations in shower Monte Carlo programs: the POWHEG BOX". In: *JHEP* 06 (2010), p. 043. DOI: 10.1007/JHEP06(2010)043. arXiv: 1002.2581 [hep-ph].

[217] Simone Alioli et al. "NLO single-top production matched with shower in POWHEG: s- and t-channel contributions". In: *JHEP* 09 (2009), p. 111. DOI: 10.1088/1126-6708/2009/09/111. arXiv: 0907.4076 [hep-ph].

[218] P. Kant, O.M. Kind, et al. "HatHor for single top-quark production: Updated predictions and uncertainty estimates for single top-quark production in ha-dronic collisions". In: *Computer Physics Communications* 191 (2015), pp. 74–89. ISSN: 0010-4655. DOI: https://doi.org/10.1016/j.cpc.2015.02.001. URL: http://www.sciencedirect.com/science/article/pii/S0010465515000454.

[219] Nikolaos Kidonakis. "Two-loop soft anomalous dimensions for single top quark associated production with a W^- or H^-". In: *Phys. Rev. D* 82 (2010), p. 054018. DOI: 10.1103/PhysRevD.82.054018. arXiv: 1005.4451 [hep-ph].

[220] Nikolaos Kidonakis. "Top Quark Production". In: *Proceedings, Helmholtz International Summer School on Physics of Heavy Quarks and Hadrons (HQ 2013)* (JINR, Dubna, Russia, July 15–28, 2013), pp. 139–168. DOI: 10.3204/DESY-PROC-2013-03/Kidonakis. arXiv: 1311.0283 [hep-ph].

[221] Stefano Frixione et al. "Single-top hadroproduction in association with a W boson". In: *JHEP* 07 (2008), p. 029. DOI: 10.1088/1126-6708/2008/07/029. arXiv: 0805.3067 [hep-ph].

[222] The ATLAS Collaboration. *Studies on top-quark Monte Carlo modelling for Top2016*. ATL-PHYS-PUB-2016-020. 2016. URL: https://cds.cern.ch/record/2216168.

[223] S Dawson et al. *Handbook of LHC Higgs Cross Sections: 1. Inclusive Observables*. en. 2011. DOI: 10.5170/CERN-2011-002. URL: http://cds.cern.ch/record/1318996.

[224] S. Dittmaier et al. *Handbook of LHC Higgs Cross Sections: 2. Differential Distributions*. CERN Yellow Reports: Monographs. The authors dedicate this Report to the memory of Robert Brout and Simon van der Meer. Geneva: CERN, 2012. DOI: 10.5170/CERN-2012-002. URL: https://cds.cern.ch/record/1416519.

[225] Kyle Cranmer. *Practical Statistics for the LHC*. 2015. arXiv: 1503.07622 [physics.data-an].

[226] A L Read. "Presentation of search results: the CLs technique". In: *Journal of Physics G: Nuclear and Particle Physics* 28.10 (Sept. 2002), p. 2693. DOI: 10.1088/0954-3899/28/10/313.

[227] G. Aad et al. "Measurement of the total and differential Higgs boson production cross-sections at $\sqrt{s} = 13$ TeV with the ATLAS detector by combining the H $\rightarrow$ ZZ* $\rightarrow$ 4 and H $\rightarrow \gamma\gamma$ decay channels". In: *Journal of High Energy Physics* 2023.5 (May 2023). ISSN: 1029-8479. DOI: 10.1007/jhep05(2023)028.

[228] A. Bazavov et al. "Up-, down-, strange-, charm-, and bottom-quark masses from four-flavor lattice QCD". In: *Phys. Rev. D* 98 (5 Sept. 2018), p. 054517. DOI: 10.1103/PhysRevD.98.054517.

[229] The ATLAS Collaboration. *Extrapolation of ATLAS sensitivity to $H \rightarrow b\bar{b}$ and $H \rightarrow c\bar{c}$ decays in VH production at the HL-LHC*. Tech. rep. Geneva: CERN, 2021. URL: https://cds.cern.ch/record/2788490.

[230] O. Aberle et al. *High-Luminosity Large Hadron Collider (HL-LHC): Technical design report*. CERN Yellow Reports: Monographs. Geneva: CERN, 2020. DOI: 10.23731/CYRM-2020-0010. URL: https://cds.cern.ch/record/2749422.

[231] *High Luminosity LHC Project*. Apr. 2024. URL: https://hilumilhc.web.cern.ch/content/hl-lhc-project.

[232] Burkhard Schmidt. "The High-Luminosity upgrade of the LHC: Physics and Technology Challenges for the Accelerator and the Experiments". In: *Journal of Physics: Conference Series* 706.2 (Apr. 2016), p. 022002. DOI: 10.1088/1742-6596/706/2/022002.

[233] The ATLAS Collaboration. *Expected performance of the ATLAS detector at the High-Luminosity LHC*. Tech. rep. Geneva: CERN, 2019. URL: https://cds.cern.ch/record/2655304.

[234] The ATLAS Collaboration. *Expected performance of the ATLAS detector under different High-Luminosity LHC conditions*. Tech. rep. Geneva: CERN, 2021. URL: https://cds.cern.ch/record/2776650.

[235] The ATLAS Collaboration. *Snowmass White Paper Contribution: Physics with the Phase-2 ATLAS and CMS Detectors*. Tech. rep. Geneva: CERN, 2022. URL: https://cds.cern.ch/record/2805993.

[236] The ATLAS Collaboration. *Technical Design Report for the ATLAS Inner Tracker Pixel Detector*. Tech. rep. Geneva: CERN, 2017. DOI: 10.17181/CERN.FOZZ.ZP3Q. URL: https://cds.cern.ch/record/2285585.

[237] The ATLAS Collaboration. *Technical Design Report for the ATLAS Inner Tracker Strip Detector*. Tech. rep. Geneva: CERN, 2017. URL: https://cds.cern.ch/record/2257755.

[238] Stefano Terzo and the ATLAS Collaboration. "Novel pixel sensors for the Inner Tracker upgrade of the ATLAS experiment". In: (2023). URL: https://cds.cern.ch/record/2870239.

[239] Jacobus Willem van Hoorn. "Study and Development of a novel Silicon Pixel Detector for the Upgrade of the ALICE Inner Tracking System". Presented 24 Nov 2015. TU Vienna, 2015. URL: https://cds.cern.ch/record/2119197.

[240] Maurice Garcia-Sciveres, Flavio Loddo, and Jorgen Christiansen. *RD53B Manual*. Tech. rep. Geneva: CERN, 2019. URL: https://cds.cern.ch/record/2665301.

[241] Dengfeng Zhang. "The ATLAS ITk Strip Detector System for the Phase-II LHC Upgrade". In: (2023). URL: https://cds.cern.ch/record/2879056.

[242] The ATLAS Collaboration. *Technical Design Report: A High-Granularity Timing Detector for the ATLAS Phase-II Upgrade*. Tech. rep. Geneva: CERN, 2020. URL: https://cds.cern.ch/record/2719855.

[243] The ATLAS Collaboration. *Technical Design Report for the Phase-II Upgrade of the ATLAS TDAQ System*. Tech. rep. Geneva: CERN, 2017. DOI: 10.17181/CERN.2LBB.4IAL. URL: https://cds.cern.ch/record/2285584.

[244] The ATLAS Collaboration. *Technical Design Report for the Phase-II Upgrade of the ATLAS Muon Spectrometer*. Tech. rep. Geneva: CERN, 2017. URL: https://cds.cern.ch/record/2285580.

[245] The ATLAS Collaboration. *ATLAS Liquid Argon Calorimeter Phase-II Upgrade: Technical Design Report*. Tech. rep. Geneva: CERN, 2017. DOI: 10.17181/CERN.6QIO.YGHO. URL: https://cds.cern.ch/record/2285582.

[246] The ATLAS Collaboration. *Technical Design Report for the Phase-II Upgrade of the ATLAS Tile Calorimeter*. Tech. rep. Geneva: CERN, 2017. URL: https://cds.cern.ch/record/2285583.

[247] The ATLAS Collaboration. *ATLAS HL-LHC Computing Conceptual Design Report*. Tech. rep. Geneva: CERN, 2020. URL: https://cds.cern.ch/record/2729668.

[248] Frank Hartmann. *Evolution of Silicon Sensor Technology in Particle Physics*. Springer International Publishing, 2017. ISBN: 9783319644363. DOI: 10.1007/978-3-319-64436-3.

[249] Charles Kittel and Herbert Kroemer. *Thermal Physics*. W. H. Freeman, 1980. ISBN: 978-0716710882.

[250] Charles Kittel. *Introduction to Solid State Physics*. Wiley, 2005. ISBN: 978-0471415268.

[251] Steven M. Girvin and Kun Yang. *Modern Condensed Matter Physics*. Cambridge University Press, Feb. 2019. ISBN: 9781107137394. DOI: 10.1017/9781316480649.

[252] *P-N Junction*. Apr. 2024. URL: https://devxplained.eu/en/blog/p-n-junction.

[253] *Forward biasing and reverse biasing*. Apr. 2024. URL: https://www.electrical4u.com/pn-junction/#google_vignette.

[254] F. Faccio et al. "Radiation-Induced Short Channel (RISCE) and Narrow Channel (RINCE) Effects in 65 and 130 nm MOSFETs". In: *IEEE Transactions on Nuclear Science* 62.6 (2015), pp. 2933–2940. DOI: 10.1109/TNS.2015.2492778.

[255] F. Faccio and G. Cervelli. "Radiation-induced edge effects in deep submicron CMOS transistors". In: *IEEE Transactions on Nuclear Science* 52.6 (2005), pp. 2413–2420. DOI: 10.1109/TNS.2005.860698.

[256] Federico Faccio et al. "Influence of LDD Spacers and H+ Transport on the Total-Ionizing-Dose Response of 65-nm MOSFETs Irradiated to Ultrahigh Doses". In: *IEEE Transactions on Nuclear Science* 65.1 (2018), pp. 164–174. DOI: 10.1109/TNS.2017.2760629.

[257] Giulio Borghello et al. "Dose-Rate Sensitivity of 65-nm MOSFETs Exposed to Ultra-high Doses". In: *IEEE Transactions on Nuclear Science* 65.8 (2018), pp. 1482–1487. DOI: 10.1109/TNS.2018.2828142.

[258] Daniela Bortoletto et al. *Dose rate dependence of TID damage to 65 nm CMOS transistors in X-ray irradiations of the ATLAS ITk Pixel ASIC (ITkPix)*. 2024. arXiv: 2404.10963 [physics.ins-det].

[259] A. Ducourthial et al. "Thin and edgeless sensors for ATLAS pixel detector upgrade". In: *Journal of Instrumentation* 12.12 (Dec. 2017), pp. C12038–C12038. ISSN: 1748-0221. DOI: 10.1088/1748-0221/12/12/c12038.

[260] B. Mandelli. "The Pixel Detector of the ATLAS Experiment for the Run 2 at the Large Hadron Collider". In: *Nuclear and Particle Physics Proceedings* 273-275 (2016). 37th International Conference on High Energy Physics (ICHEP), pp. 1166–1172. ISSN: 2405-6014. DOI: https://doi.org/10.1016/j.nuclphysbps.2015.09.183. URL: https://www.sciencedirect.com/science/article/pii/S2405601415006720.

[261] Maurice Garcia-Sciveres. *The RD53A Integrated Circuit*. Tech. rep. Geneva: CERN, 2017. URL: https://cds.cern.ch/record/2287593.

[262] Maurice Garcia-Sciveres. *RD53C Chip Manual*. Tech. rep. Geneva: CERN, 2024. URL: https://cds.cern.ch/record/2890222.

[263] Maurice Garcia-Sciveres. *Production chip combined requirements for ATLAS and CMS*. Tech. rep. Geneva: CERN, 2018. URL: https://cds.cern.ch/record/2632187.

[264] Timon Heim. "YARR - A PCIe based Readout Concept for Current and Future ATLAS Pixel Modules". In: *Journal of Physics: Conference Series* 898.3 (Oct. 2017), p. 032053. DOI: 10.1088/1742-6596/898/3/032053.

[265] Timon Heim. *X-ray machine introduction*. May 2024. URL: https://indico.physics.lbl.gov/event/1229/contributions/5028/attachments/2389/3110/2020_09_04-xrm-theim.pdf.

[266] Maria Mironova. "Search for Higgs Boson decays to charm quarks with the ATLAS experiment and development of novel silicon pixel detectors". Presented 06 Jul 2022. University of Oxford, 2022. URL: https://cds.cern.ch/record/2837159.

[267] *X-ray heel effect*. May 2024. URL: https://en.wikipedia.org/wiki/Heel_effect.

[268] *RD53B Anamon Repository*. https://gitlab.cern.ch/berkeleylab/labremote-apps/rd53b_anamon. Accessed: 2024-06-17.

[269] Grafana Labs. *Grafana*. Accessed: 2024-06-17. 2004. URL: https://grafana.com.

[270] Aleksandra Dimitrievska. "Low dose rate irradiation of the RD53A chip with Kr-85 beta source. TWEPP 2021 Topical Workshop on Electronics for Particle Physics". In: (2021). URL: https://cds.cern.ch/record/2782378.

[271] The ATLAS Collaboration. *ATLAS Physics Plots: FTagging 2023-01*. Accessed: 2024-06-24. 2023. URL: https://atlas.web.cern.ch/Atlas/GROUPS/PHYSICS/PLOTS/FTAG-2023-01/#tables_header.

[272] A. Tumasyan et al. "Search for Higgs Boson Decay to a Charm Quark-Antiquark Pair in Proton-Proton Collisions at $\sqrt{s} = 13$ TeV". In: *Phys. Rev. Lett.* 131 (6 Aug. 2023), p. 061801. DOI: 10.1103/PhysRevLett.131.061801.

[273] The ATLAS Collaboration. *Transformer Neural Networks for Identifying Boosted Higgs Bosons decaying into $b\bar{b}$ and $c\bar{c}$ in ATLAS*. Tech. rep. Geneva: CERN, 2023. URL: https://cds.cern.ch/record/2866601.

[274] Ben Carlson, Tao Han, and Sze Ching Iris Leung. "Higgs boson to charm quark decay in vector boson fusion plus a photon". In: *Phys. Rev. D* 104 (7 Oct. 2021), p. 073006. DOI: 10.1103/PhysRevD.104.073006.

[275] I. Agapov et al. *Future Circular Lepton Collider FCC-ee: Overview and Status*. 2022. arXiv: 2203.08310 [physics.acc-ph].

[276] The CEPC Study Group. *CEPC Technical Design Report – Accelerator (v2)*. 2024. arXiv: 2312.14363 [physics.acc-ph].

[277] Carlotta Accettura et al. *Towards a Muon Collider*. 2023. arXiv: 2303.08533 [physics.acc-ph].

[278] Yu Bai et al. "Measurements of decay branching fractions of H $\to b\bar{b}/c\bar{c}/gg$ in associated $(e^+e^-/\mu^+\mu^-)$H production at the CEPC*". In: *Chinese Physics C* 44.1 (Jan. 2020), p. 013001. DOI: 10.1088/1674-1137/44/1/013001.

[279] Matthew Forslund and Patrick Meade. "High precision higgs from high energy muon colliders". In: *Journal of High Energy Physics* 2022.8 (Aug. 2022). ISSN: 1029-8479. DOI: 10.1007/jhep08(2022)185.

[280] Markus Klute. *Hcc at the Snowmass 2021 Workshop*. Accessed: 2024-06-17. 2021. URL: https://indico.cern.ch/event/951830/contributions/3999002/attachments/2095110/3521328/Hcc_SNOWMASS21-EF2_EF0_Markus_Klute-162.pdf.

[281] Hartmut F-W Sadrozinski, Abraham Seiden, and Nicolò Cartiglia. "4D tracking with ultra-fast silicon detectors". In: *Reports on Progress in Physics* 81.2 (Dec. 2017), p. 026101. DOI: 10.1088/1361-6633/aa94d3.

[282] W. Snoeys. "Monolithic pixel detectors for high energy physics". In: *Nuclear Instruments and Methods in Physics Research Section A: Accelerators, Spectrometers, Detectors and Associated Equipment* 731 (2013). PIXEL 2012, pp. 125–130. ISSN: 0168-9002. DOI: https://doi.org/10.1016/j.nima.2013.05.073. URL: https://www.sciencedirect.com/science/article/pii/S0168900213006840.

[283] I. P. Ivanov. "Minkowski space structure of the Higgs potential in the two-Higgs-doublet model". In: *Phys. Rev. D* 75 (3 Feb. 2007), p. 035001. DOI: 10.1103/PhysRevD.75.035001.

[284] M. B. Gavela et al. "Standard Model CP-violation and Baryon asymmetry". In: *Modern Physics Letters A* 09.09 (Mar. 1994), pp. 795–809. ISSN: 1793-6632. DOI: 10.1142/s0217732394000629.

[285] Planck Collaboration et al. "Planck 2015 results. I. Overview of products and scientific results". In: *arXiv preprint arXiv:1502.01582* (2015). URL: https://arxiv.org/abs/1502.01582.

[286] Shreya P. Kumar and Martin B. Plenio. "On quantum gravity tests with composite particles". In: *Nature Communications* 11.1 (Aug. 2020), p. 3900. ISSN: 2041-1723. DOI: 10.1038/s41467-020-17518-5.